ENVIRONMENTAL APPLICATIONS FOR PHOTOGRAMMETRY WITH UAS

By

VICTORIA ALEXANDER NATALIE

Bachelors of Science in Mechanical Engineering
Texas A & M - Kingsville
Kingsville, TX
2012

Submitted to the Faculty of the
Graduate College of
Oklahoma State University
in partial fulfillment of
the requirements for
the Degree of
MASTERS OF SCIENCE
MAY, 2019

ENVIRONMENTAL APPLICATIONS FOR PHOTOGRAMMETRY WITH UAS

Thesis Approved:

Dr. Jamey Jacob

Thesis Advisor

Dr. Brian Elbing

Dr. Adam Mathews

ACKNOWLEDGMENTS

I'd like to acknowledge all of my friends and family who helped me get to this point.

My parents, who pushed me to keep trying when I felt like quitting.

My friends who kept reminding me that I am capable of completing whatever I set my mind to.

I especially want to thank my best friend and husband, Paul. He is the best partner I could ever imagine being lucky enough to find.

Name: Victoria Natalie Date of Degree: MAY, 2019

Institution: Oklahoma State University Location: Stillwater, Oklahoma

Title of Study: ENVIRONMENTAL APPLICATIONS FOR PHOTOGRAMMETRY WITH UAS

Pages in Study: 232 Candidate for the Degree of Masters

Major Field: Mechanical and Aerospace Engineering

To explore current applications for the combination of Structure from Motion and Unmanned Aerial System technology in varying environments and with project specific goals, quantitative and qualitative datasets were gathered and compared. Lessons learned and results are shared for each of four main case studies that touch on tracking fluvial geomorphology, aeolian structure mapping, automating data processing and acquisition methodologies, and combining retrospective and current datasets.

Within each case study, goals and objectives are described in detail. Platform type and any required modifications are explored. Data collection and research locations are discussed. Data analysis, metric derivation, and processing automation is discussed, as well as error analysis metrics and the resulting comparisons. Overall lessons learned and methodology alterations are discussed and outlined to provide future work suggestions for projects with similar sites and datasets.

TABLE OF CONTENTS

LIST OF FIGURES

Figure Page

CHAPTER I

Introduction

I.1 Motivation

Understanding and documenting our surroundings is a huge part of the human experience. We stand on the shoulders of giants in order to advance our society and tools. We are constantly adapting the cutting edge of varied disciplines to solve problems and one of the best ways to achieve this is to combine multidisciplinary methods in order to map and develop new techniques and technologies.

With new disciplines adding expertise and knowledge to applications, construction, and products associated with Unmanned Aerial Systems (UAS), it is important to note that this project touches on portions of Geography, Environmental Sciences, Biology, Computer Science, and Computer Engineering. However the main focus of this study stems from a Mechanical and Aerospace Engineering perspective.

Figure I.1: Phantom 4 Pro with multiple photogrammetric sensors

The rise in popularity of UAS has coincided with the development of more robust

ways to process photogrammetric data. Structure from Motion (SfM), which was developed in the 1980s has reduced the need to control certain aspects and orientations of how photogrammetric images are collected[15]. UAS technology has given rise to the ability to take high fidelity aerial images quickly and cheaply. The meeting of these two technologies has yielded an efficient and cost effective way to accurately map and process high resolution models. Utilization of these models can give us surveying information, geomorphological mapping, structural maintenance monitoring, animal and vegetation mapping, city planning and surveying, urban light surveying, and a multitude of other applications.

Although we can already use this technology for many projects, methods also are continuing to be perfected in order to get the most accurate and useful data sets possible. In order to develop these methods, researchers are acquiring an understanding of the best ways to gather data and make it work well with current and developing processing procedures.

I.2 Background

I.2.1 Structure from Motion

Photogrammetry is the process of taking measurements from images. Traditional aerial photogrammetry is derived from the use of a pair of images taken at similar times but at slightly different locations.

As shown in Figure I.2, this stereo image combination gives a 3D effect when viewed close together through a stereoscope. When information about the camera and distance from the camera to the object is known, the viewer can measure the perceived depth and derive object dimensions and other distances within the image.

Aspects of photogrammetry have been used since at least the early 1830s but, were combined with the newly created aerospace industry during WWII in order to

Figure I.2: stereoscope and matching pair of stereo images

get accurate battle maps[16]. Although photogrammetry has been used since WWII, the ability to process data without taking the time to meticulously combine images by hand has been a more recent development.

Structure from Motion allows an end user to turn 2D imagery into 3D models. This is done through feature detection, keypoint correspondence, keypoint filtering, and structure from motion bundling. Additional steps can include scaling, georeferencing, image clustering, and multi-view stereo blending.[2]

The hallmark of this technology is its lack of reliance on consistent camera specifications and image angles and altitudes. SfM, in fact, works well when the data is gathered at varying angles and altitudes. However, in order to generate enough keypoints, images should have sufficient image overlap around an object, shown in Figure I.4.

I.2.2 Unmanned Aerial Systems

Much like the combination of photogrammetry with manned aircraft in WWII, a new frontier is forming that blends Structure from Motion (SfM) technology with Unmanned Aerial Systems(UAS).

Figure I.3: Lockheed F-5 Lightning against the English countryside [1]

Unmanned Aerial Systems mostly come in two different designs, rotary and fixed wing. There are hybrid UAS platforms, but for the purpose of this study and for most photogrammetry applications, hybrid systems don't provide added efficiency yet and will, therefore, be disregarded.

Fixed wing UASs utilize their movement through the air in order to glide forward. This design aspect makes prolonged flight efficient and allows these vehicles to travel longer distances on less battery. [15]

Unfortunately for certain photogrammetric applications, this aerial efficiency can become detrimental, since these vehicles must be constantly moving and cannot hover to steady the camera when taking images. However, this issue can be minimized when using global shutter cameras and fixed wing photogrammetry aircraft are still a great choice for certain applications.

Applications that involve low light scenarios, capturing objects that have a high

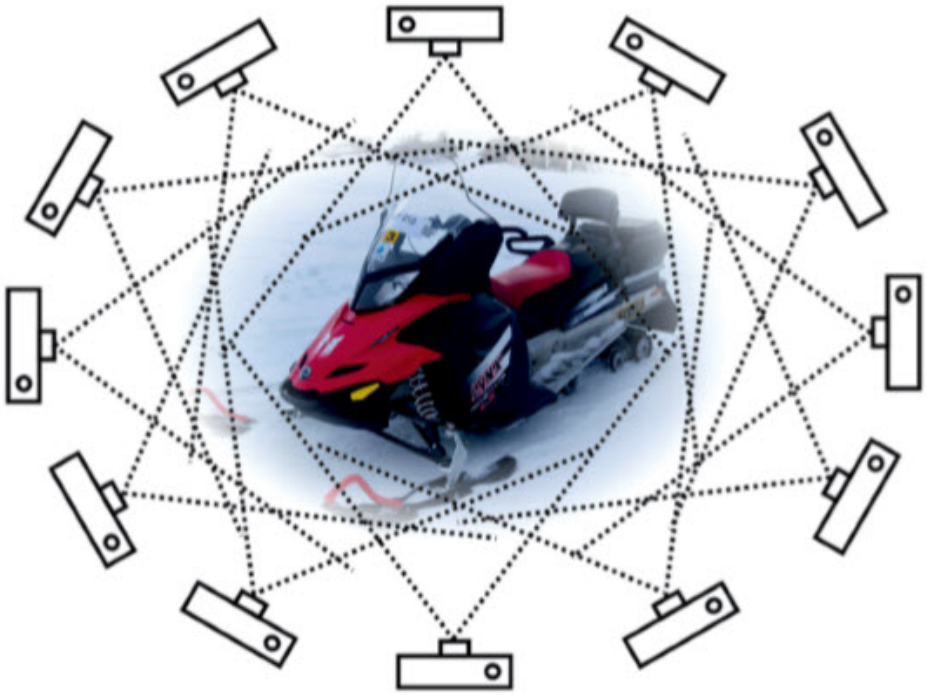

Figure I.4: example of camera path around an object[2]

chance of blur, and flying in an area where extra space to turn around outer waypoints is not available are not ideal for fixed wing aircraft and can require a larger amount of post processing to correct and throw out bad images. However, fixed wing vehicles can be an ideal solution when images need to be gathered over an extended distance.

Rotary UAS allow for more control when capturing images. Although this type of vehicle has less efficient battery rotary platforms can also take off in tight locations, pause and hover while capturing images, and in high wind situations, apply more control to image overlap during flight. These features make the rotary platform type attractive for photogrammetric applications. For these reasons, a rotary vehicle was selected for the purposes of this thesis.

I.3 Goals and Objectives

This project explores current techniques for gathering data within varying environments and evaluates tools and methods in order to obtain accurate and repeatable

(a) fixed wing design

(b) rotary design

(c) hybrid design

Figure I.5: Commercial UAS platforms.

results when measuring data within certain terrains and under certain conditions. Varied scenarios are explored in detail with different terrain and data goals but all utilize UAS driven data collection and SfM processing. This is done through examining case studies of note that contain data gathering techniques and processing based on Structure from Motion and Unmanned Aerial System tool and methods. The project culminates in a deep dive on a single case study and what datasets and methodologies are the result.

I.3.1 Objectives for Case Study 1: Noteworthy SfM Examples

The first set of case studies consists of a compilation of three quick datasets that show the flexibility and robustness of datasets created from these Structure from Motion products, and particularly how well SfM and UAS is suited for each other.

I.3.2 Objectives for Case Study 2: Lake Carl Blackwell

The second case study involves mapping the surface area of invasive vegetation at Lake Carl Blackwell in Stillwater, OK. Methods for autonomously determining the plant surface area based on color and object recognition using UAS imagery are explored.

Figure I.6: Lake Carl Blackwell in Stillwater, Oklahoma

Figure I.7: Little Sahara State Park in Waynoka, Oklahoma.

I.3.3 Objectives for Case Study 3: Little Sahara

The third case study involves moderately sized rapid geomorphologic structures in the form of sand dunes at the Little Sahara State Park, near Waynoka, OK. Flights will use flight planning software to gather topographical data and this data will be run through SfM algorithms. This will allow for the creation of a model that contains atmospheric data in combination with topographical data in order to study the interaction of the boundary layer with topographical structures of moderate size.

Figure I.8: Incised South Canadian River tributary in Union City, Oklahoma.

I.3.4 Objectives for Case Study 4: Beaver Creek

The fourth case study is taken at a location that contains an incised tributary called Beaver Creek, that runs into the South Canadian River. This location is ideal to show methods for deriving qualitative and quantitative data through a temporal scale by demonstrating how the creek has been altered over time, and where these datasets can be acquired and processed.

I.4 Outline for Results: South Canadian River Project

An in depth view of the South Canadian River Project, tracking the Arkansas River Shiner fish, involves river mapping and will include bathymetric data methods for shallow and deep waterways. The river reviewed include portions of the South Canadian River, which flows through Oklahoma. In addition, an automated method for calculating river connectivity is explored. Qualitative and quantitative data are merged to represent where UAS and SfM technology is now, and how it can be applied to fluvial geomorphology in the future.

Figure I.9: South Canadian River in Union City, Oklahoma.

Within this section, goals and objectives are described in detail. Platform type and any required modifications are discussed. Data collection and research locations are discussed. Data analysis, metric derivation, and processing automation is discussed, as well as error analysis metrics and the resulting comparisons. Overall lessons learned and methodology alterations are discussed and outlined to provide future work suggestions for projects with similar sites and data sets.

CHAPTER II

Previous Work

II.1 Existing Method Overview

Before Structure from Motion began shifting into mainstream Geographic Information Systems (GIS), traditional photogrammetry and various other methods were already employed to accurately map different environments. These methods include Total Station (TS), Differential Global Positioning Systems (dGPS), Airborne Laser Scanning (ALS), and Terrestrial Laser Scanning(TLS). In Figure II.2, Carravick et al[2] records a comparison made between the different types of surveying systems, reviewed below.

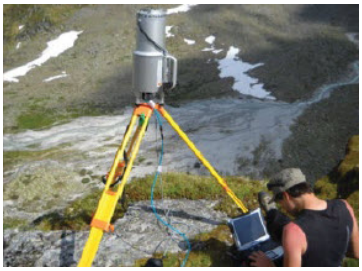

(a) Total Station[2]

(b) Differential GPS

(c) Airborne Laser Scanner[2]

Figure II.1: Different types of surveying.

Total Station (TS), shown in Figure II.1 (a), includes equipment that needs to be setup in the field, allowing information to be gathered terrestrially. It is, therefore, limited to points that surveyors can get to. Since the points are individually chosen by experts, the data can be very clean and artifact free, but is tedious to gather. Differential Global Positioning Systems (dGPS), shown in Figure II.1 (b), is similar

to TS and includes trekking equipment around the area of interest. Differential GPS does have the advantage of being able to gather thousands of points per hour, however the user needs to walk to each point individually.

In this context, Airborne Laser Scanning (ALS), shown in Figure II.1 (c), is gathered using manned aircraft. ALS is costly but can provide broad spatial coverage and typically produces a resolution on the order of 1-2 m point spacing. Finally, Terrestrial Laser Scanning (TLS) can provide sub millimeter resolution and can be used to map cliff undercuts and similarly positioned formations of interest.

Survey equipment and workflow	Typical spatial extent (km)/ typical spatial resolution (pt.m²)	Possible data acquisition rate (points per hour)	Possible 3D point accuracy (m)	Advantages	Disadvantages
TS	0.1–1.0/0.1–5.0	Hundreds	<0.001	Low cost Accurate	Line of sight required Low productivity Accuracy decreases with distance from base
dGPS	2.4–1.0/0.1–5.0	Thousands	0.005	High accuracy Range of methods have been developed to suit different surveying requirements Line of sight not required	High cost Some methods have low productivity Lock on 6+ satellites required
Photogrammetry	5.0–50.0/ 0.5–10.0	Tens of thousands	0.5	High productivity Once set up, no operator required Continuous information can be captured	Low resolution Equipment must be left in position for long periods of time (depending on survey) and may be vandalised or damaged Does not work in fog, mist, etc.
ALS	5.0–100.0/ 0.2–10.0	Millions	0.2	High productivity Can be used during the night Airborne LiDAR can survey areas that are difficult to access Not affected by vegetation cover	Very high cost Resolution may be insufficient to measure small changes Systematic errors on some landforms
TLS	0.01–5.0/ 100–10,000	Millions	0.05	High accuracy	Unable to capture all aspects of complex topographies (depending on equipment positioning)
SfM	0.01–1.0/ 1–10,000	Millions	0.01–0.2	Cheap Fast Method is independent of spatial scale	Reproducibility? Reliability?

Advantages and disadvantages are adapted with permission from Young (2013). Extent and resolution values are from figure 12 in Bangen et al. (2014).

Figure II.2: Existing surveying equipment comparison. [2]

Traditional photogrammetry was previously used onboard manned aircraft. It

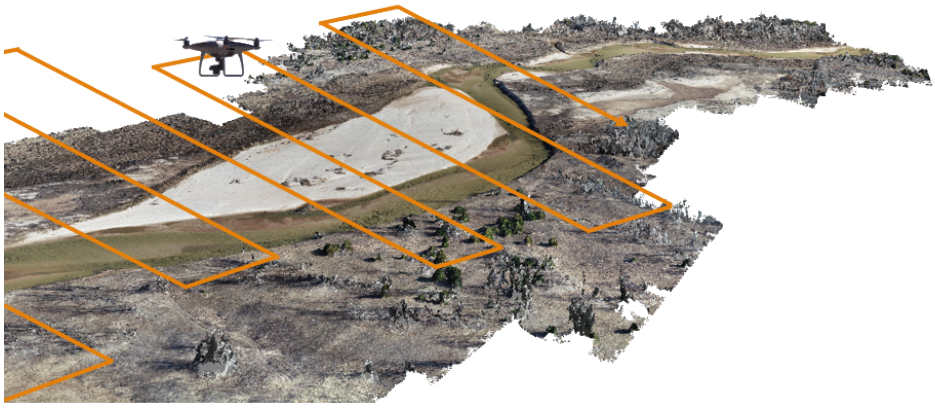

Figure II.3: Illustration of photogrammetric flight path

requires the use of a similar camera construction when stitching together images, a process that utilizes hours of tedious human visual processing after the data is collected. Similar Images are shown, and are aligned side by side but shifted enough to create a 3D affect when viewed through a stereoscope.

This process is effective, and there are some modern groups that still process aerial photogrammetry using more modern stereoscopes. In fact stereoscope technology has progressed into the digital age, an example of which is pictured in Figure II.3. Stereo based technology can be used in GIS, Computer Aided Design (CAD), and other applications.

As processing methods evolve, older technologies are moving into new rolls, and with SfM the processing time of aerial photogrammetry is greatly reduced. Overall, Structure from Motion-Multi-View Stereo (SfM-MVS) provides an enticing new method that can be used in rough terrain, cost effectively, and has relatively low processing cost.

II.2 GIS

A Geographic Information System (GIS), defined by Environmental Systems Research Institute (ESRI), integrates a multitude of data sets and data types in order to provide a framework for spatial and temporal analysis using visualizations and 3D models. By collecting data in this way, GIS can provide a unique perspective to discover previously undiscovered patterns and relationships.[17]

II.3 UAS Photogrammetry

There have been a few studies that look into the practice of using UASs to gather images, and there are even more tools and platforms coming out that are geared toward photogrammetry. Figure II.4 illustrates a typical UAS photogrammetric flight path.

Although photogrammetry doesnt necessarily need to be taken at a nadir, or down-facing, angle or at a uniform image overlap, this is often easiest when working with flight planning software to ensure uniform overlap and sidelap are recorded. When photogrammetry is taken at an angle it is called oblique. Employing these types of consistent parameters aids in the flight planning process, and allows for consistent data recording when covering a larger area.

At this point, most UAS flight planning software has mapping options or settings built in. There are also more capabilities being added all the time. Although steps need to be taken to make sure all relevant data is gathered when terrain or structures are complicated and when additional imagery is required to fully define a model, a majority of flight planning software can gather a high percentage of relevant data easily.

Figure II.4: Example of modern stereo based setup.

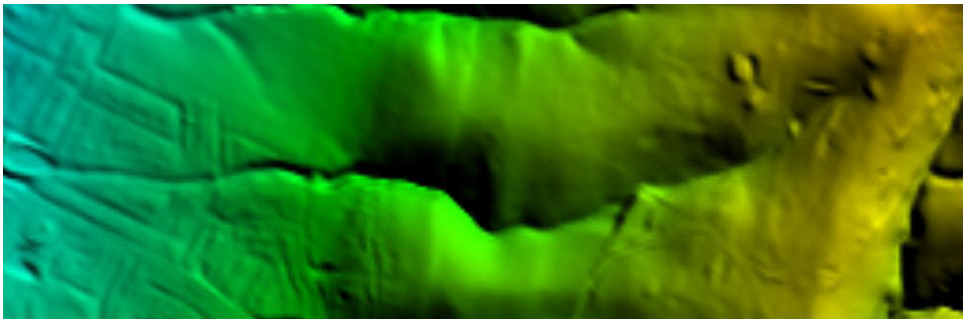

(a) Digital Terrain Model

(b) Digital Surface Model

Figure II.5: Types of DEMs. [3]

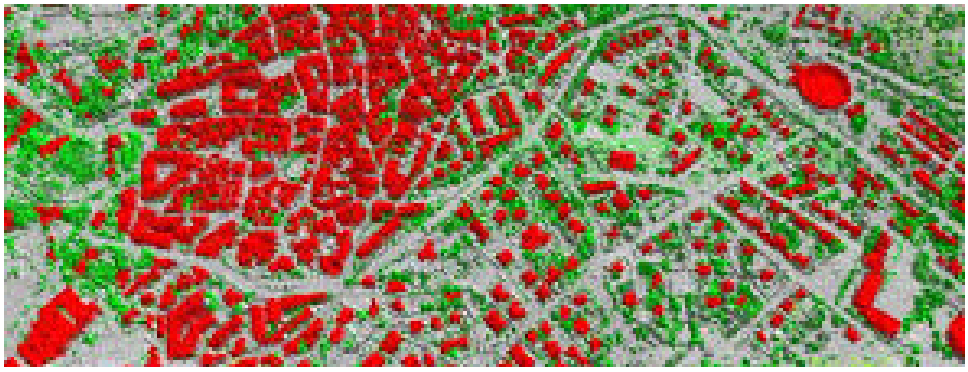

Figure II.6: Example of point cloud filtering.[3]

II.4 Types of Datasets

All of these techniques and tools yield different types of datasets, two of the most utilized are Digital Surface Models (DSM) and Digital Terrain Models (DTM). As shown in Figure II.5, DEMs include vegetation and man-made structures such as buildings or fences. DTMs are modified to remove vegetation and show the overall slope of a set of data. Both datasets can be refered to as Digital Elevation Models (DEM), and this is the convention that the SfM software refered to in this thesis utilizes.

In Structure from Motion, Digital Elevation Models tend to begin as DSMs, and can be converted to DTMs by parsing out groups of points that exhibit certain characteristics. Algorithms within SfM software have gotten better at locating and categorizing sets of points within various filters, shown in Figure II.6. Characterization of ground points can be done by hand or automatically. When done by hand, settings and criteria are chosen. Each point in the point cloud is processed and moved to the category the criteria satisfies. This results in dividing the points into specified cells and setting an allowable difference in distance and angle between those cells.

Point clouds can be compared directly or indirectly using different software. These point clouds can also be rendered into mesh outputs and brought into CAD models or exported as .stl files. These models can be 3D printed or ported into other software to

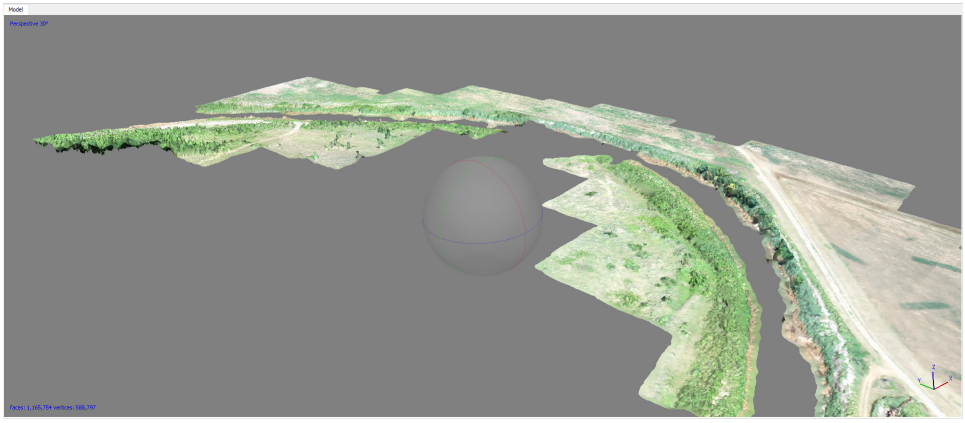

Figure II.7: Error when rendering water.

be referenced in other ways. Overall, these datasets provide important topographical information concerning the landscape and location of collected data on local and global scales. The outputs are easy to manipulate and modify and can be imported and exported as needed.

II.5 Where and When Does Error Propagate

Conditional error in the models tend to propagate when images are blurry, distorted, taken with variable light or there is not enough image overlap to render the model properly. These types of error can be minimized by choosing appropriate hardware and by taking care when data is collected.

Unmodifiable error tends to occur when mapping structures with overhang, modeling surfaces that are homogeneous and/or mobile. Water tends to be difficult since it can fall into both the homogeneous and mobile categories at once, shown in Figure II.7. Unfortunately, there is not much that can be done when collecting data to minimize this type of error. However, the SfM algorithms are becoming better at resolving this type of data and will continue to improve as computing becomes more robust and efficient.

Overall geolocation distortion and error can be improved when taking external

data into account. This tends to be done by using Ground Control Points (GCPs) in the field and independently deriving their locations using survey grade GPS. This is done so that data can be fed into the model and utilized in the derivation of the dense point cloud. However, there will always be circumstances that are beyond the control of the researcher, and the best defense is still taking more data than you think you need.

II.6 Current Studies

II.6.1 Study 1

Unlike existing data acquisition methods, structure from Motion can also be used from seemingly random data collections. Snavely et al [4] were able to take public vacation photos from across the internet and use them to reconstruct historical sites, shown in Figure II.3. This allows data to be retroactively collected based on a commodity that is become increasing more readily available: digital images.

The reconstructions shown in Figure II.8 were achieved after using any retrievable metadata in conjunction with approximating capture location details for images that did not have a recorded location or focal length. This process was based on the amount of corroborated keypoint matches and was relatively tedious. However, this exercise showed the power of using Structure from Motion to combine different types of data and how it is possible to back out initial camera placement and specifications from the imagery itself. The resulting set of models was compared with known proportions of these well-documented sites. [4] Although data like this can be retroactively geo-rectified based on accepted and accurate datasets, that is not always the case.

II.6.2 Study 2

Location, scale, and timing can prevent a dataset from having an easily comparable outside source. When this is the case, understanding how and when error is propa-

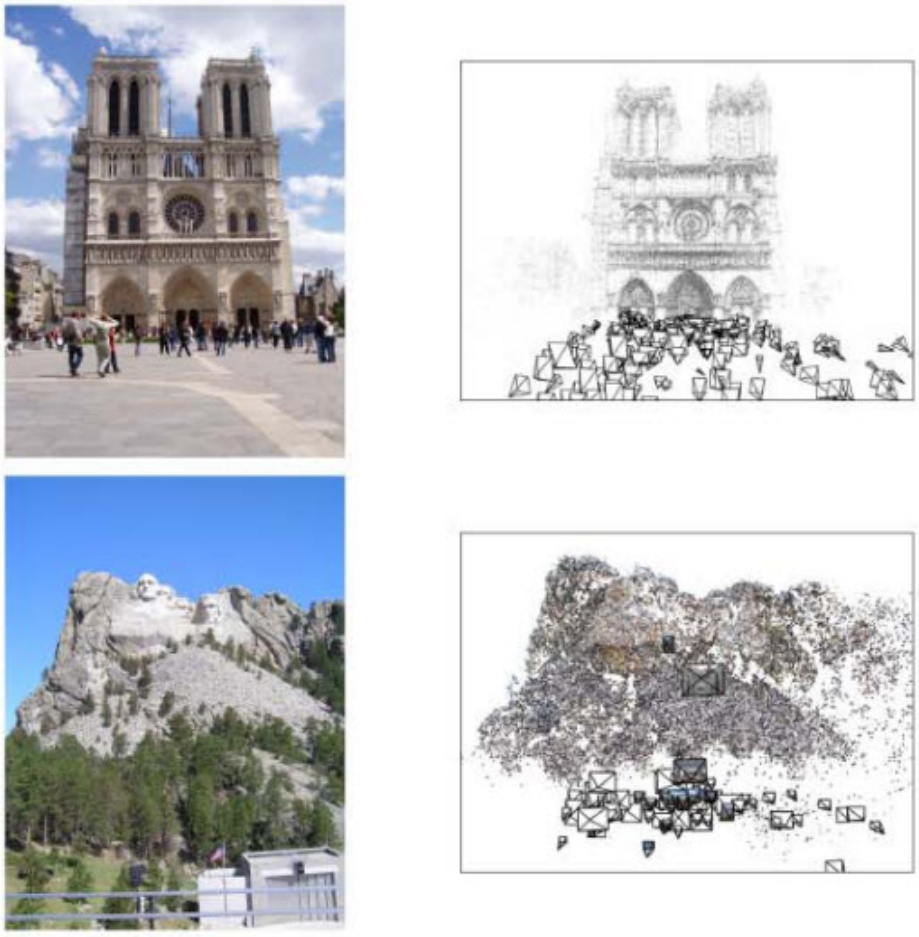

Figure II.8: Examples of models derived by Snavely et al.[4]

gated is an important metric to include with the dataset. Published in December of 2016, Day et al[5] decided to do sensor comparisons over the same location and during a relatively tight data collection window. The platforms included a manned aircraft, as well as a fixed wing and multirotor UAS. The data was all processed through the same Structure from Motion program. The flights and resulting error are detailed in Figure II.9.

As shown in Figure II.9 (b), error was worst in the Z direction, but was especially large with the lower altitudes of the UAS. This paper also highlights the need for at least three GCPs, or an equivalent way of corralling the error generated from loose GPS metadata recording.

Platform	Sensor	Bands	GSD	Altitude	Lines	Images	Time
Cessna 210	UC FalconP	RGBI	4cm	2575 ft.	2	20	4 min
Cessna 210	UC FalconP	RGBI	2cm	1375 ft.	3	48	6 min
F6500	Canon	RGB	2.76cm	400 ft.	7	192	6 min
F6500	Canon	RGB	1.38cm	200 ft.	9	231	11 min
F6500	Canon	CIR	2.76cm	400 ft.	7	192	6 min
F6500	Canon	CIR	1.38cm	200 ft.	9	231	11 min
Mavrik	Sony	RGB	1.47cm	400 ft.	4	72	5 min
Mavrik	Sony	RGB	0.72cm	200 ft.	7	285	13 min

(a)

Flight	GSD	DX in cm			DY in cm			DZ in cm		
	(cm)	2GCP RMSE	3GCP RMSE	5GCP RMSE	2GCP RMSE	3GCP RMSE	5GCP RMSE	2GCP RMSE	3GCP RMSE	5GCP RMSE
Sony 200ft	0.7	5.141	2.722	2.695	3.199	2.031	2.302	37.619	20.686	3.939
Sony 400ft	1.5	2.555	1.866	1.398	2.848	1.449	1.532	19.233	21.539	6.116
Canon 200ft	1.4	4.875	3.211	2.739	4.726	4.456	2.916	21.369	20.770	6.995
Canon 400ft	2.8	3.021	1.825	1.283	1.323	0.857	1.351	10.011	12.296	5.314
UCFp 1387ft	2.0	1.900	1.668	1.000	1.700	1.400	0.700	4.100	2.700	2.900
UCFp 2560ft	4.0	2.200	1.200	1.200	2.000	2.100	1.300	3.800	3.700	3.500

(b)

Figure II.9: Comparative flights performed by Day et al.[5]

II.6.3 Study 3

When mapping water there are a few data acquisition options, depending on how deep the water is. For deeper water, sonar units or Acoustic Doppler Current Profilers (ADCP) are reasonable solutions, however there is a depth where these sensors become ineffective and alternate sensors are required. Dietrich et al[6] derived a method to utilize optical bathymetric data by correcting for refractive error by utilizing direct photogrammetric measurements. The method was tested by modeling two different bathymetric cases.

One dataset, shown to the left in Figure II.5 was a more controlled version where Dietrich used multiple ground control points within and around a small pool and processed the data using his refraction correction script. This was manually measured using 6 GCPs in and around the 1.2 m diameter pool. The pool was filled with gravel and water in order to simulate a riverbed and the GCPs were measured using Total

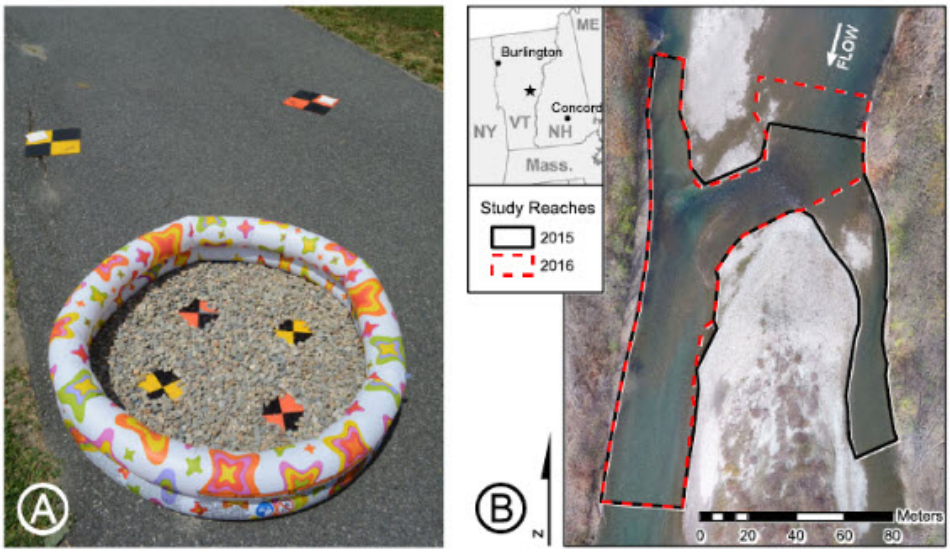

Figure II.10: Testing sites of Dietrich et al.[6]

Station.

The second dataset was taken in the field. Data was over a 250 m area near the White River in Vermont, shown to the right in Figure II.5. The White River photosets were taken over two trips and the area had been additionally mapped with GCPs around the water's edge. These points were measured with a Topcon HiperLite RTK-GPS setup. [6]

II.6.4 Study 4

As mapping using UASs becomes more popular, SfM is becoming more prevalent and more papers are been published that demonstrate the limitations, abilities, and applications of the SfM method.

Efforts, like those of Sturdivant et al[18], who used coastal imagery to produce point cloud, orthomosaic, and DEM datasets. Each dataset was evaluated for accuracy and re-sampled with various resolutions. Sturdivant was able to pull shallow bathymmetry and aeolian structures into the model.[18]

II.6.5 Study 5

Aeolian structures, such as sand dunes, tend to move quickly on a geologic scale. Because of this, they make interesting topographical subjects to map on a spatial as well as a temporal scale. Solazzo et al[19] took different types of data at the Paria Plateau and used them to quantify potential aeolian sand source areas across the plateau.After the three day campaign, there were four dunes that had multiple UAS sensor datasets. These were used to calculate the volume of the sand dunes. [19]

II.6.6 Study 6

In 2017, Rossi et al[20] performed an assessment of UAS based photogrammetry. They did a high fidelity reconstruction of topographic and geomorphic features within quarries in Italy. The images were initially nadir, even though the quarry had steep side walls, off-nadir imagery was added and the model was compared to a set of survey grade GCPs. The researchers found that sudden slope changes were the biggest issue when reviewing the fidelity of their model. In an effort to understand the results, certain shapes were located within the quarry and used as checkpoints. A total station dataset was also gathered to gather an independent dataset for comparison. Rossi et al[20] found that UASs can provide an effective solution but still need accurate GCPs.[20]

II.6.7 Study 7

The use of UAS to reconstruct coastal topography was examined by Mancini et al[21] in 2013. The researchers used SfM to process low altitude images collected by UAS. This was chosen as a topic because the technology is relatively inexpensive and automated capability and would be efficient to use in the future. This test was done at a beach dune in Italy. The dataset that was compared to the SfM dataset was a Terrestrial Laser Scanner. An average distance was found to be on the order of .015

m, a RMS of .19m, in the vertical direction. However, when the average elevations difference was compared with Digital Surface Models derived by GNSS measurements, the differences were minor. An RMS of .011 m between the TLS and GNSS measurements, and 0.15 m between the UAS dataset and the TLS. The team determined that the UAS was easy to use and the results were comparable.[21]

II.6.8 Study 8

Unmanned Aerial System based measurements during extreme flood events were discussed by Tamminga et al[22]. Because large flood events are so hard to catch, they are poorly understood. A 3D morphodynamic dataset was collected when an extreme flood even occurred between June 19 and June 23, 2013. This occurred in Canada and the area was documented to a ground resolution of 4-5cm/pixel. DEMs were produced through photogrammetry, and large scale bank erosion and channel widening was noted. An average elevation change over the area was found to be on the order of -.24 m. Shear stresses from a 2D hydrodynamic model of peak discharge was compared to critical shear stresses for surface sediment sizing. No relations were found between the two, showing how complex sediment mobilization in large scale events is. The team determined that UAS-based data acquisition is a quick an efficient way to gather important data.[22]

II.6.9 Study 9

In 1998, Lane et al[23] researched ways to use 3D Acoustic Doppler Velocimetry process when measuring channel flow. The new instrument was assessed for 3D velocity measurement capabilities in natural rivers and the best method for positioning and orienting the Acoustic Doppler Velocimeter (ADV). Since the ADV uses the Doppler shift to find small particle velocity, these measurements occur 5 cm below the sensor head. Because of this, flow field interference is minimized. [23]

II.6.10 Study 10

According to Dandois et al[24], remote sensing has changed the game with finding the spectral traits of vegetation. They examine the quality of the datasets derived from SfM and LiDAR. Structure from Motion algorithms are also explored, and data gathering techniques are discussed. These include the importance of steady lighting. SfM may be able to gather data in the critical zone of interaction between plants and light. [24]

II.7 Case Studies

II.7.1 Case Study 1-a: Cloud Mapping

Background and Data

As a demonstration of how flexible Structure from Motion can be, data was acquired and model was created while on a flight from Colorado to Oklahoma. Datasets were collected with a cell phone camera and cropped before modeling. The issue with creating cloud models is the speed at which they change shape and shadow. However, with the right tools and ample planning, this type of dataset is possible to obtain and process.

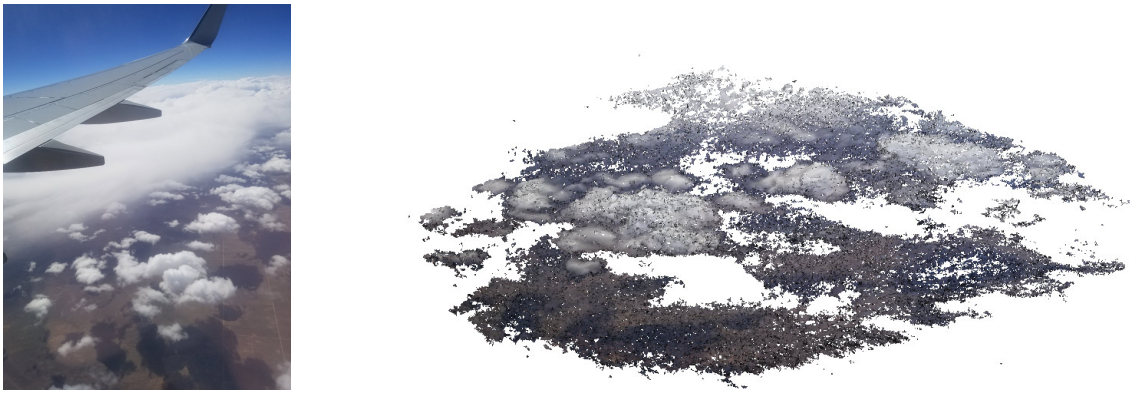

(a) Raw image (b) Dense point cloud

Figure II.11: Cloud point cloud.

Lessons Learned

Moving fast enough to get around a structure as large as a cloud is difficult. In future testing researchers suggest using multiple sensors that are well timed and are spaced far enough apart that all sides of the object will be rendered, but are not spread so far apart that keypoints cannot be matched. This would probably require different capturing strategies for different types of weather phenomena.

II.7.2 Case Study 1-b: Campus Light Survey

Background and Data

Lighting is always a concern with SfM, most objects are photographed in full sun in order to evenly illuminate the details. However, when images are collected at night in relatively well lit locations, the images can still be stitched together to provide qualitative and potentially quantitatively accurate datasets. The flight took around an hour to complete and covered an approximate area of .13 km^2.

Lessons Learned

In low light, blur becomes a major issue, two flights were completed when exploring taking photogrammetric data at night. Figure II.13 shows the result of leaving the same flight planning settings as what was used in daylight.

II.7.3 Case Study 1-c: Incised Creek at a Mammoth Dig Site

Background and Data

The location was a natural creek bed that had be incised over time to where there was a an undercut cliff face near the current stream. This location was near a mammoth dig site and was under a heavily canopied area that prevented good views and modeling from overhead. The detailed image and subsequent model was created from

(a) Raw image (b) Dense point cloud

Figure II.12: Cloud point cloud.

nine still images.

(a) Raw image (b) Point cloud

Figure II.13: Incised creek bed.

Lessons Learned

Taking detailed images was difficult due to the close proximity of the vegetation and cliff face. This method was slow and researchers were unable to ensure proper

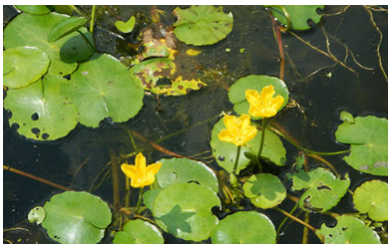

Figure II.14: Floating Yellow Heart or Nymphoides peltata.[7]

overlap and side lap in the images. However, the model is promising, and future flight planning software could cater toward similar objects that are undercut and difficult to maneuver.

II.7.4 Case Study 2: Lake Carl Blackwell

Objectives

The objective of this case study is to derive a quantitative and automated measurement of the spread of a specific vegetation in Lake Carl Blackwell. The data was gathered using Unmanned Aerial Systems and processed using Structure from Motion software to derive spatial and temporal datasets that can be assessed autonomously.

Background

Current and typical ways that changes in an aquatic systems are observed are up close and in person. This process is normally performed by technicians traveling around the affected area and taking measurements. Because the plant of interest, the Floating Yellow Heart, shown in Figure II.14, is invasive and can generated from fragmented plant sections, the use of boats and other methods to observe the change over time were not ideal. The plant itself can decrease oxygen levels in slow moving bodies of water and creates a perfect breeding ground for pests like mosquitoes. [7]

This project was done in conjunction with the Stoodley lab, the lab determined the scope of the project and locations used. Over the summer, at least four flights were

Figure II.15: Map of coves.

flown in order to track the spread of Floating Yellow Heart on Lake Carl Blackwell in Stillwater, OK. There were six specific coves that data was recorded on, shown in Figure II.15. Each cove had certain characteristics and all had a certain amount of the infestation. It was determined that cove D was bounded well enough on all sides to make for a good case to focus on. There were issues with the size of other coves, and cove A in particular had a tributary feeding in to the back of it which made it difficult to see how far the infestation was spreading on both sides.

Data Gathering and Flights

Again, a Phantom 4 Pro was used to gather images. The weather was typically clear of clouds and had low wind speeds. There were five data sets gathered over the summer and the flights were flown at an altitude of 40 m which yielded an approximate ground resolution of 1 cm/pixel. All of the sites could be flown from one location, and it was easy to observe the UAS above the trees during each flight. In total the flights took around 2 hours to complete with battery changes. The flight plan is illustrated in

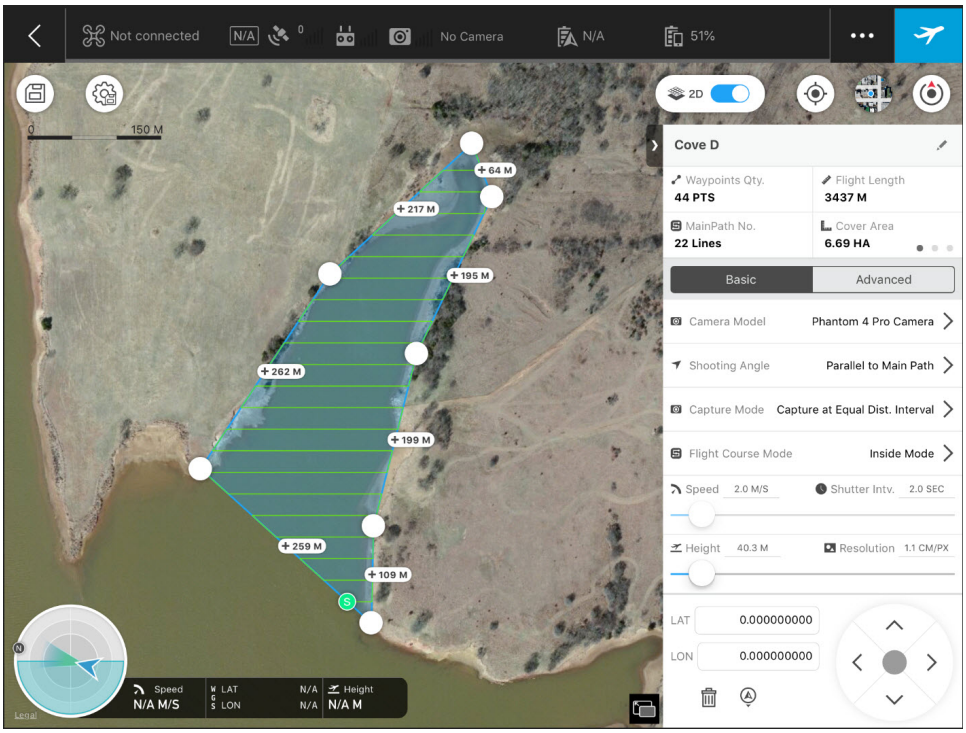

Figure II.16: Flight plan for cove D.

Figure II.16.

Data Processing and Comparisons

Agisoft Photoscan, the precursor to Metashape, was used when processing data. Typical SfM procedures were utilized in order to create orthomosaics for each cove. In Figure II.17, the Cove D orthomosaics compared temporally, a qualitative comparison shows the infestation expanding in the middle of the summer, then beginning to retreat by August.

The Matlab code tested for proof of concept and used a simple image. Figure II.18 shows the original image. A dark and a light color from the area of interest are chosen by hand. This can be altered by tweaking the color input so that different areas can be picked up. Note the difference between the color area ratio of Figure II.19 and II.20. The ratio is determined by dividing the answer value by the overall area of the image, in this case 22500 pixels. If this method is pursued, a way of automating

(a) May 9th

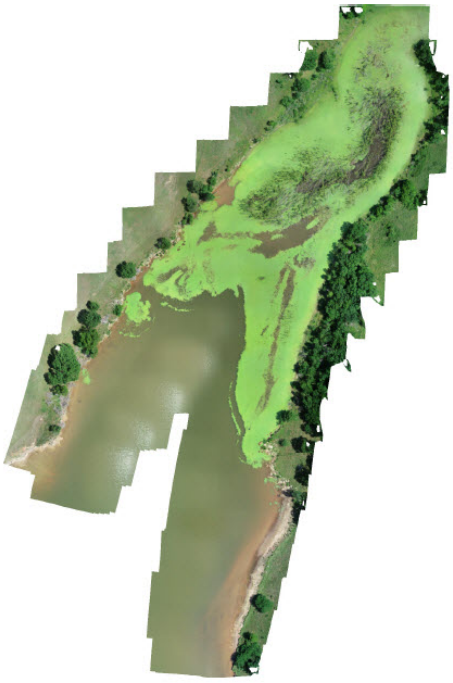

(b) June 6th

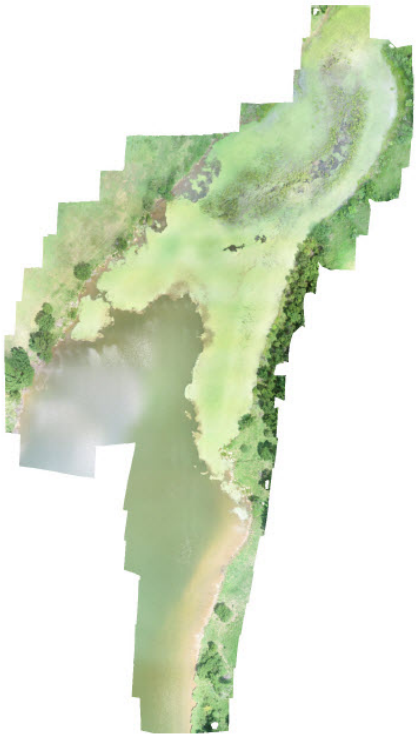

(c) July 31st

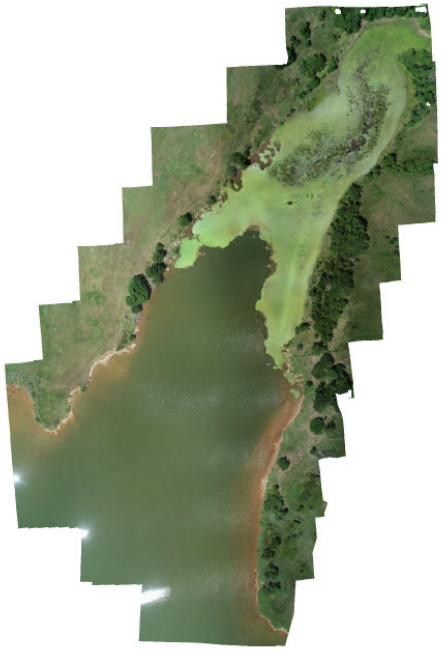

(d) August 9th

Figure II.17: Cove D through the summer.

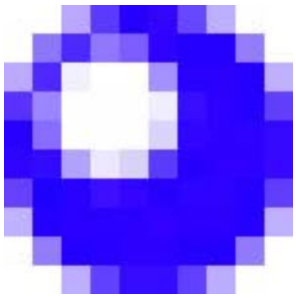

Figure II.18: Simple test image.

the color selection would be useful. However, overall, the test image works well and the ratio of pixels of interest counted to background pixels makes sense. There were issues when testing out the complex image, shown in FigureII.21, but there should be a way to tweak the settings so the code works properly.

Lessons Learned

In future vegetative tracking, looser ground resolution will be observed and more options with object mapping algorithms will be explored. Collecting data on large bodies of water with full sun proved to be more of an issue than expected. Future datasets for this project or similar datasets work best under fully cloudy conditions. The diffused light does not leave a sunspot in the majority of the images and makes the orthomosaic lighting more consistent.

II.7.5 Case Study 3: Little Sahara

Objectives

The objective of this case study is to make a point to point comparison between two sets of data that were taken at different altitudes over a homogeneous surface. In addition to determining if atmospheric data can be tied into topographical data to observe ground effects and geomorphic processes.

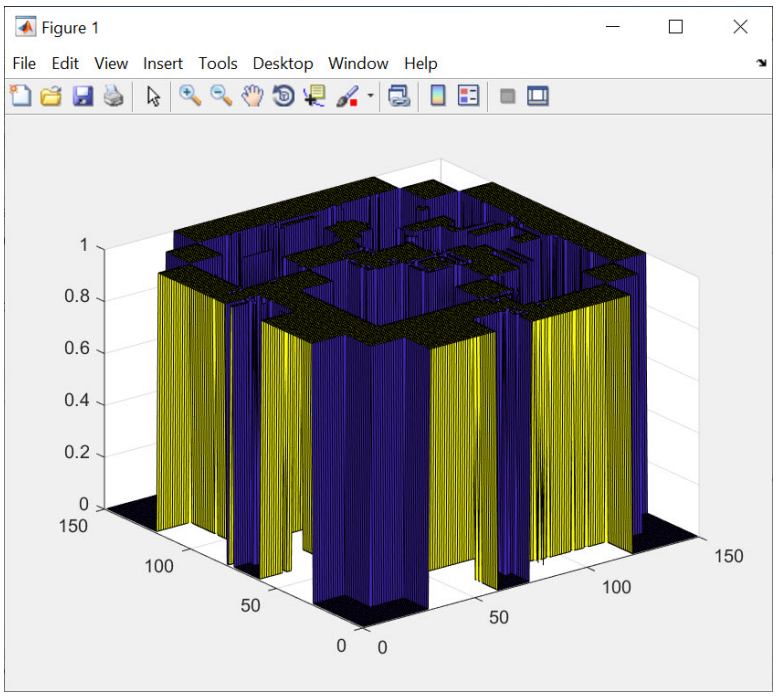

(a) Result 1

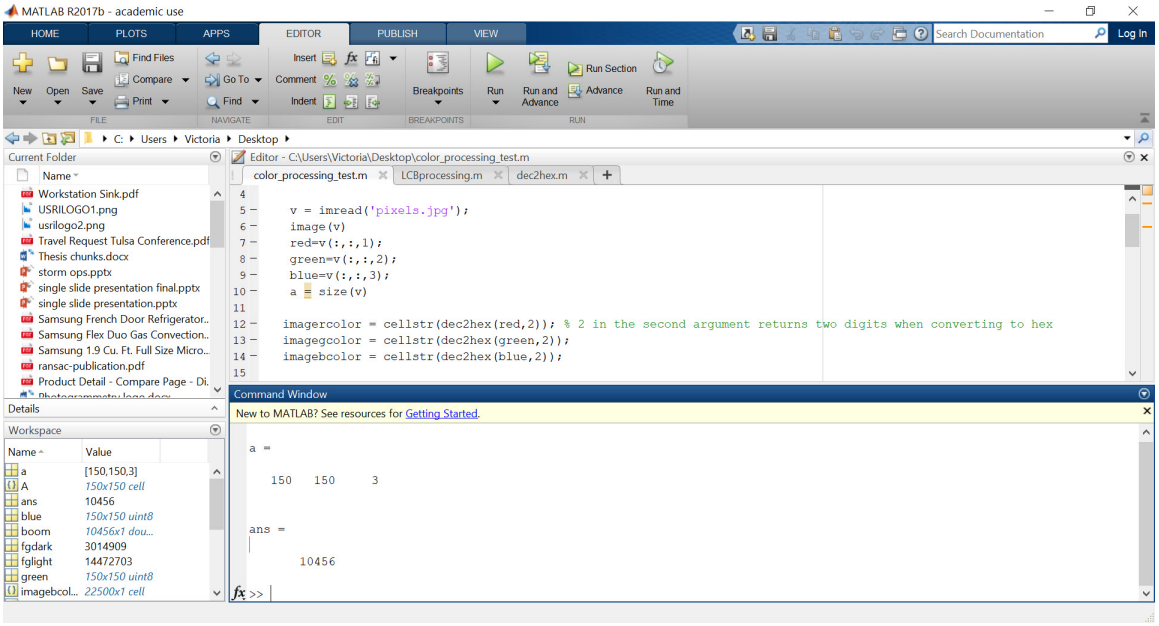

(b) Code 1

Figure II.19: The first run yielded a ratio of 47% pixels of interest to background.

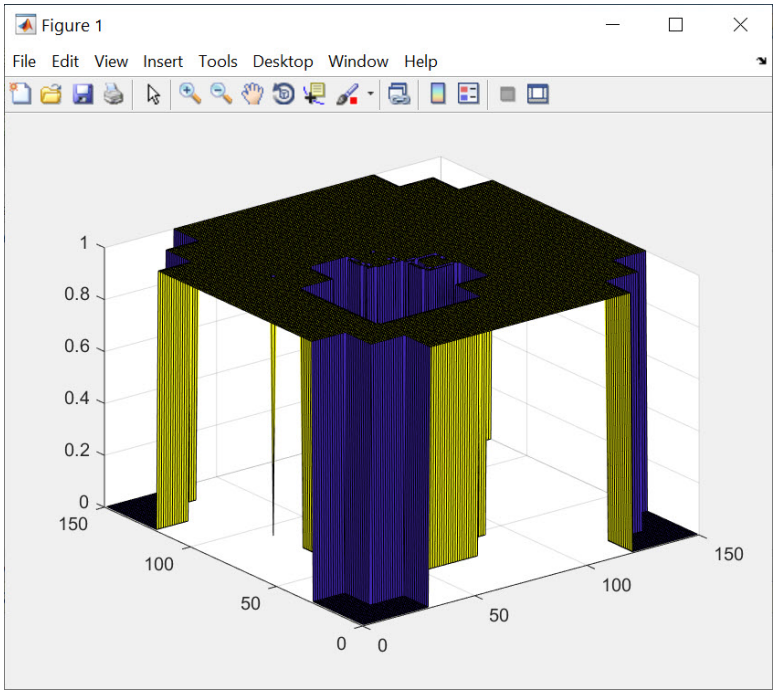

(a) Result 2

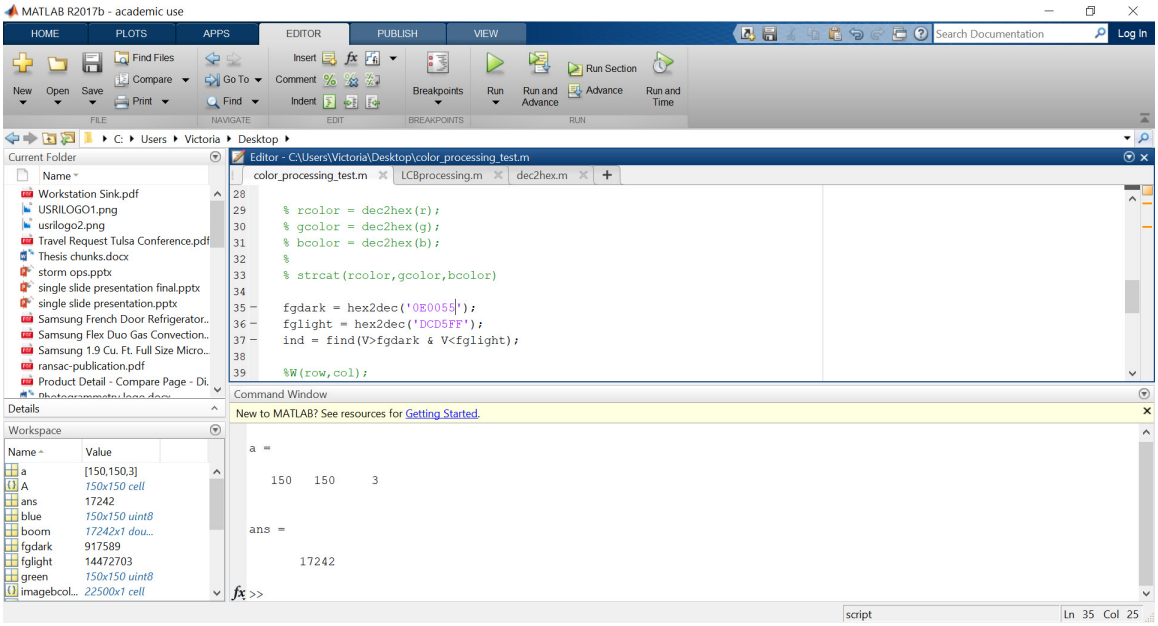

(b) Code 2

Figure II.20: This second run yielded a ratio of 77% pixels of interest to background.

Background and Flights

Two flights were performed to at the Little Sahara site. Each was taken at a different altitude. Sand is normally a difficult medium to feed into Structure from Motion

(a) Result 1

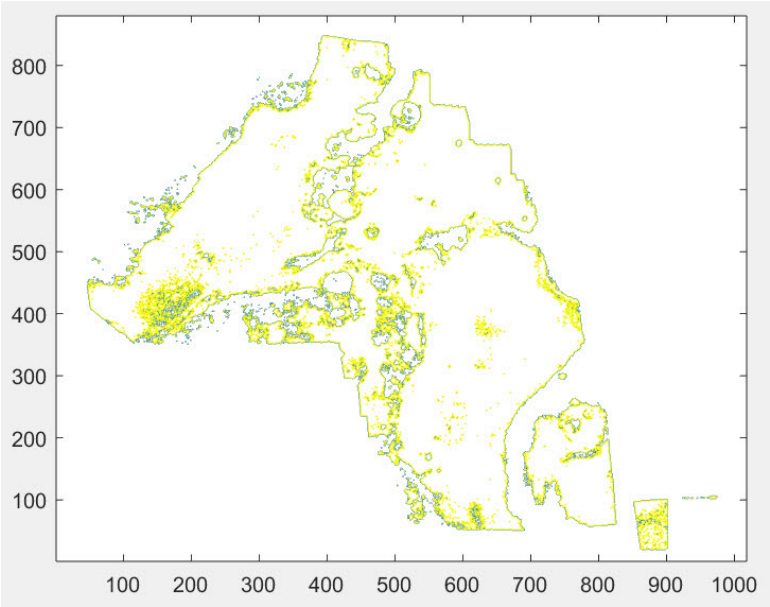

(b) Code 1

Figure II.21: Complex image Test.

algorithms and expect usable data on the other side, however the datasets acquired when testing at Little Sahara looked promising. The researchers have speculated that this may be due to tire tracks, a comparison between an image taken at the site and

Figure II.22: Image of atmospheric data being taken at Little Sahara.

(a) Image

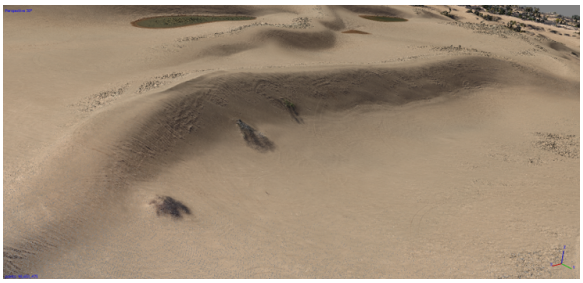

(b) Point cloud

Figure II.23: Comparison between an image and point cloud.

the point cloud is shown in Figure II.23.

Data Processing and Comparisons

The datasets were collected during the same date, The two were processed with default SfM settings and the respective point clouds were imported into Cloud Compare. The point clouds were registered, a process that performs a best fit function between two 3D datasets and the farthest point removal setting was checked. A comparison was

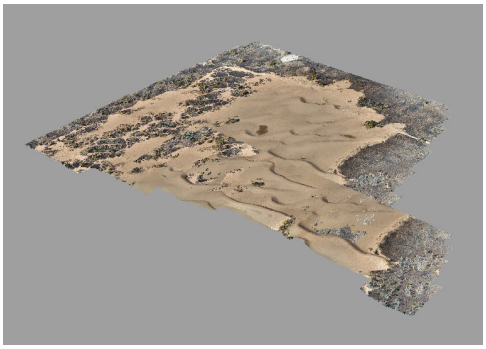

(a) Both datasets brought in at a local coordinate system.

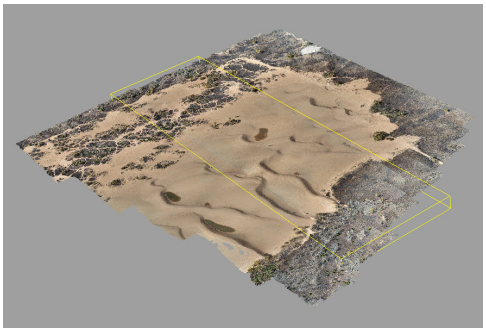

(b) Matching point clouds before the registration process

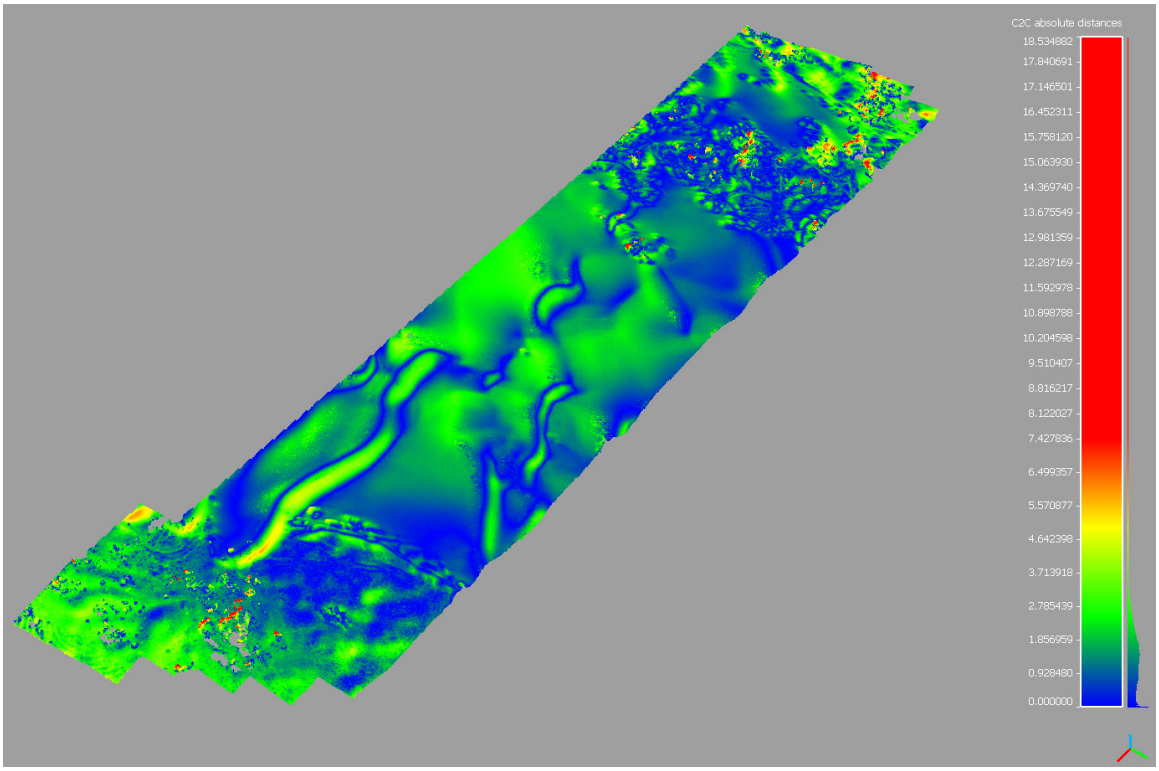

(c) Point to point

Figure II.24: Point cloud process and comparison.

made to determine the fidelity of a homogeneous and notoriously difficult to process surface at a higher altitude. The comparison appeared to be fairly close, the noisiest sections were around the foliage, but that is to be expected. That comparison was then broken into three axes to see where the discrepancies were worst. The distance remained under 2 m in the X and Y directions, discrepancies in the Z direction were

on the order of 5 m.

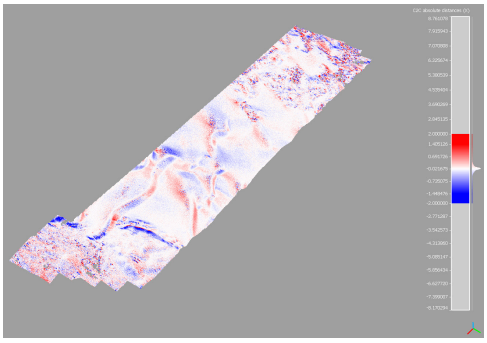

(a) Comparison in X.

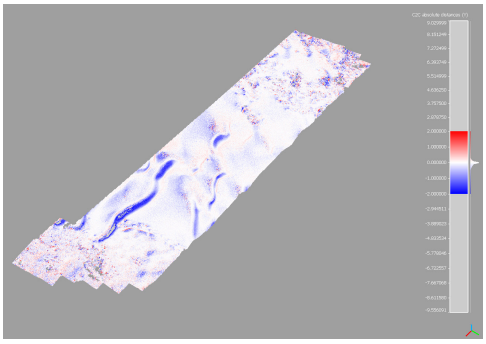

(b) Comparison in Y

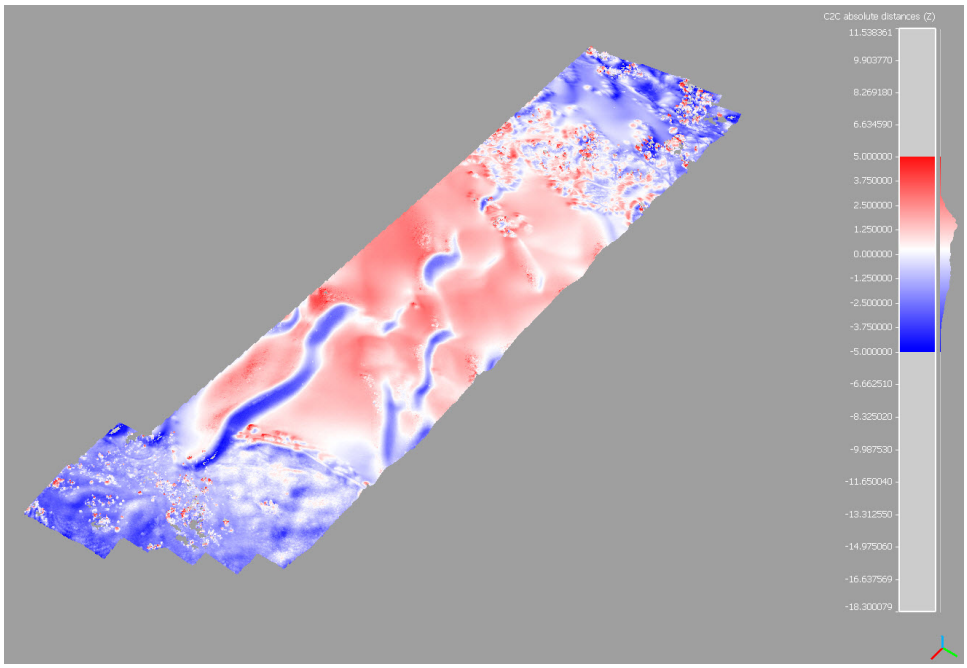

(c) Comparison in Z

Figure II.25: Point to point comparison in 3 dimensions.

Although there was no expectation of noticeable geomorphology, the wind was gusting at 40 mpg on that day and for future flights, a comparison would be interesting. A Digital Elevation Model was created in order to determine if atmospheric flights could be tied into the topographical data. A cross section of the DEM was reviewed in detail to determine if topography could viably tie into aircraft telemetry to match different the different datasets together. The fidelity of this cross section

was impressive and this technique will be used in the future.

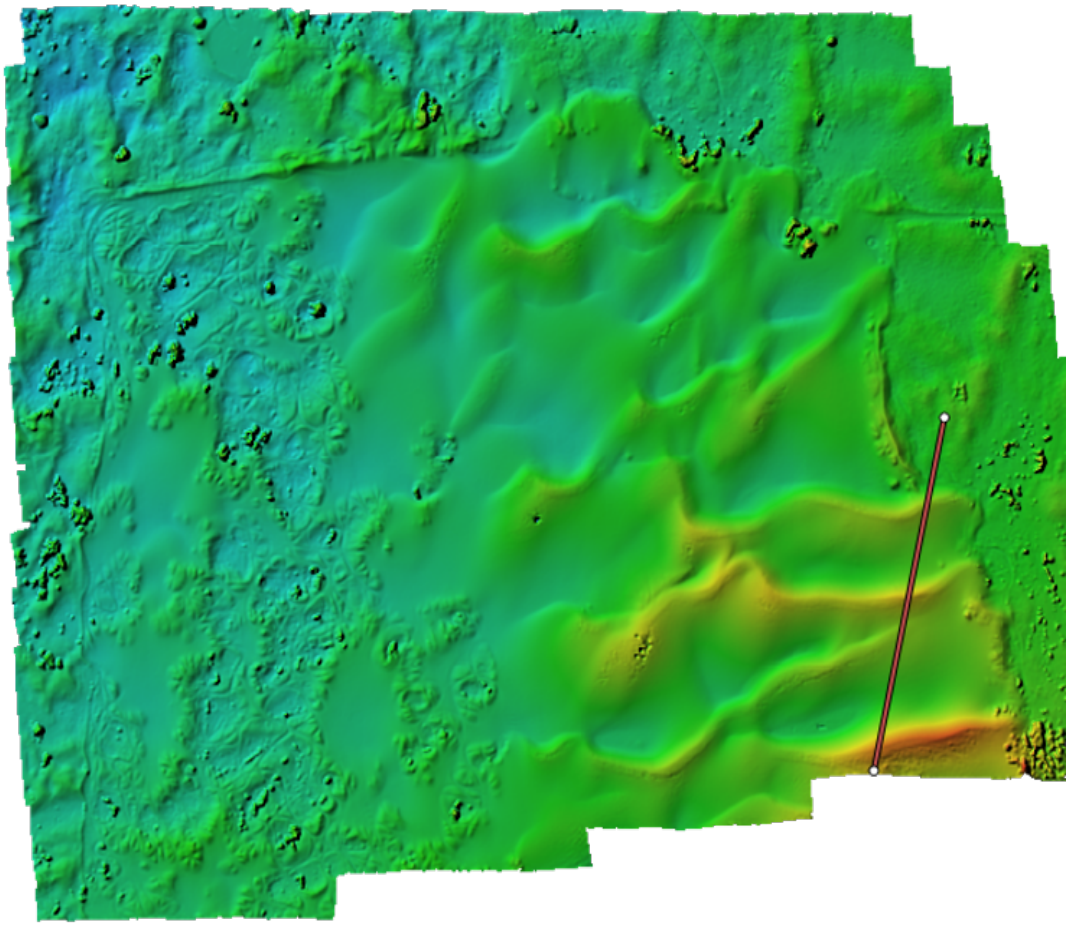

(a) Digital Elevation Model

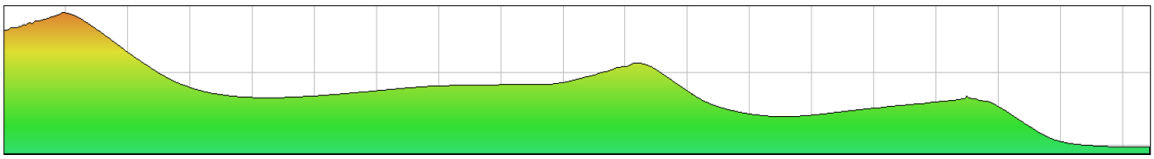

(b) Cross section of DEM

Figure II.26: DEM analysis.

Lessons Learned

Because the sand dunes were difficult to get to, the team flew from a viewing platform around .5km away. This made it difficult to know how high above the dunes each aircraft was flying. When tying in topographical and atmospheric data on the scale

found in Little Sahara, it is important to know exactly how high the craft is below the crest of the dune. For future flights an onboard laser altimeter is suggested.

II.7.6 Case Study 4: Beaver Creek

Objectives

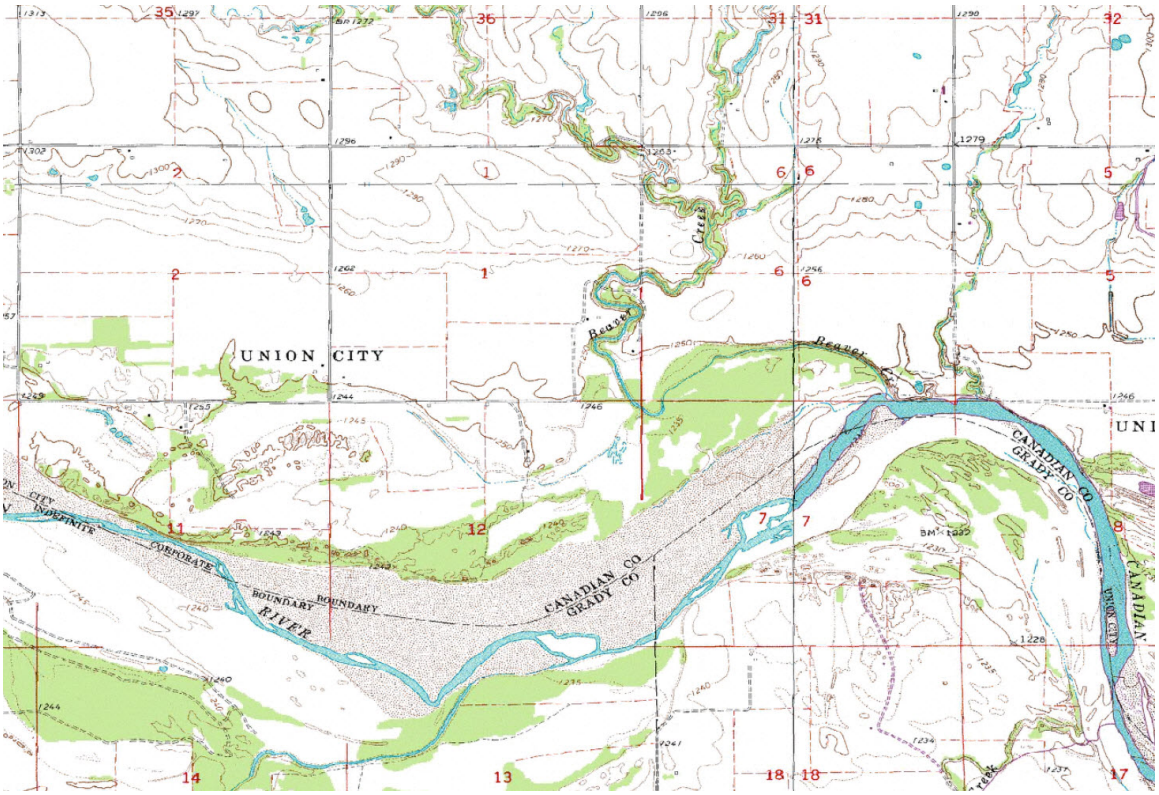

Figure II.27: USGS land and river survey map.

The objectives of this case study are to determine how helpful winter foliage is to getting accurate data compared to working with summer foliage in addition to tracking down older datasets to qualitatively show the rapid geomorphology and potentially quantitatively tie them into newer data to temporal and spatial changes. Figure II.27 shows an a survey taken by USGS, in it Beaver Creek is depicted as flowing along a different path than the path it flows now. This older path is the same one that shows up on the Google Earth Pro map.

Background and Flights

(a) Photograph of Beaver Creek from the winter of 1971

(b) Drone image taken in the Winter of 2019

Figure II.28: Old and new images Beaver Creek.

Figure II.28 shows images taken from 1971 and depicts a low creek behind the house. The creek incision must have occurred between 1971 and 1995, based on the imagery the researchers were able to find. The farm near Union City, OK, has gone through rapid fluvial geomorphological changes over the past three decades. The farm location was flown twice. The first time it was flown summer foliage seemed to be in

(a) 1995

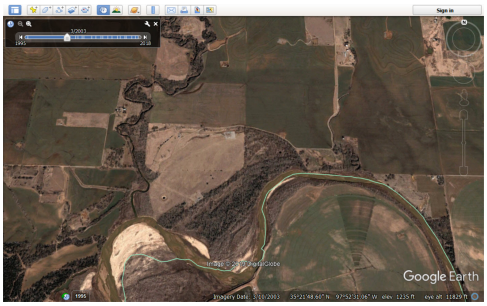

(b) 2003

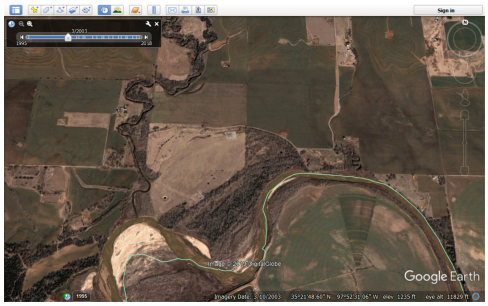

(c) 2014

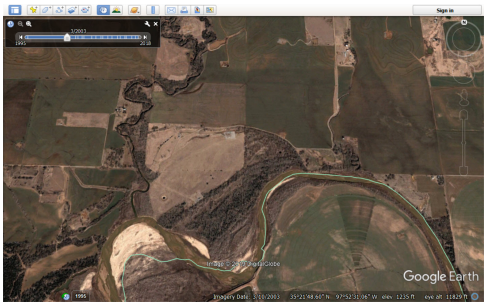

(d) 2018

Figure II.29: Google Earth Pro satellite imagery.

the way. Since the dataset was taken again in the winter, the comparison between the two is shown in FigureII.30

Data Processing and Comparisons

Google Earth Pro was used to pull satellite data. The records went back to 1995, unfortunately this was not before the stream flow was altered, but the fluvial geomorphology can be seen in the progression of images can be seen in Figure **??**.

Lessons Learned

Tying into older technology can work, ensuring that good georeferencing practices are followed helps when looking through data that needs to be looked up based on those references and when they don't have them.

(a) Summer foliage

(b) Winter foliage

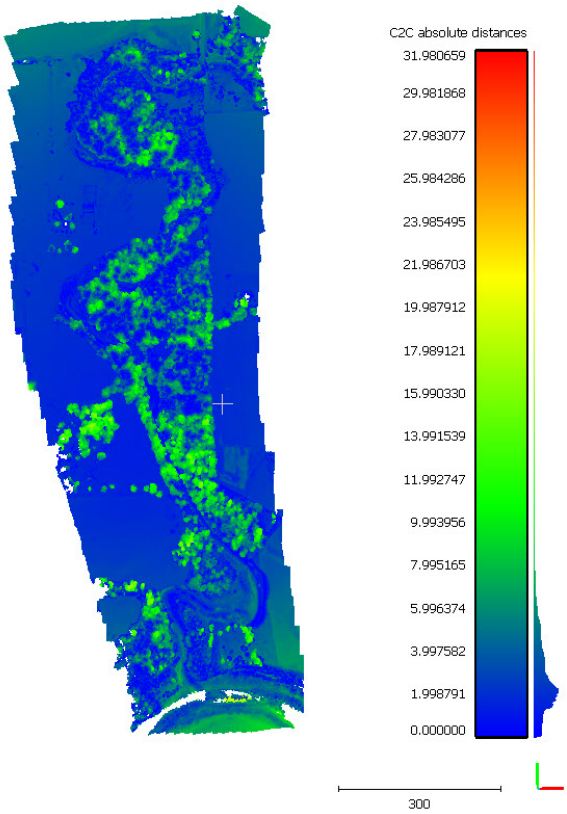

(c) Point cloud comparison

Figure II.30: Orthomosaics and point cloud comparison.

CHAPTER III

Methodology

III.1 Hardware

III.1.1 UAS Platform

The unmanned aerial vehicle chosen for gathering photogrammetric data is the DJI Phantom 4 Pro platform. The Phantom 4 pro is an easy to pilot and robust system that allows for integration with commercially available flight planning software. Since the software is designed for similar applications, control and options when crafting a photogrammetric flight plan is easy.

The Phantom 4 Pro specifications, as shown in Figure III.1, include a maximum ascent speed of 5 m/s and descent speed of 3 m/s, allowing for stable but quick flight to and from image gathering altitude. The platform also has a maximum wind speed resistance of 10 m/s or 22 mph.[9] During testing, a Phantom 4 Pro was flown in 20 mph sustained wind conditions with gusts around 40 mph. The platform handled well, but was landed in manual mode to ensure no ground affects overturned the vehicle as it landed.

The standard camera for the Phantom 4 Pro is completely integrated with the platform, this allows for easy transportation and easy software integration. Using the sensor is intuitive and requires minimal setup. The camera itself produces high resolution images that can provide centimeter to pixel accuracy when the images are rendered through SfM software. Additional camera specifications are shown in III.2.[9]

(a)

DJI Phantom 4 Pro Specifications	
AIRCRAFT	
Weight (Battery & Propellers Included)	3.06 lbs
Diagonal Size (Propellers Excluded)	35 cm
Max Ascent Speed	P-mode: 5 m/s
Max Descent Speed	P-mode: 3 m/s
Max Speed	P-mode: 31 mph (50 kph)
Max Tilt Angle	P-mode: 25°
Max Service Ceiling Above Sea Level	19685 feet (6000 m)
Max Wind Speed Resistance	10 m/s
Max Flight Time	Approx. 30 minutes
Operating Temperature Range	32° to 104°F (0° to 40°C)
Satellite Positioning Systems	GPS/GLONASS
Hover Accuracy Range	Vertical:
	±0.1 m (with Vision Positioning) ±0.5 m (with GPS Positioning)
	Horizontal:
	±0.3 m (with Vision Positioning) ±1.5 m (with GPS Positioning)

(b)

Figure III.1: UAS specifications.[8][9]

(a)

DJI Phantom 4 Pro Specifications	
GIMBAL	
Stabilization	3-axis (pitch, roll, yaw)
Controllable Range	Pitch: -90° to +30°
Max Controllable Angular Speed	Pitch: 90°/s
Angular Vibration Range	±0.02°
CAMERA	
Lens	FOV 84° 8.8 mm/24 mm (35 mm format equivalent) f/2.8 - f/11 auto focus at 1 m - ∞
Mechanical Shutter Speed	8 - 1/2000 s
Electronic Shutter Speed	8 - 1/8000 s
Image Size	3:2 Aspect Ratio: 5472 × 3648 4:3 Aspect Ratio: 4864 × 3648 16:9 Aspect Ratio: 5472 × 3078
Still Photography Modes	Single Shot Burst Shooting: 3/5/7/10/14 frames
Focal Length	24mm

(b)

Figure III.2: Sensor specifications.[9][10]

Figure III.3: Components needed for field collection

This platform has an approximate 30 minute flight time[9] in reasonable wind conditions and is quick to set up and break down. Since it is a quad copter, it can also be taken off in small spaces and is compact and easy to travel with, the entire setup can be seen in Figure III.3.

III.1.2 Survey Grade GPS

Figure III.4: Leica GPS/GNSS

A Leica Viva GS14 was used to geo-tag ground control points (GCPs). The system had a base station and a wand that was moved around to take the measurements in relation to the base station. The base station required a certain amount of setup time and has an operating radius of 2km.

(a) underwater

(b) land

Figure III.5: Ground control Points.

III.1.3 Ground Control Points

Ground Control Points (GCPs) were created for terrestrial and aquatic applications. The underwater GCPs were poured out of concrete and painted. They are approximately 30 cm in length and have a domed top to prevent sediment from burying them when placed in the river. Wooden disks were used to create the land GCPs, these were approximately 60 cm in length and were also painted.

III.1.4 Secchi Tube

Figure III.6: Secchi Tube [11]

Since the water that was being examined was relatively shallow, a secchi tube was

used to measure water clarity as opposed to a secchi disk. Both instruments use a specific symbol that the researcher views through a column of water to determine the clarity. In the case of the secchi tube, the column of water is fished out of the river and looked at, instead of the disk being lowered down.

III.1.5 Acoustic Doppler Current Profiler

(a)

River Surveyor - M9 ADCP Specifications	
SENSOR	
Profiling Range — Distance	0.06 to 40m
Profiling Range[1] — Velocity	±20 m/s
Velocity — Accuracy	±0.25% of measured velocity ±0.2cm/s
Velocity — Resolution	0.001 m/s
Number of Cells	Up to 128
Cell Size	0.02 to 4m
Transducer Configuration	Nine (9) Transducers
	Dual 4-beam 3.0 MHz/1.0 MHz Janus 25° Slant Angle 0.5 MHz Vertical Beam Echosounder
Depth — Range	0.20 to 80m
Depth — Accuracy	1%
Depth — Resolution	0.001 m
Discharge Measurement Range — Bottom-Track	0.3 to 40m
Discharge Measurement Range — RTK GPS	0.3 to 80 m
Discharge Measurement — Computations	Internal

(b)

Figure III.7: ADCP Specifications.[12]

The Acoustic Doppler Current Profiler (ADCP) used was a River Surveyor - M9. Although the depth range cannot cover water shallower than around 6 cm, the ADCP was tested in deeper water and was found to be useful in determining water column velocity as well as bathymetry.

III.2 Software

Agisoft is a commercial software that utilizes Structure from Motion-Multi-View Stereo algorithms to render point clouds, meshes, digital elevation models, and or-

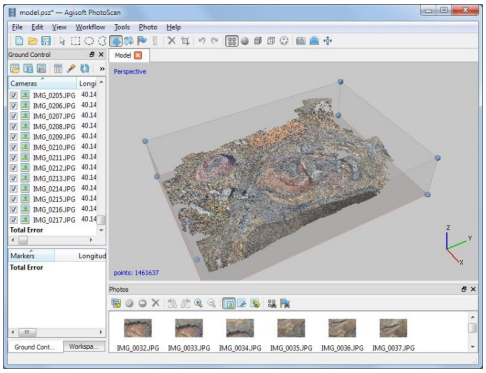

(a) Agisoft Metashape[13]

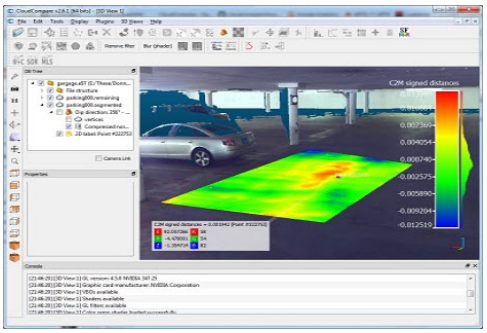

(b) Cloud Compare[25]

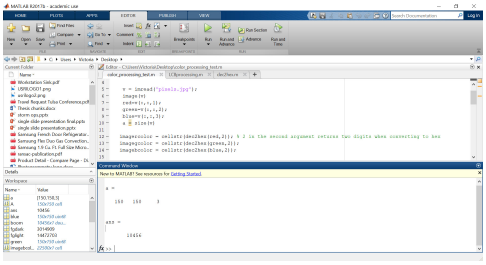

(c) Matlab

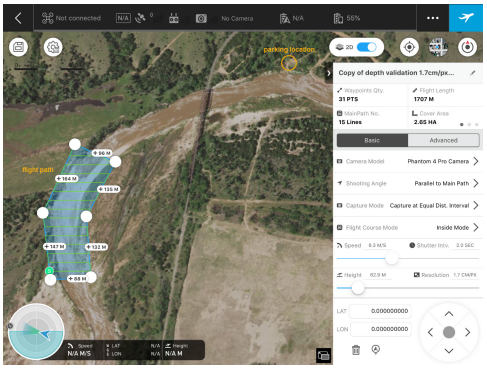

(d) GS Pro

Figure III.8: Software packages.

thomosaics using collected images. Agisoft recently switched from the Photoscan software package to the Metashape software package. The algorithms are improved in the Metashape package, and this was the software utilized for data processing. Although Metashape is adept at rendering point clouds and other datasets, there are also tools within the software that allow for measurements to be taken within DEMs and point clouds.

Cloud Compare, an open sourced, dimensionless, point cloud analysis software was also utilized. Point clouds were exported from Agisoft Metashape in text file format and imported into Cloud Compare. Different comparison methods were used, including planes within Cloud Compare for comparison within the point clouds and utilizing the internal cloud registration capabilities to match up temporally spaced point clouds.

Matlab is a scientific program that processes mathematical data, image data, and is able to do a multitude of other analyzing functions.

Ground Station Pro (GS Pro) is a flight planning software from DJI that allows the user to easily integrate with the Phantom 4 Pro platform and plan lawnmower pattern nadir and oblique angled image flights over a designated area. There are also options to set frontlap and sidelap parameters, and the planning estimates on flight time and battery count are accurate.

III.2.1 Processing Computer

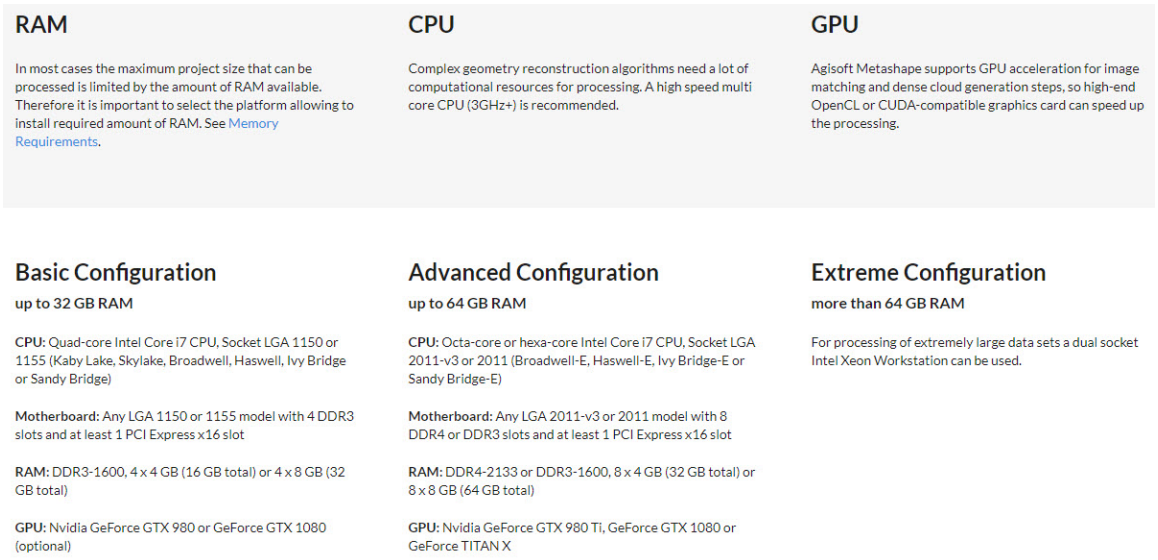

(a) Suggested computer specifications

Processor	Intel(R) Xeon(R) CPU E3-1285 v6 @ 4.10GHz 4.10 GHz
Installed RAM	64.0 GB
Device ID	12D29BC1-FA85-4510-8B7C-6FCA08CA560C
Product ID	00329-00000-00003-AA318
System type	64-bit operating system, x64-based processor

(b) Utilized specifications

Figure III.9: Required and acquired computer specifications.[13]

During this process, a 125 Gig Ram computer was used. This was based on suggestions, shown in Figure III.9, that notes Agisoft's recommendation for hardware based on computational levels. The computer utilized was a regular CPU, however a

GPU architecture is available for [13]

III.3 Algorithms

Although the process is called Structure from Motion (SfM), there is only one section of the algorithm set that is actually Structure from Motion. The overall process is is a compilation that utilizes 3D computer vision along with traditional photogrammetric techniques.

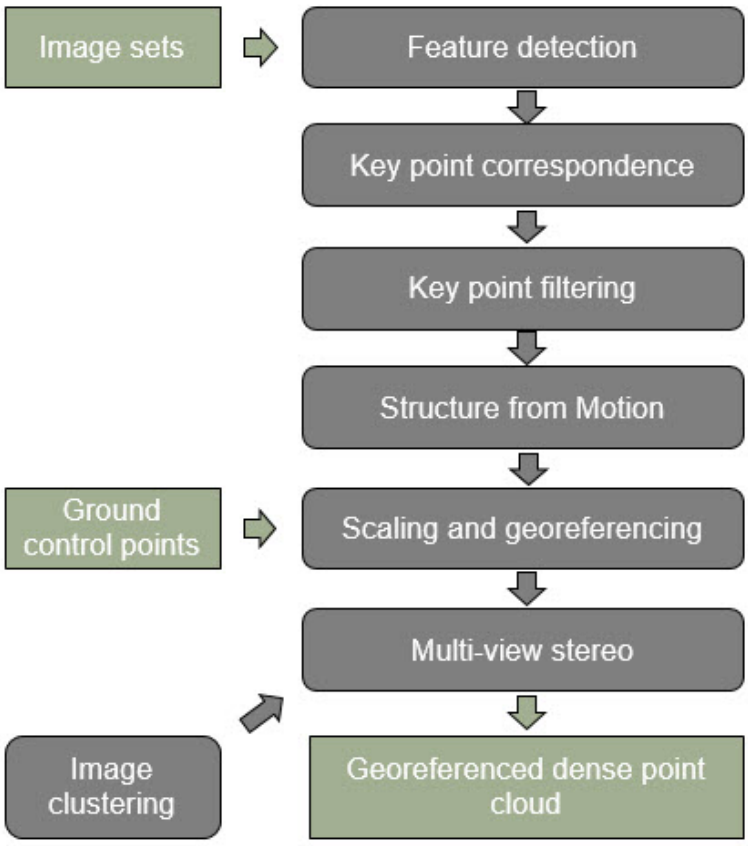

Figure III.10: SfM-MVS Algorithm Flow Chart [2]

Structure from Motion Multi-View Stereo (SFM-MVS) utilizes a group of algorithms in order to determine how to construct and connect key points in order to render a point cloud and subsequent datasets. As shown in Figure III.10, the SfM algorithms include Scale Invariance Feature Transform (SIFT), Approximate Near-

(a) (b)

Figure III.11: Feature matching.[2]

(a) (b)

Figure III.12: Keypoint selection.[2]

est Neighbors (ANN), Random Sample Consensus (RANSAC), and Structure from Motion (SfM).[2]

Scale Invariance Feature Transform (SIFT) is a computer vision algorithm that detects features. SIFT begins with the detection of spatial extrema.

Since it is invariant to scale, objects are detected by finding stable features across a continuous scale function. An intensity image goes through a Gaussian convolution at incremental scales, and the difference between the two is subtracted. The local extrema are identified through comparisons with each sample point's eight neighbors.The eight neighbors are located at different scale levels derived based on the sample point.

The next step in SIFT is keypoint localization, done by fitting a 3D quadratic function for each candidate keypoint. This checks their validity and rejected keypoints are identified and discarded. Rejected keypoints tend to have low contrast or are poorly localized along edges. Because keypoint density is based on surface texture and image resolution, the more complex and non-homogeneous images work the best.

Keypoint orientation assignment aligns keypoints through analyzing local intensity gradients. The dominant direction is chosen by using Gaussian-smoothed images. A second keypoint is subsequently created with the same location and scale, but a corrected orientation.[26]

Finally, keypoints are given a descriptor. This is based on gradient magnitudes and orientations around each keypoint. As shown in Figure III.14 the gradients are collected for each corresponding keypoint.[2]

When finding possible keypoint matches, there are a lot of extraneous matches that need to be filtered. This extra matches can be due to different reasons including objects appearing in some images but not in others.

Analysis was done on the most efficient way to shed extra matches, and a Euclidean distance when comparing the nearest neighbor to the second nearest at a minimum value of 0.8. This distance ratio was shown to eliminate 90% of the extraneous matches while leaving 95% of the correct matches.

The Approximate Nearest Neighbor (ANN) can be used to do these calculations, Lowe noted that ending the perturbations after the first 200 nearest-neighbor candidates will lose less than 5% of the correct matches but drastically cut processing time. [2]

Random Sample Consensus (RANSAC) is used to ensure that correct connections are the only ones remaining after running the data through the nearest neighbor and Euclidean distance test.

RANSAC works by assuming there are two types of keypoint data: outliers and

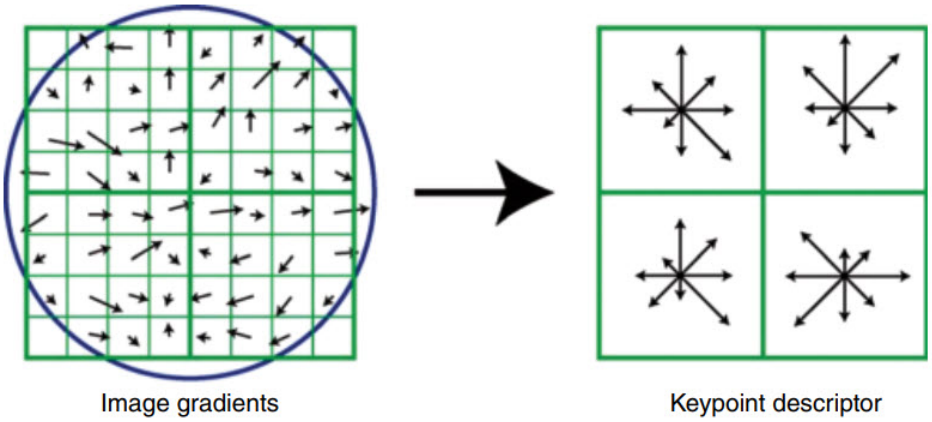

Figure III.13: Multi-view stereo.[2]

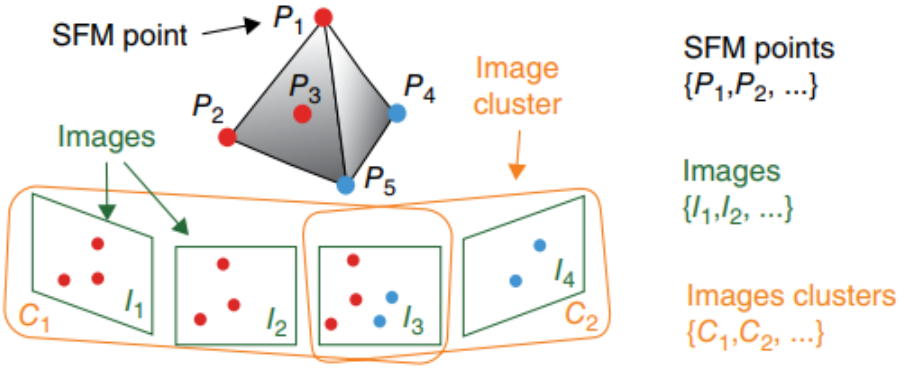

Figure III.14: Multi-view stereo.[2]

inliers. A perfect fit model would consist only of inliers. RANSAC is iteratively run through different subsets until there is a 95% chance that a subset consists of only inliers. The final model is created only using this set. Figure III.14 shows a demonstration of RANSAC compared to least squares fitting in the presence of an outlier.

The dataset can be refined further using additional algorithms, and RANSAC has been found to be unreliable when the dataset has a disproportionately large number of outliers compared to inliers. [2]

Structure from Motion (SfM) is used to estimate the geometry of a spatial dataset using camera movement. This is done by simultaneously constructing a scene, camera position, camera orientation, and, if possible, camera calibration parameters.

CHAPTER IV

Results

IV.1 Objectives

The objectives of this case study are testing ways to measure volume on and under the influence of a river surface. To determine what methods would work when obtaining visual bathymetric data, and how to deal with areas of the river that are too deep to model using SfM. To test SfM methodology and to model visually obtained bathymetric data. To record GIS data of the river on a temporal scale, and to remotely measure river bank widths within an acceptable tolerance.

IV.2 Background

Datasets used for this effort were taken during the winter, a typically dry season that was hypothesized to restrict movement of Arkansas River Shiner fish. However, the 2018 winter season proved to be a wet one, and efforts focused on proving the concept of visual bathymetry and searching for alternate methods to mark fluvial geomorphology.

The Arkansas River Shiner is a small pelagic broadcast spawning fish that is native to the great plains, shown in FigureIV.1. By tagging and tracking fish movement during dewatering and other forms of fragmentation, potential conclusions can be drawn to determine how these fishes interact and typically move within their habitat through varying river conditions and flow regimes.

Multiple sites were flown along the South Canadian River. Preliminary River data

Figure IV.1: Arkansas River Shiner

was gathered on March 22, 2018 at Green Valley Farm. The orthomosaic from this flight is shown in Figure IV.2.

Figure IV.2: Green Valley Farm Orthomosaic.

Although this was, initially, a target of opportunity, the data proved useful when exploring connectivity concepts based on riverbed topography and showing that visual bathymetry was possible in a large sandy bottom river like the South Canadian. The water was very clear during the Green Valley Farm flight and this kind of water clarity proved difficult to find during the rest of the 2018 winter season, which was markedly

rainy. Additional sites were chosen based on the efforts of the Brewer Lab, members of which conducted the capture, tagging, and release of the pelagic broadcast spawning fishes.

Figure IV.3: Sorting fish after seining.

Fish were seined and tagged at specific locations along the river, and chosen sites coincided with these locations. Flights were taken on certain days to match fish tagging and recapture sites. Figure IV.3 shows members of the Brewer lab actively sorting through their catch to find, tag, and release Arkansas River Shiner.

Flow rates were monitored using the existing USGS flow meter network along the South Canadian River. There were two critical flow meter locations utilized throughout this project, shown in Figure IV.4. The Northen-most was at Bridgeport

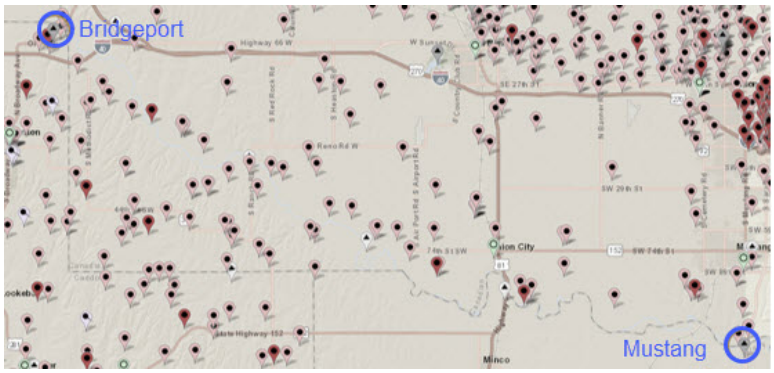

Figure IV.4: USGS Flowmeters

and the Southern-most was at Mustang. Data taken during high flow events was difficult to process, Figure IV.5 shows an event that was recorded at 448 CFS. Figure IV.6 shows the river at a flow rate of 205 CFS, almost half the flow rate shown in Figure IV.5. Both datasets were captured by a Phantom 4 Pro flown at 400 ft AGL. The swelling of the river is easily identifiable at the higher flow rate and the clarity of the water is also much lower.

This high flow obscuration is partly due to the high water, but it is also due to the turbidity of the water. Sediment is kicked up as the river swells and remains suspended in the flow for an extended period of time, making aerial riverbed observation difficult if not impossible.

Water clarity is a measurement of how many Total Suspended Solids (TSS) exist in a sample of water. This roughly translates to how far someone can see into the water, a property that greatly affects aerial bathymetry. Although the concept is simple, finding an easily repeatable quantitative metric describing constantly altering water conditions is less so. There are different tools and methods for obtaining this metric with varying degrees of accuracy and usability.

A common way to describe water clarity is through turbidity. Turbidity tends to be measured through Nephelometric Turbidity Units (NTUs), this is a measurement of scattered light in a water sample. The lower the NTU value, the clearer the water column. Turbidity is usually measured with a turbidity meter, this can be done using a hand-held unit, allowing measurements to be taken to remote locations.

A cheaper way to note water clarity is through a subjective metric that is classified based on a visual measurement where Secchi tube, shown in Figure IV.7 (a), is filled with water from the area of interest and a measurement is taken to determine how difficult it is to see the symbol pictured at the bottom of the tube. This data is dependent on a number of variables including the eyesight of the observer, and the construction of the Secchi tube itself.

Figure IV.5: South Canadian River captured on 10-16-18 at 448 CFS

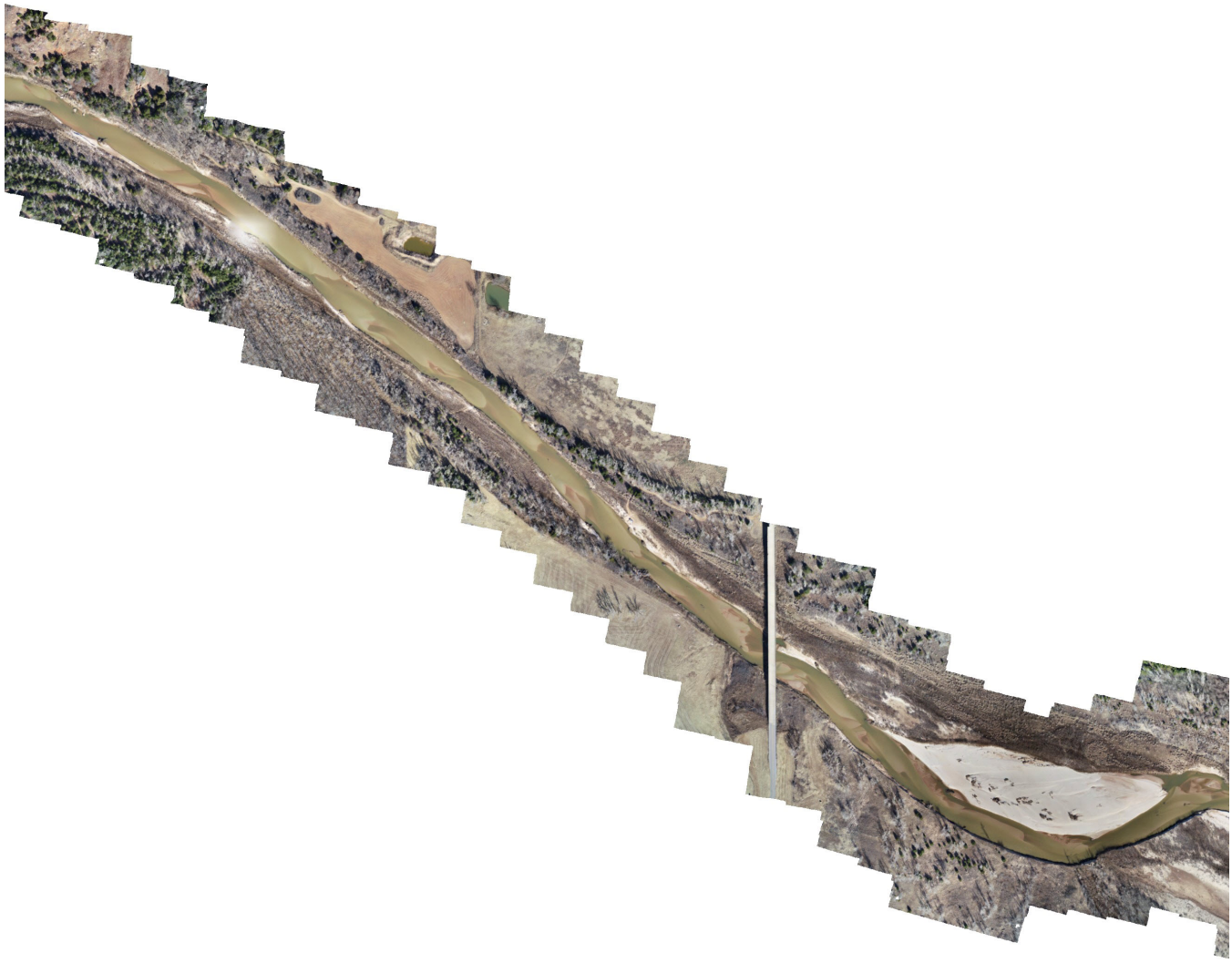

Figure IV.6: South Canadian River captured on 11-27-18 at 205 CFS

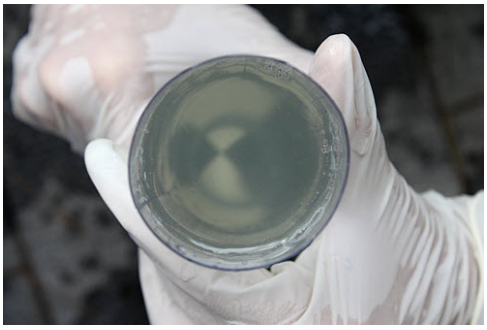

(a) Secchi Tube[27]

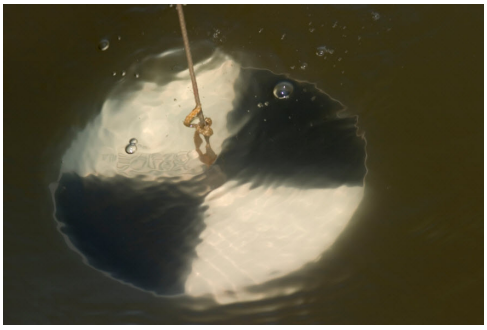

(b) Secchi Disk[28]

Figure IV.7: Clarity measurement methods.[14]

Another cost effective water clarity measurement is done by using a Secchi disk, shown in Figure IV.7 (b). The disk is lowered into the water and an average depth at which the disk is no longer visible to the observer is noted, the measurement is taken a second time and the depth is averaged. The concept of the Secchi disk is similar to the Secchi tube, and relationships between the two are assumed to have similar trends.

Water clarity, turbidity, and Secchi tube and disk measurements are closely related, and it is interesting to note that total suspended solids and Nephelometric Turbidity Units have a positive correlation when related to the depths observed with by lowering the Secchi disk, shown in Figure IV.8.

This process can also be performed in a lab setting, when a water sample is collected and evaluated by a spectrophotometer and the penetrating light is measured after passing through the sample. Seeing how easy it is to mathematically relate Secchi depth to the water clarity makes the prospect of using bathymetry to remotely determine a plausible obscuration depth an interesting prospect and could lessen the subjective nature and increase the precision and hopefully the accuracy of this metric.

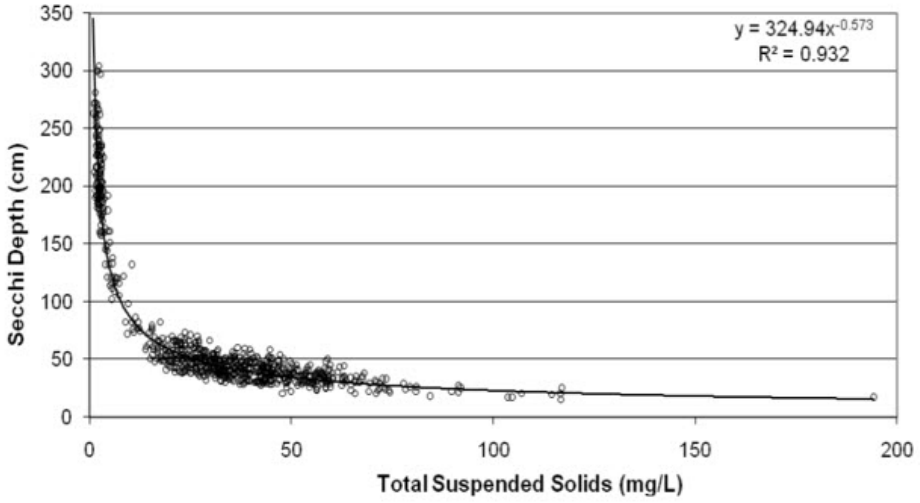

(a)

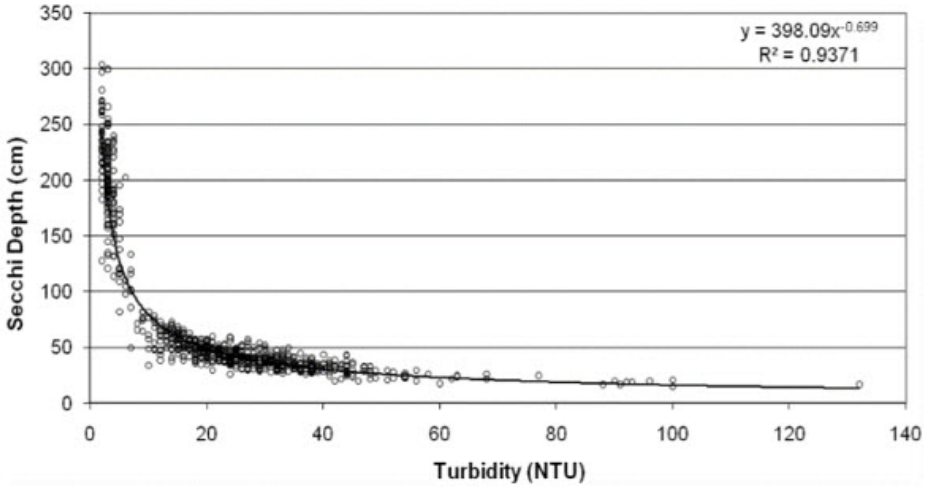

(b)

Figure IV.8: Clarity measurement comparison.[14]

Figure IV.9: Acoustic Doppler Current Profiler

IV.3 Velocity Metric Acquisition

The velocity of any river does not break down to a single value, although averages and key speeds can be isolated, there are different ways that water velocity can be autonomously measured. In order to study ways of doing this, methods were used to determine water velocity at various depths.

In an effort to find ways to map bathymetry below the visible layer of the water, an Accoustic Doppler Current Profiler (ADCP) was used. This test was performed at one of the Arkansas River Shiner tagging locations, and the results proved to be promising enough that future use of the ADCP is expected. The current ADCP setup involves pulling the device back and forth from one river bank to the other, as shown in Figure IV.9. A relationship between the location and measured bathymetry is shown in Figure IV.10. The data was roughly compared to the shape of the riverbed. It was

determined, that adding an autonomous guidance system to an unmanne watercraft would enhance the ease of use and consistently cover more area. There is also a possibly that an unmanned vehicle would allow for measurements during higher flow rates.

Water surface velocity was remotely collected through Particle Image Velocimetry (PIV), an example of PIV is shown in Figure IV.11. In order to do this, drone footage was taken and consecutive frames were extracted in order to track the immediate movement of particles naturally seeding the river. Burst photography is an option that can be explored further and may remove the need to extract consecutive frames from the video, however this was not used during testing for this thesis.

The final velocity measurement taken was by floating oranges down the river and estimating how fast they were traveling. Although the velocity of the surface of the water varied across different bathymetric points, an overall average of 6 m/s was found when comparing the flow of multiple oranges at different points along the river. Figure IV.12 shows a clip from the video with oranges and how the distance was remotely measured.

During this time, velocity measurements were also taken by members of Dr. Brewer's lab. This was done a bit further upstream at locations where fish tagging was occurring with a flow meter. Table IV.13 compares the average velocity found by the different velocity measuring methods in different locations outlined above.

IV.4 Connectivity and Bathymetry Metric Acquisition

Connectivity has varying definitions, and can be a fairly subjective metric. This is because it can be based on expert opinion, determining what kind of habitat affects fish movement. This can be due to water velocity, availability of cover, and type of habitat. For this thesis, the assumption is made that connectivity is the quantitative relationship between the ratio of water surface within bank widths versus islands or

(a) Measured transect

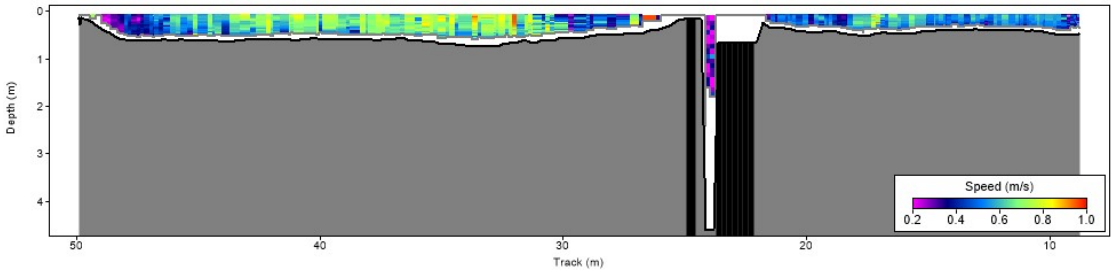

(b) Velocity in transect

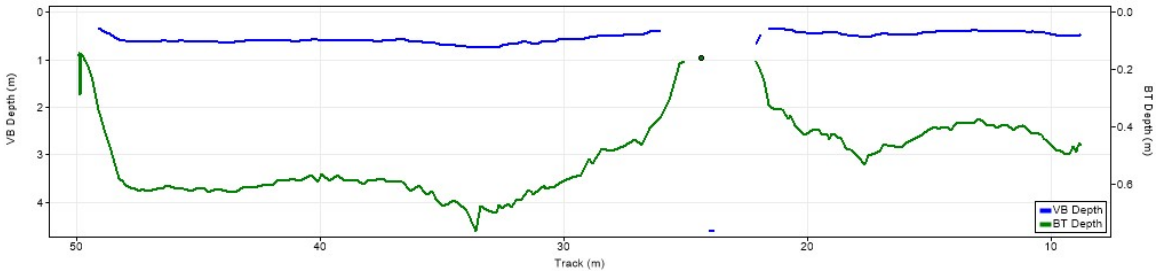

(c) Bathymetry in transect.

Figure IV.10: ADCP transect and measurements.

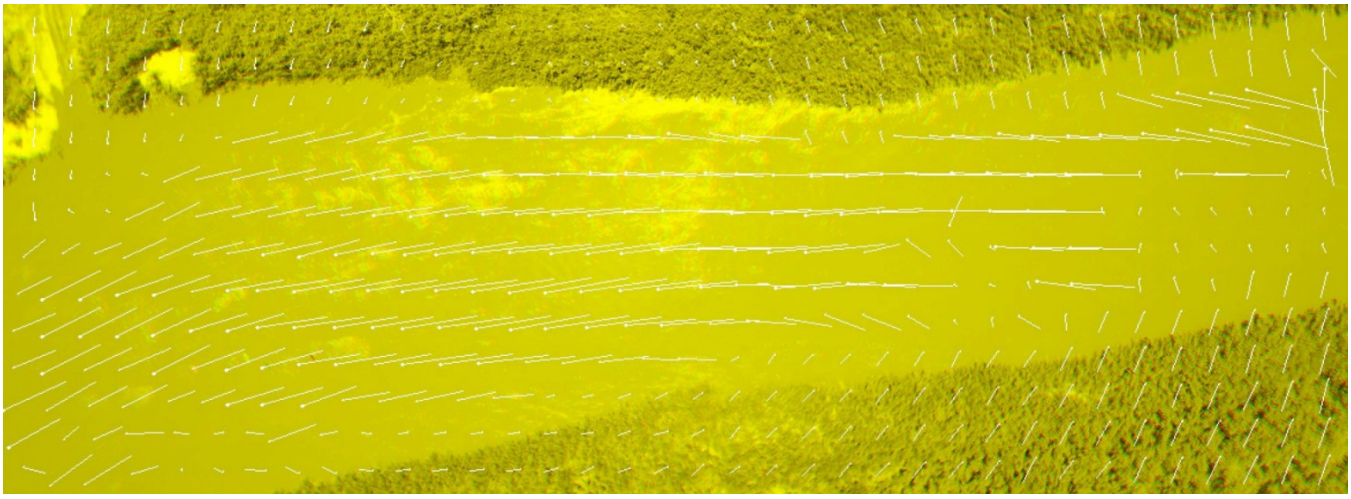

Figure IV.11: Particle Image Velocimetry example

sand bars. This concept is demonstrated in Figure IV.14, the Figure depicts the Green Valley Farm location.

Although Green Valley Farms is not a tagging site, the dataset was used because water clarity was such an issue during the dry season, detail images of the Green Valley Farm flight were used when exploring the concept of river connectivity using object mapping. Efforts were initially made to autonomously derive a connectivity metric by using color to analyze the connectivity ratio.

The interpretation of connectivity in the Arkansas River Shiner project became a percentage value and a frequency value. The percentage was determined autonomously and was based on the sand to water ratio. The frequency value was used to note whether the river completely disconnected at any point along the surveyed area.

Images were initially processed based on color alone, this was done through a Matlab code that isolated a blend of the color of the water, this was based on groups of pixels chosen by the user, shown in Figure IV.15, and classified it as foreground and background respectively.

The total number of pixels were counted and multiplied by the flight resolution

(a) Video of oranges

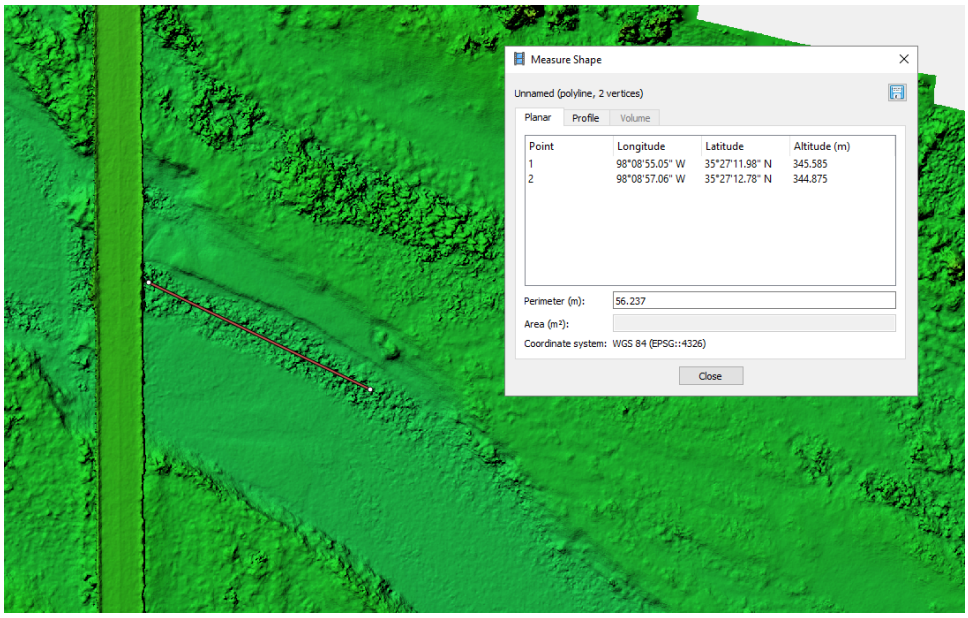

(b) Measurements from DEM of Site 4

Figure IV.12: ADCP transect and measurements.

Velocity Comparison		
Location	Method	Velocity
Site 4	Timed Float (oranges)	6 m/s
	Flow Meter	6 - 7 m/s
	Particle Image Velocimetry (PIV)	
Site 6	Acoustic Doppler Current Profiler (ADCP)	6 - 8 m/s
	Flow Meter	8 m/s

Figure IV.13: Velocity Comparison

in order to determine an area. Figure IV.15 shows the pixel selection.

Utilizing this code was able to approximately isolate the river, however the fidelity of using only color was not a good indication of where sand bars and sand island were sticking up out of the water. Figure IV.16 shows an overlay of the foreground selection, shown in pink, and the background selection, shown in green, over the original image.

IV.4.1 Bathymetric Flight 1

Cloud cover was minimal and, although the flow rate seemed high at this location, it coincided with Arkansas River Shiner tagging during that time, so it was chosen anyway. Having a low flow rate is not only important for point cloud noise reduction, but it quickly becomes unsafe to walk in the river as the flow increases. During this particular flight, the flow meter at the Bridgeport site reading above 400 CFS. The site is downstream enough that the conditions were not ideal, and if the river had swollen anymore, testing may have not yielded any results.

In this Flight, the term GCP refers to objects that were used to mark where depth measurements were taken. These GCPs did not have full GPS locations, and were not used in refining the processed data. There was a worry about underwater Ground Control Points (GCPs) getting washed away or covered with sand by the flow of the water. Because of this, the GCPs had been designed to be relatively heavy and have a dome like shape on the top. However, a river float was provided to assist with carrying the concrete underwater GCPs, shown in Figure IV.18 and came in handy

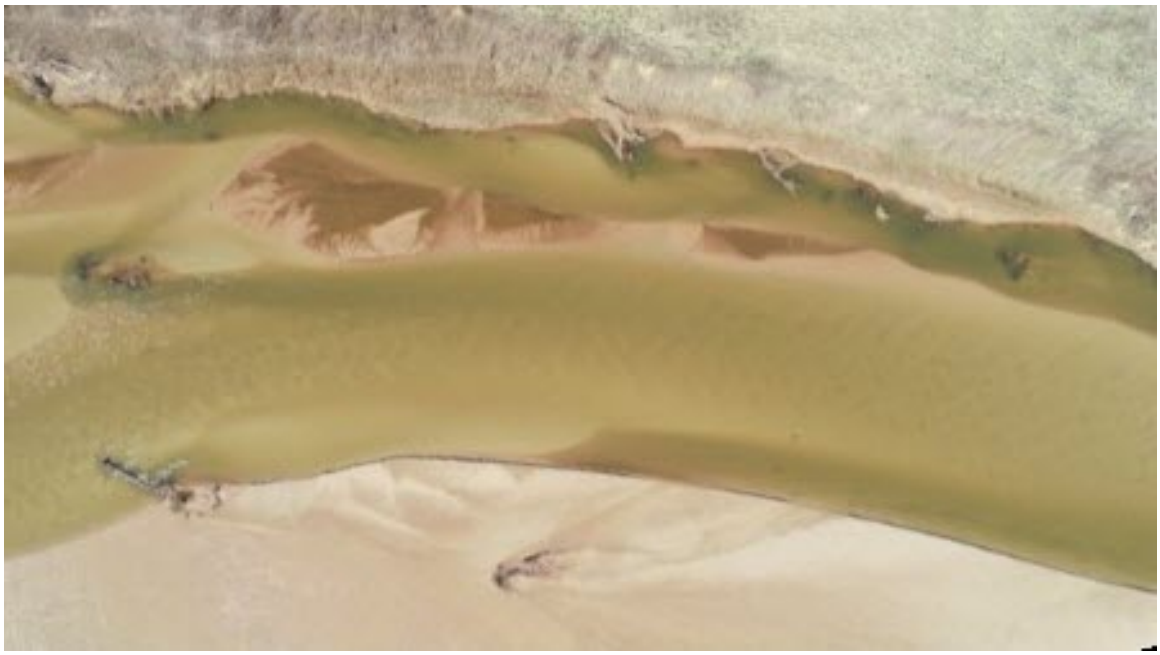

(a)

(b)

Figure IV.14: Example of how connectivity is expected to be derived.

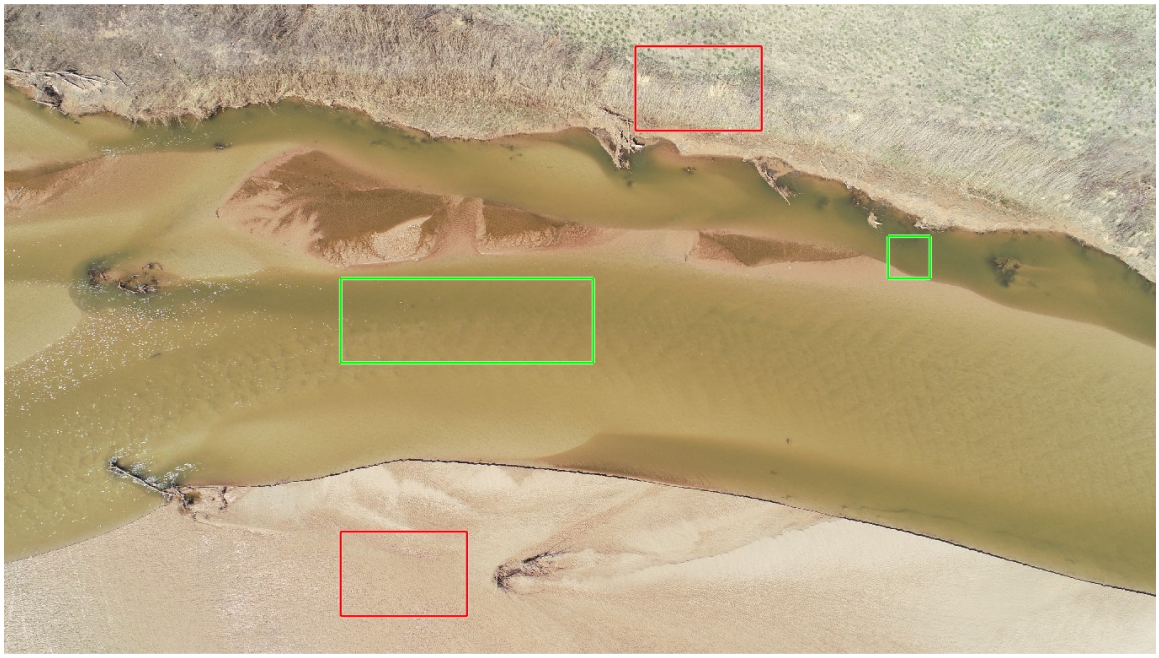

Figure IV.15: Color blend selection.

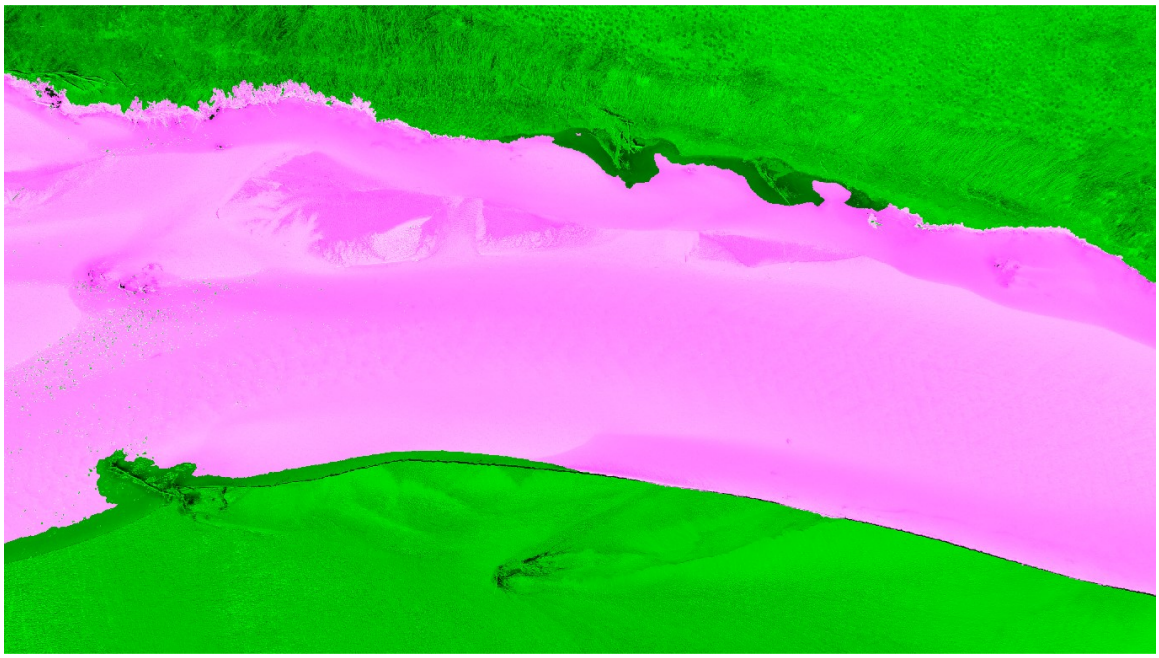

Figure IV.16: Result of using color to isolate connectivity.

since the best bathymetric location was downstream of the vehicle access and the GCPs had to be walked down to a sand bar shown in the screen-shot of GSPro flight planning software, in Figure IV.19.

Figure IV.17: View during Bathymetric Flight 1.

Figure IV.18: Parking location and flight plan.

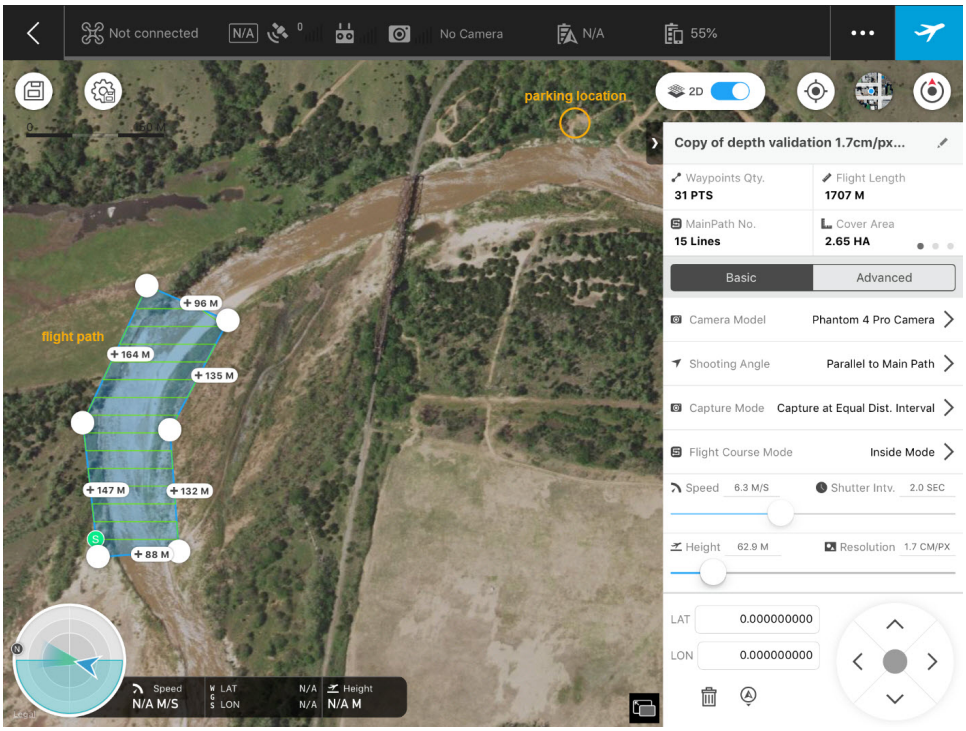

Figure IV.19: Parking location and flight plan.

Two altitudes were flown, the higher altitude was at 63 m, this was done in order to tie in to the Dietrich paper[5] by having a similar resolution of 1.7 cm per pixel. The lower altitude flown was 40 m and mimicked an altitude flown in the Dietrich paper. The flight details are shown in Figure **??**. The 40 m altitude was chosen for further processing after the data had been taken back to the lab. This was based on the difficulty the researcher had finding any underwater GCPs within the low water clarity environment. An example of GCP identification in a raw image is shown in Figure IV.20.

It is difficult to see the accurate picture quality in the field so finding assumptions have to be made that the right altitude has been chosen for each type of environment. Based on this uncertainty, multiple flights at varying altitudes are suggested to ensure that data can be processed even if GCPs prove difficult to locate in one dataset.

Because the fluvial geomorphology of a river like the South Canadian is so rapid, pre-emptively planning GCP placement is difficult when looking at imagery that

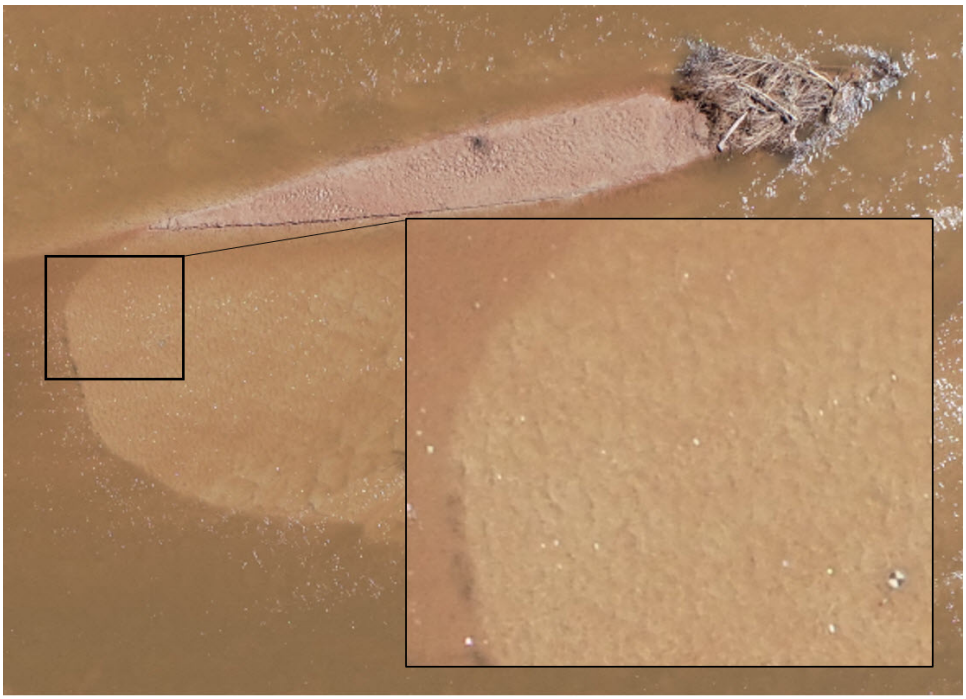

Figure IV.20: GCP example in raw image taken at an altitude of 40 m.

rapidly becomes out of date. In order to provide a realistic road map for the placement team, GCPs were planned out by flying the Phantom at 400 ft overhead, taking a snapshot, and then marking general suggestions and numbering where GCPs should be placed. This was done in a manner that attempted to collect multiple GCP data points within distinctive topographical features. Note how in Figure IV.20 GCPs 1 and 2, 4 and 5, 6 and 7, and 8 and 9 are paired along an assumed flow path together. GCPs 10 and 11 as well as 3 and 12 are paired to give shape to the outer banks and dry sand bars.

During GCP placement, the assumption was made that this initial GCP map is a guideline and can have inherent deviations as the placement team gets in the field and makes assessments based on factors like ease of access, rapid water flow, and water clarity. After processing the sparse point cloud the points were located by hand through the typical methods within Agisoft. Two GCPs could not be confidently located. GCP number 7 was in a deeper section of river that was under heavy flow,

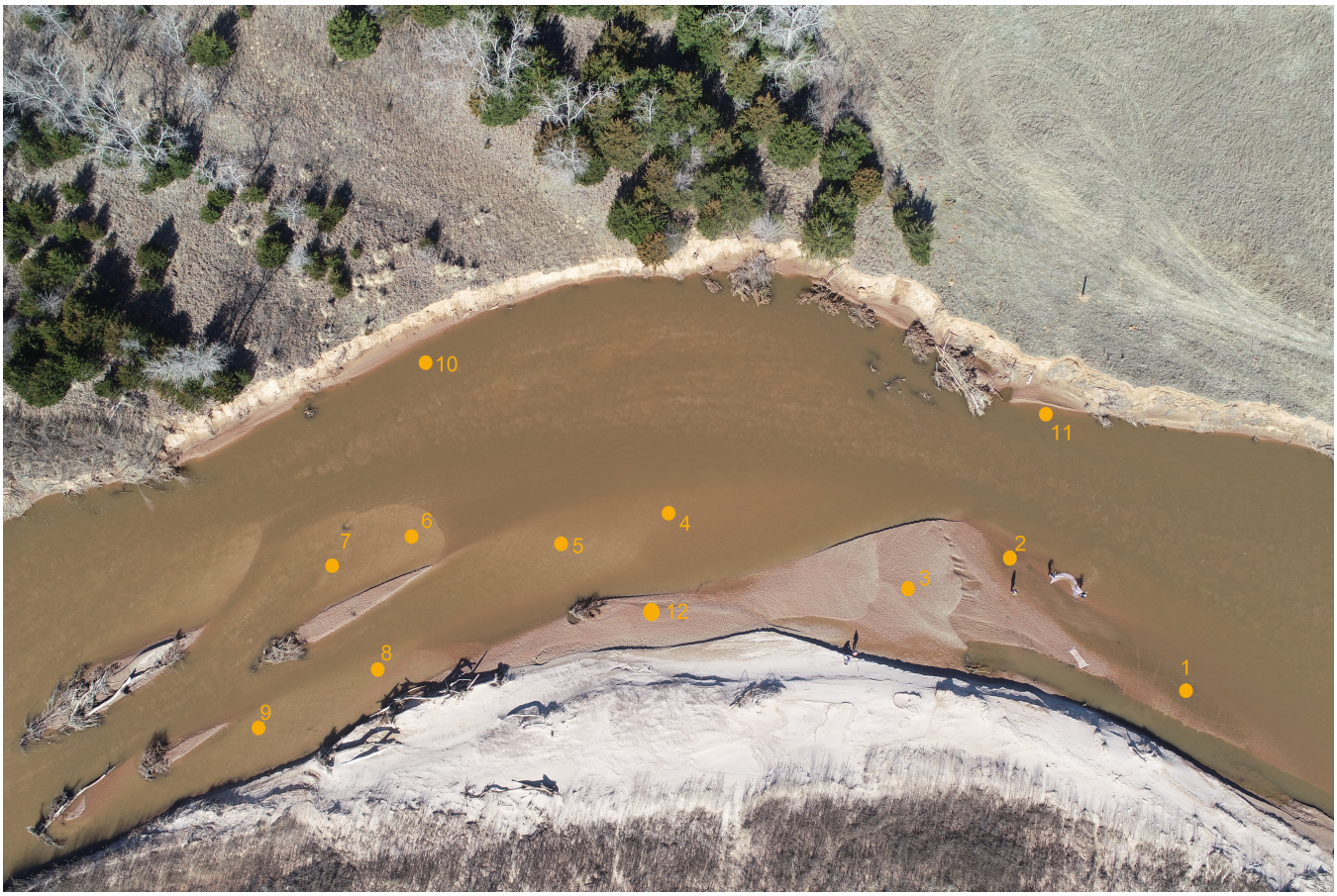

Figure IV.21: GCP placement map.

and could not be subsequently recovered by the GCP placement team. GCP 11 was on the bank furthest from the large sandbar that the GCPs were placed around, this section had a large drop to one side and was too obscured to find, however the GCP placement team was able to recover it at the end of the flight.

Figure IV.22 shows where GCPs were located in the processed point cloud. The images were reviewed individually and when a GCP was located it was marked with the number corresponding to the in situ GCP map. Two GCPs were unlocatable, and one of them had been buried by sand so fully that the GCP placement team could not recover it. This shows just how volatile the riverbed can be, and emphasizes the need for GCPs or stationary landmarks.

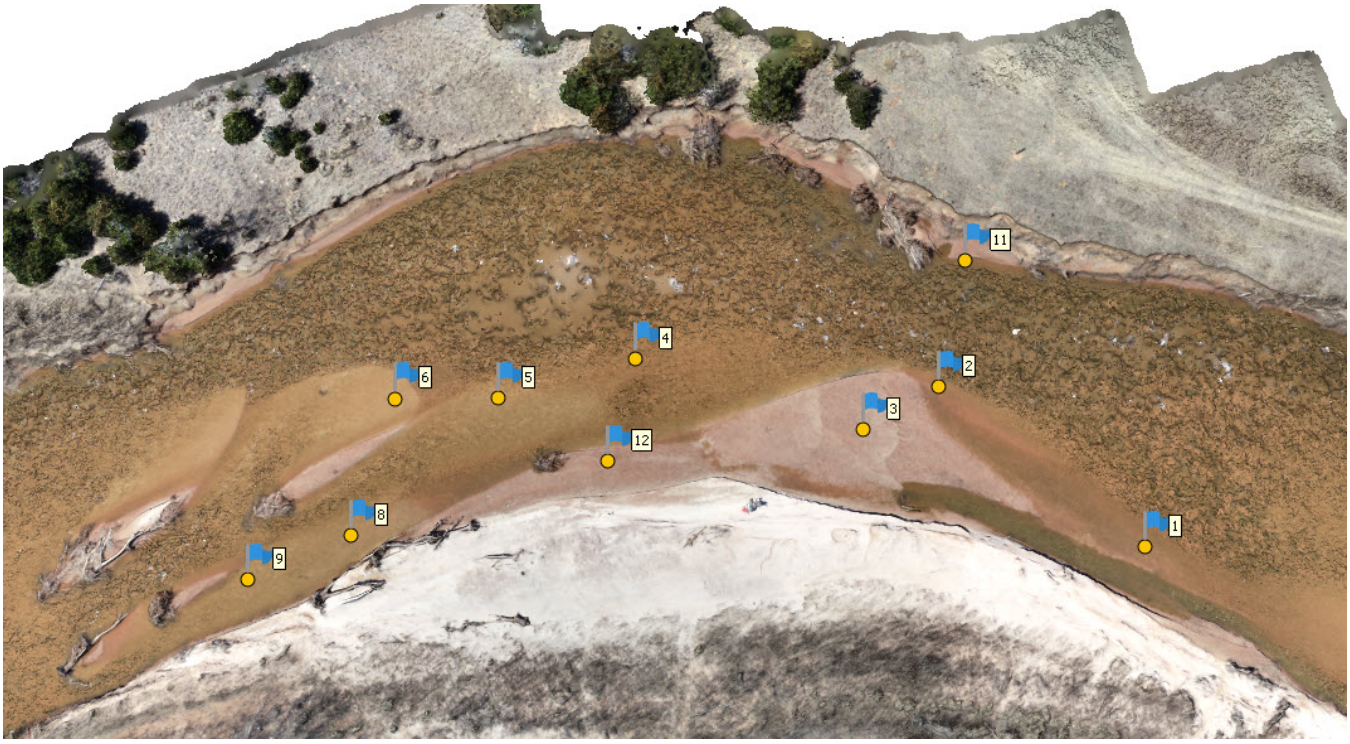

Figure IV.22: Point cloud with GCPs.

IV.4.2 Bathymetric Flight 2

The second bathymetric flight was performed near Taloga, OK. Adequate weather and flow rates were taken into consideration when choosing this date and location. The river was flowing under 400 CFM and was further upststream than previous locations, it was deemed safe to get into. The far bank was having some construction done, but the portion that was used was clear. The team parked under the bridge near the site and setup the Lecia GPS base station, shown in Figure IV.23 as soon as possible in order for it to sit long enough to get centimeter accuracy. The team made sure to not take GPS data until at least an hour had passed and the base station was fully dialed in. The group then split into sub-teams, one sub-team put on waders and placed GCPs into the water and also placed water edge flags, while the other sub-team placed and recorded the locations of land GCPs. The GCP layout was, again, dictated after the Phantom 4 was flown at 400 ft over the site and an overall

Figure IV.23: GPS base station.

image of real conditions was collected. The layout can be seen in Figure IV.24.

In the model, GCPs with the "L" prefix are on land, and the prefix "W" denotes water GCPs. Three flight paths were planned, and each included the GPS base station in case the entire GPS dataset was found to be offset buy a factor. This would allow for the geolocated GCP network to be moved together in the model in case the base station location needed to be corrected.

New practices were added to Flight 2 from lessons learned in Bathymetric Flight 1, one lesson was how difficult the water edge was to perceive when looking at the SfM model as well as the raw images themselves. This issue may have caused problems when processing the dataset from Bathymetric Flight 1. However, when the test is repeated, certain water's edge markers would be marked by the dGPS system, to allow for an easier water surface estimation.

After the GCPs were laid out and the GPS locations were taken, the Phantom 4

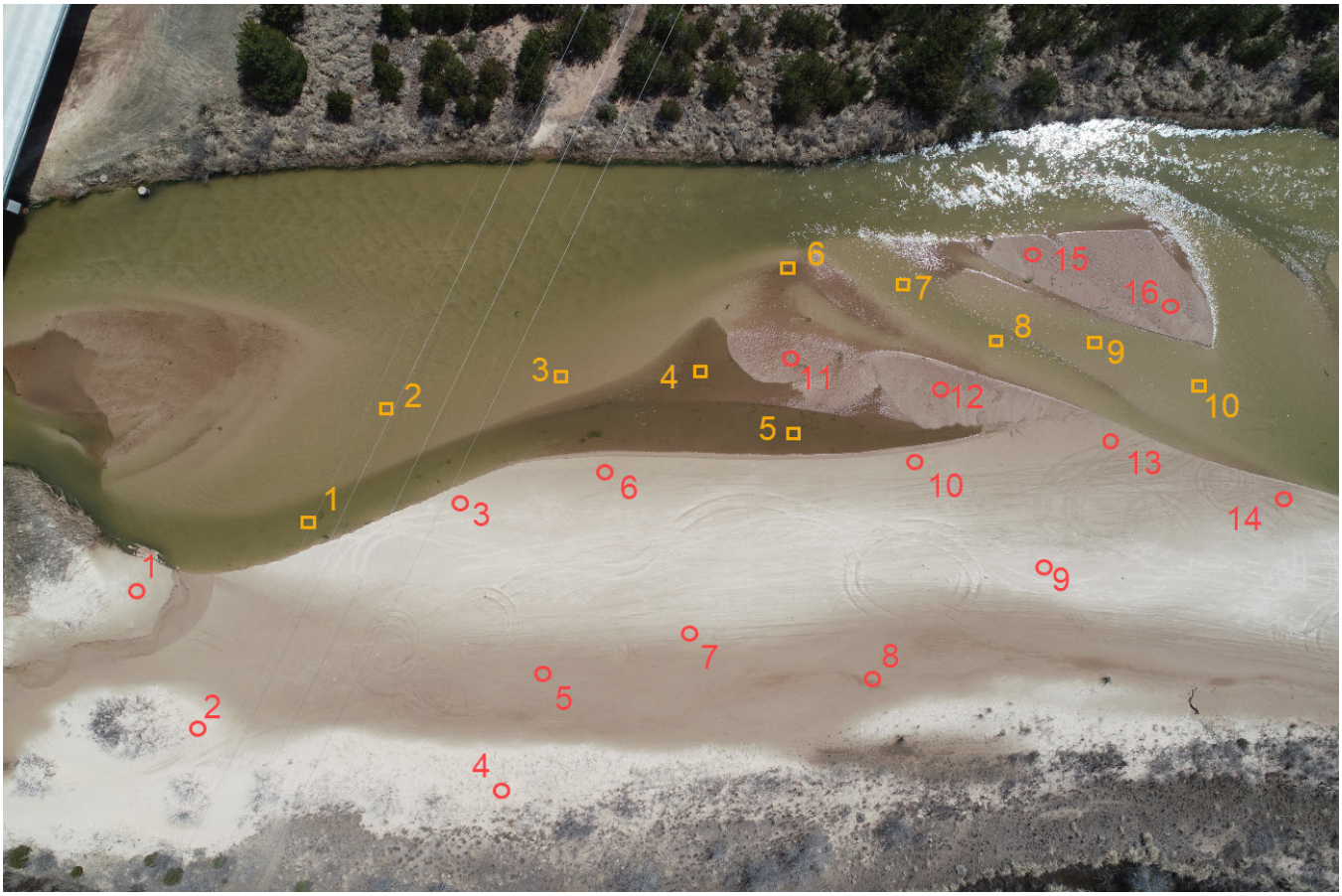

Figure IV.24: GCP placement map.

Figure IV.25: Image of phantom flying over Taloga river site.

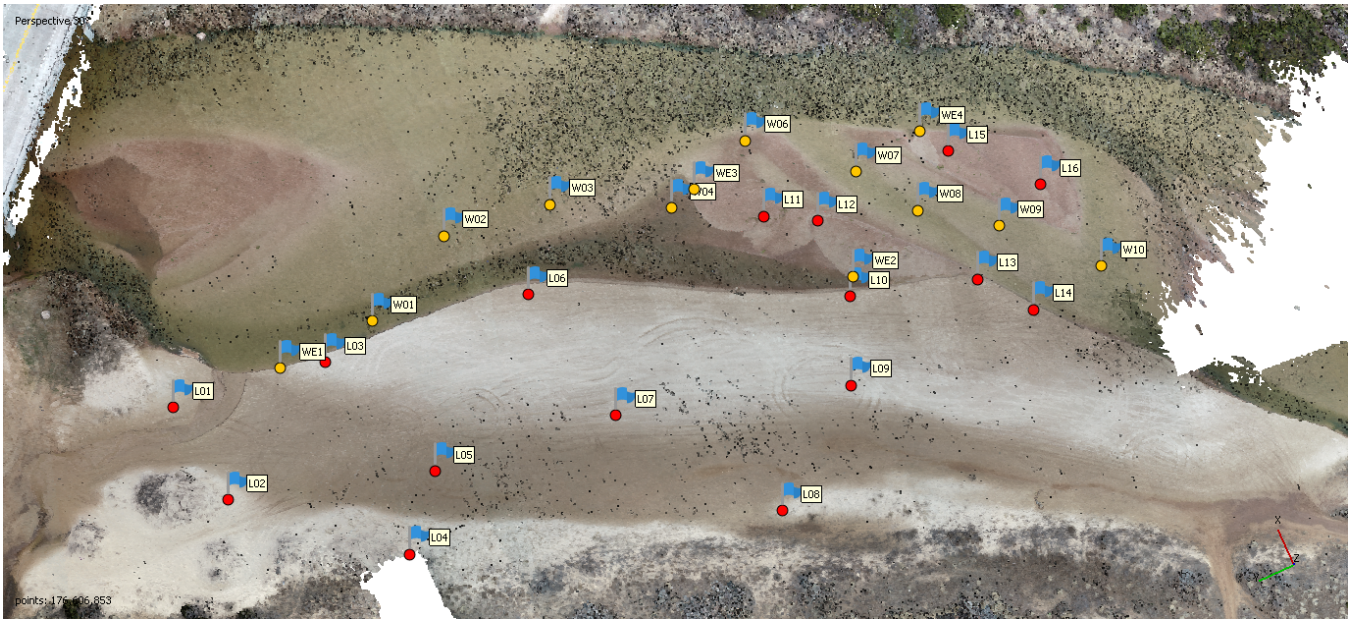

Figure IV.26: Locations of GCPs found in SfM model

Pro was flown over the site, shown in Figure IV.25. The flights lasted for approximately an hour in total, afterward the equipment was picked up and reloaded into the vehicle. At this site, all of the GCPs were recovered and approximately 100 water's edge flags were retrieved. The final set of GCPs that were able to be located in the model are shown in Figure IV.26 The GCPs positioned in the deepest locations were number 1 and 5, the team anticipated having the most issues locating these during data processing, and 5 was not able to be confidently located in the final model.

IV.4.3 Bathymetric Processing

Using Structure from Motion to model bodies of water is notoriously difficult and modeling image based bathymetry is no exception. However, when the water is clear enough, the riverbed is discernible and can be processed like other landscapes in structure from motion programs such as Agisoft. When processed this way, sections of the point cloud that are underwater are subject to refractive errors. It is interesting to remember that this is not the only part of the model that is subject to this type

of error, in fact the atmosphere itself will bend light as it passes through different atmospheric layers, however this amount of error tends to be negligible especially when the data is not being collected from outside the atmosphere. Although this needs to be remembered when viewing some satellite datasets.

When the image refraction error is as severe as it is in the riverbed, however, correcting the bathymetric data seems essential. There are a couple of methods that can accomplish this, one is to take a high well populated dataset at nadir and assume that the angle of incidence will zero out and the depth can be corrected by a factor of refractive index. However, if a higher fidelity dataset is required and oblique images need to be taken into account, the idea of using Snells Law to back out the true location of individual points has been proposed. Dietrich et al derived a method to perform this correction.[6]

Testing these methods began with collecting the sparse and dense point clouds at 40 m from Bathymetry Flight 1, as well as the georectified sparse and dense point clouds for nadir and oblique images that were also at an altitude of 40 m from Bathymetry Flight 2. Each set of data was processed in a standard way. That is outlined in the Appendix. The underwater GCPs were found and marked within both datasets and the land GCPs were geolocated and marked for the nadir and East facing oblique datasets from Flight 2.The orthomosaic for Flight 1 is shown in Figure IV.27, and the orthomosaics for Flight 2 are shown in Figures IV.28 and IV.29 respectively.

Although Structure from Motion can utilize varying camera types and capturing angles, this set of tests will use a dataset from a lawnmower pattern since data gathered with consistency is the easiest to manipulate. Each image has a particular amount of overlap with the next image, this concept is illustrated in Figure IV.30. Although the overlap in IV.30 is not as high as what is usually used, the illustration demonstrates the amount of images one point in the point cloud will have been

Figure IV.27: Bathymetry Flight 1 Nadir Orthomosaic.

Figure IV.28: Bathymetry Flight 2 Nadir Orthomosaic.

Figure IV.29: Bathymetry Flight 2 Oblique Orthomosaic.

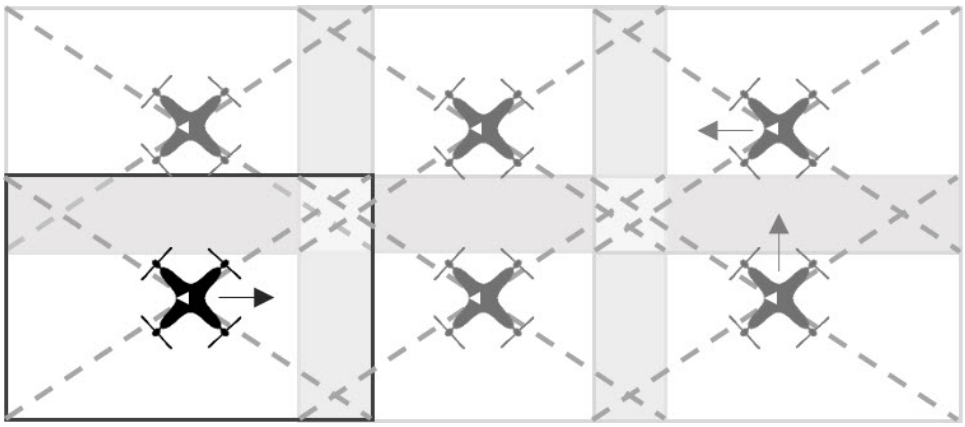

Figure IV.30: Illustration capturing photogrammetric data.

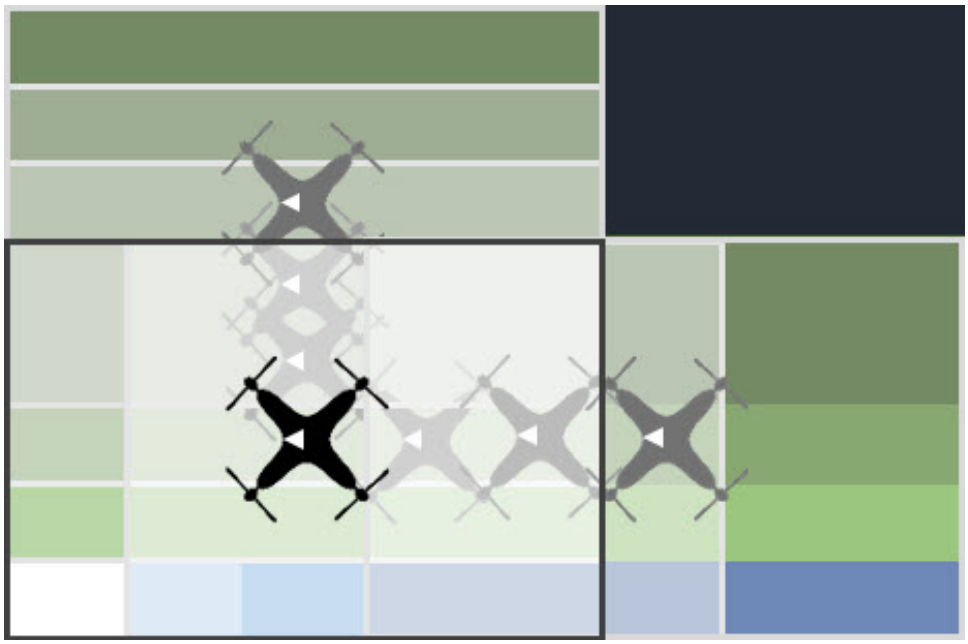

Figure IV.31: Illustration of normal image overlap.

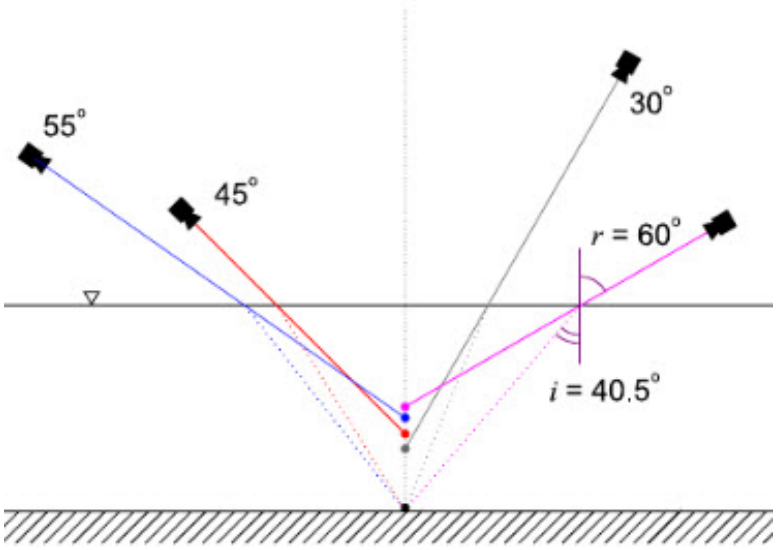

Figure IV.32: Depiction of multiple camera angles capturing the same point.[6]

captured in. When the overlap is set to 80% by 80%, as shown in Figures IV.31 and IV.32, the massive amount of pictures per point becomes more apparent. This is important to note since it affects the way data alterations can occur.

An accepted method for correcting for refraction is to take nadir images and assume that as long as the angle of incidence remained below 10 degrees, the error is considered negligible. When the assumption that the refractive index of fresh water is 1.337, mathematically an offset can be applied to rendered underwater points within a point cloud.

1)

$$\frac{n_1}{n_2} = \frac{sin(i)}{sin(r)}$$

2)

$$\sin i \cong \tan i = \frac{x}{h}$$

3)

$$\sin r \cong \tan r = \frac{x}{h_a}$$

4)

$$h = 1.337 h_a$$

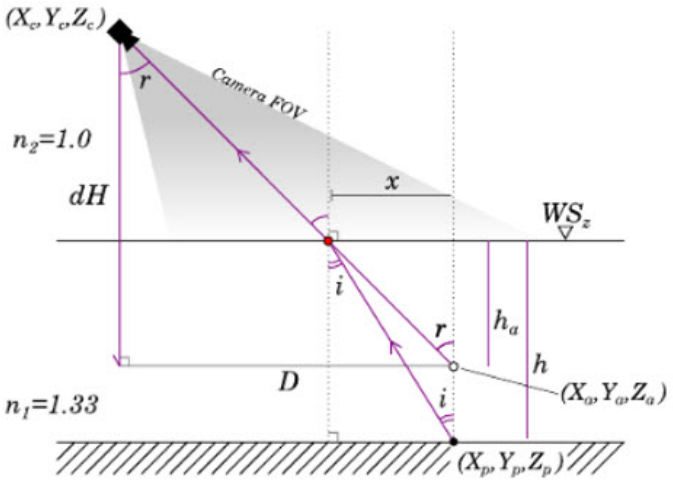

Variable	Description
X_a, Y_a, Z_a	apparent coordinates of the Structure-from-Motion (SfM) point
X_p, Y_p, Z_p	true coordinates of the point
D	Euclidean distance to the SfM point from the camera
dH	flying height above SfM point
r	angle of refraction (from nadir to the SfM point)
i	angle of incidence
x	distance from the SfM point to the air/water interface point
h_a	apparent depth to the SfM point
h	true depth of point (X_p, Y_p, Z_p)
n_1	refractive index of fresh water (1.337)
n_2	refractive index of air (1.0)

Figure IV.33: Illustration of underwater refractive point correction.[6]

However, Dietrich attempts to use a python script to solve this issue when images are taken at oblique angles. Oblique angles can be useful in certain situations, particularly when data is gathered next to vertical ledge structures like the banks of the South Canadian

The point cloud is initially processed using normal SfM procedures, afterword the point cloud is exported as a text file and is then imported into a point cloud editing software. Cloud Compare was used for this test. Although some of the images were nadir, only points directly below the camera will have a true angle of incidence of 0. This concept is demonstrated in Figure IV.34. Because of this possible distortion the researcher chose to run all datasets, nadir and oblique, through the Python script. If Cloud Compare is utilized for further processing, exporting the point cloud in a local coordinate system is preferred. Data that is not exported this way can come in as a single line of RGB data. Care was taken do all analysis within the same coordinate system for each respective program.

In order to port over GCP locations, measurements were taken in Metashape before the point clouds were moved to Cloud Compare, these measurements are shown in Figures IV.35, IV.36 and IV.37. In order to run the python script, three docu-

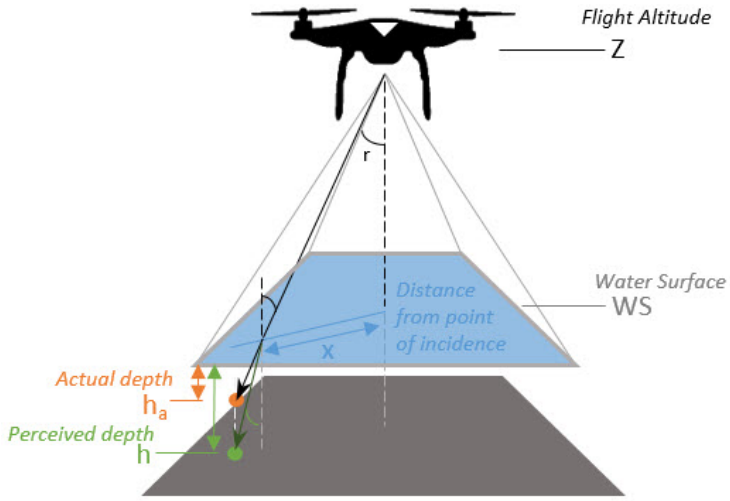

Figure IV.34: Possible distortion within a nadir image.

ments were prepared based on the point cloud data, camera locations, and camera specifications. The script is written so data just needs to be properly labeled in order for the columns to be queried properly.

The first step in the Python code finds the field of view for each image taken. This uses the camera GPS locations, camera metadata, and point cloud to determine which points need to be adjusted. In Bathymetric Flight 1 the water edge was only based on its visibility in the raw images, in Bathymetric Flight 2, flags were laid out to help the researcher with water edge selection. Once the water edge is established, the model is divided and the portion that should be underwater is saved separately. These points are then down sampled. After this,the underwater points are saved as their own text file and exported.

The camera location file can be exported from telemetry data that is integrated with UAS software, however since the camera locations within any Structure from Motion software is based off of the data itself, as shown in Figure IV.38. The camera array derived from Metashape is overlaid on the GSPro flight plan for Flight 1. The green lines denote the expected path of the UAS, but there are visible gaps at equal

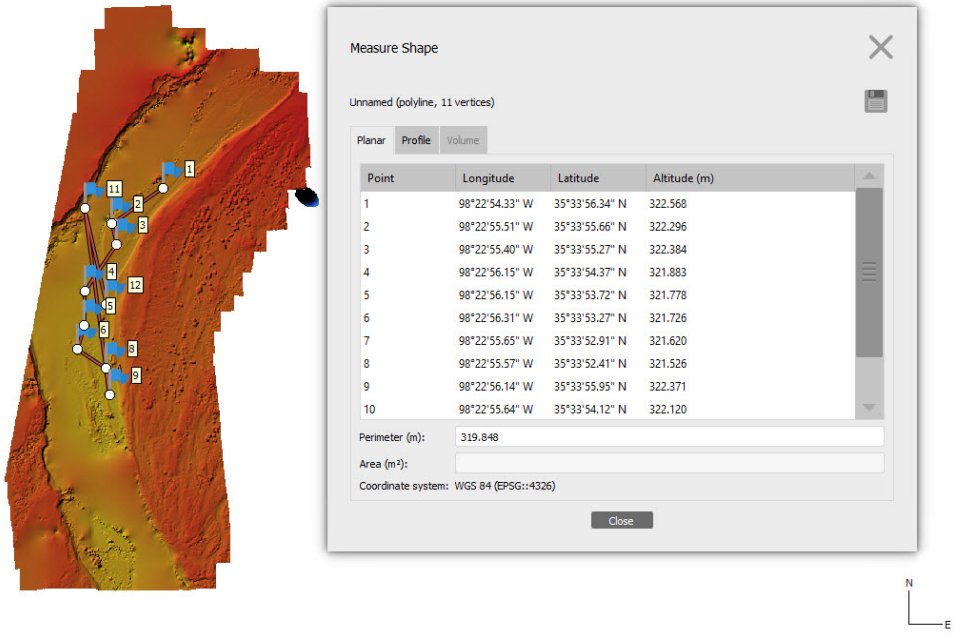

Figure IV.35: Flight 1 GCP depth measurements in Metashape.

distance intervals. These kind of discrepancies appear to mean the most consistent camera locations with relation to the data should come from the SfM program. In Metashape, the cameras can be exported in a couple of different ways, but the best way is through the main menu. This allows them to be exported in a local coordinate system.

The camera specification file contains the sensor focal length and size in millimeters. This information is used in the Python script determine Field Of View (FOV) relative to each camera.

The Python script is an iterative setup that calculates refraction corrections for each point in addition to each camera that can view that point. This is based on the camera locations as well as the pitch roll and yaw estimates for each location. Again, this data can be derived from the UAS telemetry logs, but Dietrich also recommends using Agisoft's roll pitch and yaw estimations since they are based on the processed and georeferenced data. [6]

Within each iteration, the refraction angle, which is derived from the center of

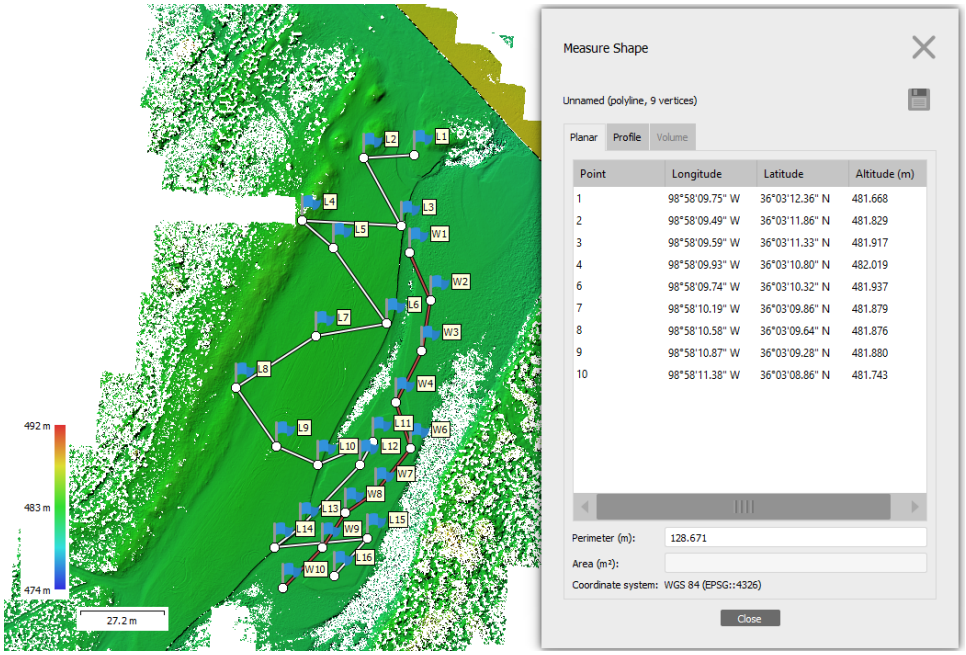

(a) Water GCPs

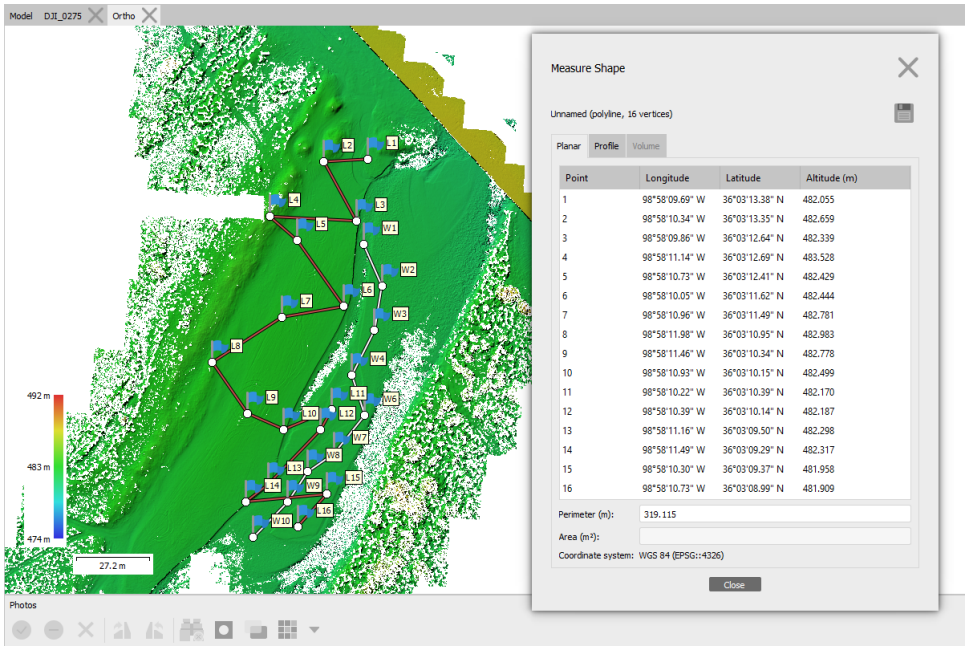

(b) Land GCPs

Figure IV.36: Flight 2 Nadir GCP depth measurements in Metashape.

the camera through the center of the sensor is calculated using equation 5, this is not equivalent to the pitch of the vehicle. Variable D is the Euclidean distance between the camera and point of interest and is defined further by equation 5a. Variable dH is

(a) Water GCPs

(b) Land GCPs

Figure IV.37: Flight 2 Oblique GCP depth measurements in Metashape.

the difference in height between the camera and point of interest, noted by equation 5b.

5)

$$r = \tan^{-1} \frac{D}{dH}$$

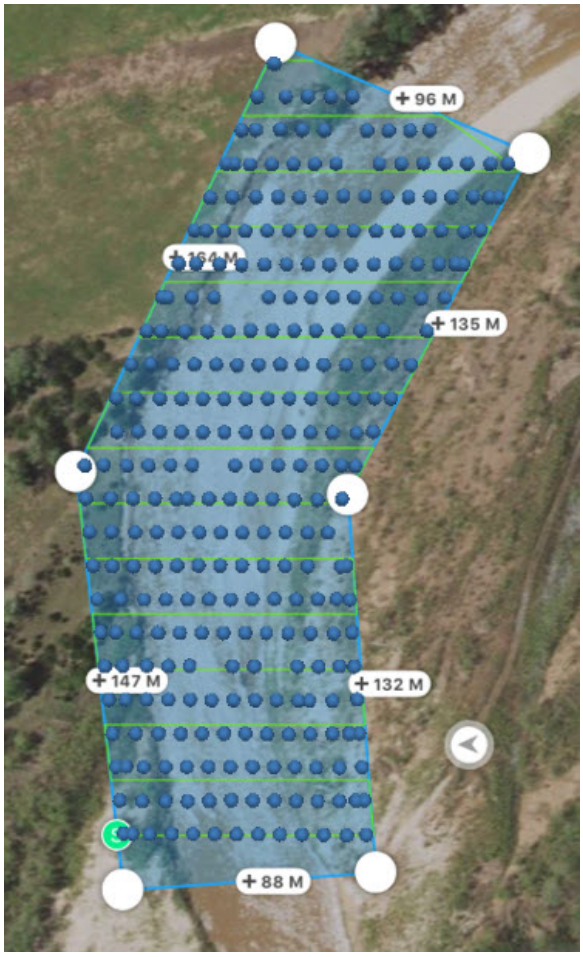

Figure IV.38: Camera locations generated by Metashape for Flight 1.

5a)

$$D = \sqrt{(X_c - X_a)^2 + (Y_c - Y_a)^2}$$

5b)

$$dH = Z_c - Z_a$$

The water surface elevation is defined in equation 6, and is assumed to be planar. Establishing the water's edge is critical to these equations. Using GPS to mark the edge is an important lesson learned.

6)

$$h_a = WS_z - Za$$

After the refraction angle and water surface elevation are collected, the remaining

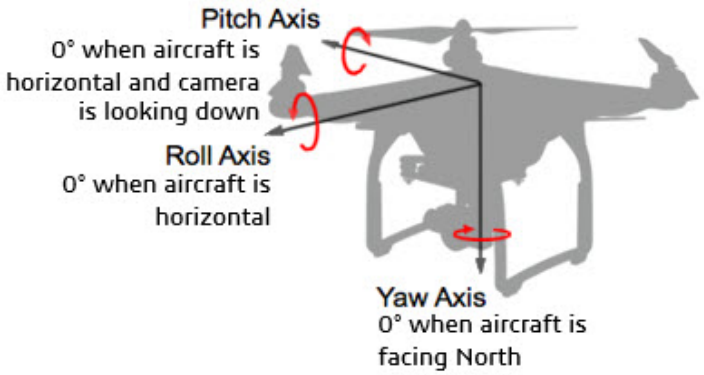

Figure IV.39: Expected roll, pitch, and yaw conventions in the Python script [6]

unknown values are calculated. The angle of incidence is defined by equation 7, the distance from the point of incidence is defined by equation 8, and the model point depth is defined by equation 9. The original Z location for the point of interest is defined by equation 10.

7)

$$i = \sin^{-1}(\frac{n_2}{n_1} * \sin r)$$

8)

$$x = h_a * \tan r$$

9)

$$h = \frac{x}{\tan i} = \frac{h_a * \tan r}{\tan(\sin^{-1}(\frac{n_2}{n_1} * \sin r))}$$

10)

$$Z_p = WS_z - \bar{h}$$

It is assumed that Z_a, the Z location of the point of interest, being a fixed value drives h_a, the depth value of the point of interest, to be a fixed value. There is a variability between x, the distance between the point of incident and the points of interest, and h, the modeled depth. In order to combat this, the average of all of the camera corrections for each point is taken as opposed to choosing a single value.

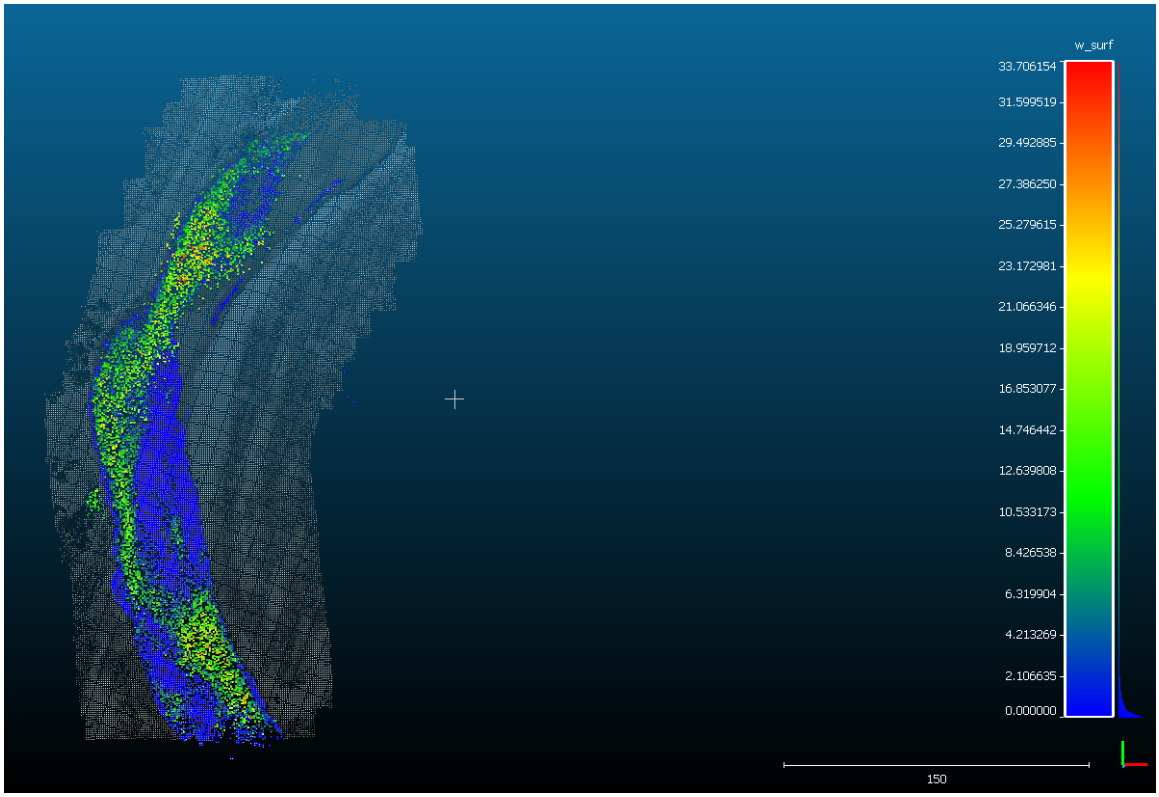

Figure IV.40: Example of underwater point isolation.

Although the index of refraction for water can change depending on many variables including whether the water is fresh, the temperature, and clarity of the water, the assumption is made that the index of refraction for this thesis is 1.337, this value is reasonable and mimics the Dietrich paper.

As shown in Figure IV.42, the depth results were measured plotted in a chart that compared depths measured per GCP in the field with depths that were modeled in the point cloud. There is a noticeable trend with GCPs 1,2,3, and 4 that begins to deviate as the model moves toward the GCPs placed in deeper water. This is an expected result.

When the second flight was analyzed, a refraction corrected dataset was created. This is shown in Figure IV.44, where the dataset was exported, trimmed, and run through the refraction correction python script. There were issues with the resulting model, evident at the red edges where the model seemed to fall off the face of the

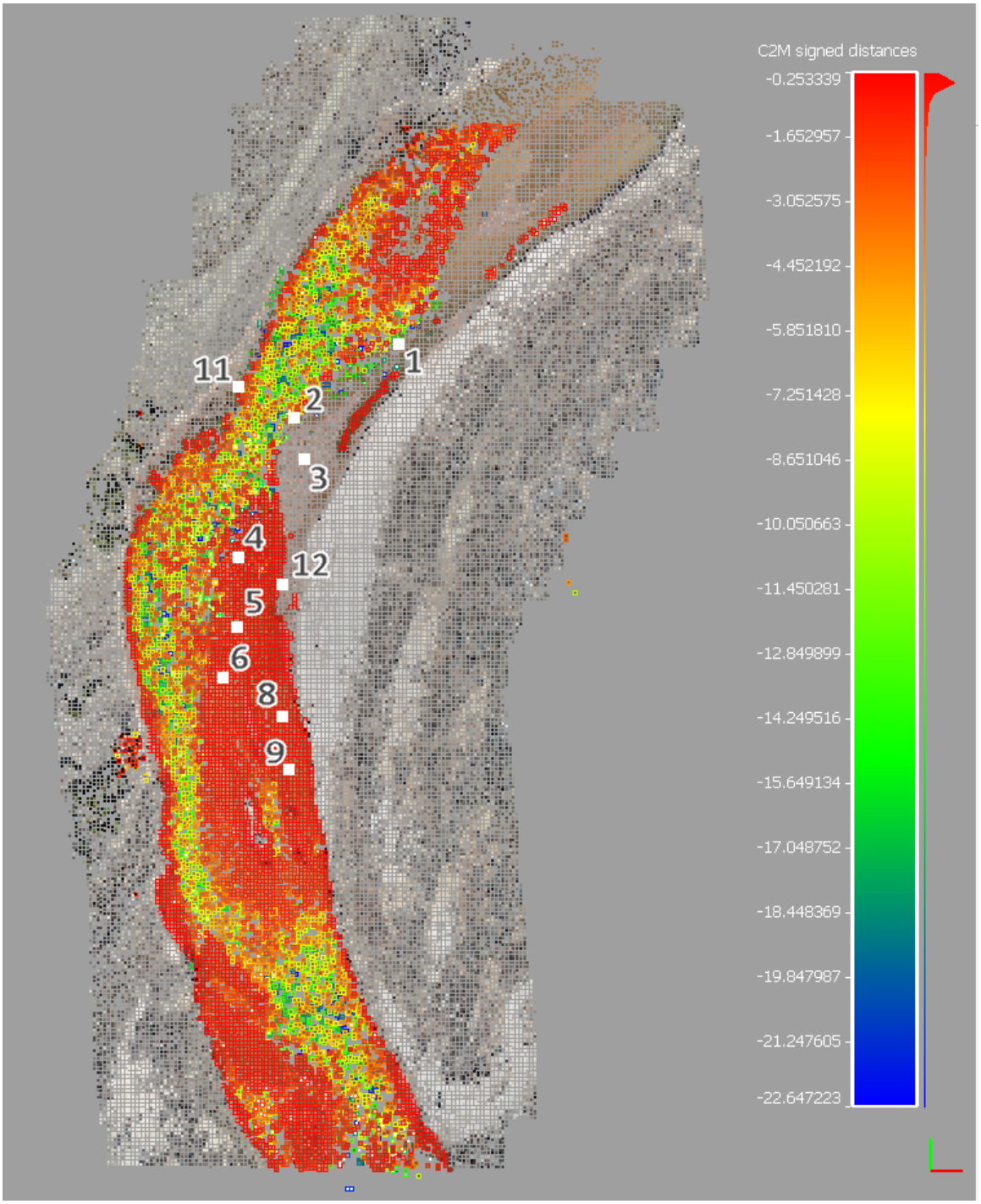

Figure IV.41: Example of corrected bathymetry.

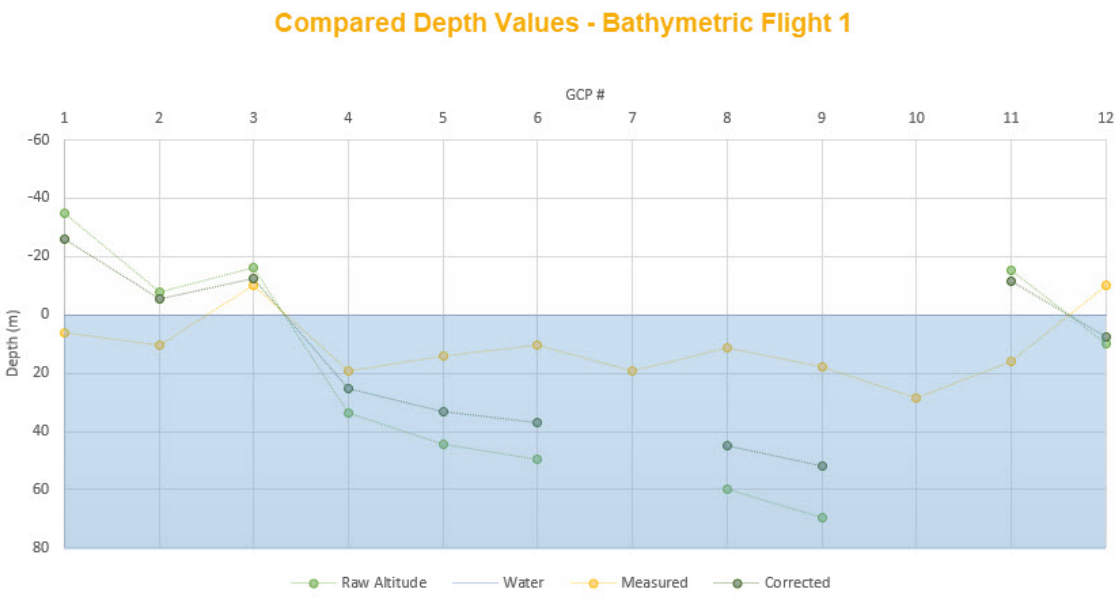

(a)

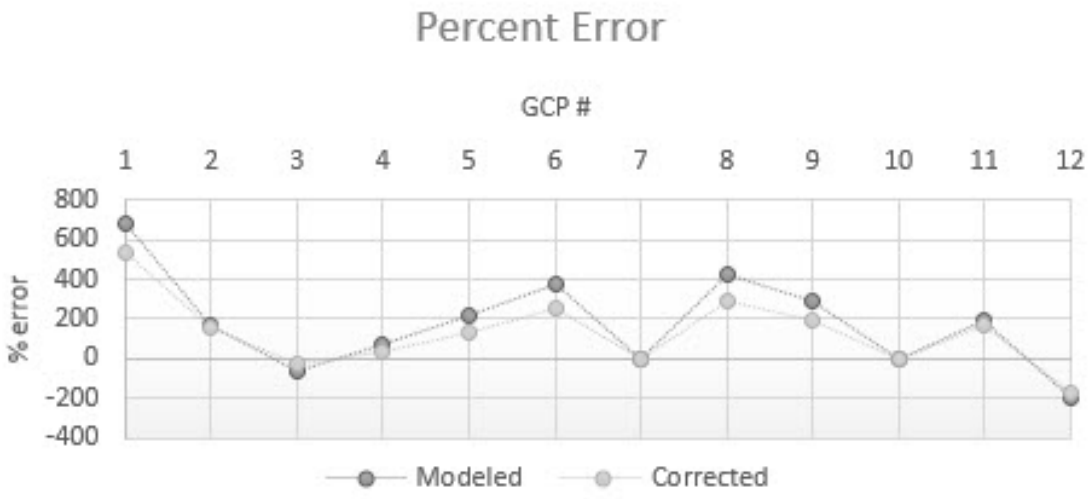

(b)

Figure IV.42: Graph of depth per GCP for Flight 1.

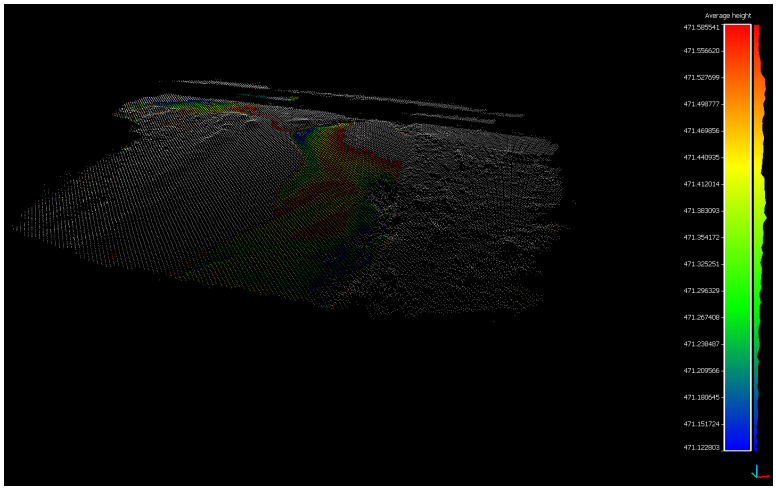

(a) Point cloud with selected underwater point in color

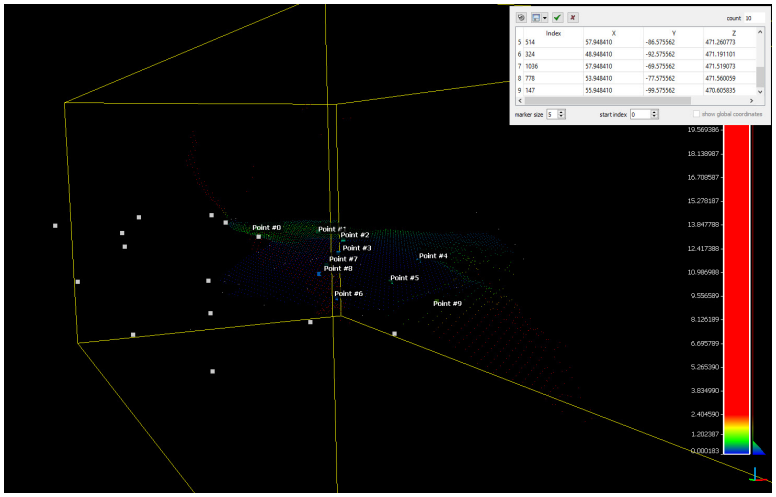

(b) Point model with located GCPs

Figure IV.43: Refraction correction model processing.

earth. This result was unexpected, however, this seems to occur where the altitude was lowest, shown by the blue points in IV.43 (a). The reasons for this are good future work, and could be indicative of locations that should have been trimmed. For future use, this method could become more automated so that points aren't chosen by eye and the results would be more repeatable.

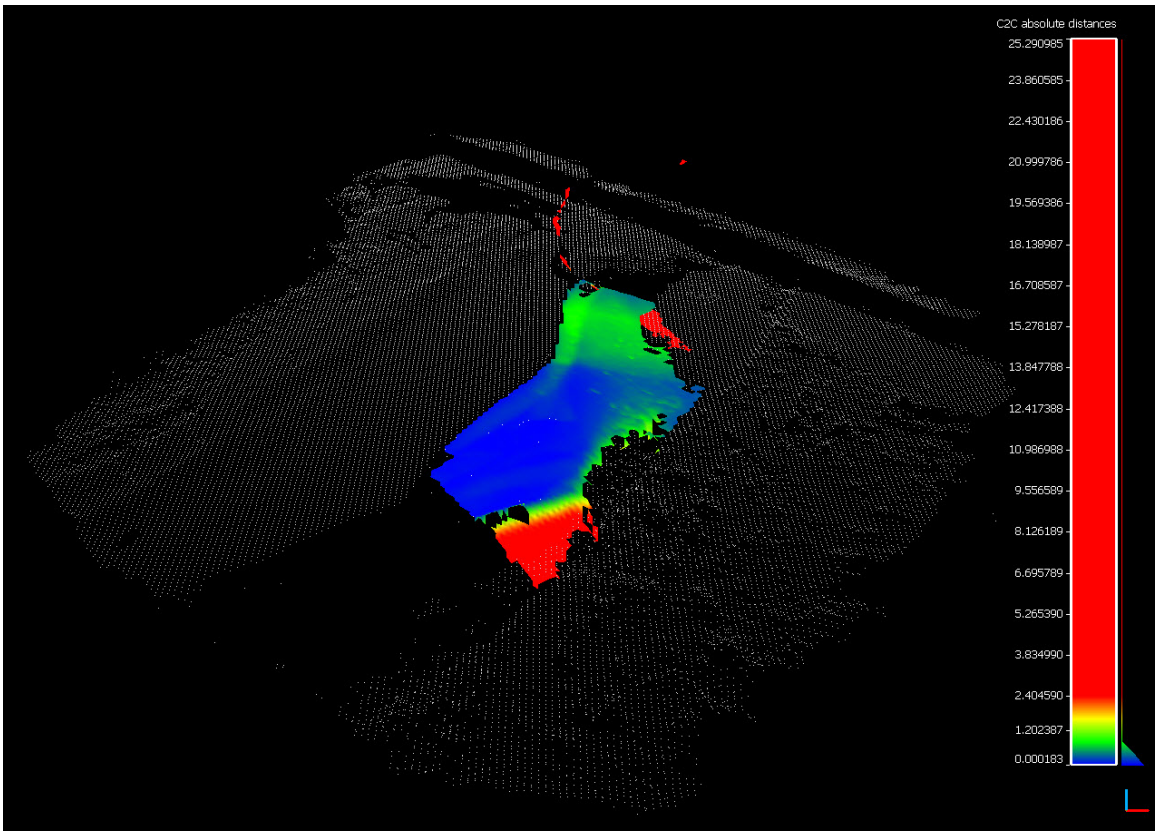

Figure IV.44: Refraction correction model mesh.

IV.5 Bank Width Metric Acquisition

Bank width is traditionally measured by hand or through surveying equipment, these measurements can have low to high tolerances depending on the application. For the Arkansas River Shiner project, a bank width tolerance on the order of a meter was deemed appropriate. This was tested by comparing nadir and oblique datasets of land GCPs to the survey grade GPS points recorded in the field and determining the error between the two, the comparison is shown in Figure IV.45.

When the graphs were compared, it was determined that there was no discernible difference between nadir, oblique, and nadir and oblique image datasets. All of the models resulted in a 10 meter vertical offset, however each was within 2% error for all directions, as shown in Figure IV.48. GCPs are most useful when pulling the model into the correct geolocation within global projections.

IV.6 Lessons Learned

Overall, researchers learned how important it is to plan ahead and gather as much data as possible during the first outing. With conditions changing constantly, there may only be one shot to gather good data when the project is dependent on so many uncontrollable variables. Specifically, through determining velocity remotely, correlations were found to be promising and were acceptable when providing a remotely sensed metric for the Arkansas River Project. When working with bathymetry, there are certain corrections that can be done to maintain tolerances required of certain tests, however many options are available to tweak and correct data that may be simple to use and work for most tasks.

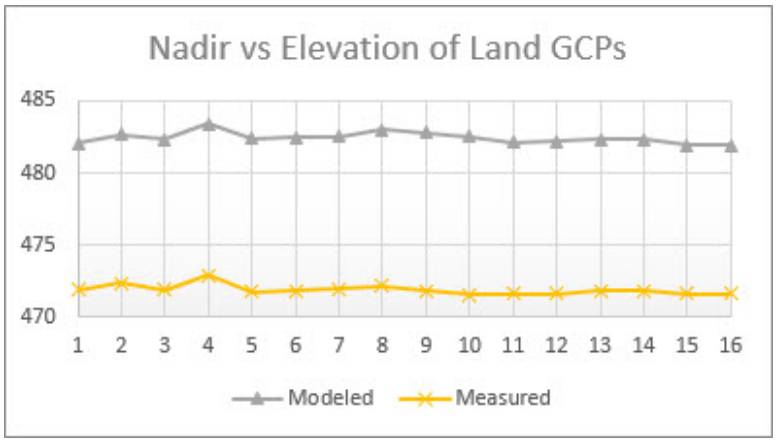

(a) Elevation (m)

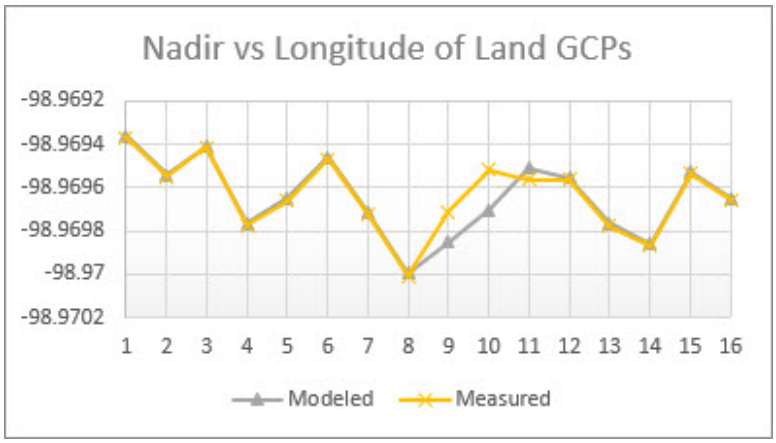

(b) Latitude (m)

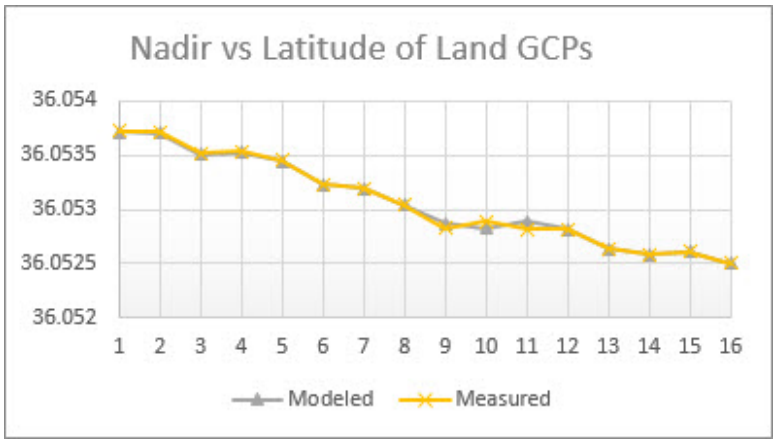

(c) Longitude (m)

Figure IV.45: Accuracy of Land GCPs from Nadir dataset.

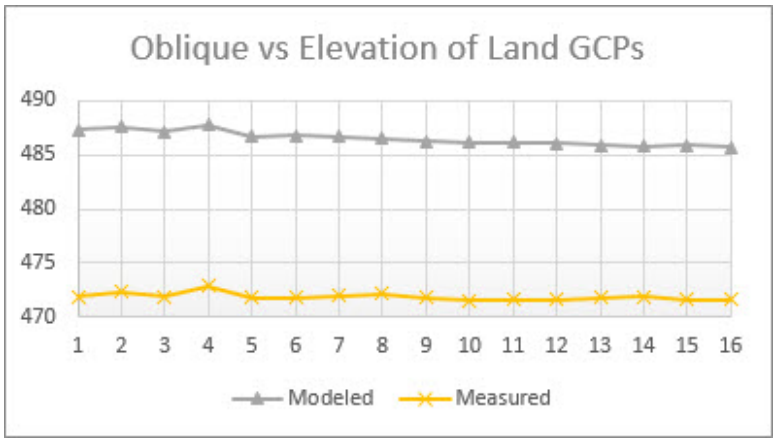

(a) Elevation (m)

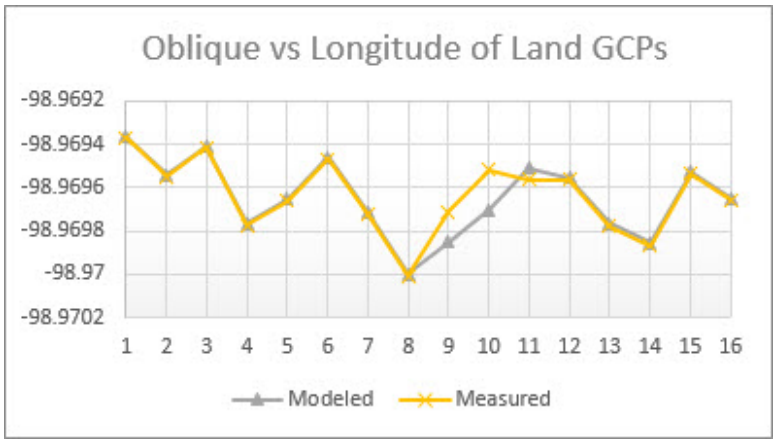

(b) Latitude (m)

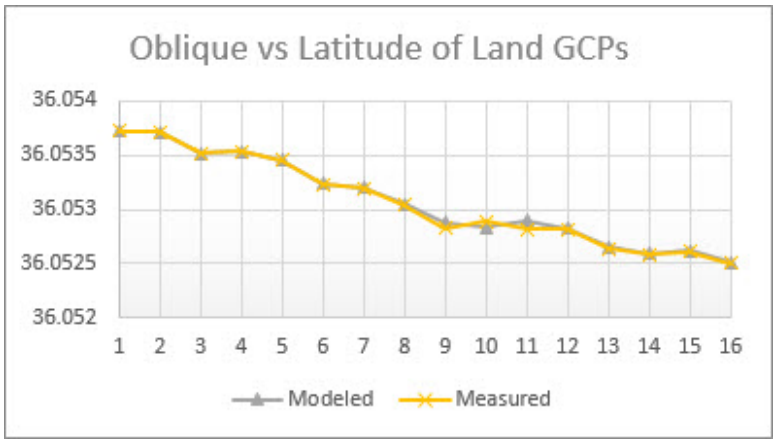

(c) Longitude (m)

Figure IV.46: Accuracy of Land GCPs from Oblique dataset.

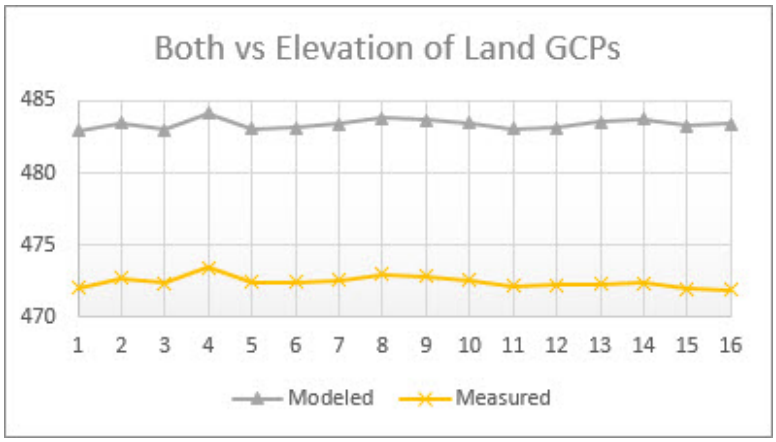

(a) Elevation (m)

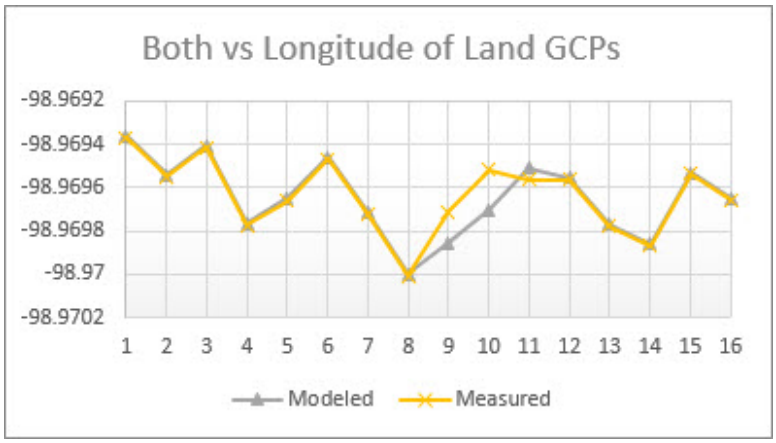

(b) Latitude (m)

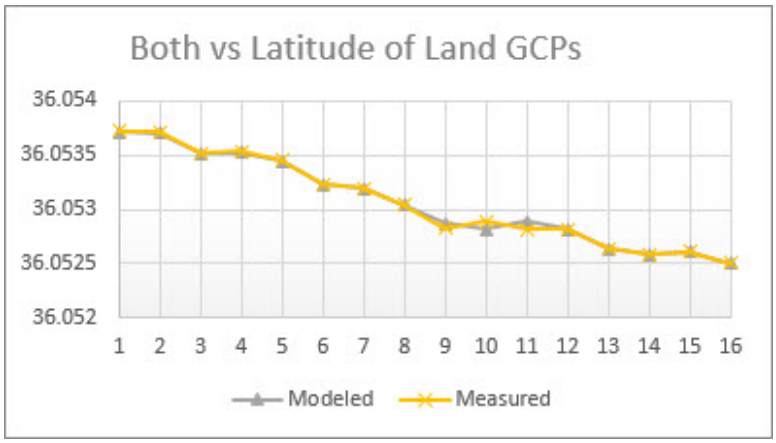

(c) Longitude (m)

Figure IV.47: Accuracy of Land GCPs from Both datasets.

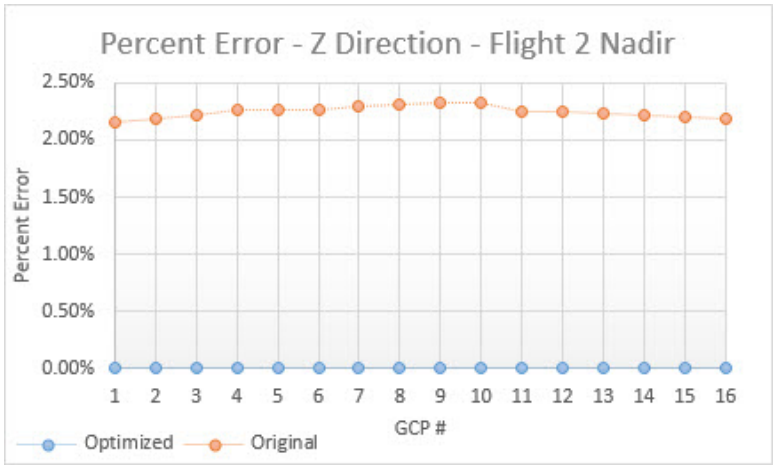

(a) Elevation (m)

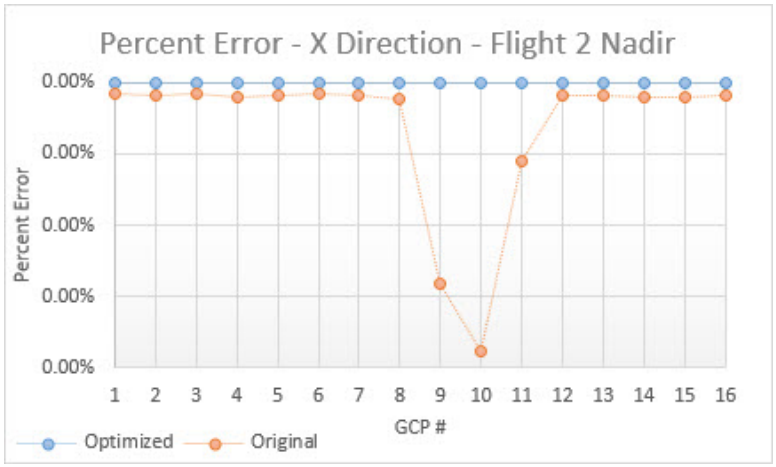

(b) Latitude (m)

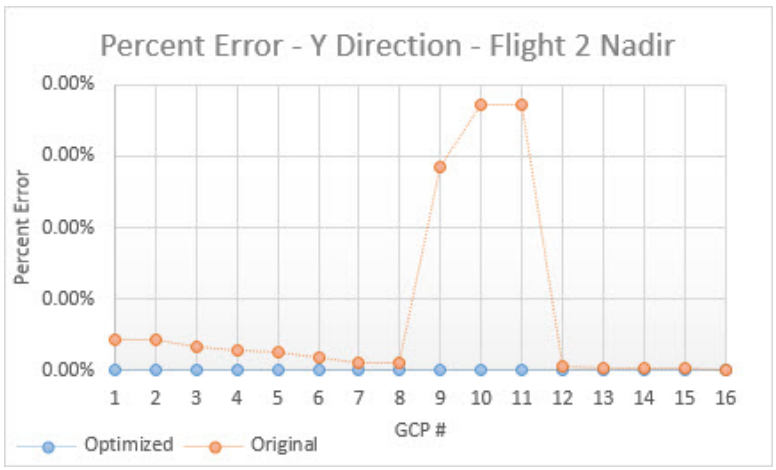

(c) Longitude (m)

Figure IV.48: Percent Error for Nadir dataset.

CHAPTER V

Conclusions

V.1 Case Study 1: South Canadian River

Different methods for discerning bathymetric data were explored. This included example data sets for water that was too deep and not clear enough to derive bathymetric data using visual means, as well as visual methods for correcting refractive error in order to generate bathymetric data for shallow sections of bodies of water. Water conditions including flow rates, turbidity, and connectivity were explored in relation to gathering and processing data, including assessing datasets across temporal and spacial scales. Methods for determining datasets that are needed for other research were explored, these metrics included the derivation of river connectivity, a multitude of methods to gather water velocity, and using acceptable tolerances for bank with measurements were tested. This was done to determine if these large datasets would be acceptable as additional field measurements for the Brewer lab.

The methods for remotely discerning velocity were compared and found to be viable options when working within the initial parameters. Visual bathymetry needed some tweaking, and the researcher's current data collection method will remain taking nadir images to minimize the refraction error in shallow water depths until more autonomous and reliable methodologies can be used to minimize the error further. When comparing the geolocated GCP locations to the GCPs modeled by running nadir, oblique, and a set of both images, it was determined that the model may have an overall offset of 10 meters when compared to global projection, however the model was extremely accurate within itself. This was well within the accepted parameters

for the Arkansas River Shiner project.

V.2 Original Contribution

Although elements of using Structure from Motion with Unmanned Aerial Systems have been examined in concentrated portions by other researchers, this thesis has provided a thorough examination of current methods and tools that span a multitude of environments, datasets, sensors, methodologies, and data processing procedures. Only through joining these technologies together will truly autonomous and robust systems be designed in the future.

BIBLIOGRAPHY

[1] Unknown, "http://www.maxwell.af.mil/au/afhra/photo$_g$alleries/merhar/photos/01097628$_0$47.j

[2] D. J. Q. Jonathan L. Carrivick, Mark W. Smith, *Structure from Motion in the Geosciences*, vol. 1 of *10*. The address: The name of the publisher, 3 ed., 7 2016. An optional note.

[3] Unknown, "http://www.gisresources.com/confused-dem-dtm-dsm/."

[4] R. S. Noah Snavely, Steven M. Seitz, "Modeling the world from internet photo collections," *Springer*, 2007.

[5] L. W. David Day, Wes Weaver, "Accuracy of uas photogrammetry: A comparative evaluation," *Photogrammetric Engineering and Remote Sensing*, vol. 82, no. 12, pp. 909–914, 2016.

[6] J. T. Dietrich, "Bathymetric structure-from-motion: extracting shallow stream bathymetry from multi-view stereo photogrammetry," *Earth Surface Processes and Landforms*, 2016.

[7] Unknown, "https://www.michigan.gov/invasives/0,5664,7-324-68002$_7$1240$_7$3848 − 367858 − −, 00.*html*."

[8] Unknown, "https://www.blueskiesdronerental.com/product/dji-phantom-4-pro-2/."

[9] Unknown, "https://www.dji.com/phantom-4-pro/info/specs."

[10] Unknown, "https://express.google.com/u/0/product/1381514611904440946$_1$174003348487036678$_1$114 $google_shoppingutm_medium = tu_cuutm_content = eid - lsjeuxoeqt\%2ceid -$

$vqiqlmovzsgtim = cpqnwc25ss_2sweq5p_l4tgft9duarjayafnaiidvvnekpdug - yfmprvkduutm_campaign = 111425530gclid = cj0kcqjw19dlbrcsarisaonfrejmmryzl-pn1pznk0hdpxpz09bgdwpqn43thha9bvohs8arwqd0s1aaamree$

[11] Unknown, "https://www.forestry-suppliers.com/product$_p$ages/products.php?mi = 50731itemnum = 77107."

[12] SonTek, "https://www.sontek.com/riversurveyor-s5-m9."

[13] Agisoft, "System requirements." https://www.agisoft.com/downloads/system-requirements/, 7 1993. An optional note.

[14] Unknown, "http://www.dakotaswcd.org/pdfs/mm$_w$atclar$_f$s.pdf."

[15] P. Bolstad, *GIS Fundamentals A First Text on Geographic Information Systems*, vol. 1 of *10*. The address: The name of the publisher, 3 ed., 7 2012. An optional note.

[16] Aerometrex, "https://aerometrex.com.au/photogrammetry/a-brief-history-of-aerial-photogrammetry/."

[17] ESRI, "https://www.esri.com/en-us/what-is-gis/overview."

[18] E. R. T. A. S. F. K. M. W. . D. P. R. S. M. Emily J. Sturdivant, Erika E. Lentz and R. E. Henderson, "Uas-sfm for coastal research: Geomorphic feature extraction and land cover classication from high-resolution elevation and optical imagery," *Remote Sensing*, vol. 9, no. 1020, pp. 1–21, 2017.

[19] T. T. S. S. M. M. Daniel Solazzo, Joel B. Sankey, "Mapping and measuring aeolian sand dunes with photogrammetry and lidar from unmanned aerial vehicles (uav) and multispectral satellite imagery on the paria plateau, az, usa," *Elsevier*, vol. 319, pp. 174–185, 2018.

[20] M. D. F. M. A. C. Paolo Rossi, Francesco Mancini, "Combining nadir and oblique uav imagery to reconstruct quarry topography: methodology and feasibility analysis," *European Journal of Remote Sensing*, vol. 50, no. 1, pp. 211–221, 2017.

[21] M. G. F. S. S. F. G. G. Francesco Mancini, Marco Dubbini, "Using unmanned aerial vehicles (uav) for high-resolution reconstruction of topography: The structure from motion approach on coastal environments," *Remote Sensing*, vol. 5, no. 12, pp. 6880–6898, 2013.

[22] C. H. H. Aaron D. Tamminga, Brett C. Eaton, "Uas-based remote sensing of fluvial change following an extreme flood event," *Earth Surface Processes and Landforms*, vol. 40, pp. 1464–1476, 2015.

[23] K. B. J. B. J. C. M. C. S. M. K. R. A. R. S.N. Lane, P.M. Biron, "Three-dimensional measurement of river channel flow processes using acoustic doppler velocimetry," *Earth Surface Processes and Landforms*, vol. 23, pp. 1247–1267, 1998.

[24] M. O. G. G. P. E. C. E. Jonathan P. Dandois, Matthew Baker, "What is the point? evaluating the strucutre, color, and semantic traits of computer vision point clouds of vegetation," *Remote Sensing*, vol. 9, no. 355, pp. 1–20, 2017.

[25] 2016, "https://www.cloudcompare.org/doc/wiki/index.php?title=main$_page$."

[26] D. G. Lowe, "Distinctive image features from scale-invariant keypoints," *International Journal of Computer Vision*, vol. 60, no. 2, pp. 91–110, 2004.

[27] Unknown, "https://freshwaterwatch.thewaterhub.org/content/scientific-tests."

[28] Unknown, "https://www.mysticseaport.org/voyage/mass-maritime/scientific-frisbee/."

[29] J. Gundlach, *Designing Unmanned Aircraft Systems A Comprehensive Approach*, vol. 1 of *10*. The address: The name of the publisher, 3 ed., 7 2012. An optional note.

[30] A. et al., "An optimal algorithm for approximate nearest neighbor searching in fixed dimensions," *Journale of the ACM*, vol. 45, no. 6, pp. 891–923, 1998.

[31] R. C. B. Martin A. Fischler, "Random sample consensus: A paradigm for model fitting with applications to image analysis and automated cartography," *Communications of the ACM*, vol. 24, no. 6, pp. 381–395, 2004.

[32] J. H. C. Rene Wackrow, "Minimising systematic error surfaces in digital elevation models using oblique convergent imagery," *The Photogrammetric Record*, vol. 26, no. 133, pp. 16–31, 2011.

[33] K. K. A. L. A. Kevin V. Stefanik, Jason C. Gassaway, "Uav-based stereo vision for rapid aerial terrain mapping," *GIScience and Remote Sensing*, vol. 48, no. 1, pp. 24–49, 2013.

[34] B. C. C. J. L. J. P. E. C. Mark A. Fonstad, James T. Dietrich, "Topographic structure from motion: a new development in photogrammetric measurement," *Earth Surface Processes and Landforms*, vol. 38, pp. 421–430, 2013.

[35] E. C. E. Jonathan P. Dandois, Marc Olano, "Optimal altitude, overlap, and weather conditions for computer vision uav estimates of forest structure," *Remote Sensing*, vol. 7, pp. 13895–13920, 2015.

[36] S. M. d. J. Darren Turner, Arko Lucieer, "Time series analysis of landslide dynamics using an unmanned aerial vehicle (uav)," *Remote Sensing*, vol. 7, pp. 1736–1757, 2015.

[37] J. T. D. Patrice E. Carbonneau, "Cost-effective non-metric photogrammetry from consumer-grade suas: implications for direct georeferencing of structure from motion photogrammetry," *Earth Surface Processes and Landforms*, vol. 42, pp. 473–486, 2017.

[38] S. R. Mike R. James, "Mitigating systematic error in topographic models derived from uav and ground-based image networks," *Earth Surface Processes and Landforms*, vol. 39, pp. 1413–1420, 2014.

[39] A. F. Kunwar K. Singh, "A meta-analysis and review of unmanned aircraft system (uas) imagery for terrestrial applications," *International Journal of Remote Sensing*, 2018.

[40] S. R. J. T. M. J. U. Niethammer, M. R. James, "Uav-based remote sensing of the super-sauze landslide: Evaluation and results," *Engineering Geology*, vol. 128, pp. 2–11, 2011.

[41] J. I. S. Khan, L. Aragao, "A uav-lidar system to map amazonian rainforest and its ancient landscape transformations," *International Journal of Remote Sensing*, vol. 38, no. 8-10, pp. 2313–2330, 2017.

[42] C. W. D. T. Luke Wallace, Arko Lucieer, "Development of a uav-lidar system with application to forest inventory," *Remote Sensing*, vol. 4, pp. 1519–1543, 2012.

[43] P. B. R. Z. F. M. F. M. J. T. Javier Baluja, Maria P. Diago, "Assessment of vineyard water status variability by thermal and multispectral imagery using an unmanned aerial vehicle (uav)," *Springer*, vol. 30, pp. 511–522, 2012.

[44] A. J. Mathews, "A practical uav remote sensing methodology to generate multi-spectral orthophotos for vineyards: Estimation of spectral reflectance using compact digital cameras," *International Journal of Applied Geospatial Research*, vol. 6, no. 4, pp. 65–87, 2015.

[45] E. F. L. G. E. L. A. M. F. P. V. Jacopo Primicerio, Salvatore Filippo Di Gennaro, "A flexible unmanned aerial vehicle for precision agriculture," *Springer*, vol. 13, pp. 517–523, 2012.

[46] A. J. Mathews, "Object-based spatiotemporal analysis of vine canopy vigor using an inexpensive unmanned aerial vehicle remote sensing system," *Journal of Applied Remote Sensing*, vol. 8, no. 085199, pp. 1–17, 2014.

[47] C. J. Legleiter, "Remote measurement of river morphology via fusion of lidar topography and spectrally based bathymetry," *Earth Surface Processes and Landforms*, vol. 37, pp. 499–518, 2012.

[48] A. H. M. Muste, I. Fujita, "Large-scale particle image velocimetry for measurements in riverine environments," *Water Resources Research*, vol. 44, pp. 1–14, 2008.

[49] E. M. Musaab Khalid, Lionel Penard, "Application of optical flow for river velocimetry," *IGARSS*, pp. 6243–6246, 2017.

[50] J. M. N. Carl J. Legleiter, Paul J. Kinzel, "Remote measurement of river discharge using thermal particle image velocimetry (piv) and various sources of bathymetric information," *Journal of Hydrology*, vol. 554, pp. 490–506, 2017.

[51] G. J. B. R. S. L. F. B. Camille C.D. Lelong, Philippe Burger, "Assessment of unmanned aerial vehicles imagery for quantitative monitoring of wheat crop in small plots," *Sensors*, vol. 8, pp. 3557–3585, 2008.

[52] E. C. E. Jonathan P. Dandois, "High spatial resolution three-dimensional mapping of vegetation spectral dynamics using computer vision," *Remote Sensing of Environment*, vol. 136, pp. 259–276, 2013.

[53] C. W. Darren Turner, Arko Lucieer, "An automated technique for generating georectified mosaics from ultra-high resolution unmanned aerial vehicle (uav) imagery, based on strucutre from motion (sfm) point clouds," *Springer*, vol. 4, pp. 1392–1410, 2012.

[54] B. R. E. J. D. J. Benjamin L. Hemingway, Amy E. Frazier, "Vertical sampling scales for atmospheric boundary layer measurements from small unmanned aircraft systems (suas)," *Atmosphere*, vol. 8, no. 176, pp. 1–18, 2017.

[55] B. L. H. C. C. E. M. S. W. S. Amy E. Frazier, Adam J. Mathews, "Integrating small unmanned air-craft systems (suas) into meteorology and atmospheric science: Challenges and opportunities for giscience," *GI Forum*, vol. 2, pp. 189–199, 2017.

[56] J. v. d. S. Dion J. Wiseman, "Alternative methods for developing and assessing the accuracy of uav-derived dems," *International Journal of Applied Geospatial Research*, vol. 6, no. 3, pp. 58–77, 2015.

[57] Unknown, "https://commons.wikimedia.org/w/index.php?curid=745618."

[58] Unknown, "https://commons.wikimedia.org/w/index.php?curid=745618."

[59] Unknown, "https://www.unmannedsystemstechnology.com/2017/09/phoenix-lidar-jouav-announce-hybrid-long-distance-lidar-mapping-uav/."

[60] Unknown, "https://www.3d-pluraview.com/en/specificationsmodels-dimensions."

appendix

APPENDIX A

Appendix

A.1 MATLAB Code

```
clear all;
clc;
close all;

 v = imread('pixels.jpg');
 image(v)
 red=v(:,:,1);
 green=v(:,:,2);
 blue=v(:,:,3);
 a = size(v)

imagercolor = cellstr(dec2hex(red,2)); % 2 in the second argument returns two
digits when converting to hex
imagegcolor = cellstr(dec2hex(green,2));
imagebcolor = cellstr(dec2hex(blue,2));

A = reshape(strcat(imagercolor,imagegcolor,imagebcolor),a(2),a(1));

V = hex2dec(A);

W = reshape(V,a(2),a(1));

% image(red)
% surf(red)

% r = 20;
% g = 20;
% b = 255;

% rcolor = dec2hex(r);
% gcolor = dec2hex(g);
% bcolor = dec2hex(b);
%
% strcat(rcolor,gcolor,bcolor)

fgdark = hex2dec('0E0055');
fglight = hex2dec('DCD5FF');
ind = find(V>fgdark & V<fglight);

%W(row,col);

X = zeros(size(imagercolor,1),1);
X(ind)=V(ind);
X = reshape(X,a(2),a(1));
%X(row,col)=W(row,col);

Y = logical(X);

Z = double(Y);

contour(Z)

surf(Z)


boom = find(X);
length(ind)
```

Figure A.1: Color based image division code.

A.2 Processed Summaries

C1A - Cloud point cloud

Processing Report

17 April 2019

Survey Data

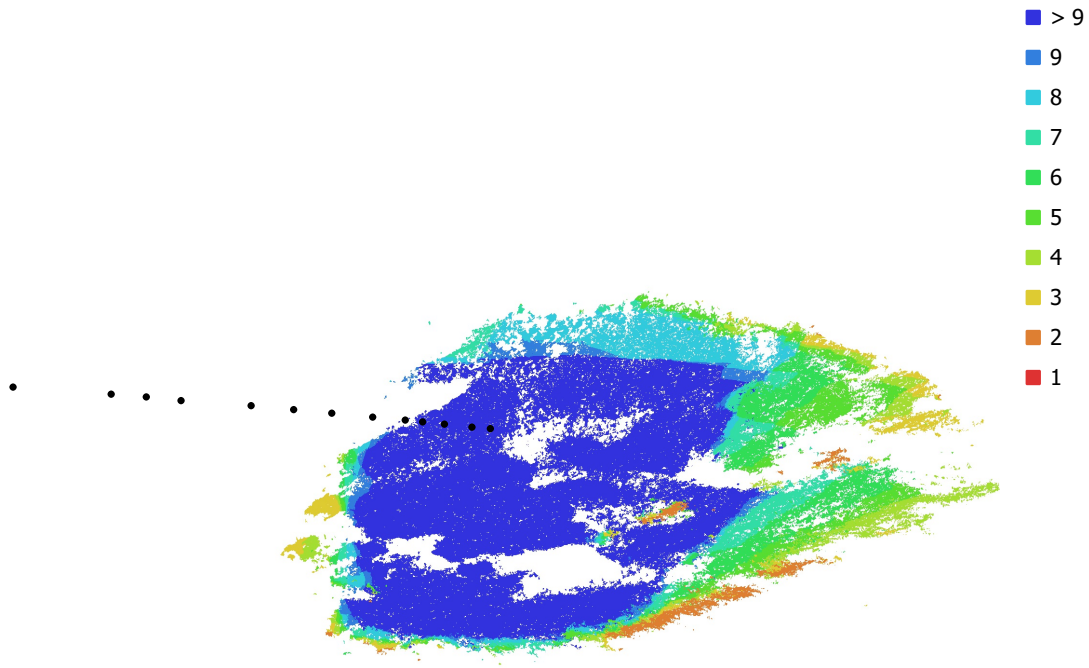

Fig. 1. Camera locations and image overlap.

Number of images:	13	Camera stations:	13
		Tie points:	3,668
		Projections:	9,475
		Reprojection error:	1.41 pix

Camera Model	Resolution	Focal Length	Pixel Size	Precalibrated
SM-G892A (4.25mm)	1494 x 1595	4.25 mm	3.24 x 3.24 µm	No
SM-G892A (4.25mm)	1895 x 1891	4.25 mm	2.64 x 2.64 µm	No
SM-G892A (4.25mm)	1846 x 1973	4.25 mm	2.62 x 2.62 µm	No
SM-G892A (4.25mm)	1904 x 1670	4.25 mm	2.79 x 2.79 µm	No
SM-G892A (4.25mm)	1456 x 1675	4.25 mm	3.19 x 3.19 µm	No

Camera Model	Resolution	Focal Length	Pixel Size	Precalibrated
SM-G892A (4.25mm)	1817 x 1506	4.25 mm	3 x 3 µm	No
SM-G892A (4.25mm)	1889 x 2035	4.25 mm	2.55 x 2.55 µm	No
SM-G892A (4.25mm)	2000 x 2030	4.25 mm	2.48 x 2.48 µm	No
SM-G892A (4.25mm)	2440 x 2000	4.25 mm	2.24 x 2.24 µm	No
SM-G892A (4.25mm)	1968 x 1857	4.25 mm	2.61 x 2.61 µm	No
SM-G892A (4.25mm)	2290 x 1874	4.25 mm	2.39 x 2.39 µm	No
SM-G892A (4.25mm)	1725 x 1620	4.25 mm	2.99 x 2.99 µm	No
SM-G892A (4.25mm)	1916 x 1553	4.25 mm	2.87 x 2.87 µm	No

Table 1. Cameras.

Camera Calibration

Fig. 2. Image residuals for SM-G892A (4.25mm).

SM-G892A (4.25mm)

1 images

Type	Resolution	Focal Length	Pixel Size
Frame	**1494 x 1595**	**4.25 mm**	**3.24 x 3.24 µm**

	Value	Error	F	Cx	Cy	K1	K2	K3	P1	P2
F	**2870.64**	63	1.00	-0.26	0.43	0.14	0.10	-0.23	0.10	0.36
Cx	**-211.333**	32		1.00	0.17	-0.02	-0.07	0.01	0.79	0.07
Cy	**-294.084**	28			1.00	0.05	0.20	-0.35	0.29	0.63
K1	**0.211246**	0.045				1.00	-0.87	0.73	0.09	0.11
K2	**-0.0668955**	0.58					1.00	-0.96	-0.10	0.17
K3	**-2.45416**	2.5						1.00	-0.01	-0.32
P1	**0.00339838**	0.0061							1.00	0.19
P2	**0.022557**	0.0034								1.00

Table 2. Calibration coefficients and correlation matrix.

Camera Calibration

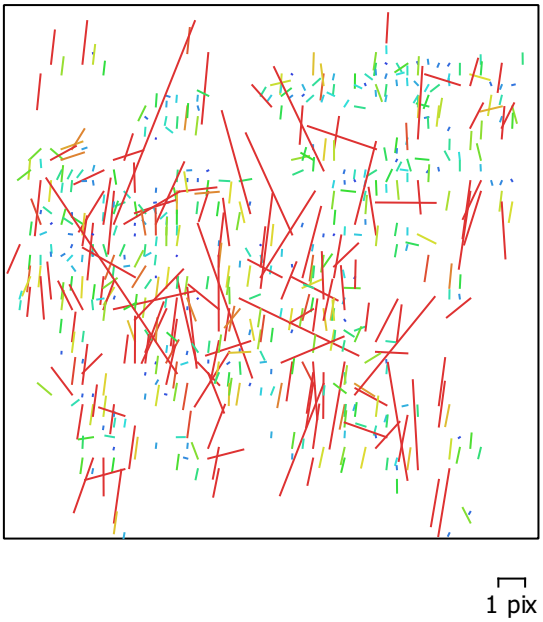

Fig. 3. Image residuals for SM-G892A (4.25mm).

SM-G892A (4.25mm)

1 images

Type	Resolution	Focal Length	Pixel Size
Frame	**1895 x 1891**	**4.25 mm**	**2.64 x 2.64 µm**

	Value	Error	F	Cx	Cy	K1	K2	K3	P1	P2
F	**2879.14**	63	1.00	-0.47	0.25	0.37	-0.14	-0.07	-0.05	0.22
Cx	**-355.925**	31		1.00	0.22	-0.26	0.01	0.02	0.74	0.08
Cy	**-358.724**	23			1.00	0.24	-0.13	-0.09	0.34	0.60
K1	**0.227201**	0.025				1.00	-0.77	0.56	-0.09	0.24
K2	**-0.509689**	0.15					1.00	-0.92	-0.09	-0.10
K3	**0.156045**	0.36						1.00	0.05	-0.11
P1	**0.000787256**	0.0046							1.00	0.16
P2	**0.0151413**	0.0028								1.00

Table 3. Calibration coefficients and correlation matrix.

Camera Calibration

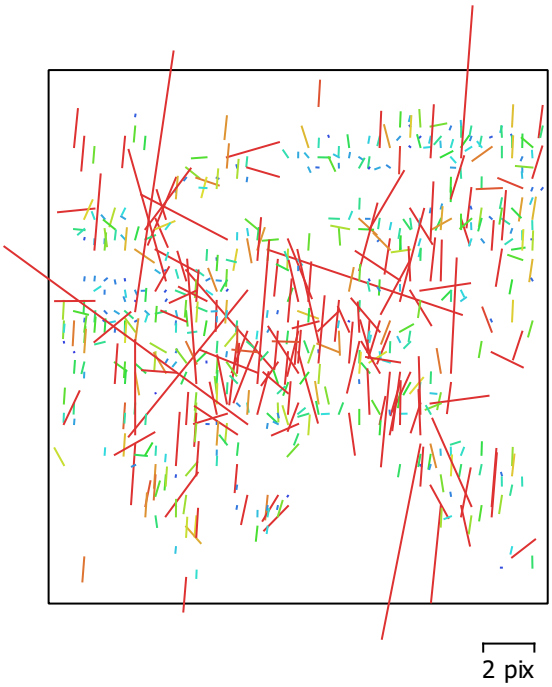

Fig. 4. Image residuals for SM-G892A (4.25mm).

SM-G892A (4.25mm)

1 images

Type	Resolution	Focal Length	Pixel Size
Frame	**1846 x 1973**	**4.25 mm**	**2.62 x 2.62 µm**

	Value	Error	F	Cx	Cy	K1	K2	K3	P1	P2
F	**2881.42**	64	1.00	-0.34	0.31	0.34	-0.22	0.02	-0.01	0.28
Cx	**-163.722**	26		1.00	0.21	-0.14	-0.07	0.06	0.74	0.07
Cy	**-364.902**	24			1.00	0.26	-0.24	0.03	0.36	0.58
K1	**0.265927**	0.026				1.00	-0.81	0.63	-0.02	0.23
K2	**-0.852817**	0.19					1.00	-0.92	-0.14	-0.12
K3	**0.656473**	0.52						1.00	0.09	-0.08
P1	**-0.00466928**	0.0044							1.00	0.19
P2	**0.0182368**	0.0028								1.00

Table 4. Calibration coefficients and correlation matrix.

Camera Calibration

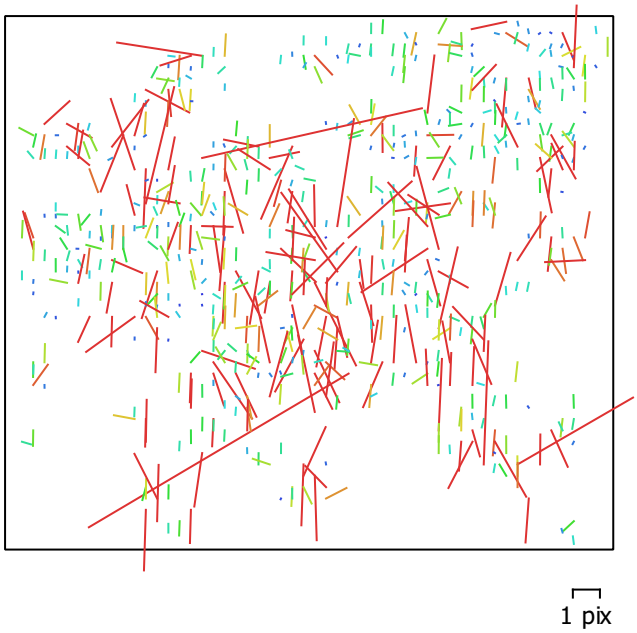

Fig. 5. Image residuals for SM-G892A (4.25mm).

SM-G892A (4.25mm)

1 images

Type	Resolution	Focal Length	Pixel Size
Frame	**1904 x 1670**	**4.25 mm**	**2.79 x 2.79 µm**

	Value	Error	F	Cx	Cy	K1	K2	K3	P1	P2
F	**2894.22**	65	1.00	-0.37	0.16	0.33	-0.35	0.29	-0.09	0.22
Cx	**-198.553**	25		1.00	0.17	-0.09	-0.13	0.15	0.72	0.06
Cy	**-539.607**	22			1.00	0.21	-0.37	0.32	0.28	0.59
K1	**0.272347**	0.022				1.00	-0.76	0.65	-0.03	0.08
K2	**-1.0015**	0.14					1.00	-0.96	-0.21	-0.24
K3	**1.21061**	0.32						1.00	0.23	0.17
P1	**-0.0114173**	0.0037							1.00	0.16
P2	**0.0174815**	0.0028								1.00

Table 5. Calibration coefficients and correlation matrix.

Camera Calibration

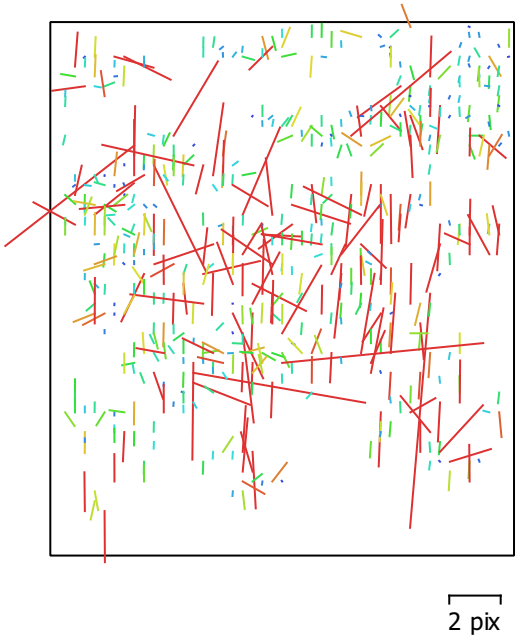

Fig. 6. Image residuals for SM-G892A (4.25mm).

SM-G892A (4.25mm)

1 images

Type	Resolution	Focal Length	Pixel Size
Frame	**1456 x 1675**	**4.25 mm**	**3.19 x 3.19 µm**

	Value	Error	F	Cx	Cy	K1	K2	K3	P1	P2
F	**2900.21**	66	1.00	-0.33	0.19	0.24	-0.19	0.10	-0.13	0.24
Cx	**-306.863**	25		1.00	0.11	-0.07	-0.11	0.10	0.74	0.03
Cy	**-538.487**	24			1.00	0.23	-0.32	0.23	0.17	0.61
K1	**0.273736**	0.029				1.00	-0.83	0.74	-0.12	0.11
K2	**-1.00081**	0.23					1.00	-0.96	-0.05	-0.19
K3	**1.13501**	0.62						1.00	0.05	0.10
P1	**-0.0133058**	0.0042							1.00	0.10
P2	**0.0199337**	0.003								1.00

Table 6. Calibration coefficients and correlation matrix.

Camera Calibration

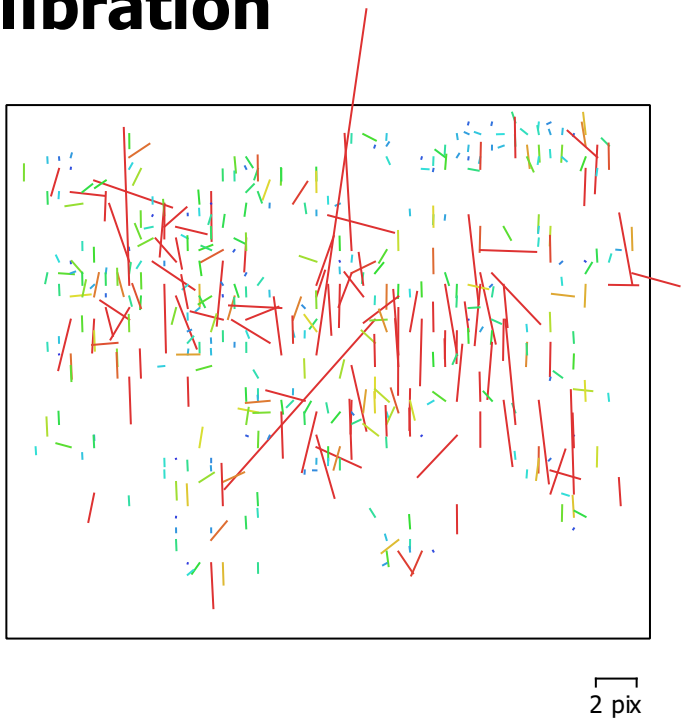

Fig. 7. Image residuals for SM-G892A (4.25mm).

SM-G892A (4.25mm)

1 images

Type	Resolution	Focal Length	Pixel Size
Frame	**1817 x 1506**	**4.25 mm**	**3 x 3 µm**

	Value	Error	F	Cx	Cy	K1	K2	K3	P1	P2
F	**2901.09**	66	1.00	-0.46	0.00	0.19	-0.14	0.04	-0.26	0.20
Cx	**-254.223**	26		1.00	0.12	-0.21	0.00	0.00	0.73	0.06
Cy	**-787.244**	21			1.00	0.05	-0.19	0.13	0.11	0.50
K1	**0.226904**	0.025				1.00	-0.80	0.71	-0.30	-0.17
K2	**-0.699852**	0.14					1.00	-0.97	0.06	-0.07
K3	**0.577497**	0.31						1.00	-0.05	0.02
P1	**-0.0201244**	0.0036							1.00	0.13
P2	**0.0206665**	0.0027								1.00

Table 7. Calibration coefficients and correlation matrix.

Camera Calibration

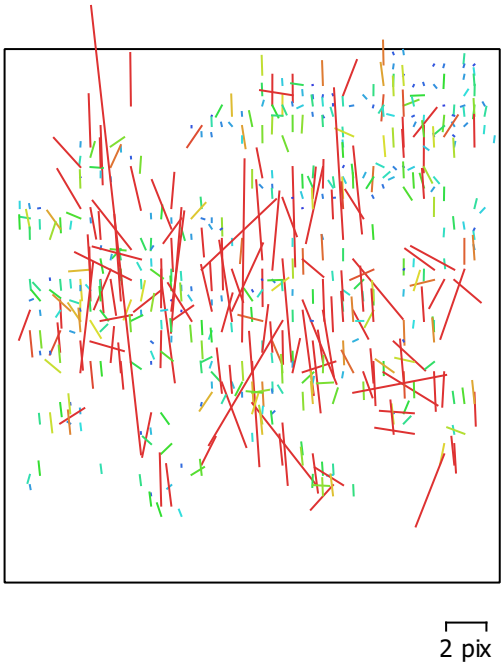

Fig. 8. Image residuals for SM-G892A (4.25mm).

SM-G892A (4.25mm)

1 images

Type	Resolution	Focal Length	Pixel Size
Frame	**1889 x 2035**	**4.25 mm**	**2.55 x 2.55 µm**

	Value	Error	F	Cx	Cy	K1	K2	K3	P1	P2
F	**2927.7**	69	1.00	-0.49	0.07	0.32	-0.38	0.39	-0.32	0.30
Cx	**-367.816**	25		1.00	0.10	-0.21	-0.06	0.08	0.69	-0.02
Cy	**-616.588**	21			1.00	0.16	-0.36	0.37	0.04	0.50
K1	**0.299993**	0.025				1.00	-0.78	0.69	-0.36	0.01
K2	**-1.16976**	0.15					1.00	-0.98	0.05	-0.31
K3	**1.61969**	0.34						1.00	-0.00	0.31
P1	**-0.0303226**	0.0038							1.00	0.06
P2	**0.0248364**	0.0027								1.00

Table 8. Calibration coefficients and correlation matrix.

Camera Calibration

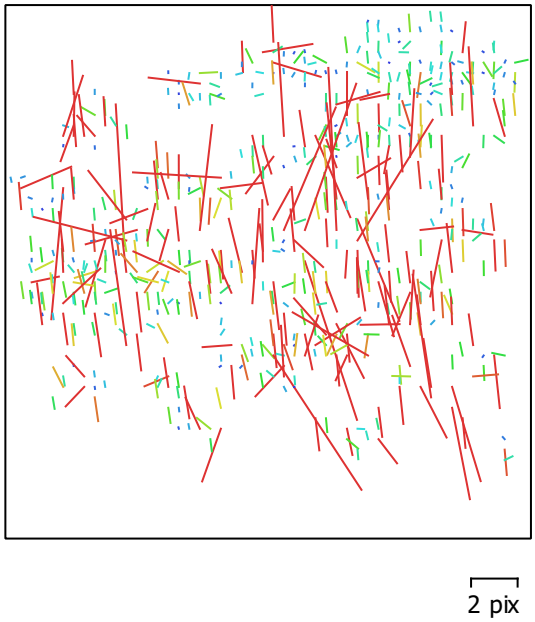

Fig. 9. Image residuals for SM-G892A (4.25mm).

SM-G892A (4.25mm)

1 images

Type	Resolution	Focal Length	Pixel Size
Frame	**2000 x 2030**	**4.25 mm**	**2.48 x 2.48 µm**

	Value	Error	F	Cx	Cy	K1	K2	K3	P1	P2
F	**2933.33**	70	1.00	-0.49	0.07	0.36	-0.41	0.40	-0.35	0.30
Cx	**-499.064**	26		1.00	0.15	-0.26	-0.08	0.13	0.68	0.01
Cy	**-589.781**	22			1.00	0.13	-0.38	0.38	0.07	0.54
K1	**0.278329**	0.024				1.00	-0.72	0.62	-0.47	-0.04
K2	**-0.889675**	0.1					1.00	-0.97	0.09	-0.32
K3	**0.978046**	0.19						1.00	-0.01	0.32
P1	**-0.0319173**	0.004							1.00	0.09
P2	**0.0249913**	0.0028								1.00

Table 9. Calibration coefficients and correlation matrix.

Camera Calibration

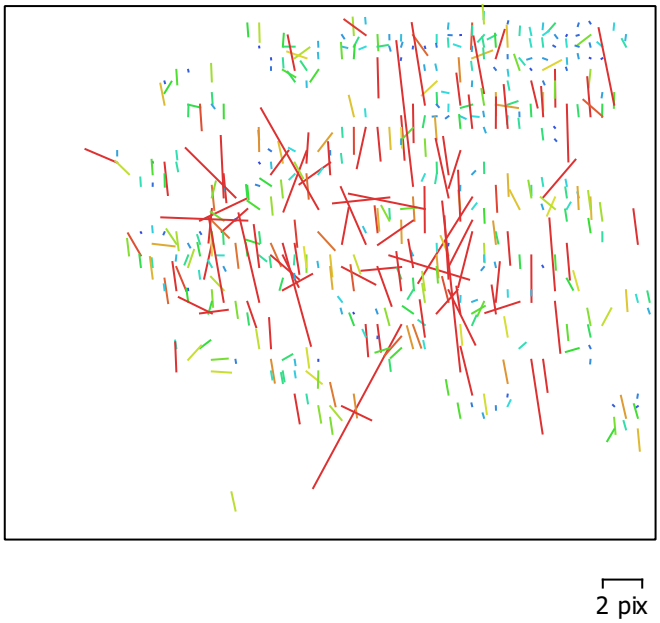

Fig. 10. Image residuals for SM-G892A (4.25mm).

SM-G892A (4.25mm)

1 images

Type	Resolution	Focal Length	Pixel Size
Frame	**2440 x 2000**	**4.25 mm**	**2.24 x 2.24 µm**

	Value	Error	F	Cx	Cy	K1	K2	K3	P1	P2
F	**2953.94**	74	1.00	-0.43	0.10	0.36	-0.34	0.29	-0.36	0.28
Cx	**-307.52**	26		1.00	0.20	-0.21	-0.14	0.18	0.67	0.07
Cy	**-675.855**	24			1.00	0.10	-0.39	0.36	0.12	0.63
K1	**0.278469**	0.027				1.00	-0.73	0.62	-0.48	-0.07
K2	**-0.804607**	0.11					1.00	-0.97	0.14	-0.30
K3	**0.813014**	0.19						1.00	-0.07	0.28
P1	**-0.0342686**	0.0043							1.00	0.10
P2	**0.025494**	0.0032								1.00

Table 10. Calibration coefficients and correlation matrix.

Camera Calibration

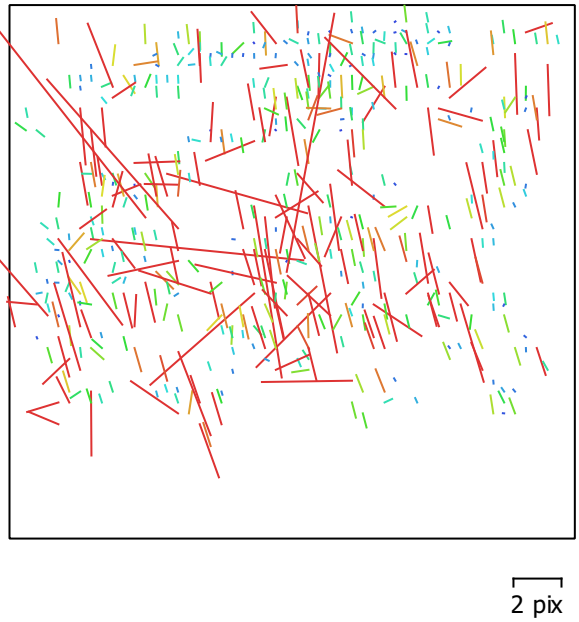

Fig. 11. Image residuals for SM-G892A (4.25mm).

SM-G892A (4.25mm)

1 images

Type	Resolution	Focal Length	Pixel Size
Frame	**1968 x 1857**	**4.25 mm**	**2.61 x 2.61 µm**

	Value	Error	F	Cx	Cy	K1	K2	K3	P1	P2
F	**2995.15**	77	1.00	0.08	-0.10	0.30	-0.38	0.38	-0.07	0.12
Cx	**-481.427**	31		1.00	0.30	-0.02	-0.45	0.49	0.74	0.34
Cy	**-686.553**	35			1.00	-0.30	-0.17	0.27	0.31	0.71
K1	**0.296947**	0.037				1.00	-0.68	0.52	-0.22	-0.46
K2	**-0.998021**	0.17					1.00	-0.96	-0.16	-0.15
K3	**1.36368**	0.38						1.00	0.24	0.27
P1	**-0.0276949**	0.0058							1.00	0.25
P2	**0.0202844**	0.0053								1.00

Table 11. Calibration coefficients and correlation matrix.

Camera Calibration

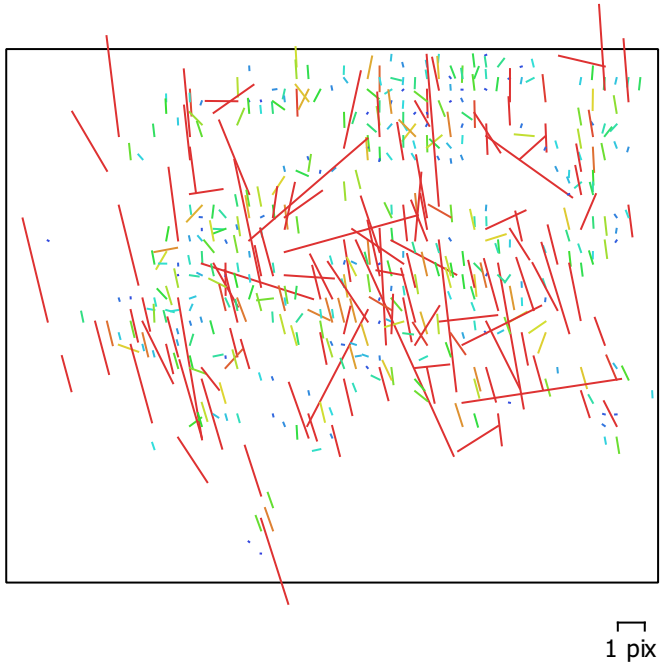

Fig. 12. Image residuals for SM-G892A (4.25mm).

SM-G892A (4.25mm)

1 images

Type	Resolution	Focal Length	Pixel Size
Frame	**2290 x 1874**	**4.25 mm**	**2.39 x 2.39 µm**

	Value	Error	F	Cx	Cy	K1	K2	K3	P1	P2
F	**3002.81**	81	1.00	-0.01	0.03	0.47	-0.50	0.46	-0.09	0.15
Cx	**-411.804**	29		1.00	0.45	0.03	-0.49	0.50	0.73	0.39
Cy	**-685.174**	31			1.00	-0.04	-0.43	0.45	0.43	0.77
K1	**0.441659**	0.042				1.00	-0.71	0.60	-0.23	-0.21
K2	**-1.25895**	0.21					1.00	-0.98	-0.24	-0.36
K3	**1.42872**	0.39						1.00	0.29	0.40
P1	**-0.0362455**	0.0062							1.00	0.36
P2	**0.0230734**	0.0053								1.00

Table 12. Calibration coefficients and correlation matrix.

Camera Calibration

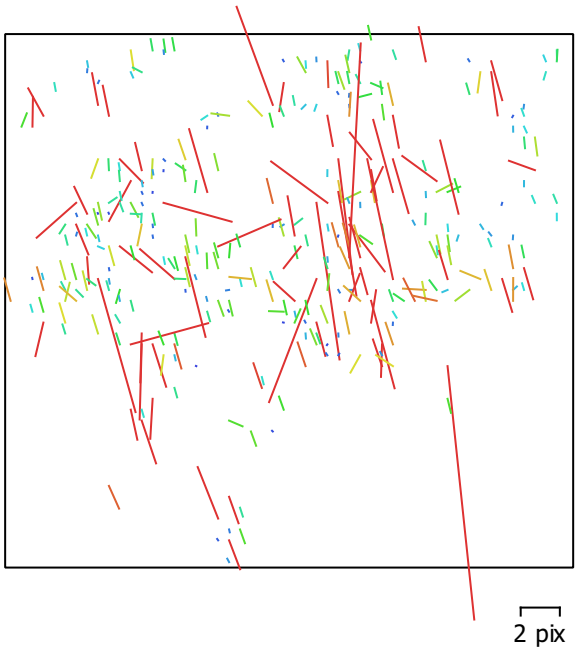

Fig. 13. Image residuals for SM-G892A (4.25mm).

SM-G892A (4.25mm)

1 images

Type	Resolution	Focal Length	Pixel Size
Frame	**1725 x 1620**	**4.25 mm**	**2.99 x 2.99 µm**

	Value	Error	F	Cx	Cy	K1	K2	K3	P1	P2
F	**2985.23**	82	1.00	-0.03	0.00	0.58	-0.60	0.61	-0.07	0.06
Cx	**-612.963**	33		1.00	0.49	0.06	-0.51	0.55	0.76	0.43
Cy	**-768.764**	32			1.00	0.02	-0.47	0.53	0.44	0.79
K1	**0.620764**	0.058				1.00	-0.74	0.64	-0.23	-0.19
K2	**-2.1875**	0.38					1.00	-0.99	-0.32	-0.38
K3	**3.5673**	0.97						1.00	0.40	0.46
P1	**-0.0392119**	0.0076							1.00	0.45
P2	**0.0206125**	0.0061								1.00

Table 13. Calibration coefficients and correlation matrix.

Camera Calibration

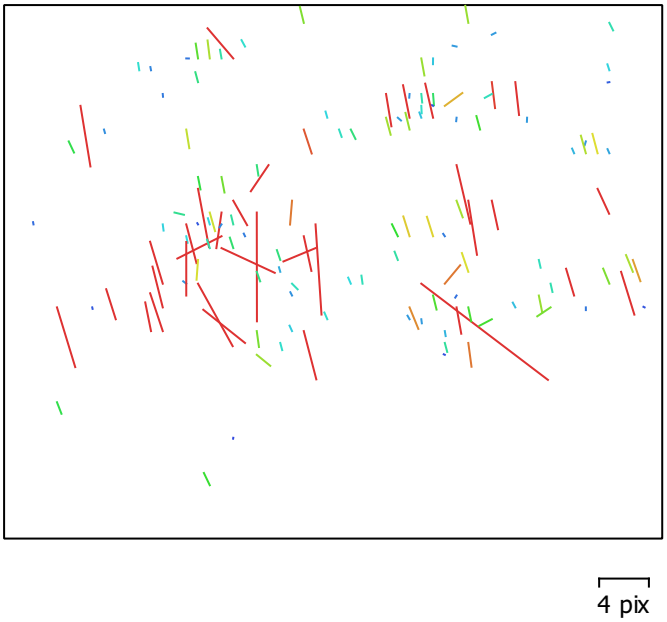

Fig. 14. Image residuals for SM-G892A (4.25mm).

SM-G892A (4.25mm)

1 images

Type	Resolution	Focal Length	Pixel Size
Frame	**1916 x 1553**	**4.25 mm**	**2.87 x 2.87 µm**

	Value	Error	F	Cx	Cy	K1	K2	K3	P1	P2
F	**3075.23**	95	1.00	0.09	0.01	0.65	-0.51	0.34	-0.02	-0.08
Cx	**-574.691**	46		1.00	0.45	0.12	-0.49	0.34	0.80	0.39
Cy	**-695.46**	48			1.00	0.01	-0.46	0.42	0.42	0.84
K1	**0.638569**	0.083				1.00	-0.74	0.64	-0.20	-0.28
K2	**-1.22201**	0.4					1.00	-0.95	-0.32	-0.32
K3	**0.620064**	0.66						1.00	0.21	0.32
P1	**-0.0418521**	0.013							1.00	0.54
P2	**0.0128105**	0.011								1.00

Table 14. Calibration coefficients and correlation matrix.

Digital Elevation Model

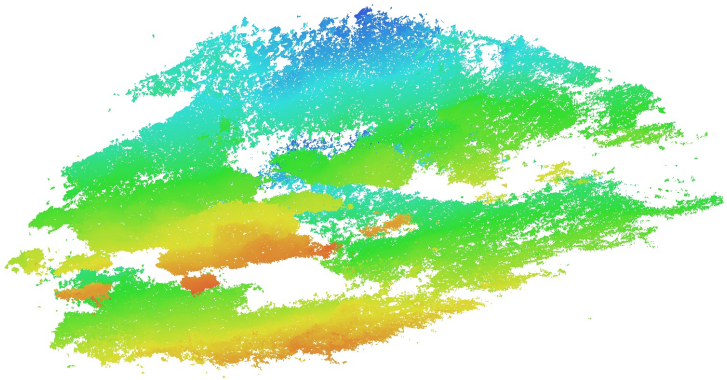

Fig. 15. Reconstructed digital elevation model.

Processing Parameters

General	
Cameras	13
Aligned cameras	13
Coordinate system	WGS 84 (EPSG::4326)
Rotation angles	Yaw, Pitch, Roll
Point Cloud	
Points	3,668 of 3,940
RMS reprojection error	0.175577 (1.41333 pix)
Max reprojection error	0.528556 (22.3893 pix)
Mean key point size	7.67268 pix
Point colors	3 bands, uint8
Key points	No
Average tie point multiplicity	2.6901
Alignment parameters	
Accuracy	High
Generic preselection	Yes
Reference preselection	Yes
Key point limit	40,000
Tie point limit	4,000
Adaptive camera model fitting	No
Matching time	8 seconds
Alignment time	4 seconds
Depth Maps	
Count	13
Reconstruction parameters	
Quality	High
Filtering mode	Mild
Processing time	2 minutes 29 seconds
Dense Point Cloud	
Points	3,018,350
Point colors	3 bands, uint8
Reconstruction parameters	
Quality	High
Depth filtering	Mild
Depth maps generation time	2 minutes 29 seconds
Dense cloud generation time	21 seconds
Model	
Faces	603,663
Vertices	528,895
Vertex colors	3 bands, uint8
Reconstruction parameters	
Surface type	Arbitrary
Source data	Dense
Interpolation	Disabled
Quality	High
Depth filtering	Mild
Face count	603,663
Processing time	1 minutes 52 seconds
Software	
Version	1.5.1 build 7618

General

Platform	Windows 64

CS1B - Campus Light Survey

Processing Report

15 May 2019

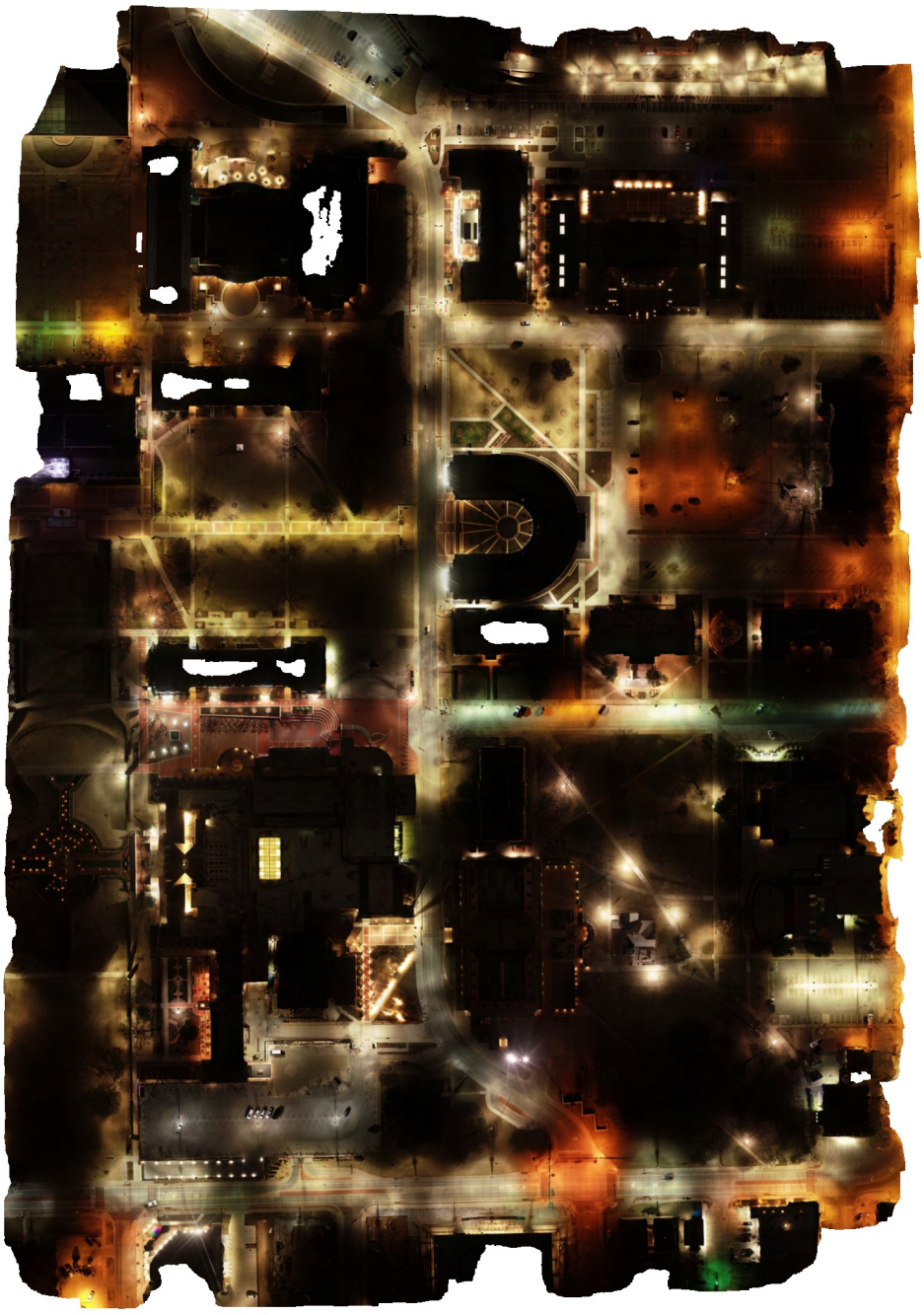

Survey Data

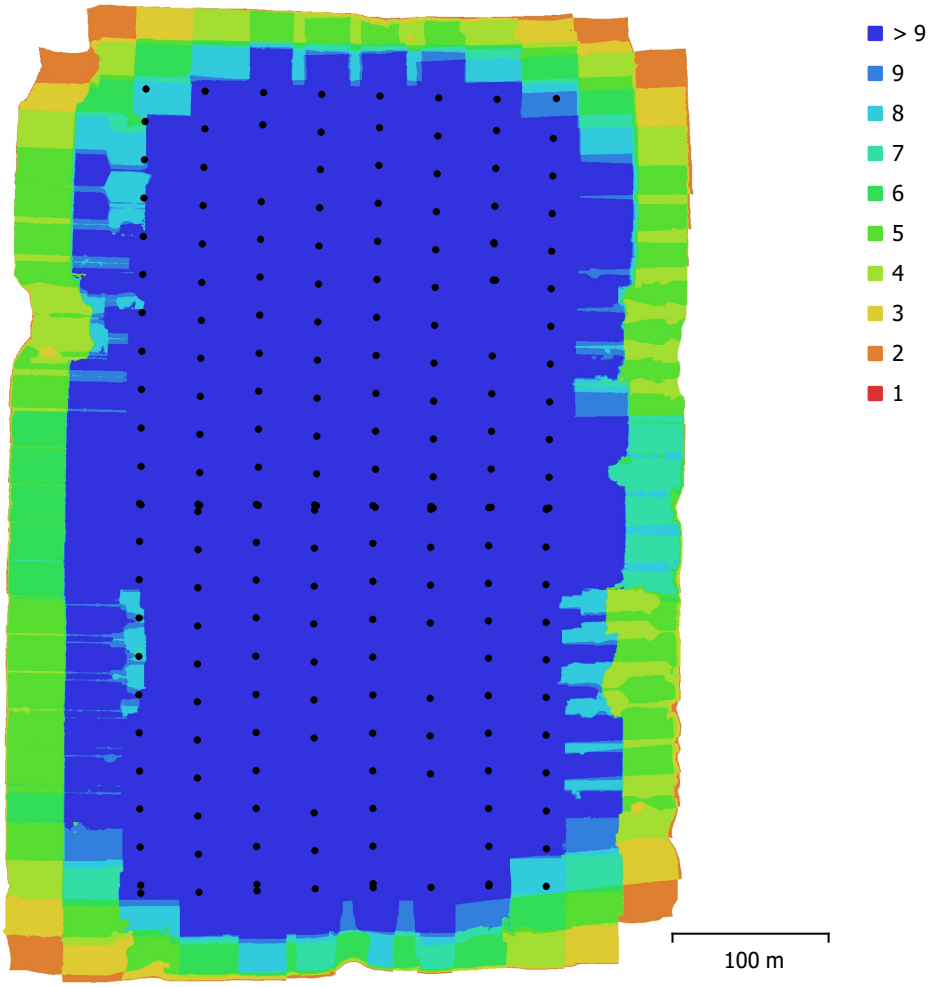

Fig. 1. Camera locations and image overlap.

Number of images:	188	Camera stations:	188
Flying altitude:	127 m	Tie points:	139,244
Ground resolution:	3.12 cm/pix	Projections:	521,132
Coverage area:	0.261 km²	Reprojection error:	1.54 pix

Camera Model	Resolution	Focal Length	Pixel Size	Precalibrated
FC6310 (8.8mm)	5472 x 3648	8.8 mm	2.41 x 2.41 µm	No

Table 1. Cameras.

Camera Calibration

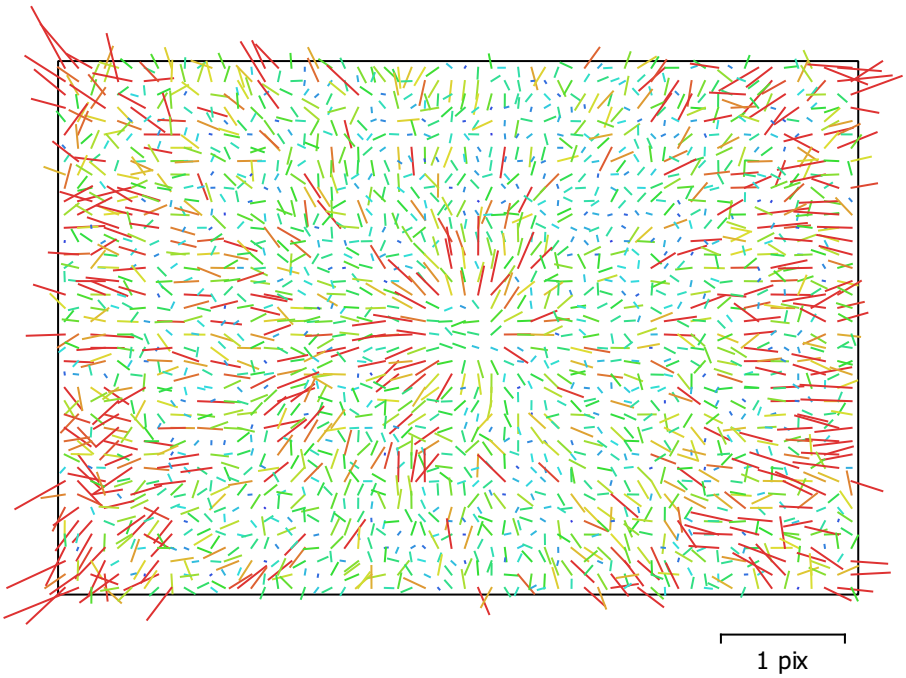

Fig. 2. Image residuals for FC6310 (8.8mm).

FC6310 (8.8mm)

188 images

Type	Resolution	Focal Length	Pixel Size
Frame	**5472 x 3648**	**8.8 mm**	**2.41 x 2.41 µm**

	Value	Error	F	Cx	Cy	K1	K2	K3	P1	P2
F	**3677.23**	12	1.00	0.03	-0.08	0.15	-0.24	0.55	-0.15	-0.07
Cx	**-107.426**	2		1.00	0.04	0.13	-0.18	0.22	0.39	0.01
Cy	**-36.0132**	2.1			1.00	-0.10	-0.02	0.00	0.05	0.44
K1	**0.00583598**	0.00018				1.00	-0.26	0.29	0.20	-0.20
K2	**-0.00305166**	0.00016					1.00	-0.92	-0.11	0.00
K3	**0.00479725**	0.00016						1.00	0.09	-0.02
P1	**-0.00381434**	9.4e-005							1.00	0.00
P2	**-0.00127712**	9.3e-005								1.00

Table 2. Calibration coefficients and correlation matrix.

Camera Locations

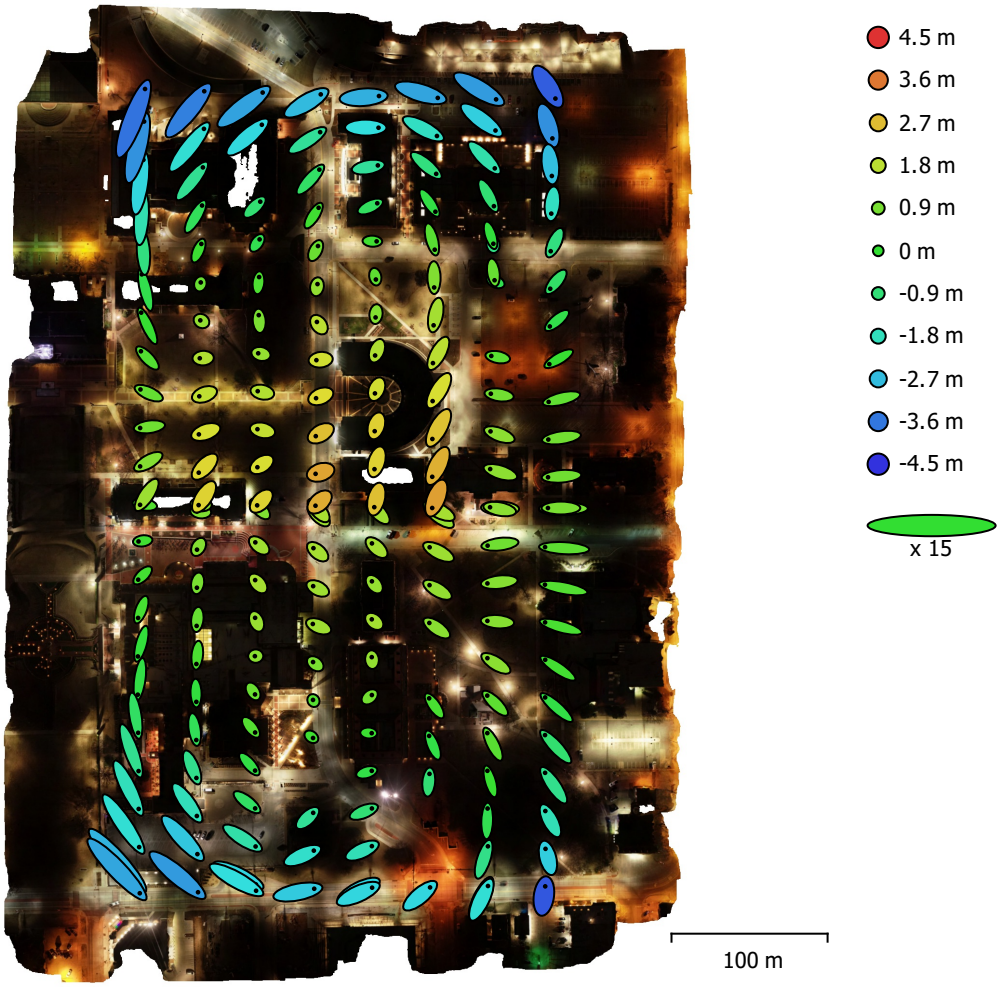

Fig. 3. Camera locations and error estimates.
Z error is represented by ellipse color. X,Y errors are represented by ellipse shape.
Estimated camera locations are marked with a black dot.

X error (m)	Y error (m)	Z error (m)	XY error (m)	Total error (m)
0.735195	0.774881	1.64448	1.06815	1.96093

Table 3. Average camera location error.
X - Longitude, Y - Latitude, Z - Altitude.

Digital Elevation Model

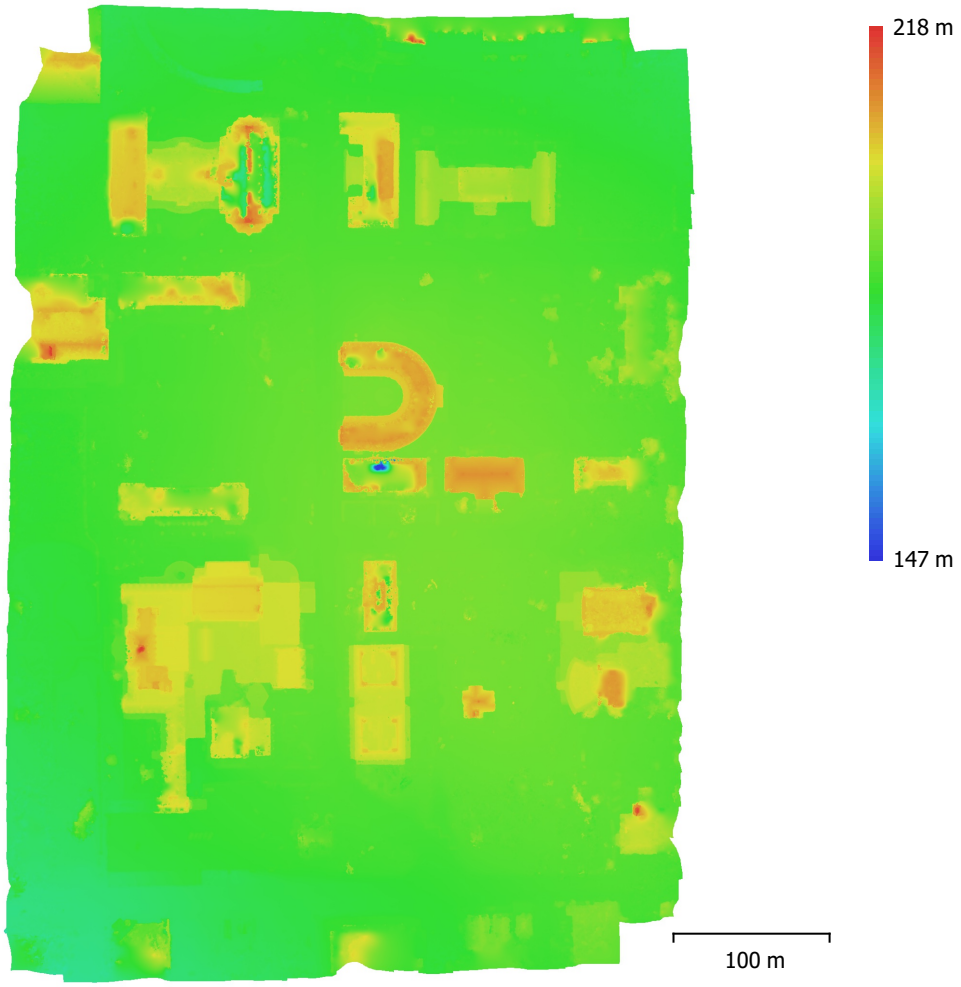

Fig. 4. Reconstructed digital elevation model.

Resolution:	12.5 cm/pix
Point density:	64 points/m²

Processing Parameters

General	
Cameras	188
Aligned cameras	188
Coordinate system	WGS 84 (EPSG::4326)
Rotation angles	Yaw, Pitch, Roll
Point Cloud	
Points	139,244 of 160,114
RMS reprojection error	0.198735 (1.53895 pix)
Max reprojection error	0.60665 (55.4552 pix)
Mean key point size	7.41931 pix
Point colors	3 bands, uint8
Key points	No
Average tie point multiplicity	4.0873
Alignment parameters	
Accuracy	High
Generic preselection	Yes
Reference preselection	Yes
Key point limit	40,000
Tie point limit	4,000
Adaptive camera model fitting	No
Matching time	18 minutes 42 seconds
Alignment time	2 minutes 57 seconds
Dense Point Cloud	
Points	18,158,200
Point colors	3 bands, uint8
Depth maps generation parameters	
Quality	Medium
Filtering mode	Aggressive
Processing time	2 hours 17 minutes
Dense cloud generation parameters	
Processing time	7 minutes 54 seconds
Model	
Faces	1,210,545
Vertices	609,296
Vertex colors	3 bands, uint8
Depth maps generation parameters	
Quality	Medium
Filtering mode	Aggressive
Reconstruction parameters	
Surface type	Arbitrary
Source data	Dense cloud
Interpolation	Enabled
Processing time	13 minutes 28 seconds
DEM	
Size	4,687 x 6,934
Coordinate system	WGS 84 (EPSG::4326)
Reconstruction parameters	
Source data	Dense cloud
Interpolation	Enabled
Processing time	16 seconds

General

Orthomosaic

Size	14,330 x 20,239
Coordinate system	WGS 84 (EPSG::4326)
Colors	3 bands, uint8

Reconstruction parameters

Blending mode	Mosaic
Surface	Mesh
Enable hole filling	Yes
Processing time	6 minutes 37 seconds

Software

Version	1.5.2 build 7838
Platform	Windows 64

CS1C - Detail Cliff Face

Processing Report

26 April 2019

Survey Data

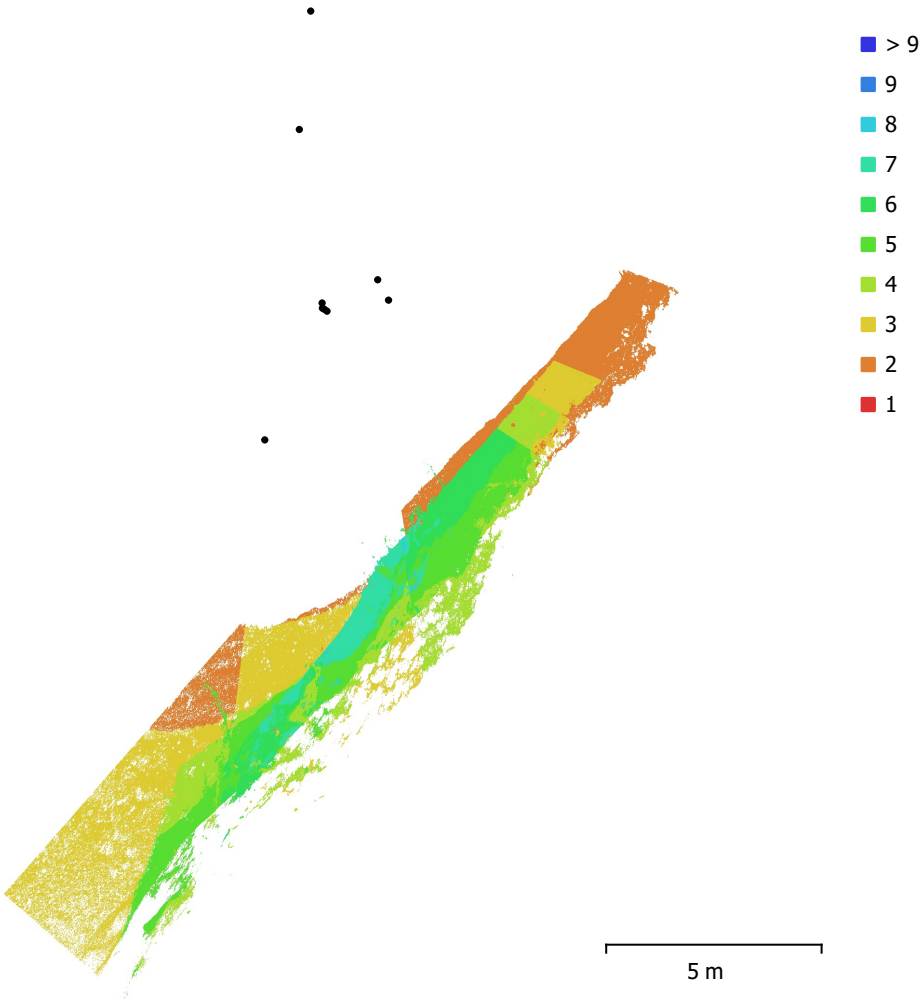

Fig. 1. Camera locations and image overlap.

Number of images:	9	Camera stations:	9
Flying altitude:	8.02 m	Tie points:	12,464
Ground resolution:	1.95 mm/pix	Projections:	32,683
Coverage area:	41.9 m²	Reprojection error:	0.417 pix

Camera Model	Resolution	Focal Length	Pixel Size	Precalibrated
FC6310 (8.8mm)	5472 x 3078	8.8 mm	2.53 x 2.53 µm	No

Table 1. Cameras.

Camera Calibration

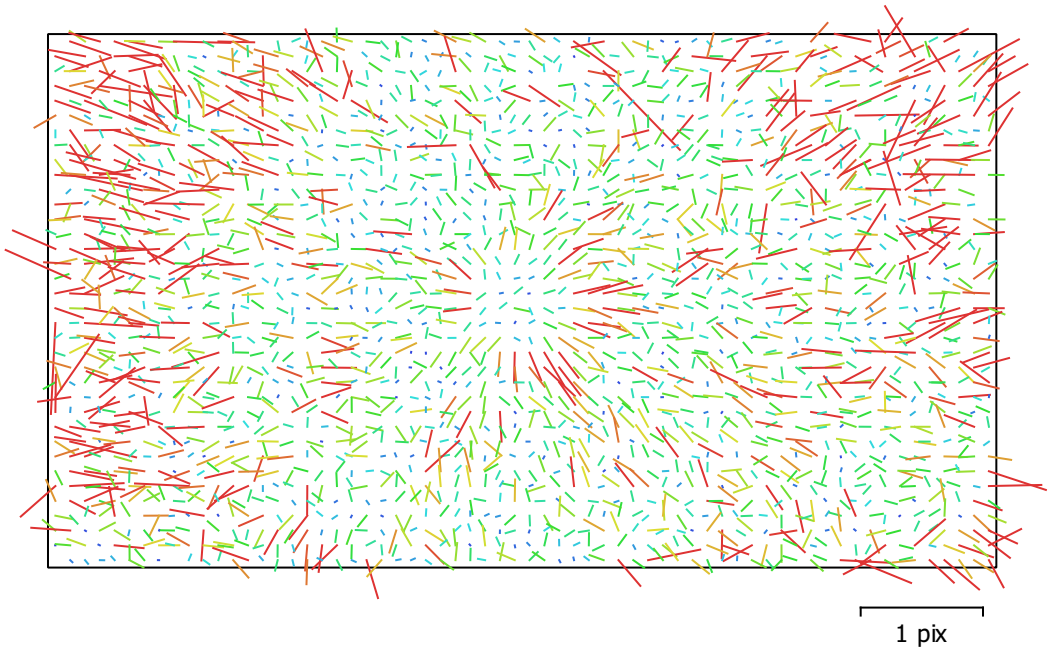

Fig. 2. Image residuals for FC6310 (8.8mm).

FC6310 (8.8mm)

9 images

Type	Resolution	Focal Length	Pixel Size
Frame	**5472 x 3078**	**8.8 mm**	**2.53 x 2.53 µm**

	Value	Error	F	Cx	Cy	K1	K2	K3	P1	P2
F	**3666.41**	0.36	1.00	0.15	-0.12	0.30	0.11	-0.13	0.15	-0.06
Cx	**-3.03569**	0.63		1.00	-0.04	0.23	-0.00	0.02	0.93	-0.03
Cy	**23.3521**	0.65			1.00	-0.07	-0.01	0.01	-0.04	0.94
K1	**0.00244551**	0.00014				1.00	-0.85	0.80	0.18	-0.08
K2	**-0.0129988**	0.00041					1.00	-0.98	0.03	0.02
K3	**0.0133886**	0.00041						1.00	-0.01	-0.02
P1	**-0.000154707**	4.3e-005							1.00	-0.00
P2	**-6.2137e-006**	4e-005								1.00

Table 2. Calibration coefficients and correlation matrix.

Camera Locations

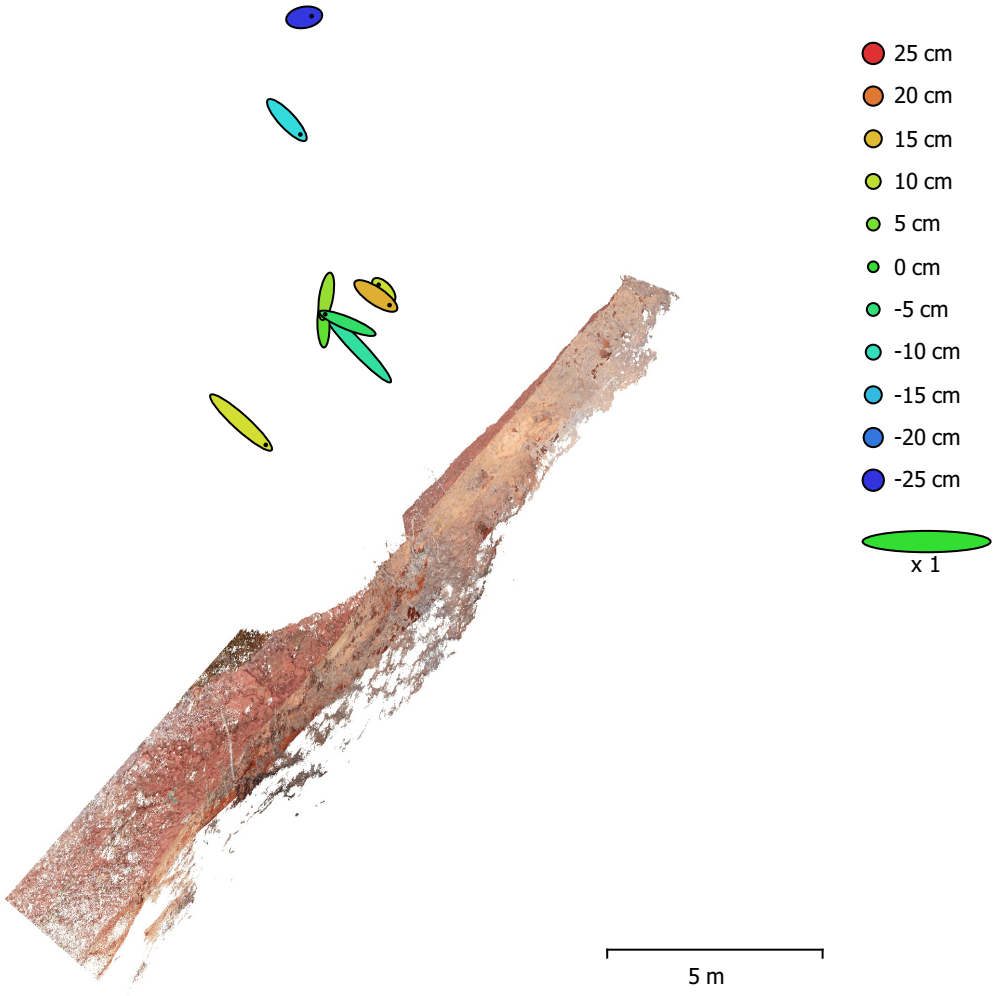

Fig. 3. Camera locations and error estimates.
Z error is represented by ellipse color. X,Y errors are represented by ellipse shape.
Estimated camera locations are marked with a black dot.

X error (m)	Y error (m)	Z error (m)	XY error (m)	Total error (m)
0.758663	0.757641	0.12571	1.07219	1.07953

Table 3. Average camera location error.
X - Longitude, Y - Latitude, Z - Altitude.

Digital Elevation Model

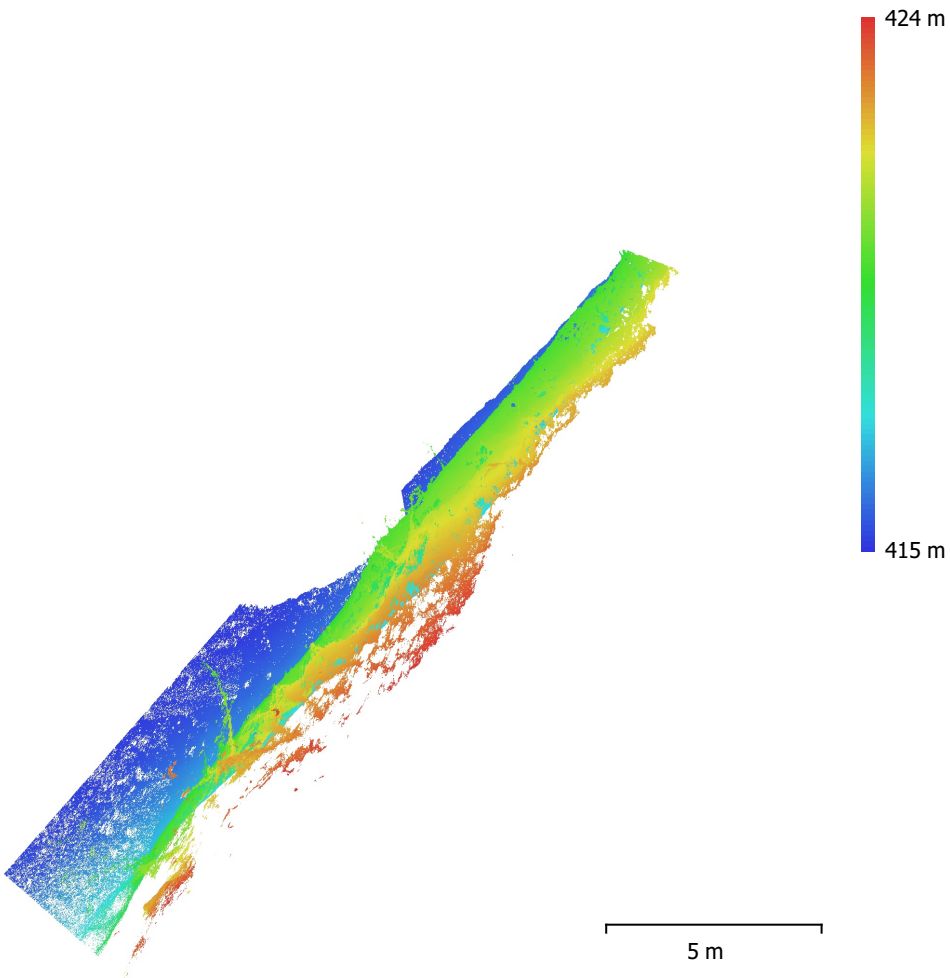

Fig. 4. Reconstructed digital elevation model.

Resolution:	3.91 mm/pix
Point density:	6.55 points/cm²

Processing Parameters

General	
Cameras	9
Aligned cameras	9
Coordinate system	WGS 84 (EPSG::4326)
Rotation angles	Yaw, Pitch, Roll
Point Cloud	
Points	12,464 of 12,851
RMS reprojection error	0.12265 (0.417274 pix)
Max reprojection error	0.368044 (9.97758 pix)
Mean key point size	3.25191 pix
Point colors	3 bands, uint8
Key points	No
Average tie point multiplicity	2.65349
Alignment parameters	
Accuracy	High
Generic preselection	Yes
Reference preselection	Yes
Key point limit	40,000
Tie point limit	4,000
Adaptive camera model fitting	No
Matching time	26 seconds
Alignment time	5 seconds
Depth Maps	
Count	9
Depth maps generation parameters	
Quality	High
Filtering mode	Mild
Processing time	9 minutes 49 seconds
Dense Point Cloud	
Points	13,778,382
Point colors	3 bands, uint8
Depth maps generation parameters	
Quality	High
Filtering mode	Mild
Processing time	9 minutes 49 seconds
Dense cloud generation parameters	
Processing time	1 minutes 0 seconds
Model	
Faces	2,755,655
Vertices	2,261,442
Vertex colors	3 bands, uint8
Depth maps generation parameters	
Quality	High
Filtering mode	Mild
Reconstruction parameters	
Surface type	Arbitrary
Source data	Dense cloud
Interpolation	Disabled
Processing time	8 minutes 38 seconds
Software	

General

Version	1.5.2 build 7838
Platform	Windows 64

CS2 - LCB May9

Processing Report

16 April 2019

Survey Data

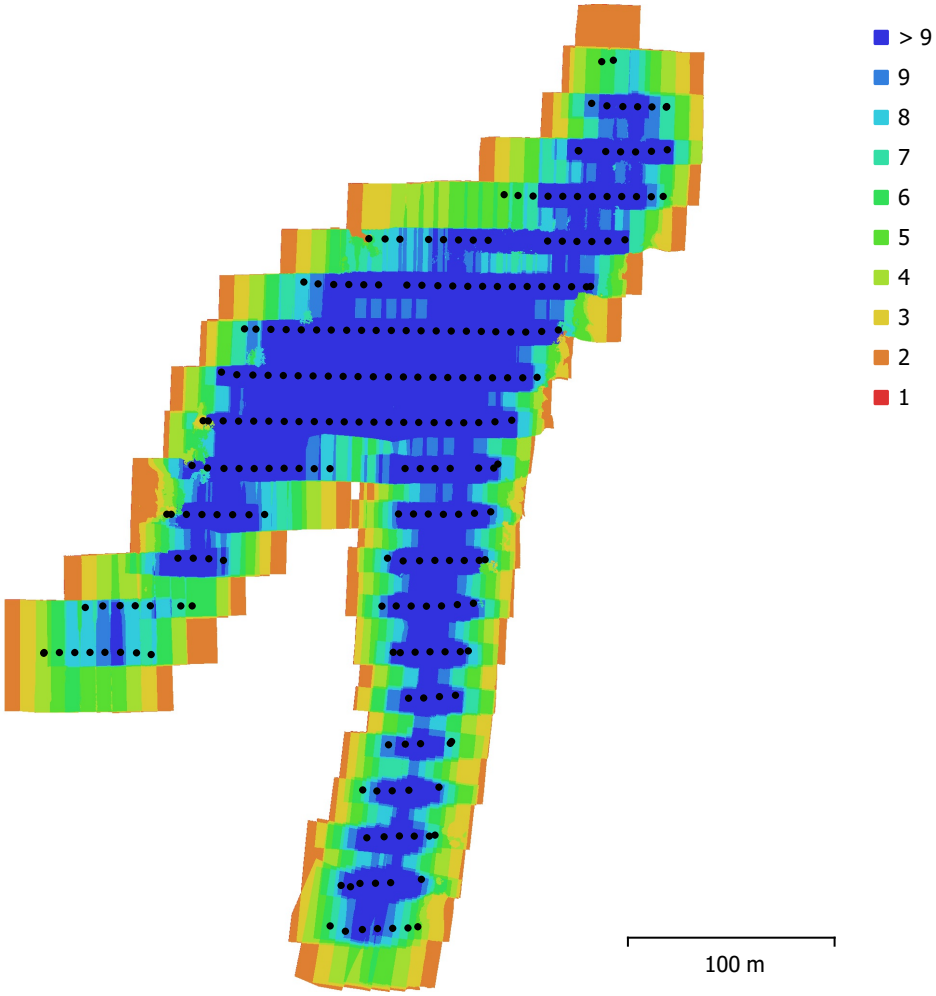

Fig. 1. Camera locations and image overlap.

Number of images:	246	Camera stations:	235
Flying altitude:	40 m	Tie points:	201,861
Ground resolution:	1.02 cm/pix	Projections:	875,113
Coverage area:	0.0621 km²	Reprojection error:	0.596 pix

Camera Model	Resolution	Focal Length	Pixel Size	Precalibrated
FC6310 (8.8mm)	5472 x 3648	8.8 mm	2.41 x 2.41 µm	No

Table 1. Cameras.

Camera Calibration

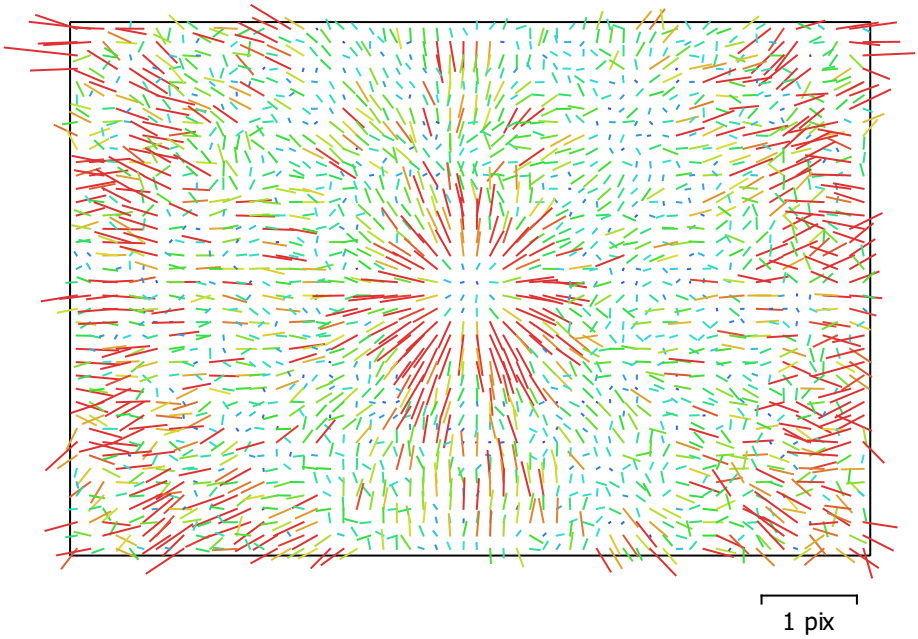

Fig. 2. Image residuals for FC6310 (8.8mm).

FC6310 (8.8mm)

246 images

Type	Resolution	Focal Length	Pixel Size
Frame	**5472 x 3648**	**8.8 mm**	**2.41 x 2.41 µm**

	Value	Error	F	Cx	Cy	K1	K2	K3	P1	P2
F	**3411.79**	14	1.00	-0.01	0.22	-0.11	-0.95	0.98	-0.13	0.20
Cx	**-10.3267**	1		1.00	-0.10	-0.09	0.02	-0.02	0.16	-0.04
Cy	**1.44919**	1.4			1.00	-0.24	-0.18	0.19	-0.08	0.21
K1	**-0.0018814**	0.00012				1.00	0.02	-0.05	-0.01	0.13
K2	**-0.0081439**	0.00014					1.00	-0.99	0.14	-0.20
K3	**0.0062157**	0.00016						1.00	-0.14	0.20
P1	**-0.000479325**	5.6e-005							1.00	-0.09
P2	**0.00348269**	5.2e-005								1.00

Table 2. Calibration coefficients and correlation matrix.

Camera Locations

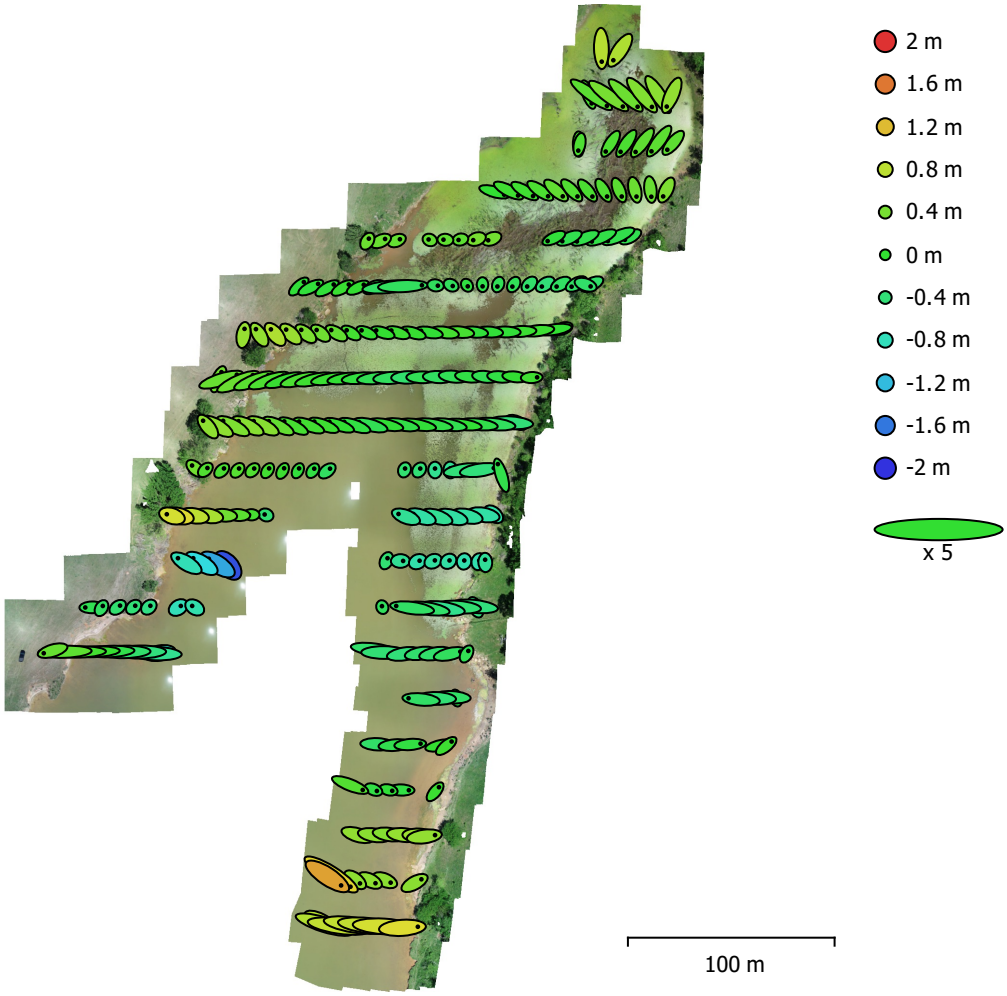

Fig. 3. Camera locations and error estimates.
Z error is represented by ellipse color. X,Y errors are represented by ellipse shape.
Estimated camera locations are marked with a black dot.

X error (m)	Y error (m)	Z error (m)	XY error (m)	Total error (m)
1.87618	0.785686	0.434162	2.03405	2.07987

Table 3. Average camera location error.
X - Longitude, Y - Latitude, Z - Altitude.

Digital Elevation Model

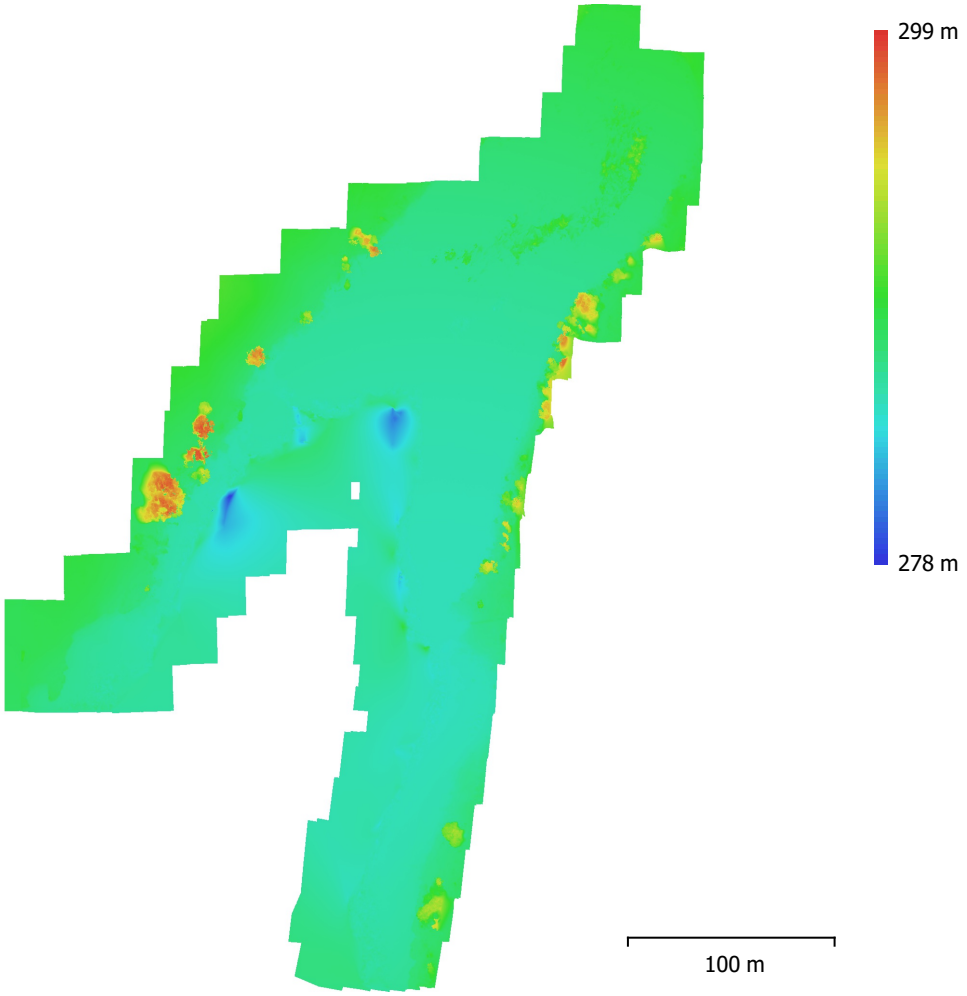

Fig. 4. Reconstructed digital elevation model.

Resolution:	4.08 cm/pix
Point density:	601 points/m²

Processing Parameters

General	
Cameras	246
Aligned cameras	235
Coordinate system	WGS 84 (EPSG::4326)
Rotation angles	Yaw, Pitch, Roll
Point Cloud	
Points	201,861 of 209,404
RMS reprojection error	0.185555 (0.596106 pix)
Max reprojection error	0.556825 (24.587 pix)
Mean key point size	2.91649 pix
Point colors	3 bands, uint8
Key points	No
Average tie point multiplicity	4.46703
Alignment parameters	
Accuracy	High
Generic preselection	Yes
Reference preselection	Yes
Key point limit	40,000
Tie point limit	4,000
Adaptive camera model fitting	No
Matching time	32 minutes 32 seconds
Alignment time	8 minutes 22 seconds
Dense Point Cloud	
Points	30,268,446
Point colors	3 bands, uint8
Reconstruction parameters	
Quality	Medium
Depth filtering	Aggressive
Depth maps generation time	1 hours 3 minutes
Dense cloud generation time	5 minutes 49 seconds
Model	
Faces	1,976,442
Vertices	993,651
Vertex colors	3 bands, uint8
Reconstruction parameters	
Surface type	Height field
Source data	Dense
Interpolation	Enabled
Quality	Medium
Depth filtering	Aggressive
Face count	2,017,896
Processing time	1 minutes 7 seconds
Orthomosaic	
Size	33,197 x 46,809
Coordinate system	WGS 84 (EPSG::4326)
Colors	3 bands, uint8
Reconstruction parameters	
Blending mode	Mosaic
Surface	Mesh
Enable hole filling	Yes

General	
Processing time	9 minutes 37 seconds
Software	
Version	1.5.1 build 7618
Platform	Windows 64

CS2 - LCB June6

Processing Report

16 April 2019

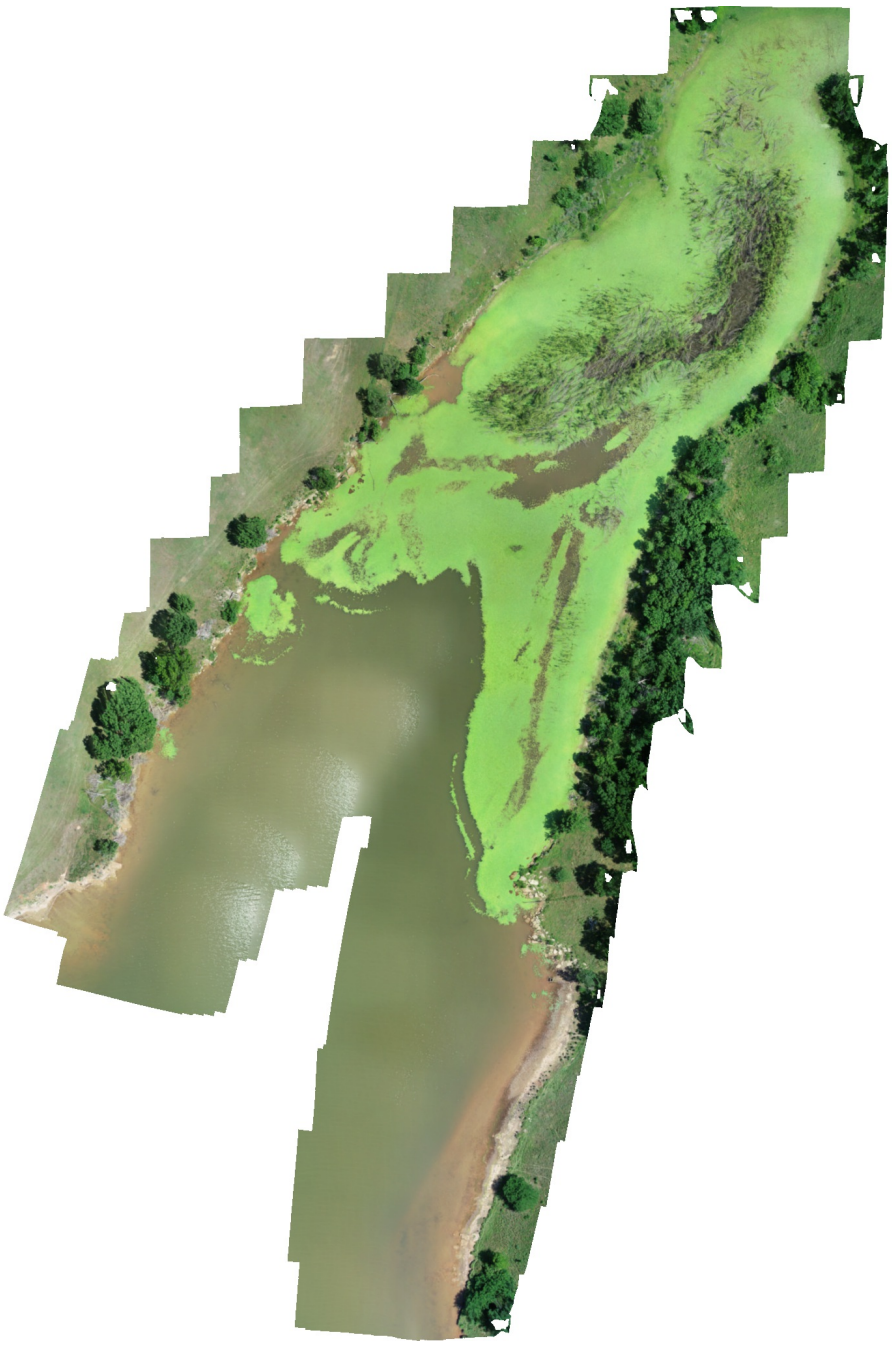

Survey Data

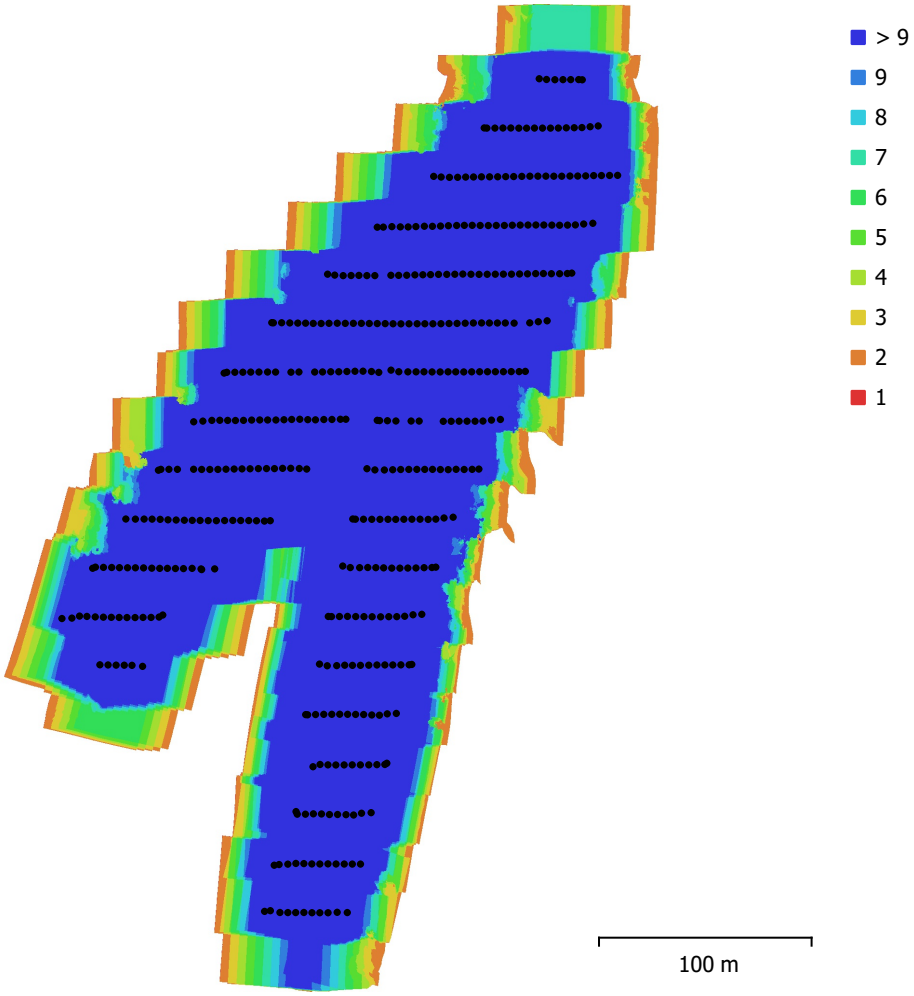

Fig. 1. Camera locations and image overlap.

Number of images:	426	Camera stations:	413
Flying altitude:	54.3 m	Tie points:	208,788
Ground resolution:	1.3 cm/pix	Projections:	1,353,133
Coverage area:	0.0695 km²	Reprojection error:	0.79 pix

Camera Model	Resolution	Focal Length	Pixel Size	Precalibrated
FC6310 (8.8mm)	5472 x 3648	8.8 mm	2.41 x 2.41 µm	No

Table 1. Cameras.

Camera Calibration

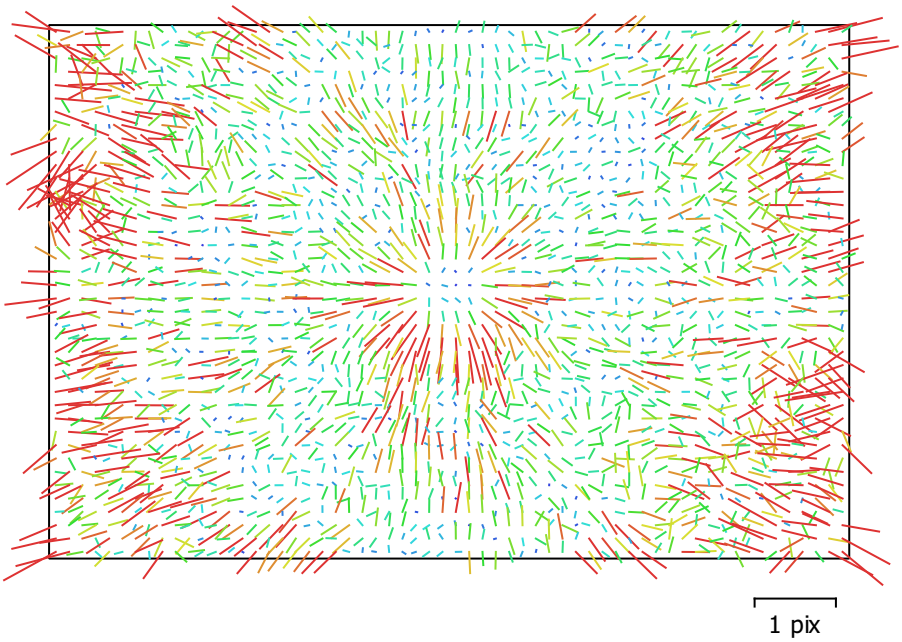

Fig. 2. Image residuals for FC6310 (8.8mm).

FC6310 (8.8mm)

426 images

Type	Resolution	Focal Length	Pixel Size
Frame	**5472 x 3648**	**8.8 mm**	**2.41 x 2.41 µm**

	Value	Error	F	Cx	Cy	K1	K2	K3	P1	P2
F	**3750.57**	11	1.00	0.10	-0.03	0.04	-0.95	0.98	0.01	0.03
Cx	**39.3769**	0.82		1.00	-0.15	-0.08	-0.05	0.06	0.16	-0.06
Cy	**-5.36561**	0.86			1.00	0.05	0.04	-0.04	0.00	0.47
K1	**-0.000410127**	0.00014				1.00	-0.14	0.11	0.04	0.13
K2	**-0.0183581**	0.00022					1.00	-0.99	0.02	-0.03
K3	**0.0163387**	0.00029						1.00	-0.01	0.03
P1	**-0.000126413**	4.7e-005							1.00	-0.05
P2	**0.00103143**	5.5e-005								1.00

Table 2. Calibration coefficients and correlation matrix.

Camera Locations

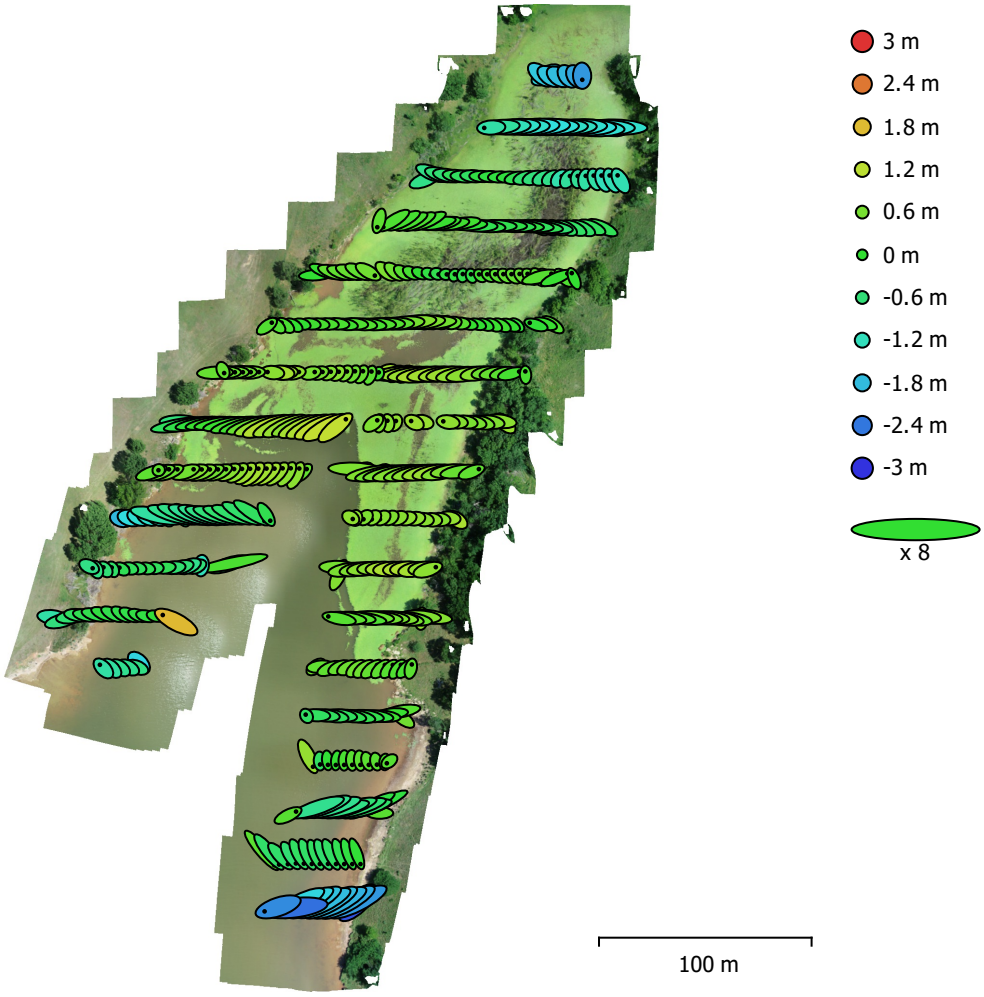

Fig. 3. Camera locations and error estimates.
Z error is represented by ellipse color. X,Y errors are represented by ellipse shape.
Estimated camera locations are marked with a black dot.

X error (m)	Y error (m)	Z error (m)	XY error (m)	Total error (m)
1.24734	0.459463	0.766694	1.32927	1.53453

Table 3. Average camera location error.
X - Longitude, Y - Latitude, Z - Altitude.

Digital Elevation Model

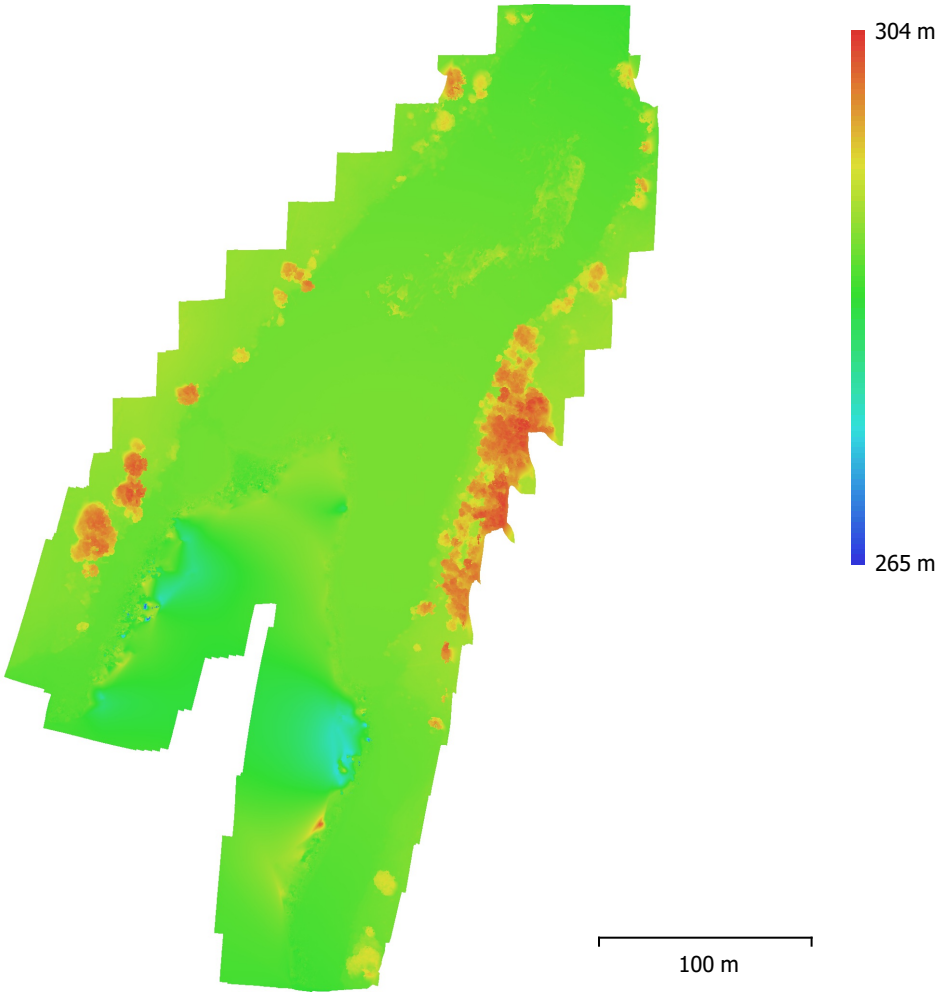

Fig. 4. Reconstructed digital elevation model.

Resolution:	5.18 cm/pix
Point density:	372 points/m²

Processing Parameters

General	
Cameras	426
Aligned cameras	413
Coordinate system	WGS 84 (EPSG::4326)
Rotation angles	Yaw, Pitch, Roll
Point Cloud	
Points	208,788 of 231,725
RMS reprojection error	0.225985 (0.790387 pix)
Max reprojection error	0.682675 (36.8717 pix)
Mean key point size	3.29388 pix
Point colors	3 bands, uint8
Key points	No
Average tie point multiplicity	7.53005
Alignment parameters	
Accuracy	High
Generic preselection	Yes
Reference preselection	Yes
Key point limit	40,000
Tie point limit	4,000
Adaptive camera model fitting	No
Matching time	46 minutes 51 seconds
Alignment time	9 minutes 50 seconds
Dense Point Cloud	
Points	25,088,322
Point colors	3 bands, uint8
Reconstruction parameters	
Quality	Medium
Depth filtering	Aggressive
Depth maps generation time	4 hours 55 minutes
Dense cloud generation time	33 minutes 46 seconds
Model	
Faces	1,638,432
Vertices	823,290
Vertex colors	3 bands, uint8
Reconstruction parameters	
Surface type	Height field
Source data	Dense
Interpolation	Enabled
Quality	Medium
Depth filtering	Aggressive
Face count	1,672,554
Processing time	58 seconds
Orthomosaic	
Size	23,762 x 35,826
Coordinate system	WGS 84 (EPSG::4326)
Colors	3 bands, uint8
Reconstruction parameters	
Blending mode	Mosaic
Surface	Mesh
Enable hole filling	Yes

General	
Processing time	17 minutes 31 seconds
Software	
Version	1.5.1 build 7618
Platform	Windows 64

CS2 - LCB July31

Processing Report
16 April 2019

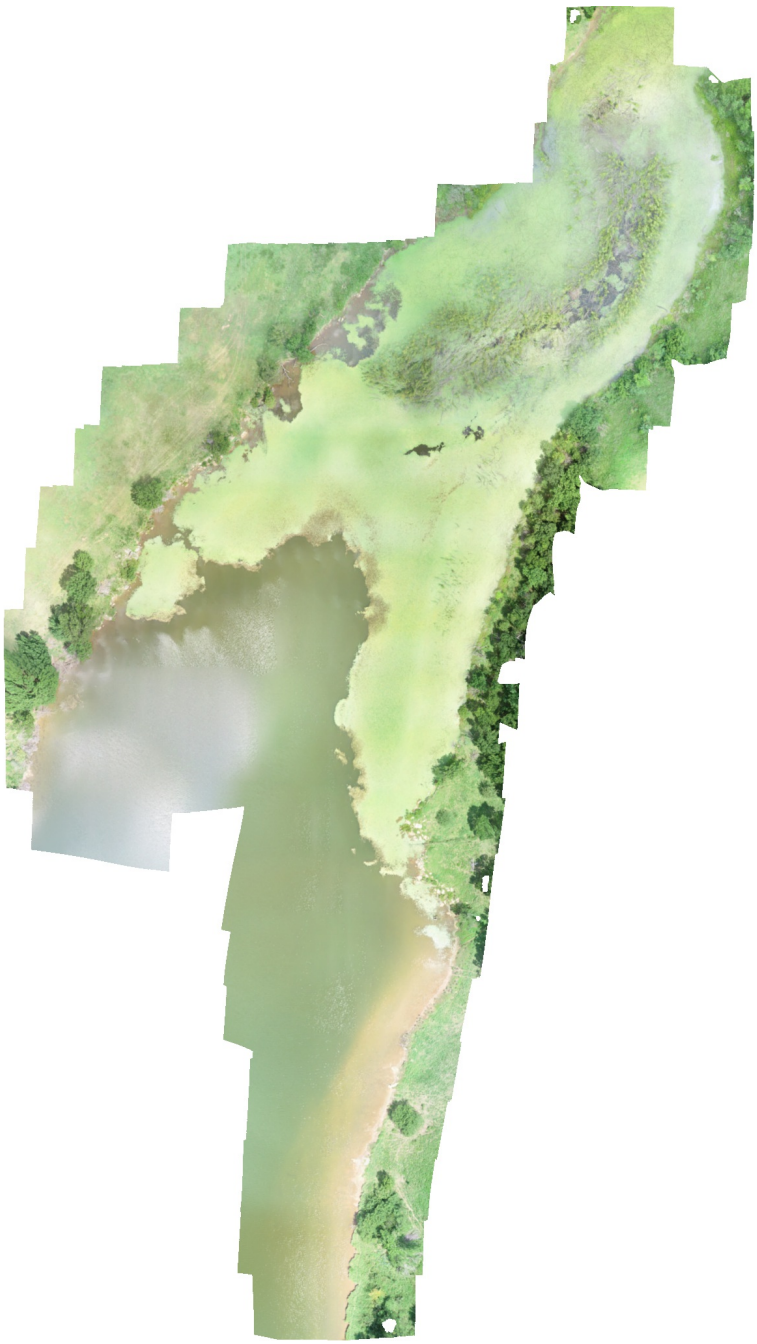

Survey Data

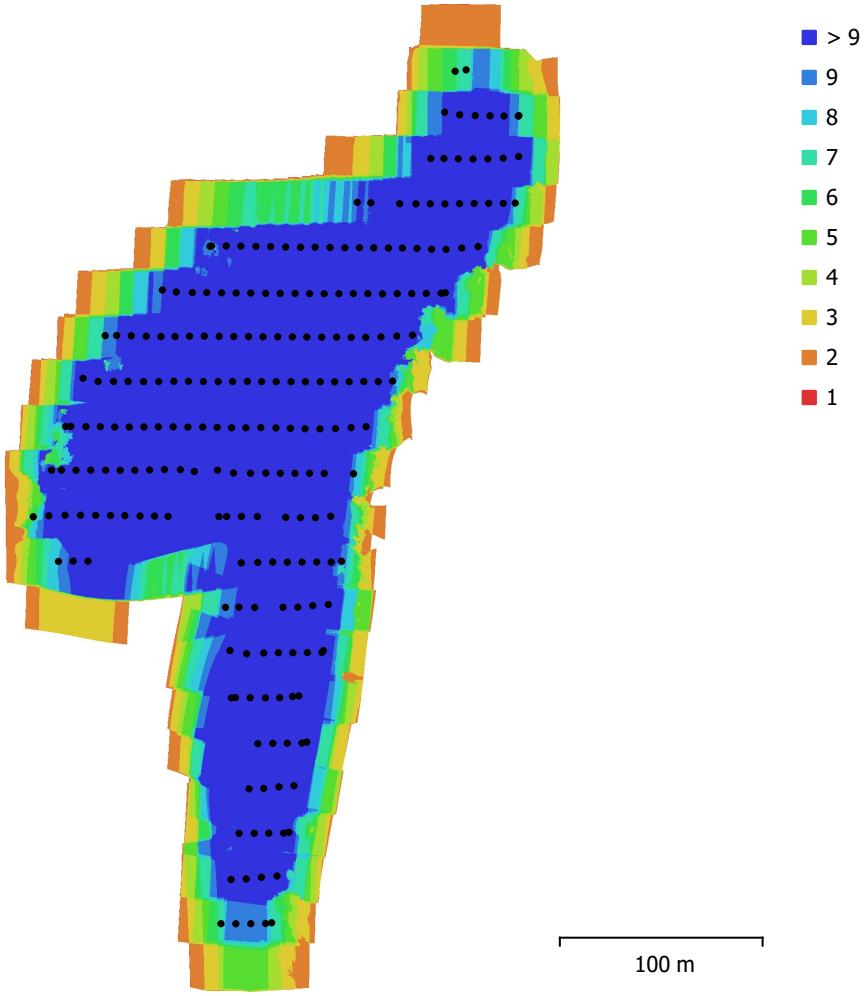

Fig. 1. Camera locations and image overlap.

Number of images:	247	Camera stations:	228
Flying altitude:	43.3 m	Tie points:	184,406
Ground resolution:	1.23 cm/pix	Projections:	753,388
Coverage area:	0.0629 km²	Reprojection error:	0.604 pix

Camera Model	Resolution	Focal Length	Pixel Size	Precalibrated
FC6310 (8.8mm)	5472 x 3648	8.8 mm	2.41 x 2.41 µm	No

Table 1. Cameras.

Camera Calibration

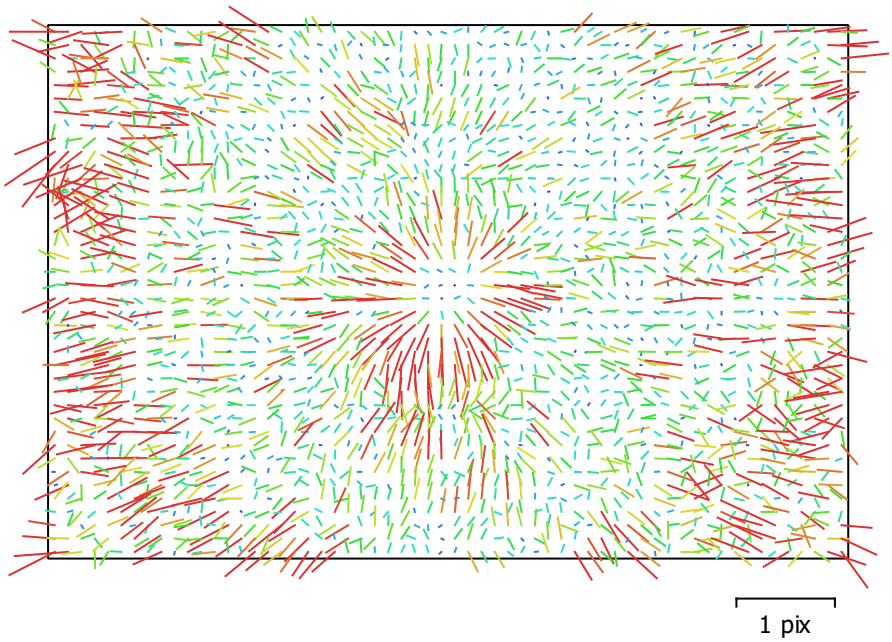

Fig. 2. Image residuals for FC6310 (8.8mm).

FC6310 (8.8mm)

247 images

Type	Resolution	Focal Length	Pixel Size
Frame	**5472 x 3648**	**8.8 mm**	**2.41 x 2.41 µm**

	Value	Error	F	Cx	Cy	K1	K2	K3	P1	P2
F	**2955.94**	42	1.00	0.14	0.43	-0.09	-0.99	1.00	-0.25	0.38
Cx	**41.3864**	1.2		1.00	-0.10	-0.07	-0.13	0.13	-0.02	0.04
Cy	**-33.9484**	1.5			1.00	-0.12	-0.42	0.42	-0.16	0.25
K1	**0.00118951**	0.00012				1.00	0.06	-0.07	0.12	0.24
K2	**-0.00582273**	0.00033					1.00	-1.00	0.25	-0.38
K3	**0.00330561**	0.00028						1.00	-0.25	0.38
P1	**-0.00069418**	5.8e-005							1.00	-0.18
P2	**0.00241841**	6.7e-005								1.00

Table 2. Calibration coefficients and correlation matrix.

Camera Locations

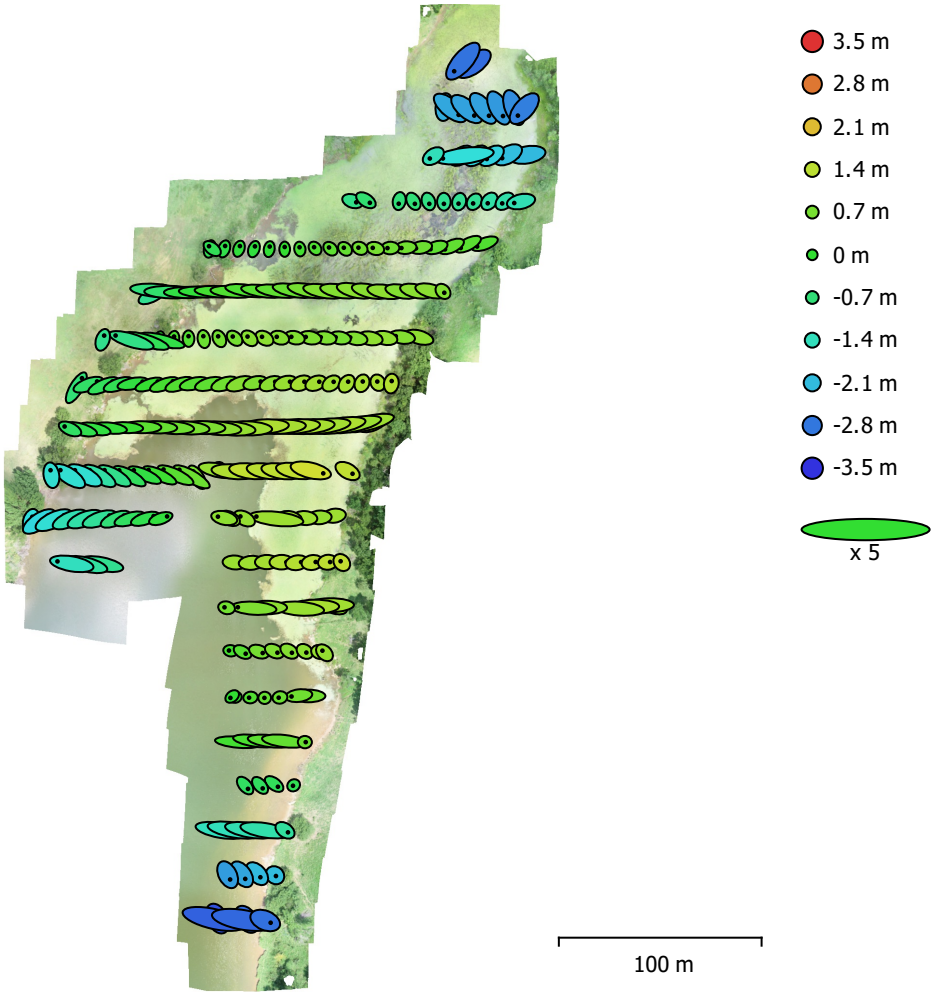

Fig. 3. Camera locations and error estimates.
Z error is represented by ellipse color. X,Y errors are represented by ellipse shape.
Estimated camera locations are marked with a black dot.

X error (m)	Y error (m)	Z error (m)	XY error (m)	Total error (m)
1.96788	0.599954	1.15571	2.0573	2.3597

Table 3. Average camera location error.
X - Longitude, Y - Latitude, Z - Altitude.

Digital Elevation Model

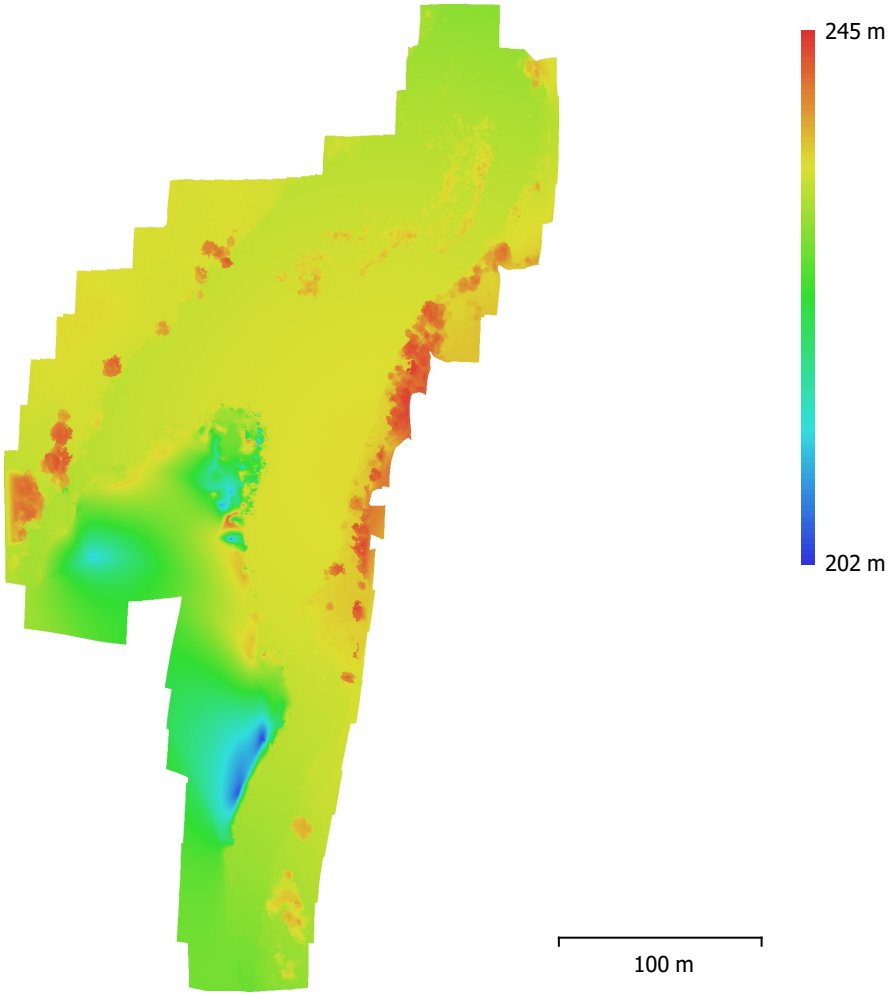

Fig. 4. Reconstructed digital elevation model.

Resolution:	4.92 cm/pix
Point density:	413 points/m²

Processing Parameters

General	
Cameras	247
Aligned cameras	228
Coordinate system	WGS 84 (EPSG::4326)
Rotation angles	Yaw, Pitch, Roll
Point Cloud	
Points	184,406 of 195,273
RMS reprojection error	0.186693 (0.604277 pix)
Max reprojection error	0.561708 (35.0212 pix)
Mean key point size	3.23406 pix
Point colors	3 bands, uint8
Key points	No
Average tie point multiplicity	4.41284
Alignment parameters	
Accuracy	High
Generic preselection	Yes
Reference preselection	Yes
Key point limit	40,000
Tie point limit	4,000
Adaptive camera model fitting	No
Matching time	18 minutes 8 seconds
Alignment time	3 minutes 42 seconds
Dense Point Cloud	
Points	22,817,902
Point colors	3 bands, uint8
Reconstruction parameters	
Quality	Medium
Depth filtering	Aggressive
Depth maps generation time	1 hours 12 minutes
Dense cloud generation time	6 minutes 58 seconds
Model	
Faces	1,488,310
Vertices	747,744
Vertex colors	3 bands, uint8
Reconstruction parameters	
Surface type	Height field
Source data	Dense
Interpolation	Enabled
Quality	Medium
Depth filtering	Aggressive
Face count	1,521,193
Processing time	59 seconds
Orthomosaic	
Size	22,260 x 39,562
Coordinate system	WGS 84 (EPSG::4326)
Colors	3 bands, uint8
Reconstruction parameters	
Blending mode	Mosaic
Surface	Mesh
Enable hole filling	Yes

General	
Processing time	10 minutes 1 seconds
Software	
Version	1.5.1 build 7618
Platform	Windows 64

CS2 - LCB Aug9

Processing Report

16 April 2019

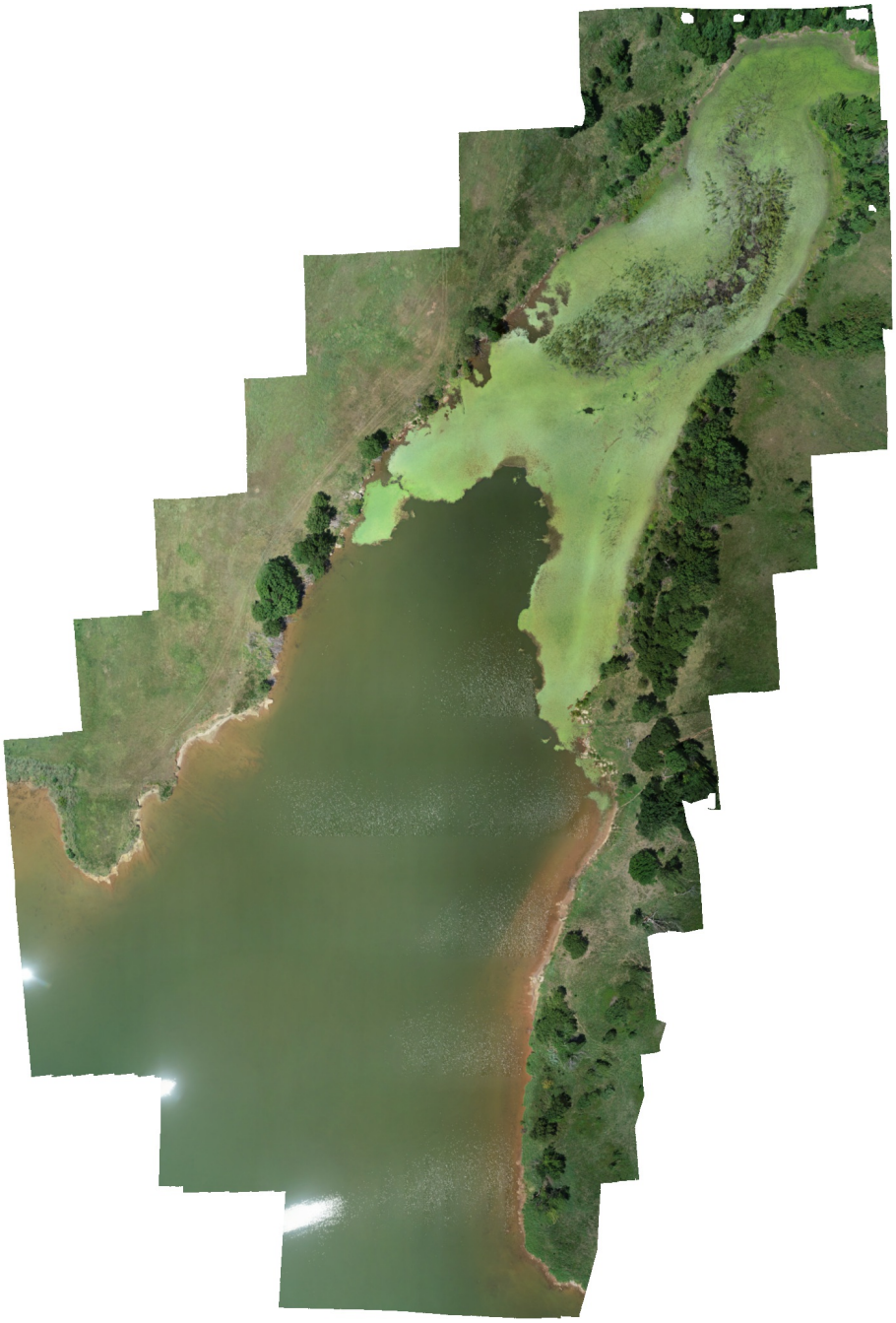

Survey Data

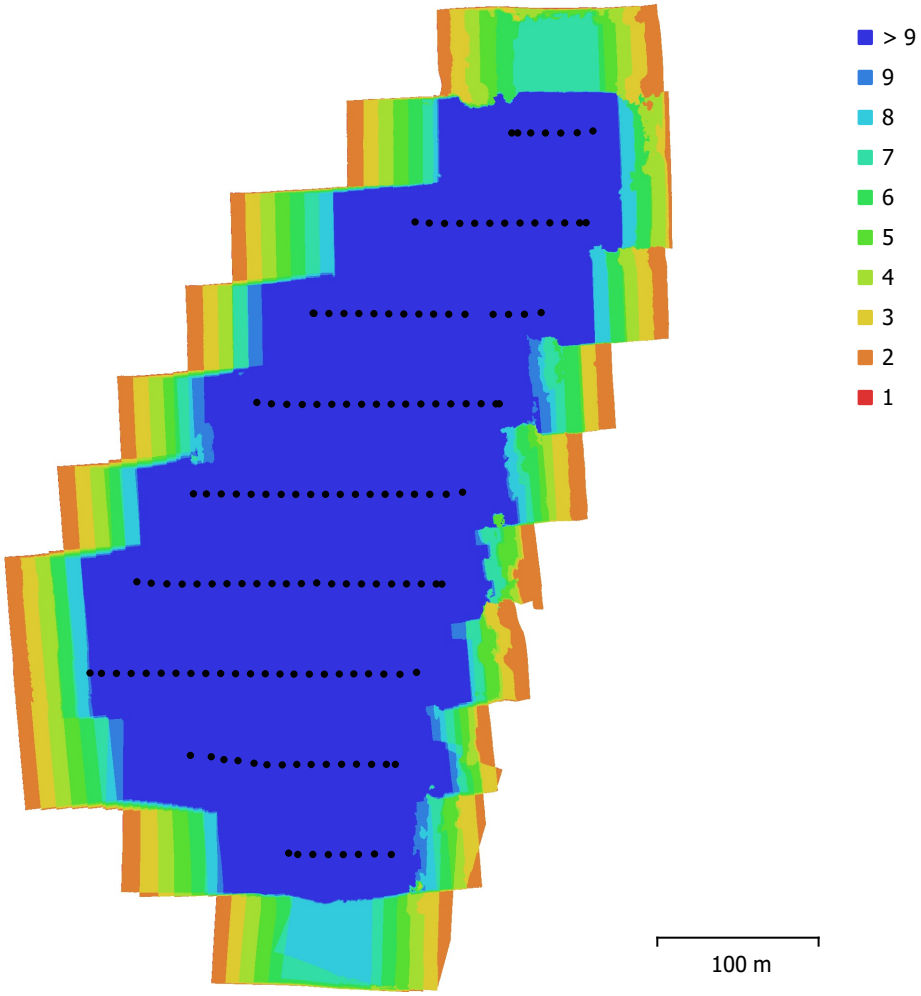

Fig. 1. Camera locations and image overlap.

Number of images:	141	Camera stations:	141
Flying altitude:	127 m	Tie points:	101,735
Ground resolution:	2.83 cm/pix	Projections:	452,553
Coverage area:	0.154 km²	Reprojection error:	0.756 pix

Camera Model	Resolution	Focal Length	Pixel Size	Precalibrated
FC6310 (8.8mm)	5472 x 3648	8.8 mm	2.41 x 2.41 µm	No

Table 1. Cameras.

Camera Calibration

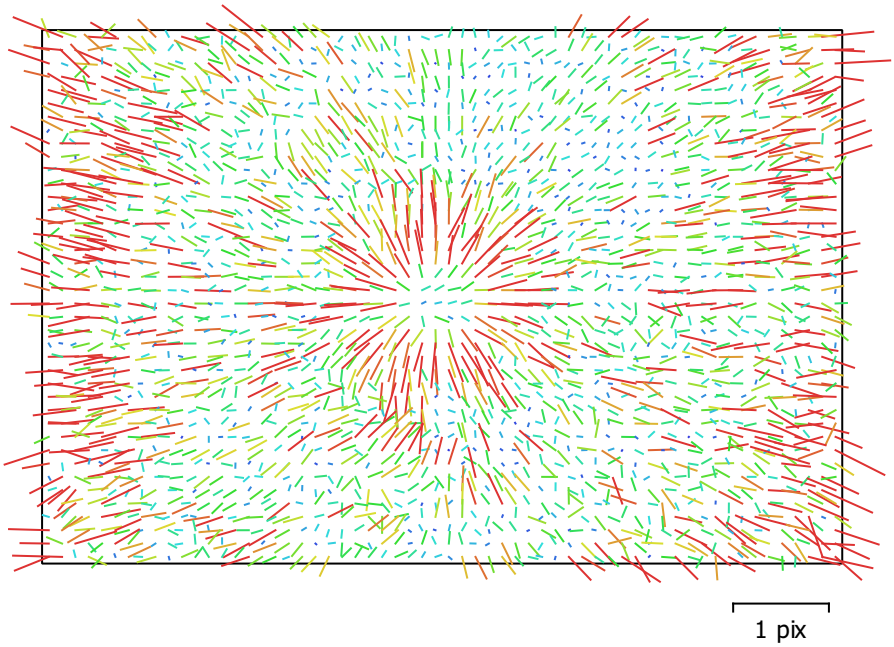

Fig. 2. Image residuals for FC6310 (8.8mm).

FC6310 (8.8mm)

141 images

Type	Resolution	Focal Length	Pixel Size
Frame	**5472 x 3648**	**8.8 mm**	**2.41 x 2.41 µm**

	Value	Error	F	Cx	Cy	K1	K2	K3	P1	P2
F	**4033.89**	19	1.00	0.02	0.05	-0.26	0.04	0.56	-0.11	-0.18
Cx	**81.1074**	2.8		1.00	0.07	-0.08	0.14	-0.14	0.54	0.10
Cy	**30.0932**	3			1.00	0.13	-0.05	0.04	0.05	0.73
K1	**-0.0110037**	0.00037				1.00	-0.29	0.02	0.18	0.26
K2	**0.00041876**	0.00015					1.00	-0.78	0.08	-0.02
K3	**0.0034014**	0.00017						1.00	-0.16	-0.12
P1	**-0.000463779**	0.0001							1.00	0.15
P2	**-0.00021519**	0.00014								1.00

Table 2. Calibration coefficients and correlation matrix.

Camera Locations

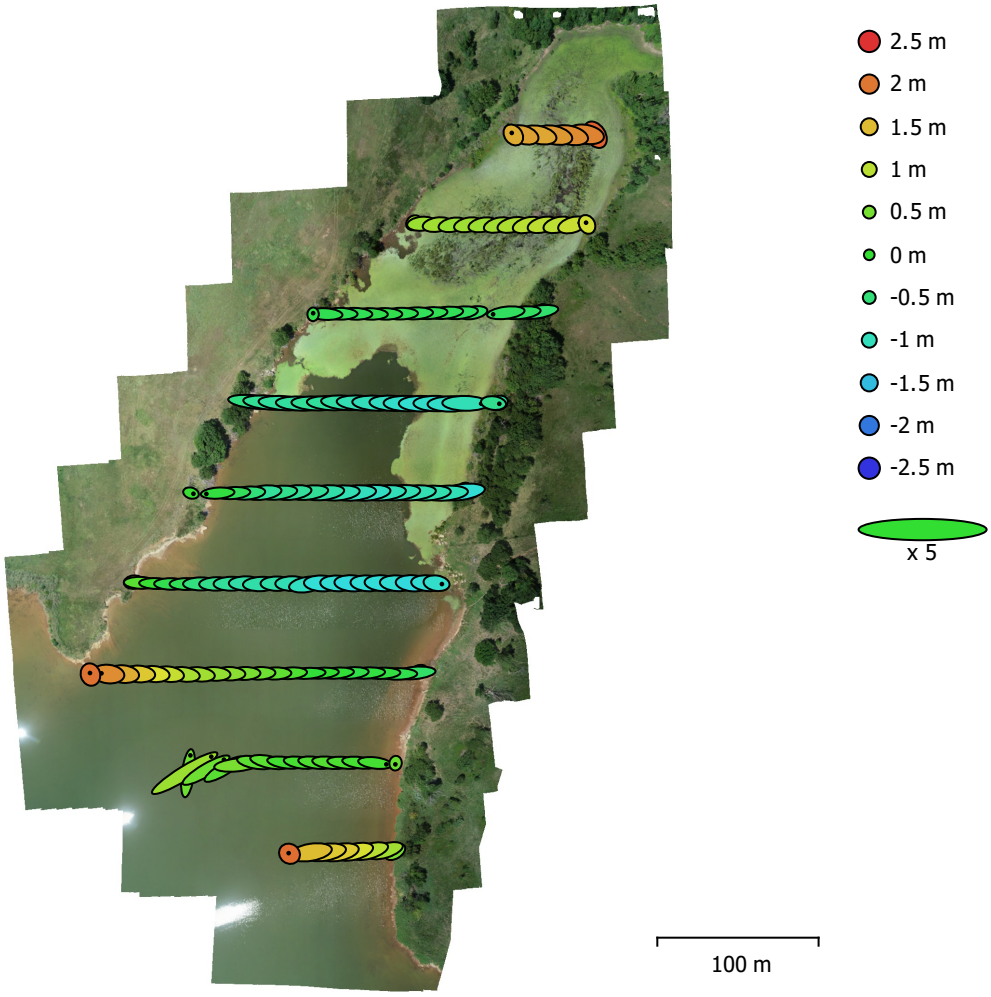

Fig. 3. Camera locations and error estimates.
Z error is represented by ellipse color. X,Y errors are represented by ellipse shape.
Estimated camera locations are marked with a black dot.

X error (m)	Y error (m)	Z error (m)	XY error (m)	Total error (m)
2.78723	0.67027	0.90026	2.86669	3.00473

Table 3. Average camera location error.
X - Longitude, Y - Latitude, Z - Altitude.

Digital Elevation Model

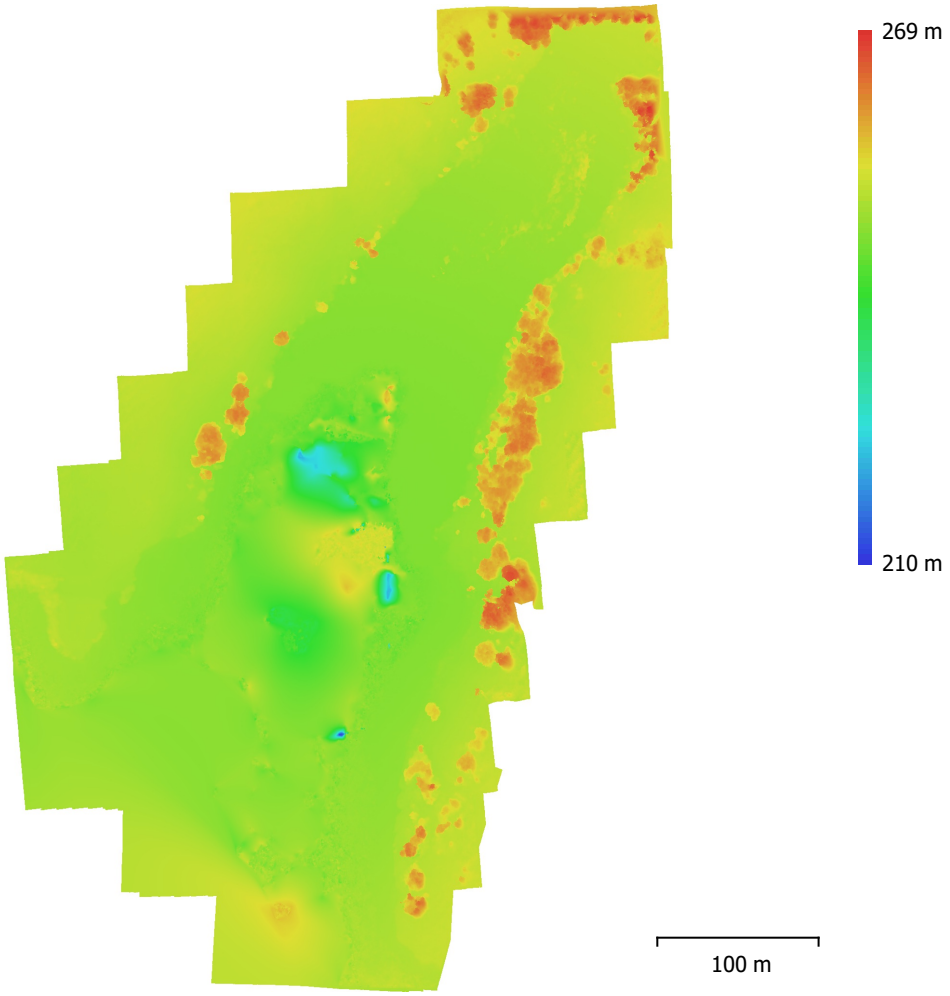

Fig. 4. Reconstructed digital elevation model.

Resolution:	11.3 cm/pix
Point density:	77.9 points/m²

Processing Parameters

General	
Cameras	141
Aligned cameras	141
Coordinate system	WGS 84 (EPSG::4326)
Rotation angles	Yaw, Pitch, Roll
Point Cloud	
Points	101,735 of 107,015
RMS reprojection error	0.200676 (0.755812 pix)
Max reprojection error	0.601826 (39.2286 pix)
Mean key point size	3.27653 pix
Point colors	3 bands, uint8
Key points	No
Average tie point multiplicity	4.64538
Alignment parameters	
Accuracy	High
Generic preselection	Yes
Reference preselection	Yes
Key point limit	40,000
Tie point limit	4,000
Adaptive camera model fitting	No
Matching time	15 minutes 39 seconds
Alignment time	5 minutes 54 seconds
Dense Point Cloud	
Points	10,217,709
Point colors	3 bands, uint8
Reconstruction parameters	
Quality	Medium
Depth filtering	Aggressive
Depth maps generation time	1 hours 42 minutes
Dense cloud generation time	3 minutes 34 seconds
Model	
Faces	665,720
Vertices	335,041
Vertex colors	3 bands, uint8
Reconstruction parameters	
Surface type	Height field
Source data	Dense
Interpolation	Enabled
Quality	Medium
Depth filtering	Aggressive
Face count	681,180
Processing time	37 seconds
Orthomosaic	
Size	14,621 x 21,600
Coordinate system	WGS 84 (EPSG::4326)
Colors	3 bands, uint8
Reconstruction parameters	
Blending mode	Mosaic
Surface	Mesh
Enable hole filling	Yes

General	
Processing time	6 minutes 19 seconds
Software	
Version	1.5.1 build 7618
Platform	Windows 64

CS3 - 300ft

Processing Report 17
April 2019

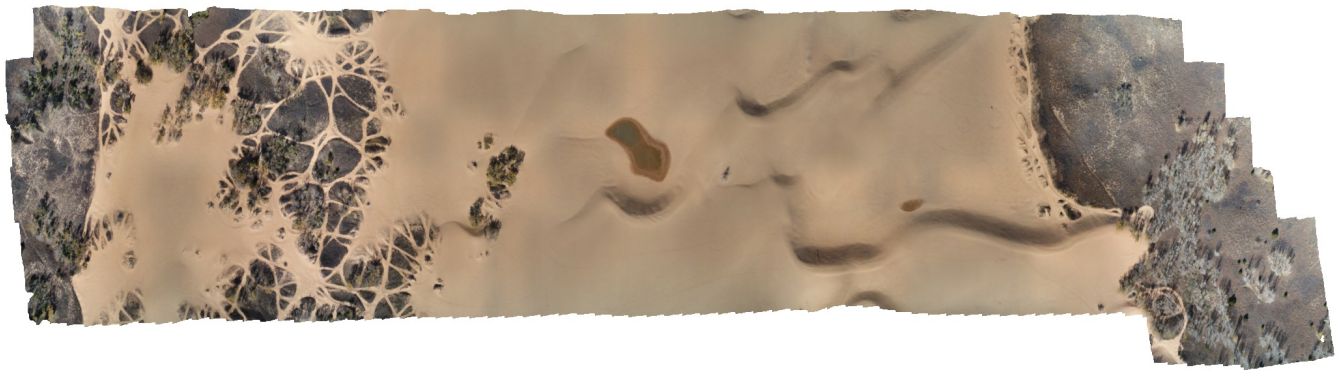

Survey Data

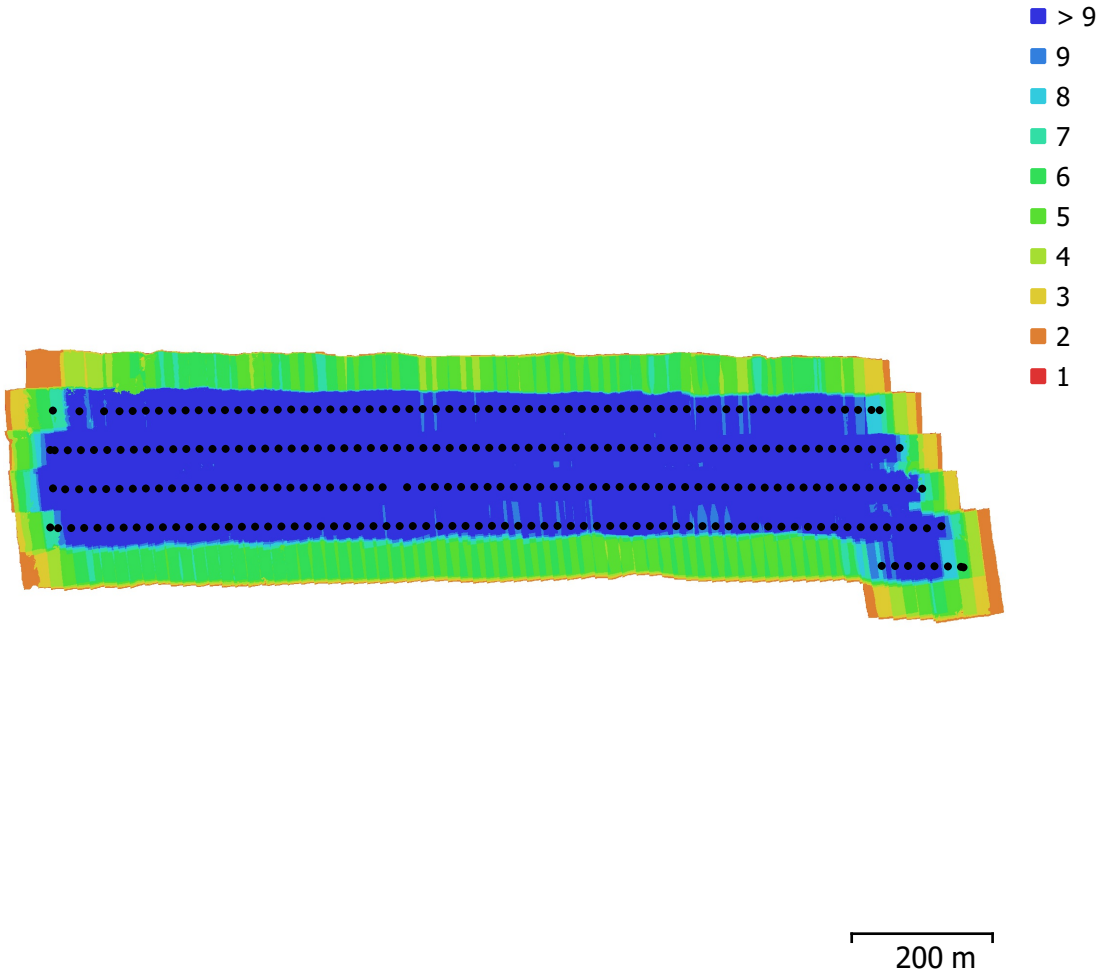

Fig. 1. Camera locations and image overlap.

Number of images:	271	Camera stations:	271
Flying altitude:	115 m	Tie points:	189,830
Ground resolution:	2.84 cm/pix	Projections:	955,241
Coverage area:	0.441 km²	Reprojection error:	0.75 pix

Camera Model	Resolution	Focal Length	Pixel Size	Precalibrated
FC6310 (8.8mm)	5472 x 3648	8.8 mm	2.41 x 2.41 µm	No

Table 1. Cameras.

Camera Calibration

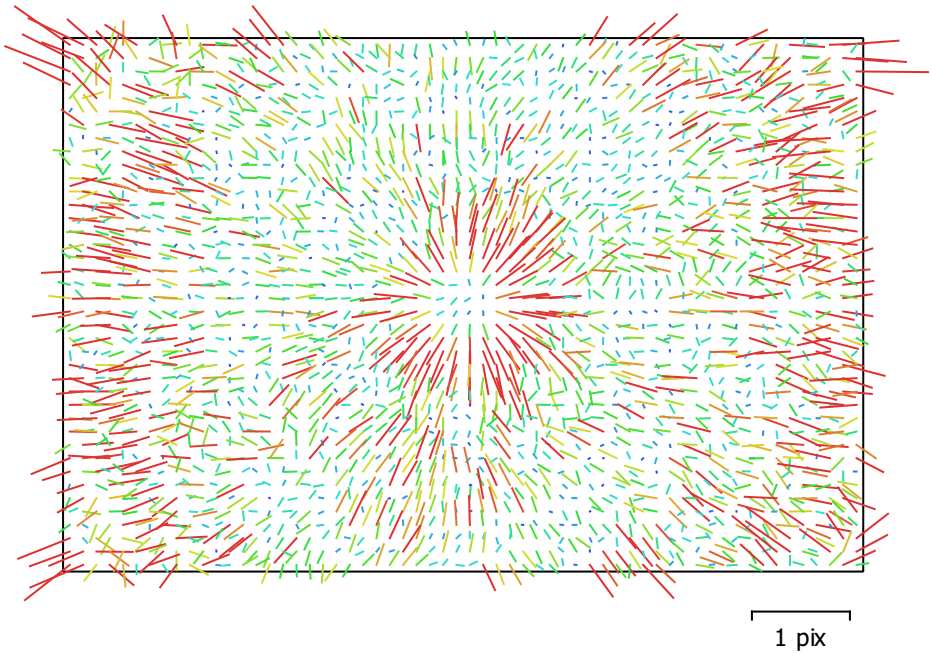

Fig. 2. Image residuals for FC6310 (8.8mm).

FC6310 (8.8mm)

271 images

Type	Resolution	Focal Length	Pixel Size
Frame	**5472 x 3648**	**8.8 mm**	**2.41 x 2.41 µm**

	Value	Error	F	Cx	Cy	K1	K2	K3	P1	P2
F	**3667.24**	0.39	1.00	0.04	0.13	0.25	-0.03	0.08	0.06	0.01
Cx	**-10.4473**	0.42		1.00	0.04	0.03	-0.05	0.07	0.99	0.03
Cy	**-2.28121**	0.44			1.00	0.08	-0.00	0.01	0.04	0.98
K1	**0.00149982**	3.4e-05				1.00	-0.69	0.67	0.02	0.05
K2	**-0.00712472**	6.9e-05					1.00	-0.98	-0.05	0.00
K3	**0.00815069**	6e-05						1.00	0.07	0.00
P1	**0.000694489**	2.7e-05							1.00	0.03
P2	**-0.000372962**	2.7e-05								1.00

Table 2. Calibration coefficients and correlation matrix.

Camera Locations

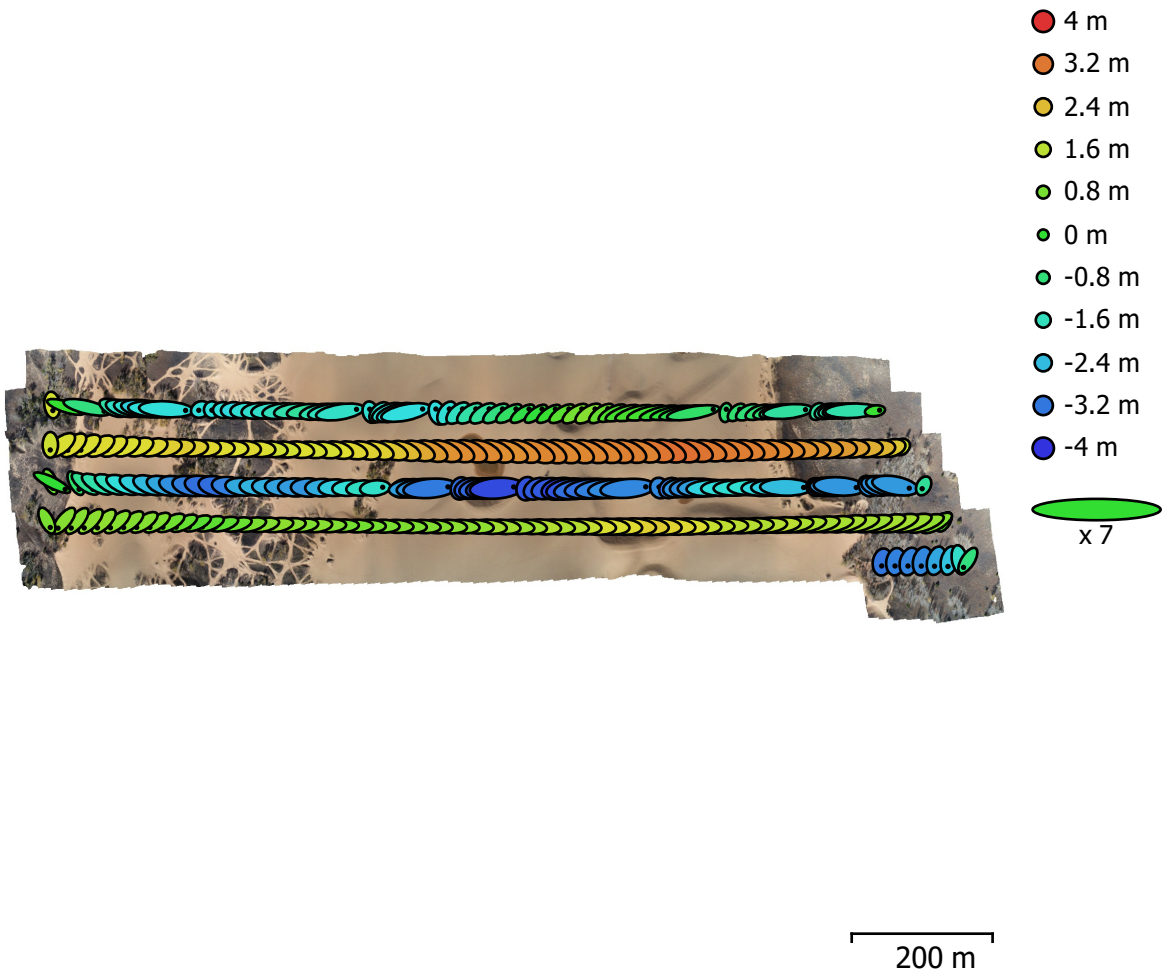

Fig. 3. Camera locations and error estimates.
Z error is represented by ellipse color. X,Y errors are represented by ellipse shape.
Estimated camera locations are marked with a black dot.

X error (m)	Y error (m)	Z error (m)	XY error (m)	Total error (m)
3.93264	1.19432	2.11616	4.10999	4.62279

Table 3. Average camera location error.
X - Longitude, Y - Latitude, Z - Altitude.

Digital Elevation Model

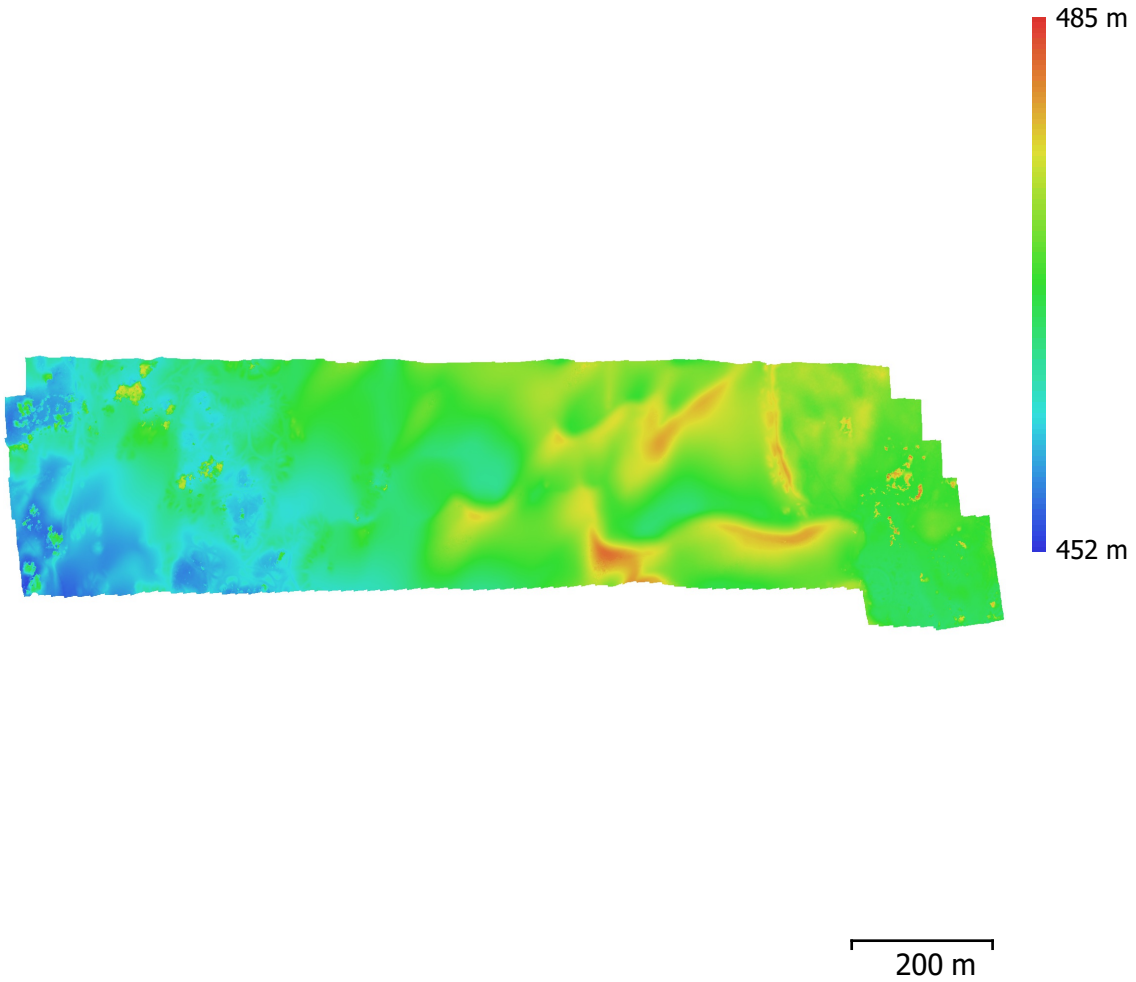

Fig. 4. Reconstructed digital elevation model.

Resolution:	11.4 cm/pix
Point density:	77.5 points/m²

Processing Parameters

General	
Cameras	271
Aligned cameras	271
Coordinate system	WGS 84 (EPSG::4326)
Rotation angles	Yaw, Pitch, Roll
Point Cloud	
Points	189,830 of 212,057
RMS reprojection error	0.207538 (0.750309 pix)
Max reprojection error	0.624974 (32.072 pix)
Mean key point size	3.41646 pix
Point colors	3 bands, uint8
Key points	No
Average tie point multiplicity	5.34175
Alignment parameters	
Accuracy	High
Generic preselection	Yes
Reference preselection	Yes
Key point limit	40,000
Tie point limit	4,000
Adaptive camera model fitting	No
Matching time	33 minutes 9 seconds
Alignment time	2 minutes 21 seconds
Dense Point Cloud	
Points	38,770,871
Point colors	3 bands, uint8
Reconstruction parameters	
Quality	Medium
Depth filtering	Aggressive
Depth maps generation time	4 hours 39 minutes
Dense cloud generation time	7 minutes 56 seconds
Model	
Faces	2,584,723
Vertices	1,297,352
Vertex colors	3 bands, uint8
Reconstruction parameters	
Surface type	Arbitrary
Source data	Dense
Interpolation	Enabled
Quality	Medium
Depth filtering	Aggressive
Face count	2,584,724
Processing time	51 minutes 59 seconds
DEM	
Size	16,480 x 5,713
Coordinate system	WGS 84 (EPSG::4326)
Reconstruction parameters	
Source data	Dense cloud
Interpolation	Enabled
Processing time	49 seconds
Orthomosaic	
Size	50,136 x 13,925
Coordinate system	WGS 84 (EPSG::4326)
Colors	3 bands, uint8
Reconstruction parameters	
Blending mode	Mosaic

Surface	Mesh
Enable hole filling	Yes
Processing time	11 minutes 4 seconds
Software	
Version	1.4.3 build 6529
Platform	Windows 64

CS3 - 400ft

Processing Report 17
April 2019

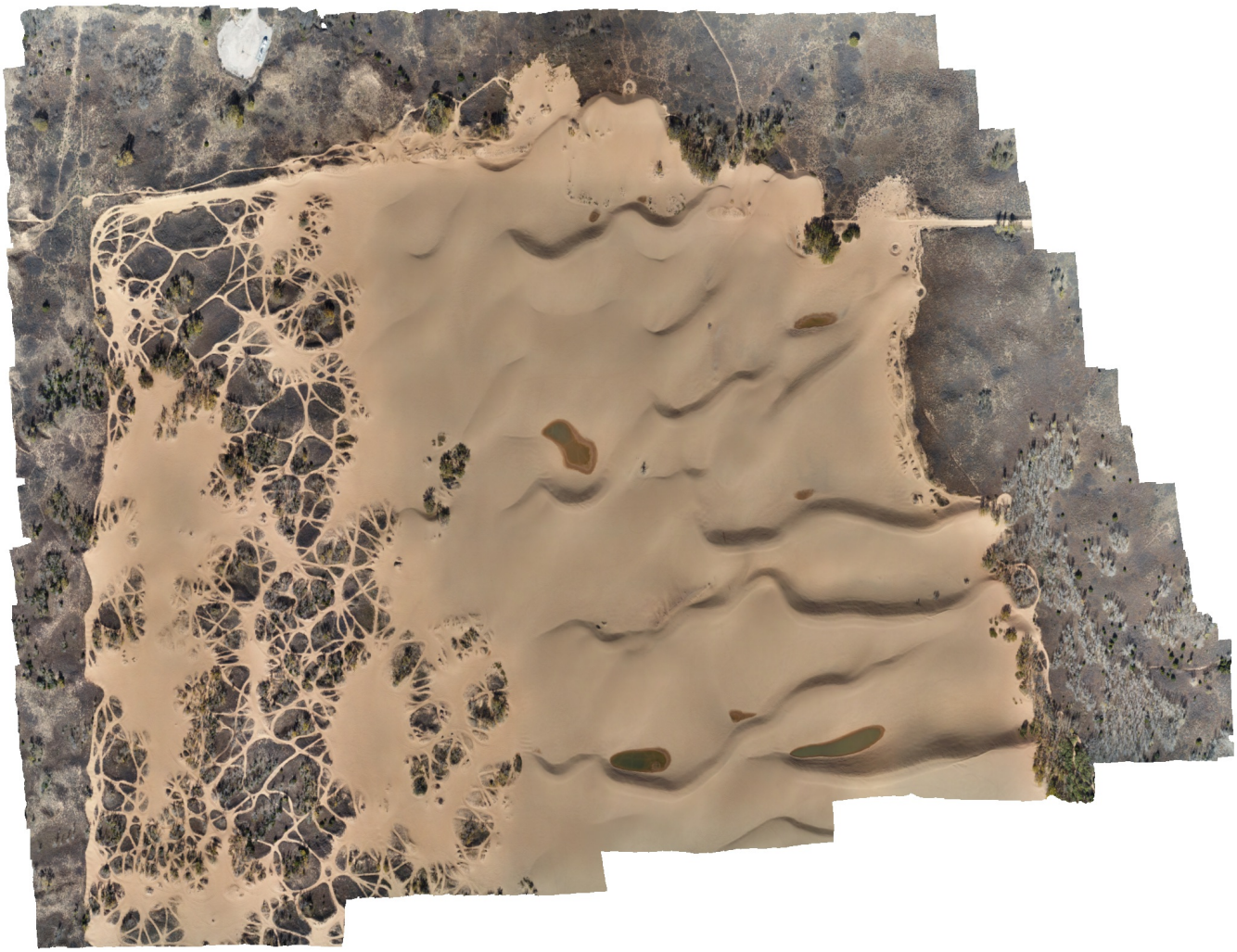

Survey Data

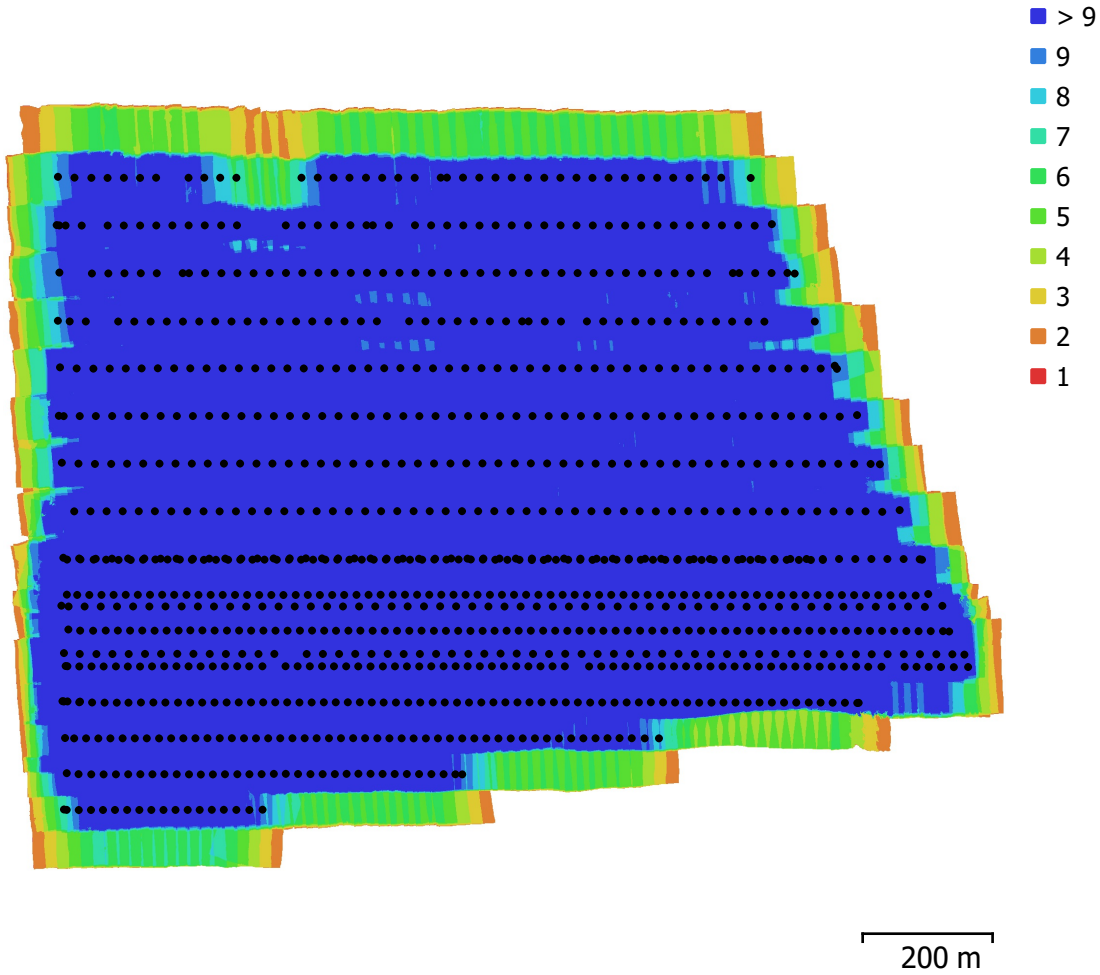

Fig. 1. Camera locations and image overlap.

Number of images:	999	Camera stations:	999
Flying altitude:	134 m	Tie points:	566,190
Ground resolution:	3.3 cm/pix	Projections:	3,466,118
Coverage area:	1.47 km²	Reprojection error:	0.834 pix

Camera Model	Resolution	Focal Length	Pixel Size	Precalibrated
FC6310 (8.8mm)	5472 x 3648	8.8 mm	2.41 x 2.41 µm	No

Table 1. Cameras.

Camera Calibration

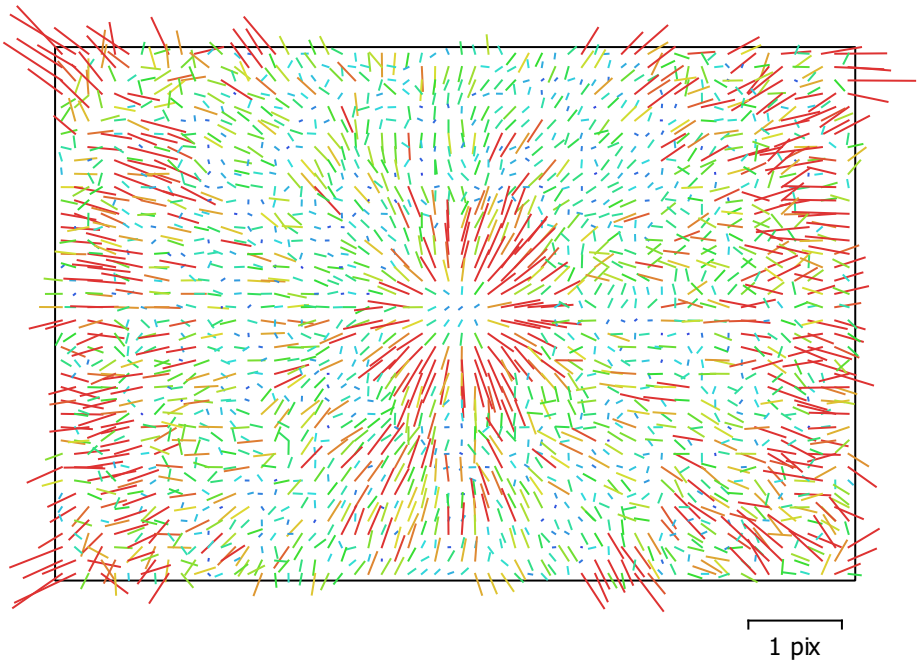

Fig. 2. Image residuals for FC6310 (8.8mm).

FC6310 (8.8mm)

999 images

Type	Resolution	Focal Length	Pixel Size
Frame	**5472 x 3648**	**8.8 mm**	**2.41 x 2.41 µm**

	Value	Error	F	Cx	Cy	K1	K2	K3	P1	P2
F	**3661.97**	0.54	1.00	-0.03	0.27	0.06	-0.10	0.21	0.09	0.02
Cx	**-1.92818**	0.13		1.00	-0.02	0.03	-0.01	0.02	0.59	-0.13
Cy	**-1.5534**	0.14			1.00	0.07	-0.02	0.05	0.08	0.51
K1	**-0.000757816**	1.7e-05				1.00	-0.71	0.67	0.04	0.03
K2	**-0.00661262**	3.6e-05					1.00	-0.98	-0.02	0.00
K3	**0.00774652**	3.2e-05						1.00	0.04	0.00
P1	**0.001303**	5.7e-06							1.00	-0.07
P2	**-0.000210805**	4.9e-06								1.00

Table 2. Calibration coefficients and correlation matrix.

Camera Locations

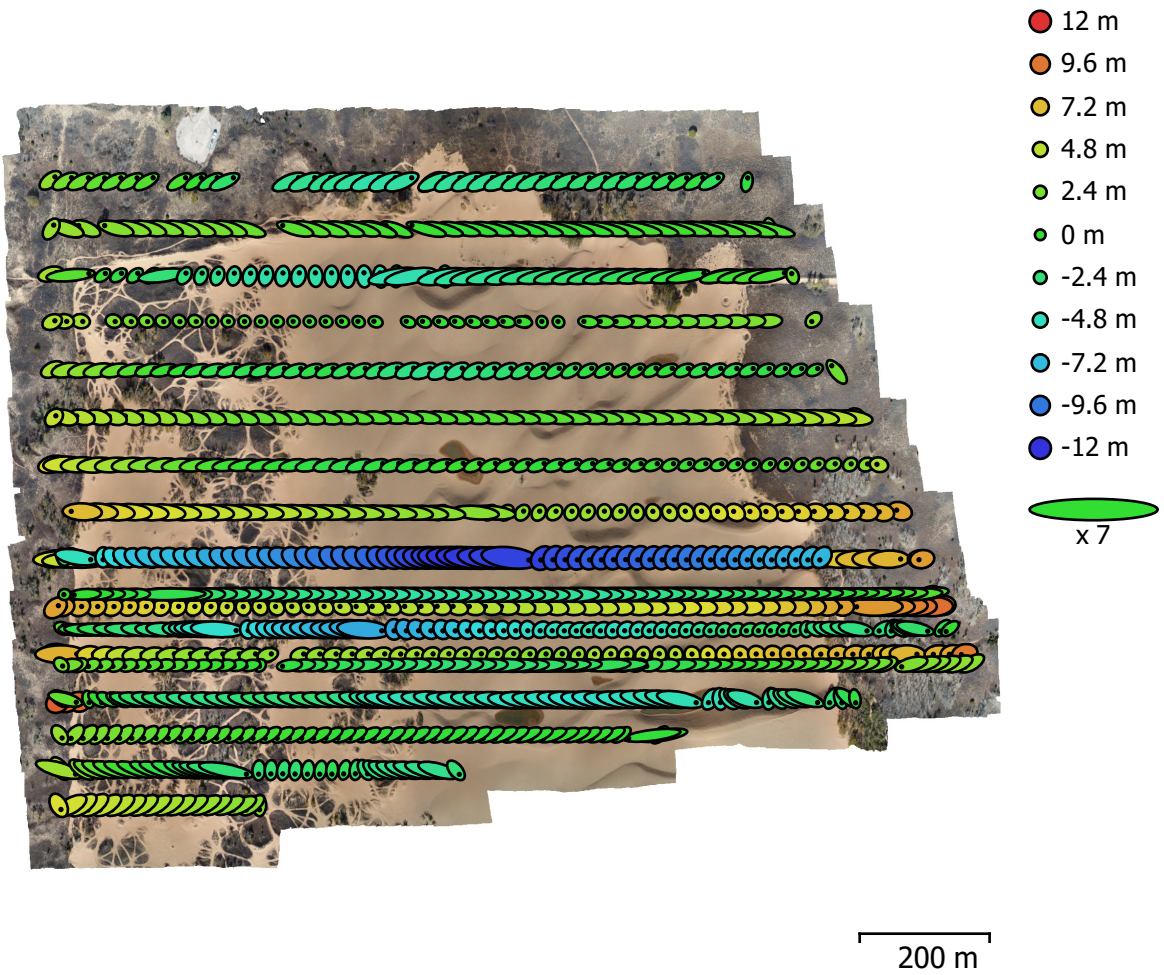

Fig. 3. Camera locations and error estimates.
Z error is represented by ellipse color. X,Y errors are represented by ellipse shape.
Estimated camera locations are marked with a black dot.

X error (m)	Y error (m)	Z error (m)	XY error (m)	Total error (m)
4.32138	1.00355	4.17172	4.43638	6.08972

Table 3. Average camera location error.
X - Longitude, Y - Latitude, Z - Altitude.

Digital Elevation Model

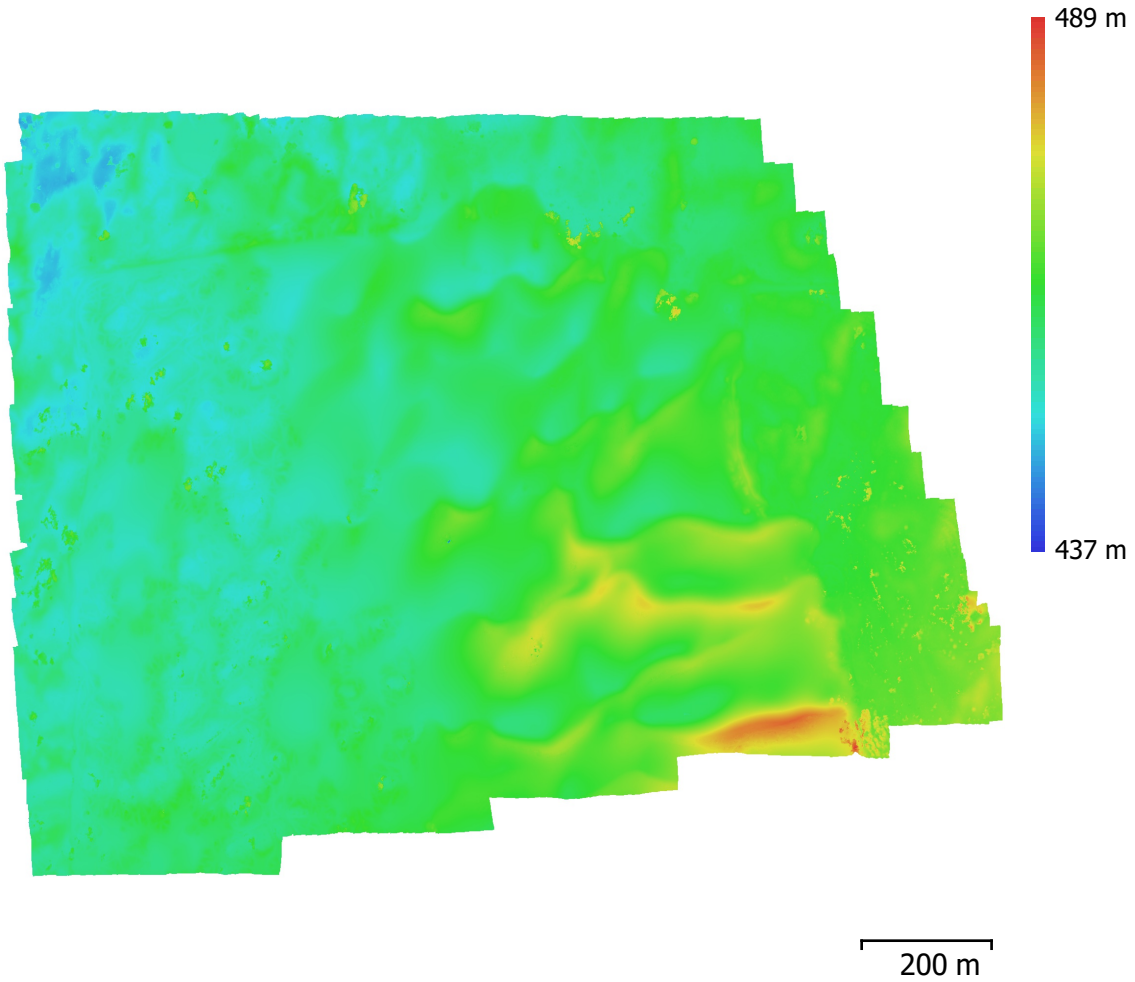

Fig. 4. Reconstructed digital elevation model.

Resolution:	13.2 cm/pix
Point density:	57.3 points/m²

Processing Parameters

General	
Cameras	999
Aligned cameras	999
Coordinate system	WGS 84 (EPSG::4326)
Rotation angles	Yaw, Pitch, Roll
Point Cloud	
Points	566,190 of 646,158
RMS reprojection error	0.230969 (0.834025 pix)
Max reprojection error	0.696641 (49.6475 pix)
Mean key point size	3.23204 pix
Point colors	3 bands, uint8
Key points	No
Average tie point multiplicity	6.75347
Alignment parameters	
Accuracy	High
Generic preselection	Yes
Reference preselection	Yes
Key point limit	40,000
Tie point limit	4,000
Adaptive camera model fitting	No
Matching time	2 hours 27 minutes
Alignment time	13 minutes 32 seconds
Dense Point Cloud	
Points	98,651,475
Point colors	3 bands, uint8
Reconstruction parameters	
Quality	Medium
Depth filtering	Aggressive
Depth maps generation time	17 hours 4 minutes
Dense cloud generation time	59 minutes 0 seconds
Model	
Faces	6,576,764
Vertices	3,295,027
Vertex colors	3 bands, uint8
Reconstruction parameters	
Surface type	Arbitrary
Source data	Dense
Interpolation	Enabled
Quality	Medium
Depth filtering	Aggressive
Face count	6,576,765
Processing time	1 hours 22 minutes
DEM	
Size	16,594 x 12,413
Coordinate system	WGS 84 (EPSG::4326)
Reconstruction parameters	
Source data	Dense cloud
Interpolation	Enabled
Processing time	1 minutes 33 seconds
Orthomosaic	
Size	46,739 x 35,922
Coordinate system	WGS 84 (EPSG::4326)
Colors	3 bands, uint8
Reconstruction parameters	
Blending mode	Mosaic

Surface	Mesh
Enable hole filling	Yes
Processing time	40 minutes 2 seconds
Software	
Version	1.4.3 build 6529
Platform	Windows 64

CS4 - summer foliage

Processing Report

17 April 2019

Survey Data

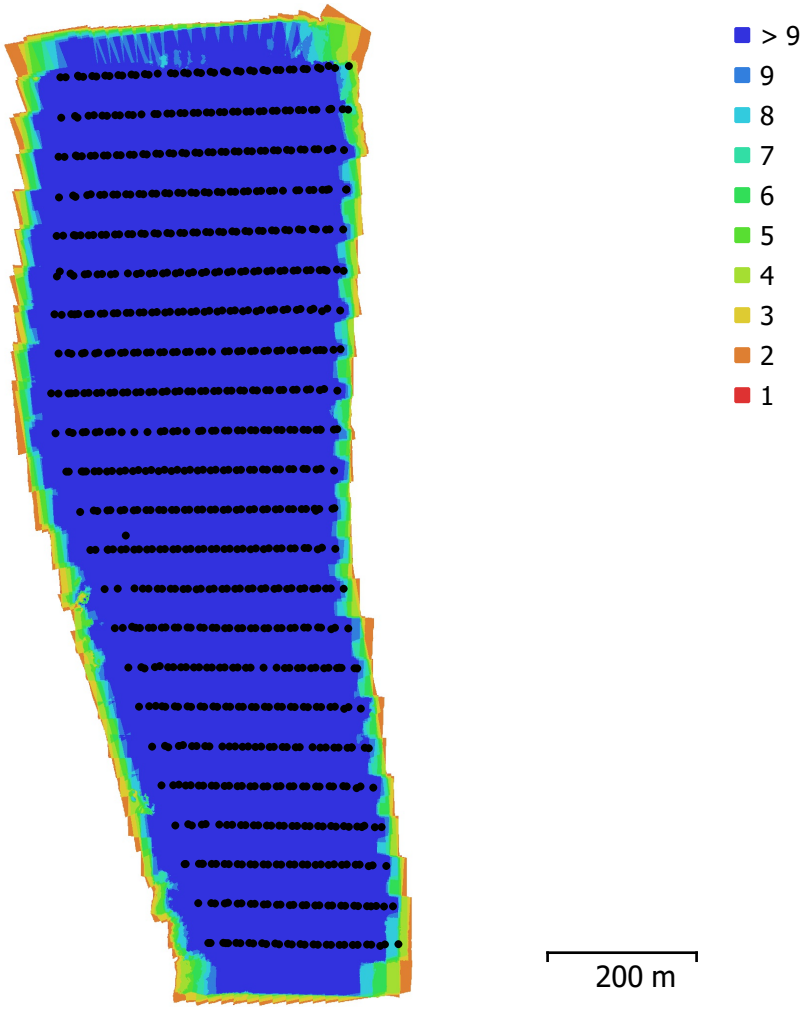

Fig. 1. Camera locations and image overlap.

Number of images:	878	Camera stations:	878
Flying altitude:	102 m	Tie points:	614,695
Ground resolution:	2.47 cm/pix	Projections:	2,646,621
Coverage area:	0.543 km²	Reprojection error:	0.869 pix

Camera Model	Resolution	Focal Length	Pixel Size	Precalibrated
FC6310 (8.8mm)	5472 x 3648	8.8 mm	2.41 x 2.41 µm	No

Table 1. Cameras.

Camera Calibration

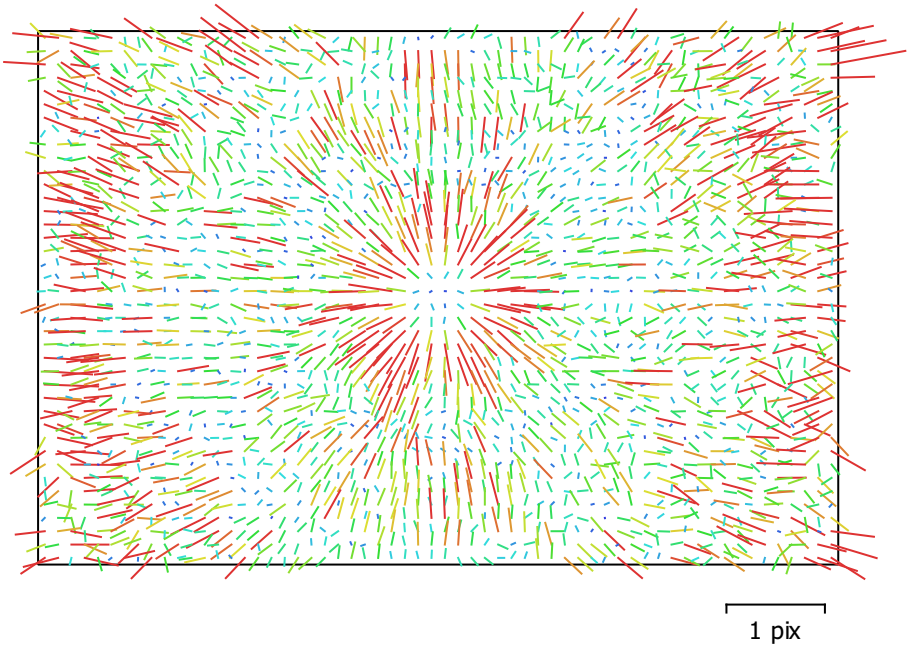

Fig. 2. Image residuals for FC6310 (8.8mm).

FC6310 (8.8mm)

878 images

Type	Resolution	Focal Length	Pixel Size
Frame	**5472 x 3648**	**8.8 mm**	**2.41 x 2.41 µm**

	Value	Error	F	Cx	Cy	K1	K2	K3	P1	P2
F	**3641.32**	0.18	1.00	0.03	-0.29	0.01	-0.02	0.06	0.03	0.06
Cx	**-11.3962**	0.1		1.00	-0.00	0.04	-0.01	0.02	0.98	-0.01
Cy	**62.483**	0.12			1.00	0.00	0.04	-0.06	-0.00	0.92
K1	**-0.000681988**	1.7e-05				1.00	-0.92	0.87	0.03	0.01
K2	**-0.0110925**	4.4e-05					1.00	-0.98	-0.01	0.02
K3	**0.0100762**	3.7e-05						1.00	0.01	-0.03
P1	**-0.00105054**	6.5e-06							1.00	-0.00
P2	**0.00334215**	6.8e-06								1.00

Table 2. Calibration coefficients and correlation matrix.

Camera Locations

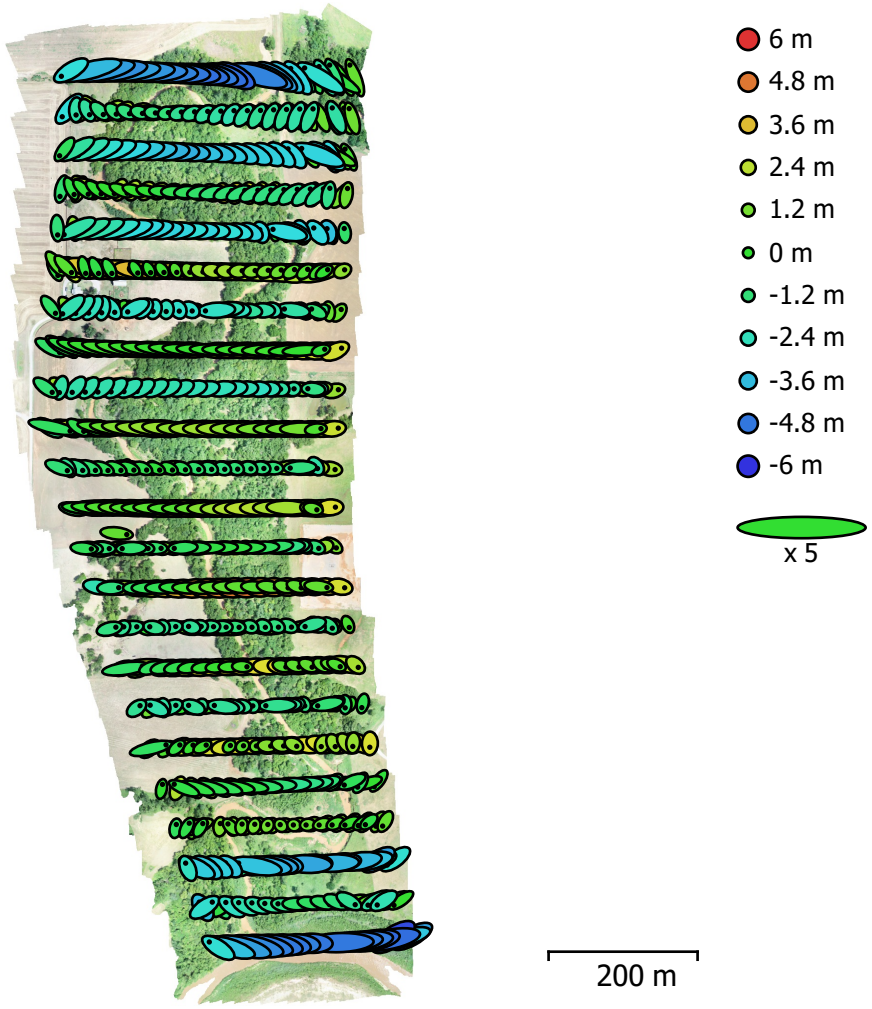

Fig. 3. Camera locations and error estimates.
Z error is represented by ellipse color. X,Y errors are represented by ellipse shape.
Estimated camera locations are marked with a black dot.

X error (m)	Y error (m)	Z error (m)	XY error (m)	Total error (m)
4.95493	1.72387	2.03241	5.24625	5.62617

Table 3. Average camera location error.
X - Longitude, Y - Latitude, Z - Altitude.

Digital Elevation Model

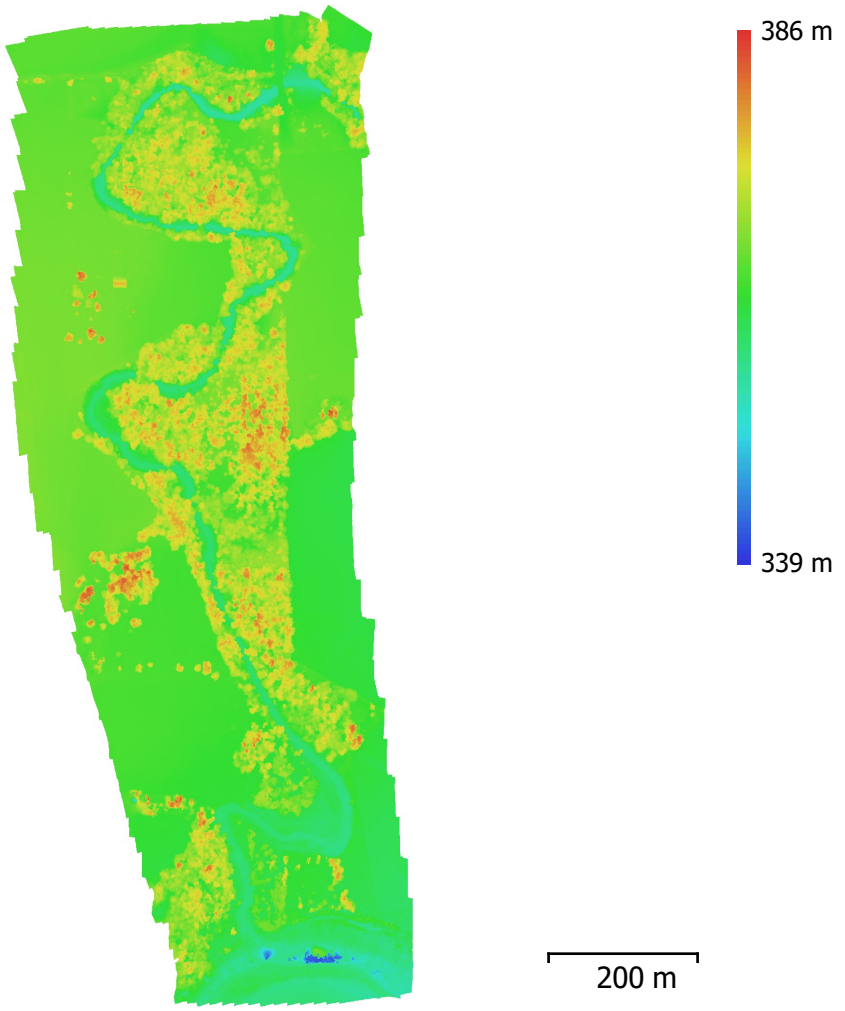

Fig. 4. Reconstructed digital elevation model.

Resolution:	9.88 cm/pix
Point density:	102 points/m²

Processing Parameters

General	
Cameras	878
Aligned cameras	878
Coordinate system	WGS 84 (EPSG::4326)
Rotation angles	Yaw, Pitch, Roll
Point Cloud	
Points	614,695 of 653,510
RMS reprojection error	0.213389 (0.868759 pix)
Max reprojection error	0.642398 (55.6632 pix)
Mean key point size	3.61358 pix
Point colors	3 bands, uint8
Key points	No
Average tie point multiplicity	4.59879
Alignment parameters	
Accuracy	High
Generic preselection	Yes
Reference preselection	Yes
Key point limit	40,000
Tie point limit	4,000
Adaptive camera model fitting	No
Matching time	1 hours 15 minutes
Alignment time	8 minutes 16 seconds
Dense Point Cloud	
Points	82,453,950
Point colors	3 bands, uint8
Reconstruction parameters	
Quality	Medium
Depth filtering	Aggressive
Depth maps generation time	9 hours 0 minutes
Dense cloud generation time	1 hours 34 minutes
Model	
Faces	5,496,930
Vertices	2,755,078
Vertex colors	3 bands, uint8
Reconstruction parameters	
Surface type	Arbitrary
Source data	Dense
Interpolation	Enabled
Quality	Medium
Depth filtering	Aggressive
Face count	5,496,930
Processing time	1 hours 8 minutes
DEM	
Size	8,623 x 18,379
Coordinate system	WGS 84 (EPSG::4326)
Reconstruction parameters	
Source data	Dense cloud
Interpolation	Enabled
Processing time	1 minutes 21 seconds
Orthomosaic	
Size	22,346 x 54,505
Coordinate system	WGS 84 (EPSG::4326)
Colors	3 bands, uint8
Reconstruction parameters	
Blending mode	Mosaic

Surface	Mesh
Enable hole filling	Yes
Processing time	37 minutes 11 seconds
Software	
Version	1.4.3 build 6529
Platform	Windows 64

CS4 - winter foliage

Processing Report

31 March 2019

Survey Data

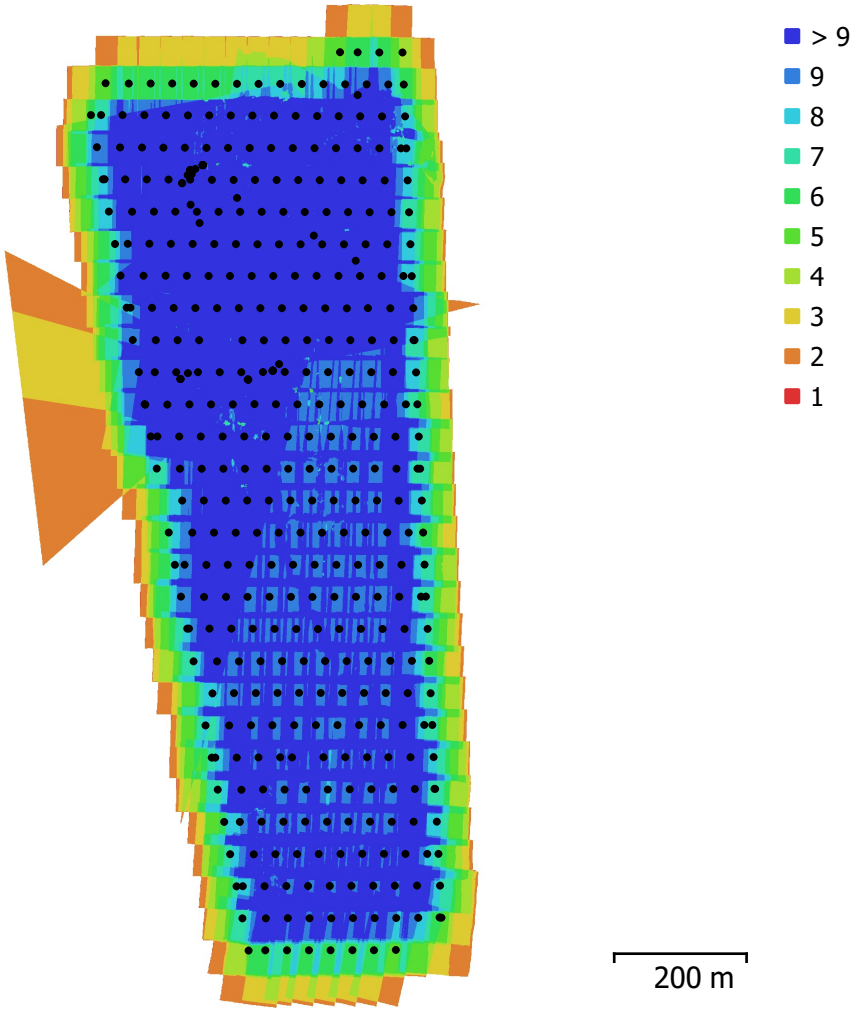

Fig. 1. Camera locations and image overlap.

Number of images:	425	Camera stations:	407
Flying altitude:	110 m	Tie points:	384,233
Ground resolution:	2.8 cm/pix	Projections:	1,455,742
Coverage area:	0.772 km²	Reprojection error:	0.519 pix

Camera Model	Resolution	Focal Length	Pixel Size	Precalibrated
FC6310 (8.8mm)	5472 x 3648	8.8 mm	2.41 x 2.41 µm	No

Table 1. Cameras.

Camera Calibration

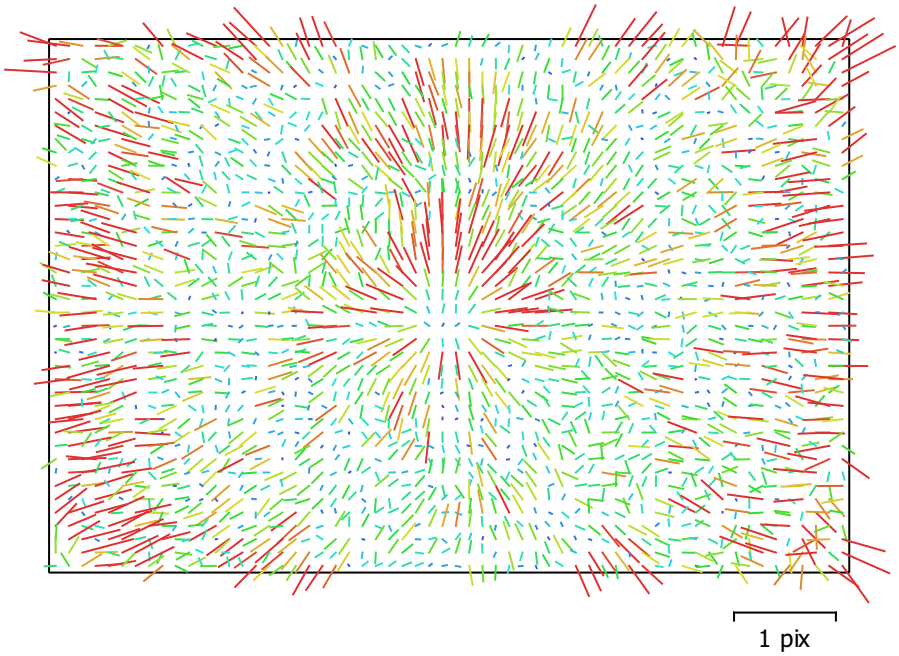

Fig. 2. Image residuals for FC6310 (8.8mm).

FC6310 (8.8mm)

425 images

Type	Resolution	Focal Length	Pixel Size
Frame	**5472 x 3648**	**8.8 mm**	**2.41 x 2.41 µm**

	Value	Error	F	Cx	Cy	K1	K2	K3	P1	P2
F	**3650.52**	0.22	1.00	0.13	-0.30	0.72	-0.04	0.07	-0.00	-0.13
Cx	**-17.0745**	0.26		1.00	-0.23	0.03	-0.04	0.05	0.91	-0.20
Cy	**21.0581**	0.27			1.00	-0.19	0.03	-0.04	-0.12	0.84
K1	**-0.000846964**	3.8e-05				1.00	-0.46	0.45	-0.07	-0.14
K2	**-0.00607219**	4.6e-05					1.00	-0.98	-0.03	0.02
K3	**0.00592567**	3.9e-05						1.00	0.04	-0.03
P1	**-0.0020569**	1.9e-05							1.00	-0.15
P2	**0.00104762**	1.8e-05								1.00

Table 2. Calibration coefficients and correlation matrix.

Camera Locations

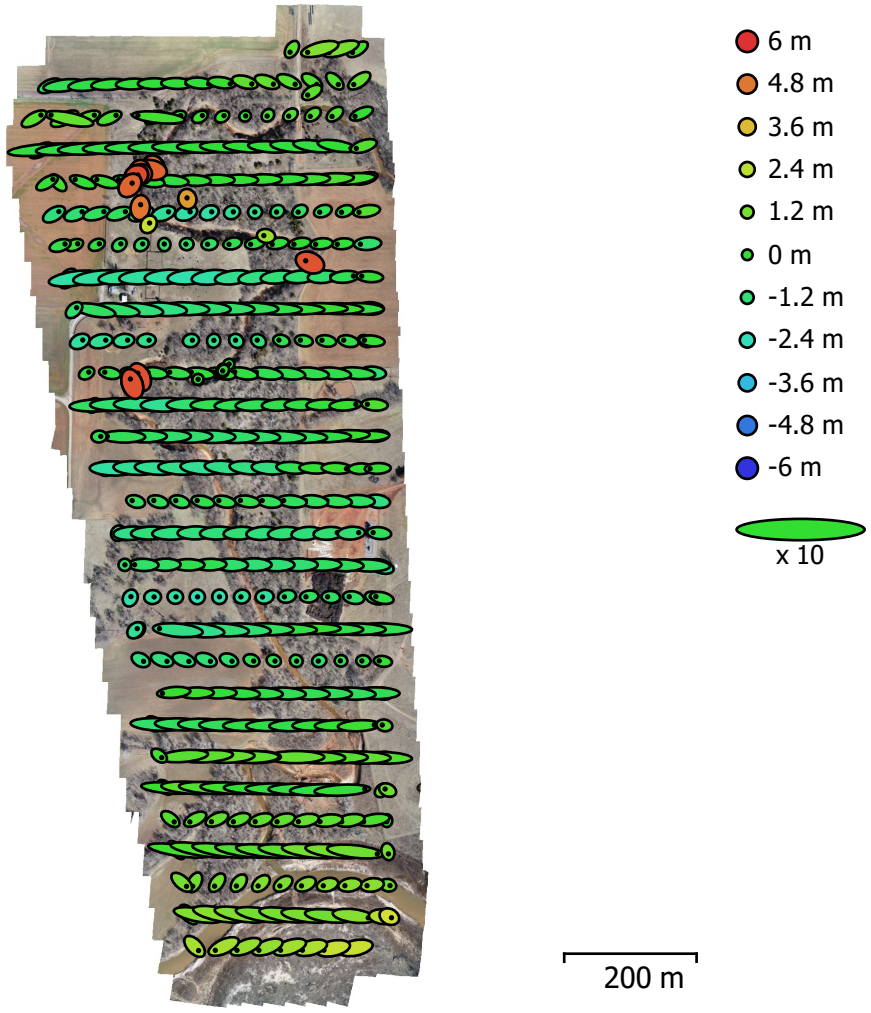

Fig. 3. Camera locations and error estimates.
Z error is represented by ellipse color. X,Y errors are represented by ellipse shape.
Estimated camera locations are marked with a black dot.

X error (m)	Y error (m)	Z error (m)	XY error (m)	Total error (m)
3.7182	0.490549	1.54397	3.75042	4.0558

Table 3. Average camera location error.
X - Longitude, Y - Latitude, Z - Altitude.

Digital Elevation Model

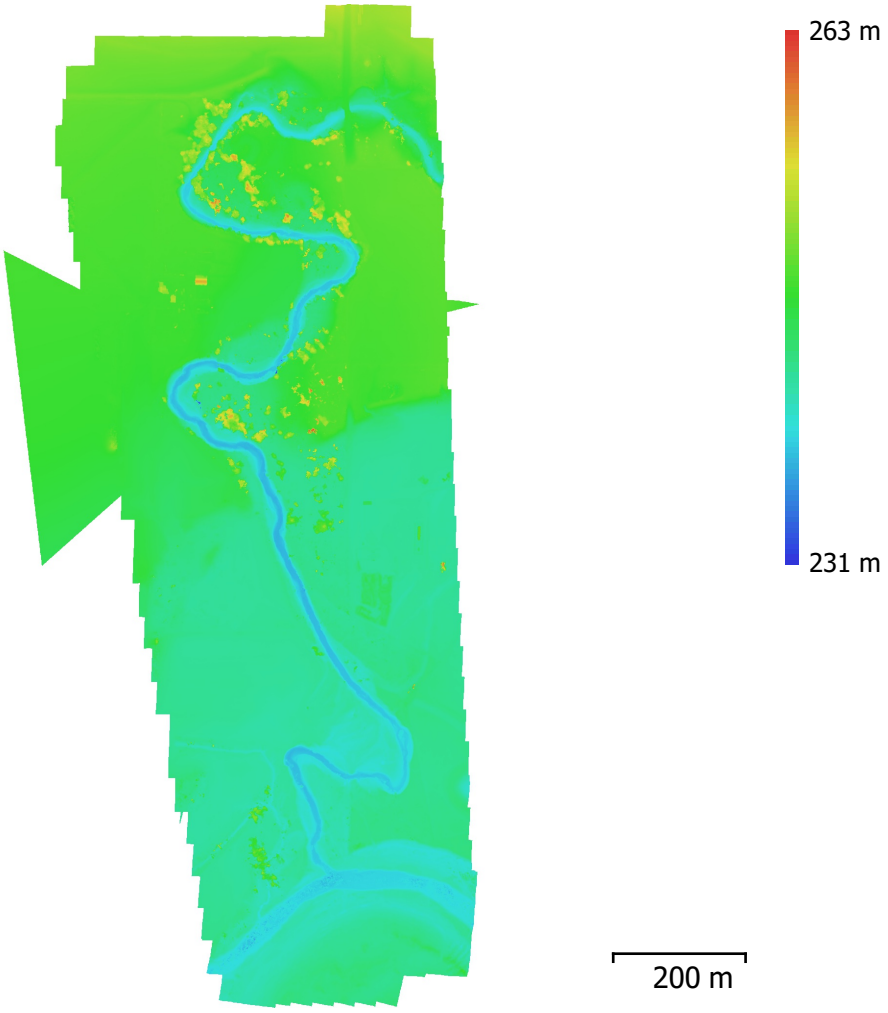

Fig. 4. Reconstructed digital elevation model.

Resolution:	11.2 cm/pix
Point density:	79.9 points/m²

Processing Parameters

General	
Cameras	425
Aligned cameras	407
Coordinate system	WGS 84 (EPSG::4326)
Rotation angles	Yaw, Pitch, Roll
Point Cloud	
Points	384,233 of 418,180
RMS reprojection error	0.19331 (0.518723 pix)
Max reprojection error	0.581201 (29.8789 pix)
Mean key point size	2.54345 pix
Point colors	3 bands, uint8
Key points	No
Average tie point multiplicity	3.80932
Alignment parameters	
Accuracy	High
Generic preselection	Yes
Reference preselection	Yes
Key point limit	40,000
Tie point limit	4,000
Adaptive camera model fitting	No
Matching time	25 minutes 9 seconds
Alignment time	6 minutes 23 seconds
Dense Point Cloud	
Points	62,479,524
Point colors	3 bands, uint8
Reconstruction parameters	
Quality	Medium
Depth filtering	Aggressive
Depth maps generation time	2 hours 23 minutes
Dense cloud generation time	10 minutes 33 seconds
Model	
Faces	4,126,139
Vertices	2,068,267
Vertex colors	3 bands, uint8
Reconstruction parameters	
Surface type	Height field
Source data	Dense
Interpolation	Enabled
Quality	Medium
Depth filtering	Aggressive
Face count	4,165,301
Processing time	2 minutes 37 seconds
DEM	
Size	9,012 x 18,403
Coordinate system	WGS 84 (EPSG::4326)
Reconstruction parameters	
Source data	Dense cloud
Interpolation	Enabled
Processing time	56 seconds
Orthomosaic	
Size	27,435 x 54,164
Coordinate system	WGS 84 (EPSG::4326)
Colors	3 bands, uint8
Reconstruction parameters	
Blending mode	Mosaic

Surface	Mesh
Enable hole filling	Yes
Processing time	20 minutes 7 seconds
Software	
Version	1.4.3 build 6529
Platform	Windows 64

Bathymetric Flight 2 - Nadir

Processing Report

26 April 2019

Survey Data

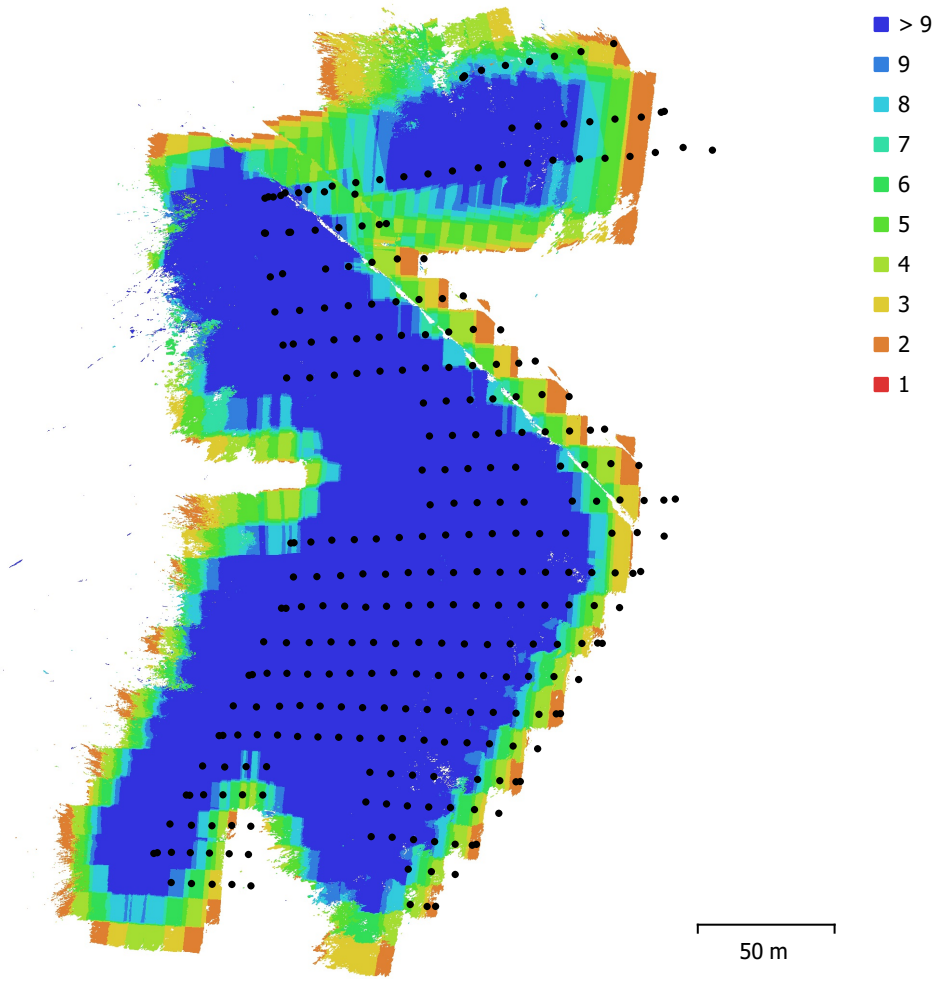

Fig. 1. Camera locations and image overlap.

Number of images:	378	Camera stations:	299
Flying altitude:	33 m	Tie points:	253,822
Ground resolution:	9.1 mm/pix	Projections:	924,303
Coverage area:	0.0464 km²	Reprojection error:	2.84 pix

Camera Model	Resolution	Focal Length	Pixel Size	Precalibrated
FC6310 (8.8mm)	5472 x 3648	8.8 mm	2.41 x 2.41 µm	No

Table 1. Cameras.

Camera Calibration

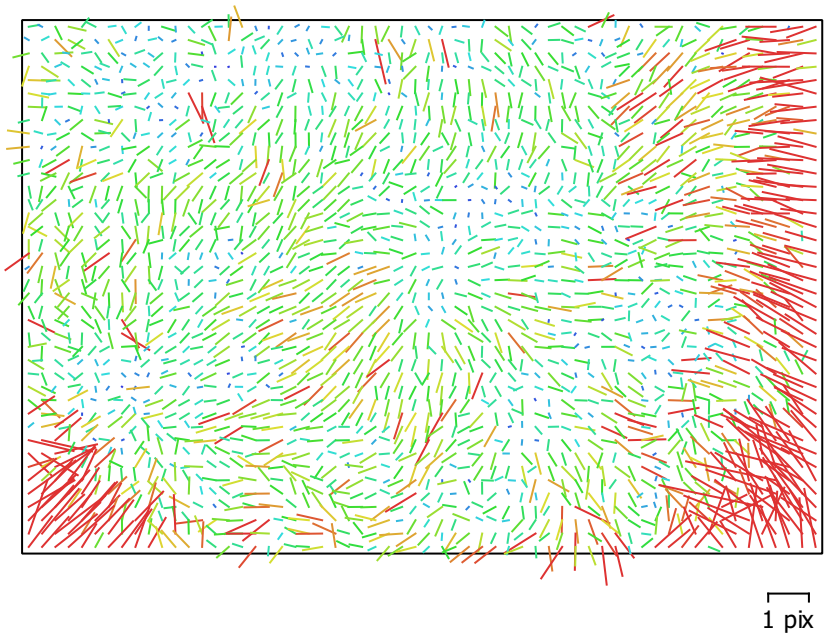

Fig. 2. Image residuals for FC6310 (8.8mm).

FC6310 (8.8mm)

378 images

Type	Resolution	Focal Length	Pixel Size
Frame	**5472 x 3648**	**8.8 mm**	**2.41 x 2.41 µm**

	Value	Error	F	Cx	Cy	K1	K2	K3	P1	P2
F	**954.036**	59	1.00	0.12	0.11	-0.95	0.96	-0.95	0.97	0.97
Cx	**664.011**	9.9		1.00	0.20	-0.11	0.10	-0.09	0.11	0.12
Cy	**2873.17**	11			1.00	-0.10	0.07	-0.07	0.08	0.08
K1	**-0.00101903**	0.0001				1.00	-0.97	0.95	-0.90	-0.90
K2	**8.89393e-006**	2.1e-006					1.00	-1.00	0.93	0.93
K3	**-6.73802e-008**	2.5e-008						1.00	-0.92	-0.93
P1	**0.00188747**	0.00012							1.00	0.96
P2	**0.00216722**	0.00014								1.00

Table 2. Calibration coefficients and correlation matrix.

Camera Locations

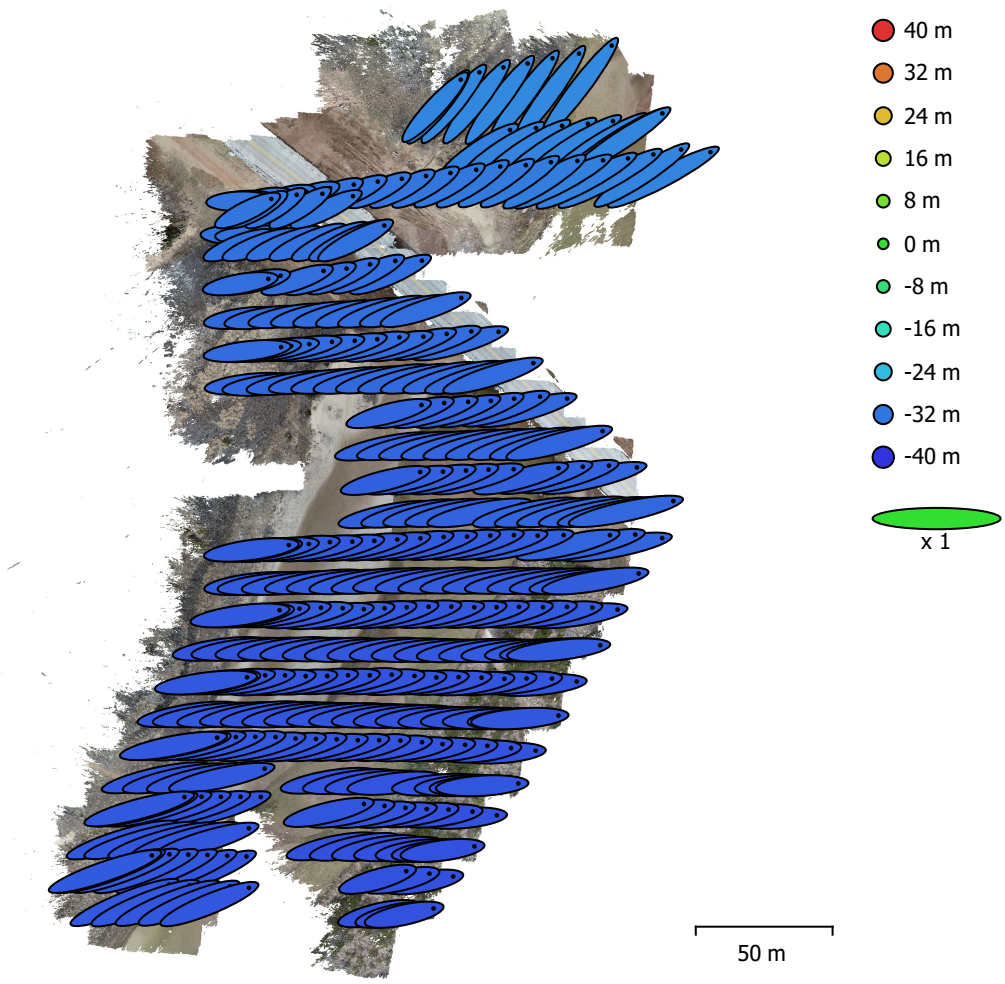

Fig. 3. Camera locations and error estimates.
Z error is represented by ellipse color. X,Y errors are represented by ellipse shape.
Estimated camera locations are marked with a black dot.

X error (m)	Y error (m)	Z error (m)	XY error (m)	Total error (m)
27.3061	8.39247	34.5221	28.5667	44.8089

Table 3. Average camera location error.
X - Longitude, Y - Latitude, Z - Altitude.

Ground Control Points

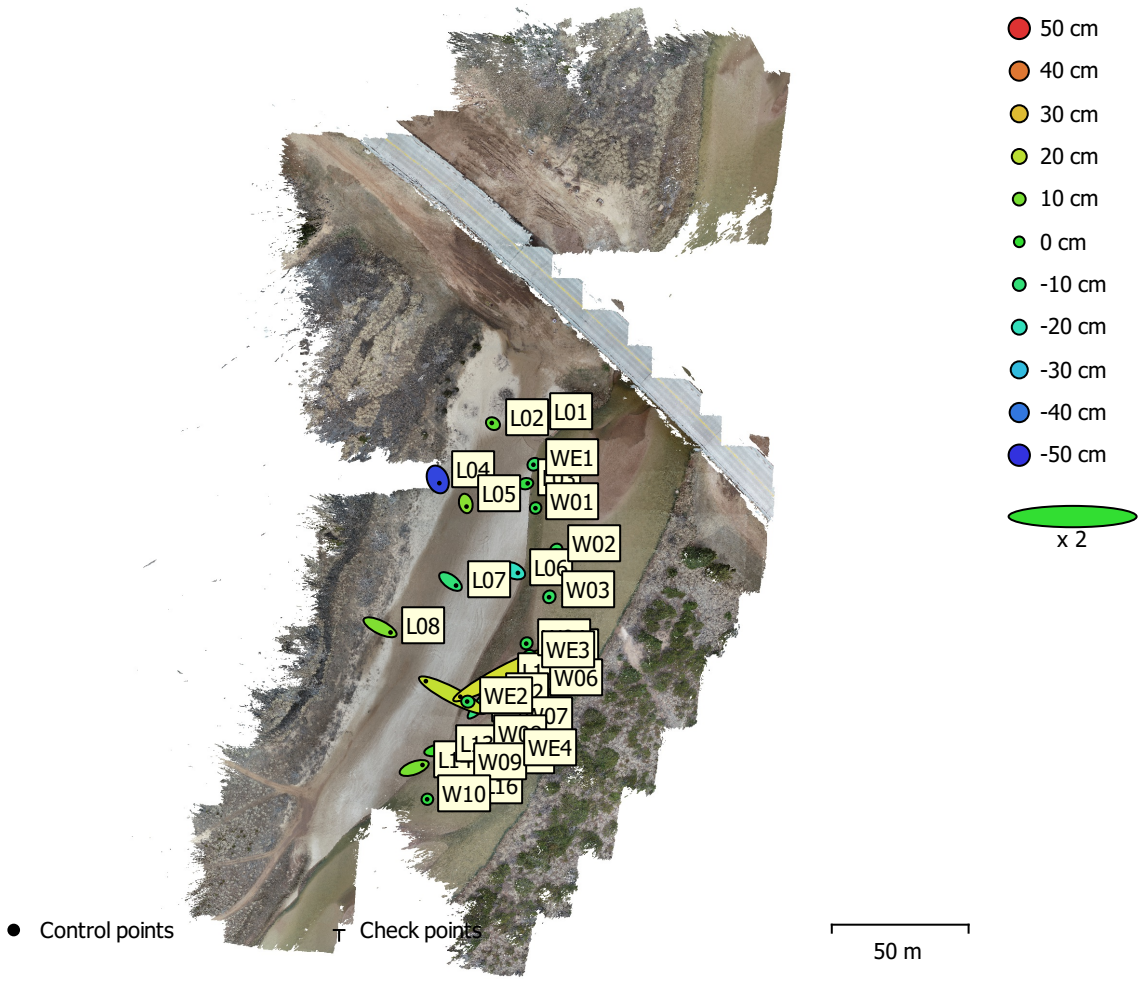

Fig. 4. GCP locations and error estimates.
Z error is represented by ellipse color. X,Y errors are represented by ellipse shape.
Estimated GCP locations are marked with a dot or crossing.

Count	X error (m)	Y error (m)	Z error (m)	XY error (m)	Total (m)
29	3.72063	2.23985	0.142085	4.34281	4.34513

Table 4. Control points RMSE.
X - Longitude, Y - Latitude, Z - Altitude.

Label	X error (m)	Y error (m)	Z error (m)	Total (m)	Image (pix)
L02	-0.426573	0.260808	0.0631091	0.503953	1.010 (16)
L01	-0.211079	1.20332	0.30168	1.25839	0.903 (20)
L04	0.577761	-1.36052	-0.472335	1.55175	0.333 (3)
L05	0.278668	-1.13525	0.125336	1.17565	1.868 (10)
L03	0.710378	0.128252	-0.0249245	0.722293	1.406 (24)
L06	1.69679	-0.78872	-0.209072	1.88278	1.115 (16)
L11	6.17188	6.48696	-0.112304	8.95463	1.821 (16)
L07	2.0217	-1.47344	-0.0994758	2.50364	2.534 (14)
L08	3.82146	-1.8912	0.112737	4.26531	2.194 (17)
L09	-9.76759	5.10655	0.211336	11.0239	2.510 (16)
L12	2.06339	-0.835458	-0.0553417	2.2268	2.288 (16)
L10	-14.8949	-7.95501	0.235506	16.8877	2.211 (16)
L14	3.03928	1.1079	0.102225	3.23653	2.127 (14)
L13	2.61647	0.48852	0.0192162	2.66176	2.356 (18)
L16	1.17159	0.836403	-0.0233169	1.4397	1.478 (16)
L15	1.1471	-0.176139	-0.160626	1.17161	1.471 (16)
W01	-0.056454	-0.0617386	-0.0346438	0.0905478	7.713 (16)
W03	-0.108936	-0.144934	-0.0676387	0.193515	9.080 (18)
W02	-0.167312	-0.192377	-0.0564425	0.261128	5.812 (20)
W04	-0.115018	-0.110134	-0.0479072	0.166294	4.953 (17)
W06	0.000156287	0.0742284	-0.0246763	0.0782227	8.008 (19)
W07	-0.131257	0.0387683	-0.0263632	0.139379	6.491 (20)
W08	-0.23097	0.0149885	-0.0484025	0.236463	6.824 (15)
W09	-0.262887	0.0329765	-0.0598682	0.271627	3.318 (18)
W10	-0.0801371	-0.0101159	-0.0273759	0.0852862	5.212 (10)
WE1	-0.247677	-0.170945	-0.0713959	0.309296	1.629 (17)
WE4	-0.0942756	-0.0351803	-0.0366676	0.107098	5.876 (17)
WE2	-0.251539	0.0387367	-0.0593136	0.261324	2.802 (18)
WE3	-0.125864	-0.0145747	-0.0505674	0.136423	5.838 (19)
Total	**3.72063**	**2.23985**	**0.142085**	**4.34513**	**4.375**

Table 5. Control points.

X - Longitude, Y - Latitude, Z - Altitude.

Digital Elevation Model

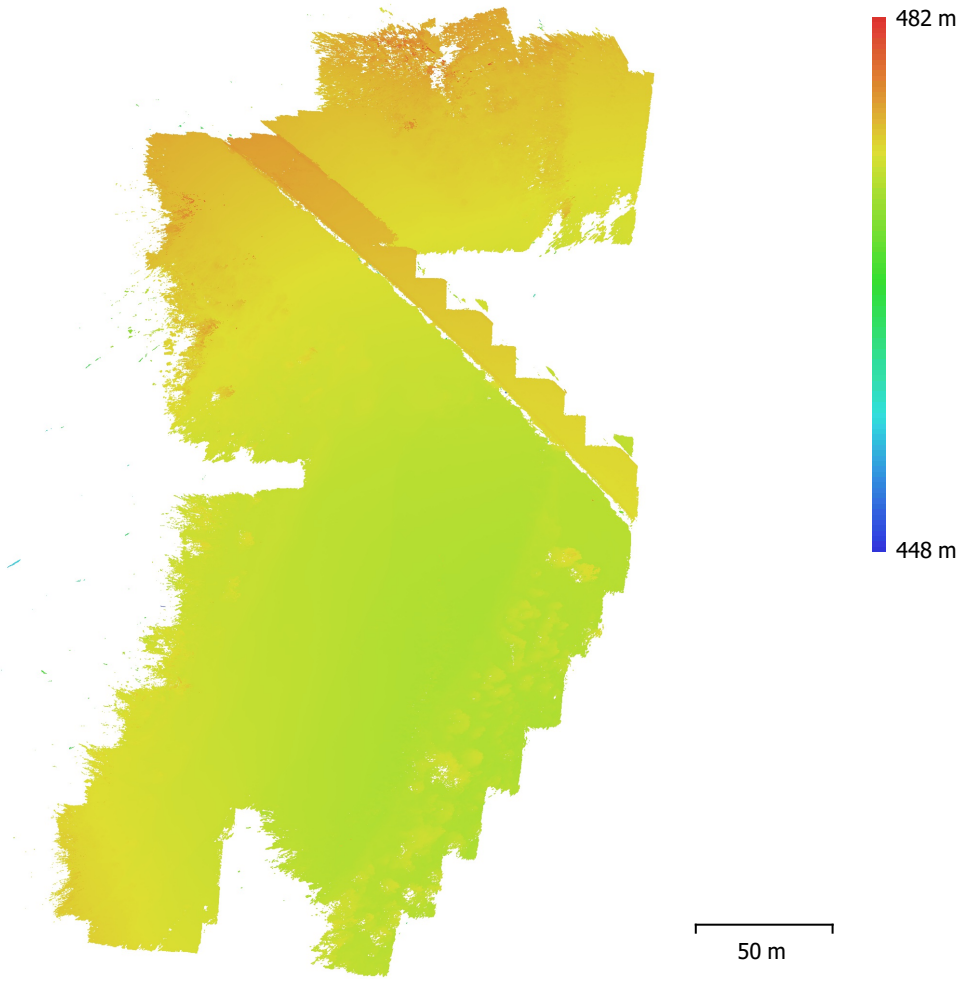

Fig. 5. Reconstructed digital elevation model.

Resolution:	unknown
Point density:	unknown

Processing Parameters

General	
Cameras	378
Aligned cameras	299
Markers	29
Shapes	
Polylines	1
Coordinate system	WGS 84 (EPSG::4326)
Rotation angles	Yaw, Pitch, Roll
Point Cloud	
Points	253,822 of 319,637
RMS reprojection error	0.895988 (2.83597 pix)
Max reprojection error	29.6573 (73.2483 pix)
Mean key point size	4.34876 pix
Point colors	3 bands, uint8
Key points	No
Average tie point multiplicity	3.81465
Alignment parameters	
Accuracy	High
Generic preselection	Yes
Reference preselection	Yes
Key point limit	40,000
Tie point limit	4,000
Adaptive camera model fitting	No
Matching time	21 minutes 9 seconds
Alignment time	7 minutes 32 seconds
Optimization parameters	
Parameters	f, cx, cy, k1-k3, p1, p2
Adaptive camera model fitting	No
Optimization time	47 seconds
Depth Maps	
Count	298
Depth maps generation parameters	
Quality	High
Filtering mode	Mild
Processing time	1 hours 47 minutes
Dense Point Cloud	
Points	176,606,853
Point colors	3 bands, uint8
Depth maps generation parameters	
Quality	High
Filtering mode	Mild
Processing time	1 hours 47 minutes
Dense cloud generation parameters	
Processing time	2 hours 14 minutes
Software	
Version	1.5.2 build 7838
Platform	Windows 64

Bathymetric Flight 2 - Oblique

Processing Report

25 April 2019

Survey Data

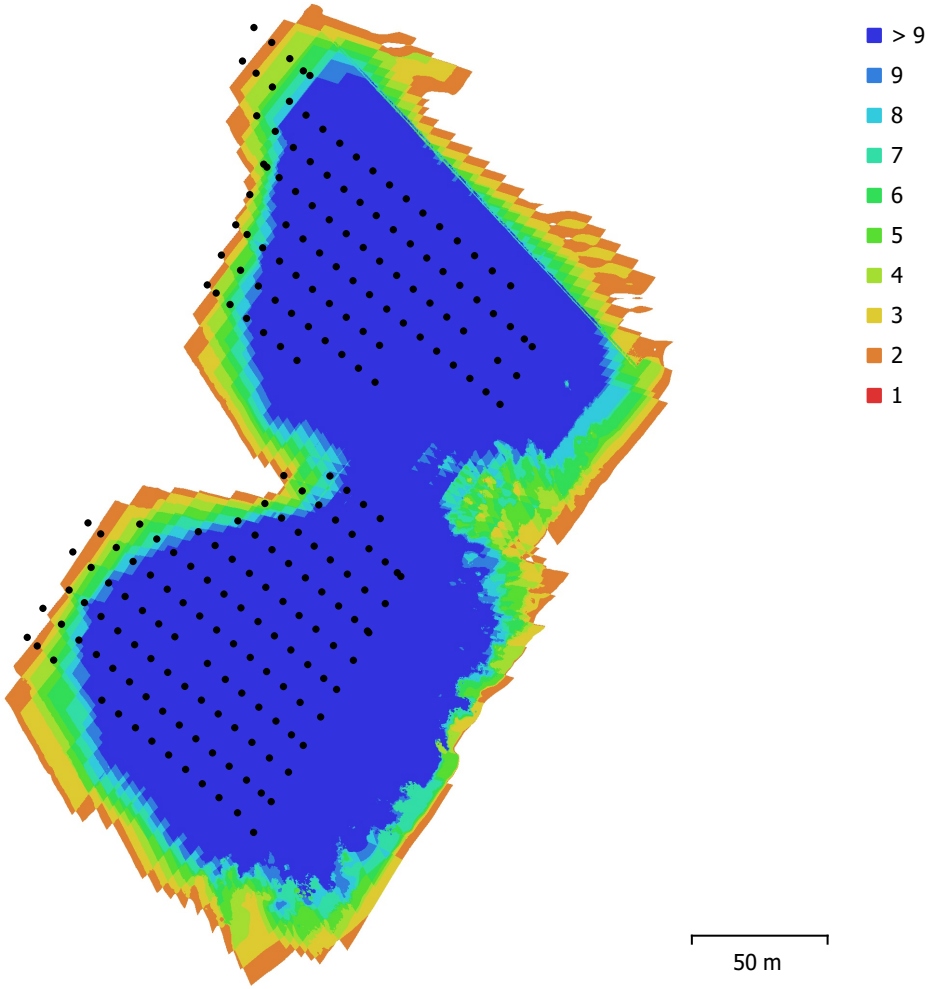

Fig. 1. Camera locations and image overlap.

Number of images:	291	Camera stations:	223
Flying altitude:	43.4 m	Tie points:	181,517
Ground resolution:	1.1 cm/pix	Projections:	641,804
Coverage area:	0.0457 km²	Reprojection error:	1.77 pix

Camera Model	Resolution	Focal Length	Pixel Size	Precalibrated
FC6310 (8.8mm)	5472 x 3648	8.8 mm	2.41 x 2.41 µm	No

Table 1. Cameras.

Camera Calibration

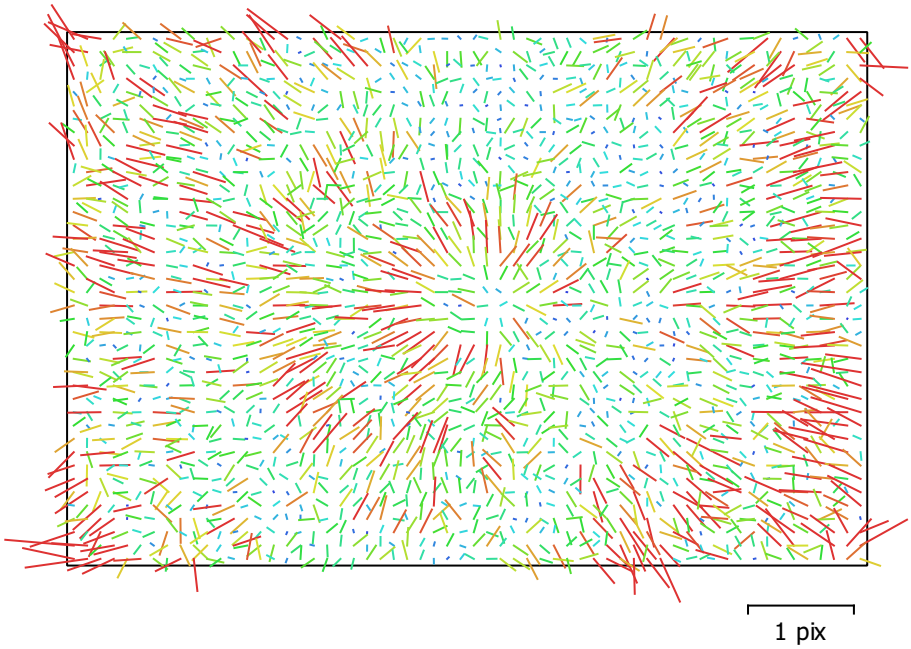

Fig. 2. Image residuals for FC6310 (8.8mm).

FC6310 (8.8mm)

291 images

Type	Resolution	Focal Length	Pixel Size
Frame	**5472 x 3648**	**8.8 mm**	**2.41 x 2.41 µm**

	Value	Error	F	Cx	Cy	K1	K2	K3	P1	P2
F	**3626.59**	6.2	1.00	-0.04	-0.98	-0.05	-0.30	0.48	-0.02	0.13
Cx	**-12.3822**	0.71		1.00	0.04	0.00	0.02	-0.02	0.39	-0.03
Cy	**19.7229**	3.6			1.00	0.05	0.29	-0.47	0.03	-0.07
K1	**0.00138834**	7.2e-005				1.00	-0.81	0.70	0.03	-0.25
K2	**-0.00854181**	0.00019					1.00	-0.97	0.01	0.02
K3	**0.00887912**	0.00019						1.00	-0.01	0.03
P1	**5.90538e-005**	2.6e-005							1.00	-0.05
P2	**-0.000835984**	1.9e-005								1.00

Table 2. Calibration coefficients and correlation matrix.

Camera Locations

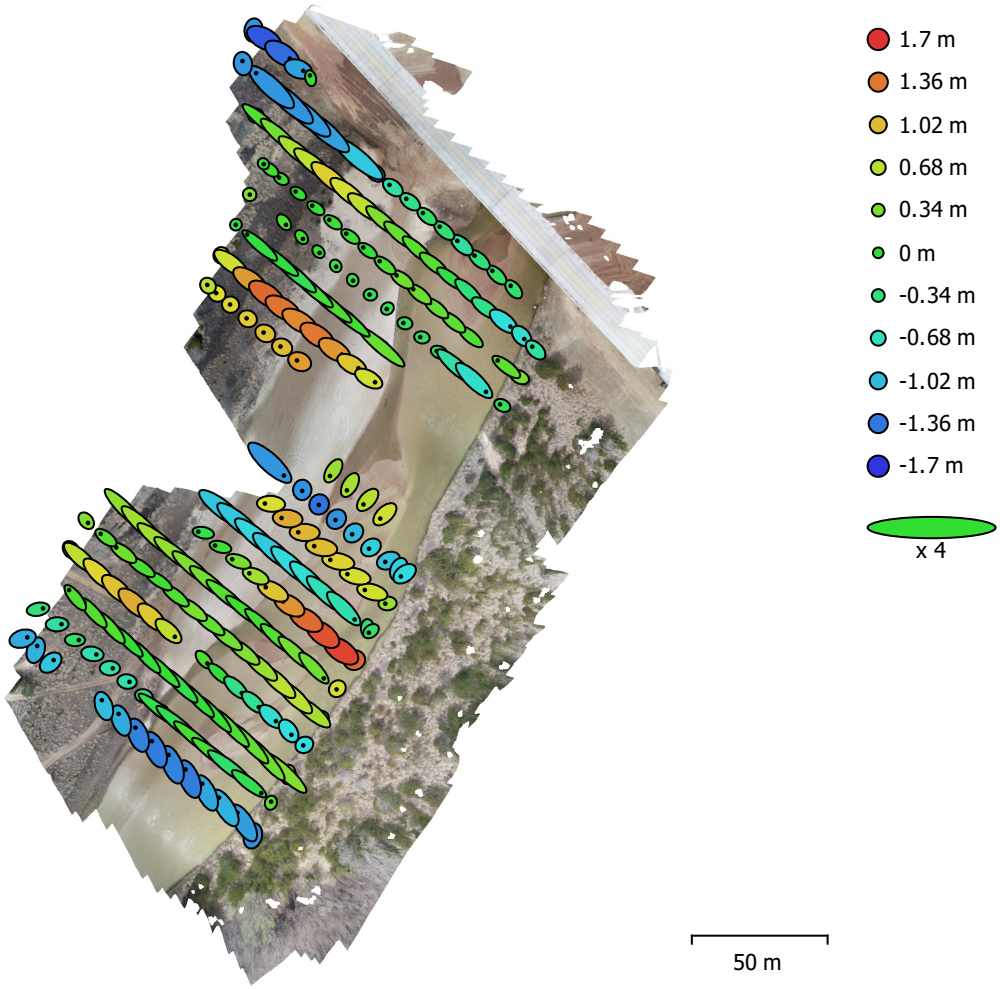

Fig. 3. Camera locations and error estimates.
Z error is represented by ellipse color. X,Y errors are represented by ellipse shape.
Estimated camera locations are marked with a black dot.

X error (m)	Y error (m)	Z error (m)	XY error (m)	Total error (m)
1.61348	1.40593	0.719891	2.14008	2.25792

Table 3. Average camera location error.
X - Longitude, Y - Latitude, Z - Altitude.

Digital Elevation Model

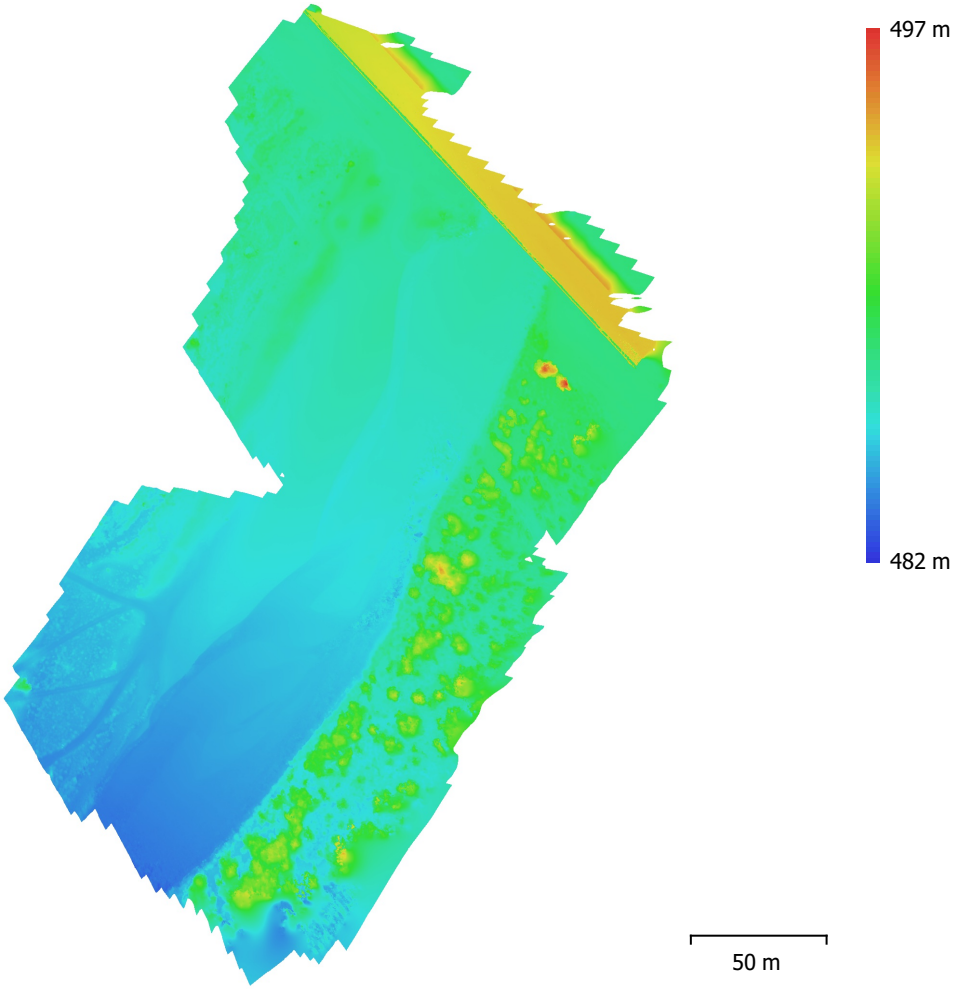

Fig. 4. Reconstructed digital elevation model.

Resolution:	2.2 cm/pix
Point density:	0.206 points/cm²

Processing Parameters

General	
Cameras	291
Aligned cameras	223
Coordinate system	WGS 84 (EPSG::4326)
Rotation angles	Yaw, Pitch, Roll
Point Cloud	
Points	181,517 of 240,771
RMS reprojection error	0.146808 (1.76727 pix)
Max reprojection error	0.442659 (55.4682 pix)
Mean key point size	9.48575 pix
Point colors	3 bands, uint8
Key points	No
Average tie point multiplicity	4.14762
Alignment parameters	
Accuracy	Medium
Generic preselection	Yes
Reference preselection	Yes
Key point limit	40,000
Tie point limit	4,000
Adaptive camera model fitting	No
Matching time	7 minutes 46 seconds
Alignment time	6 minutes 16 seconds
Software version	1.5.2.7838
Depth Maps	
Count	223
Depth maps generation parameters	
Quality	High
Filtering mode	Aggressive
Processing time	8 hours 1 minutes
Software version	1.5.2.7838
Dense Point Cloud	
Points	120,844,250
Point colors	3 bands, uint8
Depth maps generation parameters	
Quality	High
Filtering mode	Aggressive
Processing time	8 hours 1 minutes
Dense cloud generation parameters	
Processing time	1 hours 2 minutes
Software version	1.5.2.7838
Model	
Faces	7,991,082
Vertices	4,002,565
Vertex colors	3 bands, uint8
Depth maps generation parameters	
Quality	High
Filtering mode	Aggressive
Processing time	8 hours 1 minutes
Reconstruction parameters	
Surface type	Height field

General	
Source data	Dense cloud
Interpolation	Enabled
Strict volumetric masks	No
Processing time	4 minutes 59 seconds
Software version	1.5.2.7838
DEM	
Size	14,793 x 19,710
Coordinate system	WGS 84 (EPSG::4326)
Reconstruction parameters	
Source data	Dense cloud
Interpolation	Enabled
Processing time	1 minutes 47 seconds
Software version	1.5.2.7838
Orthomosaic	
Size	22,969 x 33,021
Coordinate system	WGS 84 (EPSG::4326)
Colors	3 bands, uint8
Reconstruction parameters	
Blending mode	Mosaic
Surface	Mesh
Enable hole filling	Yes
Processing time	10 minutes 52 seconds
Software version	1.5.2.7838
Software	
Version	1.5.2 build 7838
Platform	Windows 64

Bathymetric Flight 2 - both

Processing Report

24 April 2019

Survey Data

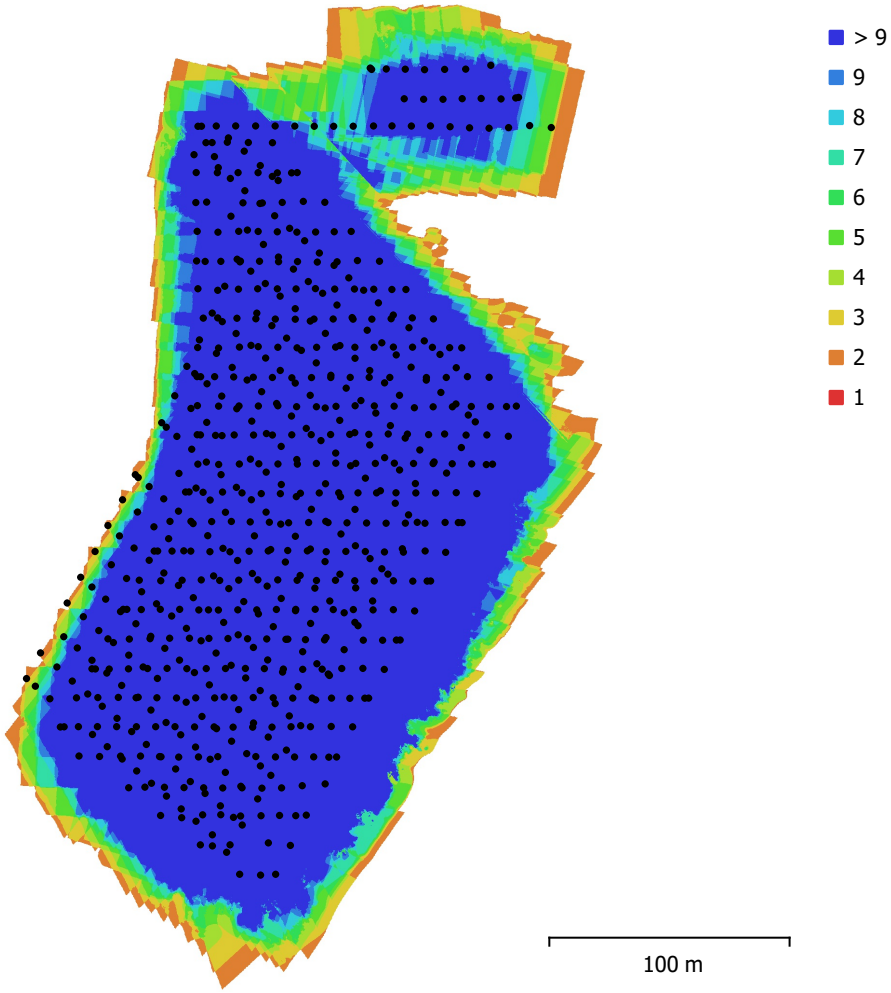

Fig. 1. Camera locations and image overlap.

Number of images:	669	Camera stations:	669
Flying altitude:	40.2 m	Tie points:	433,127
Ground resolution:	1.01 cm/pix	Projections:	1,813,554
Coverage area:	0.0605 km²	Reprojection error:	1.78 pix

Camera Model	Resolution	Focal Length	Pixel Size	Precalibrated
FC6310 (8.8mm)	5472 x 3648	8.8 mm	2.41 x 2.41 µm	No

Table 1. Cameras.

Camera Calibration

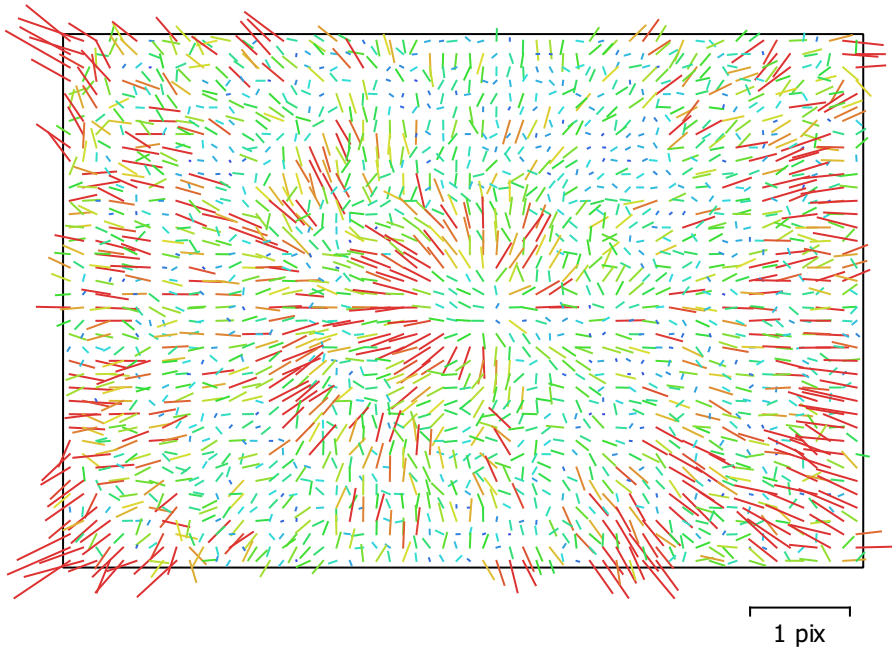

Fig. 2. Image residuals for FC6310 (8.8mm).

FC6310 (8.8mm)

669 images

Type	Resolution	Focal Length	Pixel Size
Frame	**5472 x 3648**	**8.8 mm**	**2.41 x 2.41 µm**

	Value	Error	F	Cx	Cy	K1	K2	K3	P1	P2
F	**3652.05**	0.48	1.00	0.34	-0.99	0.14	-0.04	0.07	0.09	-0.30
Cx	**-16.8682**	0.044		1.00	-0.31	0.23	-0.03	0.03	0.73	-0.49
Cy	**1.56042**	0.27			1.00	-0.13	0.05	-0.08	-0.05	0.27
K1	**-0.000490531**	3.6e-005				1.00	-0.88	0.83	0.21	-0.43
K2	**-0.00669811**	9.4e-005					1.00	-0.98	-0.03	0.04
K3	**0.0073919**	8.3e-005						1.00	0.03	-0.05
P1	**-0.000232114**	3.1e-006							1.00	-0.37
P2	**-0.000480673**	4.6e-006								1.00

Table 2. Calibration coefficients and correlation matrix.

Camera Locations

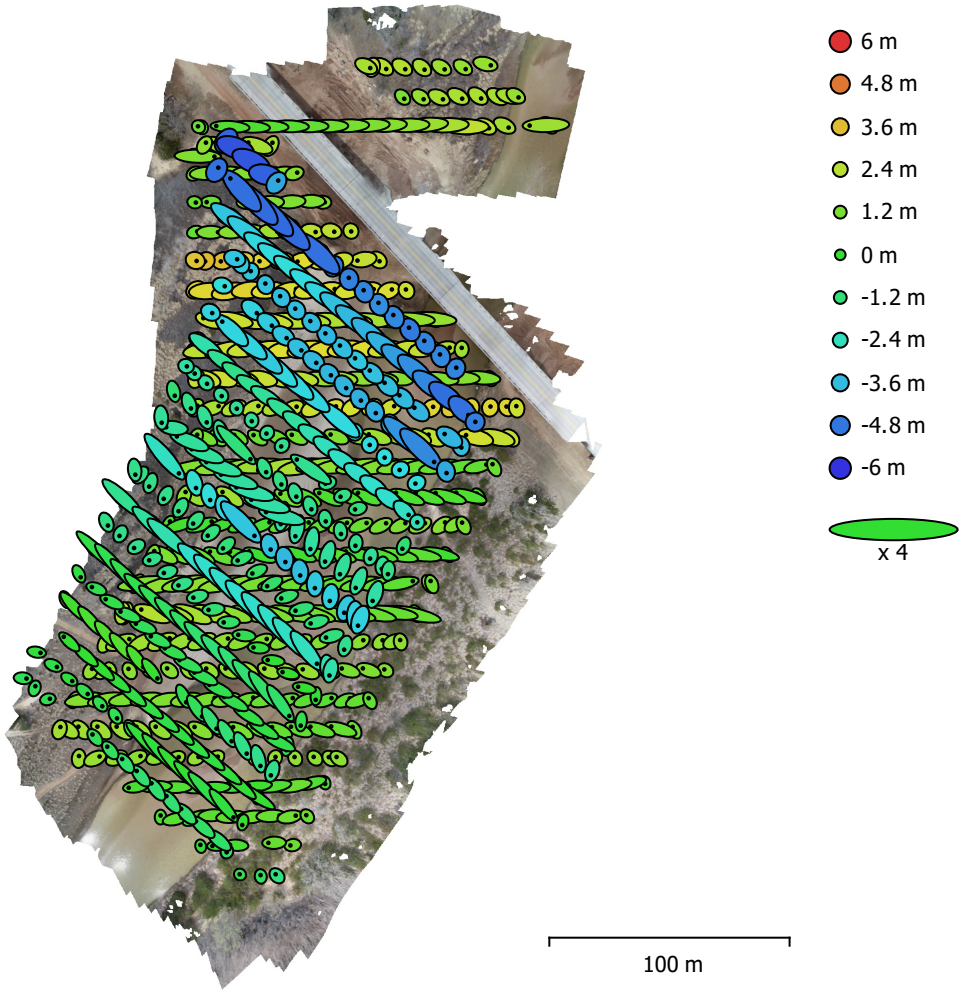

Fig. 3. Camera locations and error estimates.
Z error is represented by ellipse color. X,Y errors are represented by ellipse shape.
Estimated camera locations are marked with a black dot.

X error (m)	Y error (m)	Z error (m)	XY error (m)	Total error (m)
1.76473	1.01934	2.11847	2.03797	2.93959

Table 3. Average camera location error.
X - Longitude, Y - Latitude, Z - Altitude.

Digital Elevation Model

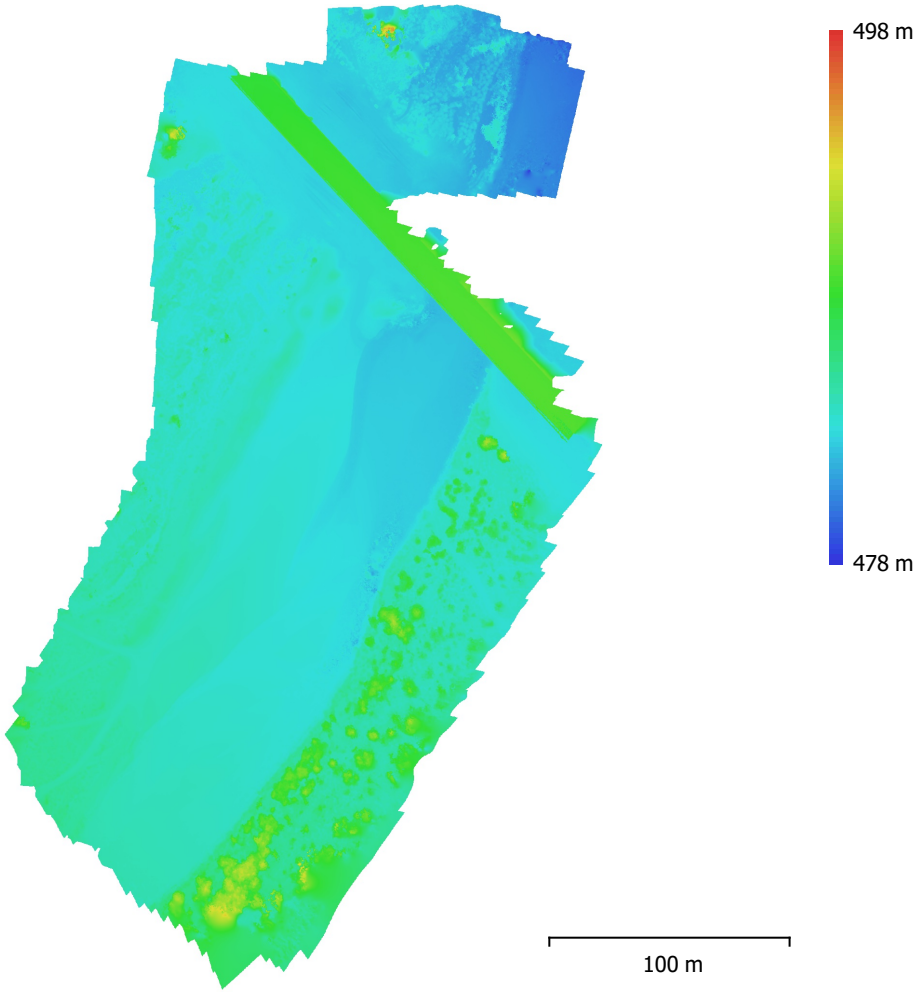

Fig. 4. Reconstructed digital elevation model.

Resolution:	2.03 cm/pix
Point density:	0.243 points/cm²

Processing Parameters

General	
Cameras	669
Aligned cameras	669
Coordinate system	WGS 84 (EPSG::4326)
Rotation angles	Yaw, Pitch, Roll
Point Cloud	
Points	433,127 of 470,960
RMS reprojection error	0.15515 (1.77576 pix)
Max reprojection error	0.468457 (64.5672 pix)
Mean key point size	9.31905 pix
Point colors	3 bands, uint8
Key points	No
Average tie point multiplicity	4.93223
Alignment parameters	
Accuracy	Medium
Generic preselection	Yes
Reference preselection	Yes
Key point limit	40,000
Tie point limit	4,000
Adaptive camera model fitting	No
Matching time	19 minutes 24 seconds
Alignment time	4 minutes 35 seconds
Software version	1.5.2.7838
Depth Maps	
Count	669
Depth maps generation parameters	
Quality	High
Filtering mode	Aggressive
Processing time	1 days 18 hours
Software version	1.5.2.7838
Dense Point Cloud	
Points	213,555,804
Point colors	3 bands, uint8
Depth maps generation parameters	
Quality	High
Filtering mode	Aggressive
Processing time	1 days 18 hours
Dense cloud generation parameters	
Processing time	6 hours 46 minutes
Software version	1.5.2.7838
Model	
Faces	14,160,829
Vertices	7,088,466
Vertex colors	3 bands, uint8
Depth maps generation parameters	
Quality	High
Filtering mode	Aggressive
Processing time	1 days 18 hours
Reconstruction parameters	
Surface type	Height field

General	
Source data	Dense cloud
Interpolation	Enabled
Strict volumetric masks	No
Processing time	9 minutes 4 seconds
Software version	1.5.2.7838
DEM	
Size	16,724 x 23,402
Coordinate system	WGS 84 (EPSG::4326)
Reconstruction parameters	
Source data	Dense cloud
Interpolation	Enabled
Processing time	2 minutes 46 seconds
Software version	1.5.2.7838
Orthomosaic	
Size	25,023 x 40,476
Coordinate system	WGS 84 (EPSG::4326)
Colors	3 bands, uint8
Reconstruction parameters	
Blending mode	Mosaic
Surface	Mesh
Enable hole filling	Yes
Processing time	28 minutes 28 seconds
Software version	1.5.2.7838
Software	
Version	1.5.2 build 7838
Platform	Windows 64

VITA

Victoria Natalie

Candidate for the Degree of

Master of Science

Thesis: ENVIRONMENTAL APPLICATIONS FOR PHOTOGRAMMETRY WITH UAS

Major Field: Mechanical and Aerospace Engineering

Biographical:

Education:

Completed the requirements for the Master of Science in Mechanical and Aerospace Engineering at Oklahoma State University, Stillwater, Oklahoma in May, 2019.

Completed the requirements for the Bachelor of Science in Mechanical Engineering at Texas A & M - Kingsville, Kingsville, Texas in May, 2012.

Experience:

Worked as a Design Engineer for L3 Technologies from 2012 to 2017.